Transactions of the ASME, Journal of Heat Transfer (ISSN 0022-1481) is published monthly by The American Society of Mechanical Engineers, Three Park Avenue, New York, NY 10016. Periodicals postage paid at New York, NY and additional mailing offices. POSTMASTER: Send address changes to Transactions of the ASME, Journal of Heat Transfer, c/o THE AMERICAN SOCIETY OF MECHANICAL ENGINEERS, 22 Law Drive, Box 2300, Fairfield, NJ 07007-2300. **CHANGES OF ADDRESS** must be received at Society headquarters seven weeks before they are to be effective. Please send old label and new address. **STATEMENT from By-Laws.** The Society shall not be responsible for statements or opinions advanced in papers or ... printed in its publications (B7.1, Para. 3).

Journal of Heat Transfer

Published Monthly by ASME

VOLUME 131 • NUMBER 3 • MARCH 2009

GUEST EDITORIAL

MICRO/NANOSCALE HEAT TRANSFER—PART I

(Contents continued on inside back cover)

This journal is printed on acid-free paper, which exceeds the ANSI Z39.48-1992 specification for permanence of paper and library materials. ♾™
♻ 85% recycled content, including 10% post-consumer fibers.

Journal of Heat Transfer **Volume 131, Number 3** **MARCH 2009**

The ASME Journal of Heat Transfer is abstracted and indexed in the following:

Applied Science and Technology Index, Chemical Abstracts, Chemical Engineering and Biotechnology Abstracts (Electronic equivalent of Process and Chemical Engineering), Civil Engineering Abstracts, Compendex (The electronic equivalent of Engineering Index), Corrosion Abstracts, Current Contents, E & P Health, Safety, and Environment, Ei EncompassLit, Engineered Materials Abstracts, Engineering Index, Enviroline (The electronic equivalent of Environment Abstracts), Environment Abstracts, Environmental Engineering Abstracts, Environmental Science and Pollution Management, Fluidex, Fuel and Energy Abstracts, Index to Scientific Reviews, INSPEC, International Building Services Abstracts, Mechanical & Transportation Engineering Abstracts, Mechanical Engineering Abstracts, METADEX (The electronic equivalent of Metals Abstracts and Alloys Index), Petroleum Abstracts, Process and Chemical Engineering, Referativnyi Zhurnal, Science Citation Index, SciSearch (The electronic equivalent of Science Citation Index), Theoretical Chemical Engineering

Journal of Heat Transfer

Guest Editorial

Special Issue on Micro/Nanoscale Heat Transfer—Part I

Research and education on micro/nanoscale heat transfer have advanced rapidly over the last decade through many dedicated individuals and teams, with direct impact now extending into other fields in both science and engineering. Continuing the synergistic efforts in 2002 and 2007,[1] ASME Micro/Nanoscale Heat Transfer International Conference (MNHT08) was held in National Cheng Kung University, Tainan, Taiwan, during January 6–9, 2008: http://www.asmeconferences.org/MNHT08/index.cfm. The conference is dedicated to Dr. Chang-Lin Tien (1935–2002), a world renowned scholar and a leader in higher education, whose intellect and unique visions have continued to inspire our most serious efforts in expanding the frontiers of micro/nanoscale heat transfer. It is with great pleasure that we present the selected papers from MNHT08 in the next two issues of the *ASME Journal of Heat Transfer*. Part II will appear as the April 2009 issue.

MNHT08 is composed of 18 technical tracks, with 5 keynote lecturers and over 300 participants from 18 countries. The 257 technical papers cover the full spectrum from microscopic thermophysical processes and properties, microfluidics and nanofluidics, heat transfer in small scale, ultrafast heat transport, interfacial heat transfer, nanofluids, microchannels, micro/nanoscale experimental heat transfer, micro/miniature two-phase systems, thermophysical and mechanical properties, ultrafast coupling in small scales, nano-systems and engineering, nano/microscale thermal radiation, computational micro/nanoscale heat and mass transfer, to micro/nanoscale heat and mass transfer in bio/medical systems. The papers included in this issue are representatives selected from these areas of research. There are a few papers in this issue that are review in nature, for the purpose of capturing the progress being made in a field as well as for presenting new challenges for the future. There are also research papers reporting innovative approaches and new findings, aiming toward advancing the state-of-the-art development in micro/nanoscale heat and mass transfer. Two salient features combined, we hope this issue will not only serve the community well, but also provide a valuable collection for inspiring new researchers to join this fascinating area of research.

Researchers in micro/nanoscale heat and mass transfer have enjoyed strong growth of the field over the past decade. Many sophisticated physical phenomena in small scales have been unveiled by dedicated individuals and research teams. The rapid evolution and continued explorations into even finer scales of space and time, however, may often generate more profound physics to be better understood. This is particularly the case when the thermal field is coupling with other fields in transporting mass, energy, momentum, and charges in micro/nanoscale. Combined approaches that integrate over analytical, experimental, and numerical phases have now become more important than ever in unveiling the interweaving physical phenomena in smaller scale. It is important to continue our endeavors in generating in-depth scientific understanding and enabling commercial technology for advancing micro/nanodevices, but it may be equally important to "wrap up" our knowledge by reviewing what we have tried to establish from time to time. This focus will remain as the ASME Micro/Nanoscale Heat Transfer International Conference continues into the future.

Special thanks are extended to the reviewers, the Editorial Assistant Shefali Patel, and publishing staff for the *ASME Journal of Heat Transfer*, who have made this special issue on *Micro/Nanoscale Heat Transfer* a reality. Enthusiastic supports from National Cheng Kung University, Chinese Society of Mechanical Engineers, and Industrial Technology and Research Institute (ITRI) in Taiwan are greatly appreciated. We wish to thank the Air Force Office of Scientific Research, Asian Office of Aerospace Research and Development (AOARD), and the Office of Naval Research Global (ONRG) for their contributions to the success of this conference.

Ping Cheng
Shanghai Jiaotong University, China

Steve Choi
Korea Institute of Energy Research, Korea;
University of Illinois at Chicago, USA

Yogesh Jaluria
Rutgers, The State University of New Jersey, USA

Dongqing Li
University of Waterloo, Canada

Pamela Norris
University of Virginia, USA

"Robert" D. Y. Tzou
University of Missouri, USA

[1]Special Issue: Micro/Nanoscale Heat Transfer, *ASME Journal of Heat Transfer*, Vol. 124, April 2002. Special Issue: Micro/Nanoscale Radiative Transfer, *ASME Journal of Heat Transfer*, Vol. 129, January 2007.

Flow and Stability of Rivulets on Heated Surfaces With Topography

Tatiana Gambaryan-Roisman

Peter Stephan

Chair of Technical Thermodynamics,
Technische Universität Darmstadt,
Petersenstrasse 30,
64287 Darmstadt, Germany

Surfaces with topography promote rivulet flow patterns, which are characterized by a high cumulative length of contact lines. This property is very advantageous for evaporators and cooling devices, since the local evaporation rate in the vicinity of contact lines (microregion evaporation) is extremely high. The liquid flow in rivulets is subject to different kinds of instabilities, including the long-wave falling film instability (or the kinematic-wave instability), the capillary instability, and the thermocapillary instability. These instabilities may lead to the development of wavy flow patterns and to the rivulet rupture. We develop a model describing the hydrodynamics and heat transfer in flowing rivulets on surfaces with topography under the action of gravity, surface tension, and thermocapillarity. The contact line behavior is modeled using the disjoining pressure concept. The perfectly wetting case is described using the usual h^{-3} disjoining pressure. The partially wetting case is modeled using the integrated 6–12 Lennard-Jones potential. The developed model is used for investigating the effects of the surface topography, gravity, thermocapillarity, and the contact line behavior on the rivulet stability. We show that the long-wave thermocapillary instability may lead to splitting of the rivulet into droplets or into several rivulets, depending on the Marangoni number and on the rivulet geometry. The kinematic-wave instability may be completely suppressed in the case of the rivulet flow in a groove. [DOI: 10.1115/1.3056593]

Keywords: rivulets, thermocapillary instability, kinematic-wave instability, disjoining pressure

1 Introduction

The rivulet has been defined as "a narrow stream of liquid located on a solid surface and sharing a curved interface with the surrounding gas" [1]. Rivulet flow may occur spontaneously, for example, following an impact of a rain droplet on a solid surface, as a result of the vapor condensation inside a heat exchanger, or as a result of a liquid film breakup [2,3]. The rivulet flows can be also produced on purpose, for example, in heat pipes [4], in falling film evaporators [5,6], or in condensers [7,8]. This can be achieved by fabrication of microgrooves or microfins on the substrate or by using chemically patterned substrates with areas of different wettabilities.

The rivulet shape and the flow regime have a decisive influence on the heat and mass transports. In many cases the film breakup and the following transition to rivulet flow regime result in a significant heat transfer deterioration. This happens when the film breakup leads to the formation of rivulets with relatively large average film thickness, constituting a considerable thermal resistance, and to the formation of large dry stripes in between, where the heat transfer rate is extremely low. However, the heat transfer rate in a rivulet flow regime can be increased due to evaporation of ultrathin film in the vicinity of the contact lines or microregion evaporation [9,10]. Due to a very small heat resistance of the very thin liquid layer, the evaporation rate at the microregion is extremely high. When the cumulative length of the contact lines per unit area of the substrate is large, the heat/mass transfer rate in the rivulet flow regime may significantly exceed the heat/mass transfer rate in the film flow regime. This feature is frequently used in the design of the heat pipe evaporators [11]. It has been recently shown that even the spontaneous film breakup due to thermocapillary instability may lead to the heat transfer intensification [12].

The rivulet flows may exhibit many kinds of instabilities [1,13–16]. First of all, all the film instability modes, including the kinematic-wave instability typical for falling and shear-driven films [17,18], the Marangoni instabilities [19], and the instabilities due to evaporation or condensation [20], may occur also in rivulet flow. In addition, the rivulets can be broken up into droplets due to the capillary instability [1] and can change their path due to the meandering instability [1,15].

Due to the immense importance of the rivulet flow regime on heat and mass transports, many studies have been focused on the investigation of different aspects of the rivulet flow and stability. Davis and co-workers [1,13,14] quantified the effects of different physical factors (contact angle behavior, capillarity, and flow) on the stability characteristics of straight isothermal rivulets on flat walls. They distinguished among the three types of the contact line behavior: fixed contact line position (contact line pinning), fixed contact line speed, and contact angles smoothly varying with the contact line speed. The authors identified the parameter regions for which either capillary or flow effects are destabilizing the rivulet.

Wilson and Duffy [21] used the lubrication approximation to investigate the gravity-driven isothermal flow of thin rivulets down a slowly varying surface. The shapes of the rivulets have been computed for several substrate profiles. The authors examined the rivulet stability under an assumption that the perturbed flow remains symmetric and unidirectional, and the motion is quasisteady. Holland et al. [22] generalized this work to include the effect of thermocapillarity.

Myers et al. [16] investigated the flow of an isothermal rivulet driven by gravity and interfacial shear. The effect of inertia has been included in their analysis. The authors analyzed the total rivulet energy in order to determine if it is energetically favorable for rivulet to split. Wilson and Duffy [23] solved a similar problem for a rivulet of perfectly wetting liquid on the underside of a planar substrate.

Contributed by the Heat Transfer Division ASME for publication in the JOURNAL OF HEAT TRANSFER. Manuscript received November 4, 2007; final manuscript received October 9, 2008; published online January 13, 2009. Review conducted by Satish G. Kandilkar. Paper presented at the Fourth International Conference on Nanochannels, Microchannels, and Minichannels (ICNMM2006), Limerick, Ireland, June 19–21 2006.

Among the works devoted to the flow and stability of rivulets, only a few focused on a classical linear stability analysis of a basic rivulet state identifying the relation between the disturbance wave number and the growth rate [13,14]. Most of the investigators utilize the thermostatic approach to the stability analysis [24]; they minimized the energy of the rivulet to identify the most stable rivulet configuration [15,16,23]. Although the energy approach is very useful in the cases where one of several predefined rivulet states should be chosen as the most likely to occur in experiment, it has rather severe restrictions. This approach is inapplicable in the cases where the instability leads to development of nonstationary, wavy flow, which occurs, for example, as a result of the long-wave instability in falling films, which in the following will be referred to as the kinematic-wave instability [14].

One of the most difficult problems in simulating the rivulet hydrodynamics is the treatment of a moving contact line. Very few studies addressed this problem. Davis and co-workers [1,13,14] postulated a phenomenological relation between the dynamic contact angle and the contact line speed and used an effective slip model to remove the singularity at the contact line [25]. This approach, which has been applied to the linear stability analysis, can also be used for simulation of rivulet dynamics. In this case, the course of the contact line should be known a priori or calculated at each time moment.

The contact line singularity can be avoided by incorporation of the concept of disjoining pressure, which arises as a result of the intermolecular forces [26]. If the disjoining pressure is negative (Derjaguin's notation), a thin adsorbed film adheres to the solid substrate ahead of the liquid meniscus. The thickness of the adsorbed film has been measured by many investigators over the past decades [26–28].

We found that the wall topography exerts a stabilizing influence on isothermal falling films [5], as well as a destabilizing influence on stagnant liquid films on heated walls [29–31]. We could also show that an isothermal rivulet with pinning contact line in a rectangular groove under the combined action of gravity and gas shear is more stable than a continuous film on a flat wall [32].

This paper is aimed at the investigation of the basic rivulet states, as well as the stability characteristics of rivulets on walls with topography under the simultaneous action of gravity and thermocapillarity. The rivulet flow is described in the framework of the long-wave theory [33] with incorporation of the disjoining pressure and the adsorbed film concepts. This approach makes it possible to model the rivulet flow without a priori knowledge of the contact line position.

2 Long-Wave Model of the Rivulet Flow

2.1 Long-Wave Evolution Equation. Modeling of hydrodynamics and heat transfer of wavy liquid films and rivulets is generally a very challenging task. In addition to the velocity components, as well as the pressure and the temperature, the position of the free surface has to be determined. Analytical treatment in most of the practically relevant cases not possible. The application of numerical methods is difficult and time-consuming due to the high aspect ratio between the lateral extent of the film (or rivulet) and the film thickness.

If the characteristic film thickness h^* is much smaller than the characteristic wavelength of the film thickness variation, and if the Reynolds and the Peclet numbers of the flow are of the unity order, the film dynamics can be described by a nonlinear partial differential equation in the framework of the long-wave theory [33]. The velocity and the temperature fields inside the film can be uniquely determined from the film thickness distribution. The liquid films on microstructured walls can also be modeled using the long-wave theory [5,6,31,32,34,35]. In this case the film thickness should be much smaller than the scale of the wall topography variation. This is possible only if the height-to-width ratio of the topographical features is small. The long-wave theory is also applicable to the description of the rivulet flow in the case of a small contact angle [13,23].

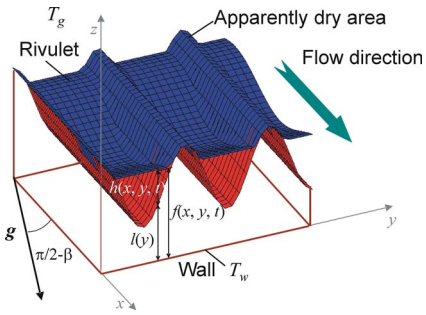

Fig. 1 The rivulet geometry

Consider a wall with a two-dimensional topography described by a function $l(y)$, where the coordinate axis x is directed along the gravity-driven flow, the coordinate axis y lies in the plane of the wall, and the coordinate axis z is perpendicular to the wall (see Fig. 1). The inclination angle between the wall and the horizon is β. The back side of the wall is kept at a constant temperature T_w. The ambient gas has a temperature T_g. The heat transfer coefficient between the film surface and the gas is constant and equal to α. We assume that the surface tension varies linearly with the temperature, so that $d\sigma/dT=-\sigma_T=\text{const}$, where σ denotes the surface tension. For the most of the common liquids, the surface tension decreases with increasing temperature ($\sigma_T>0$).

The evolution equation for the film thickness has the following form [36]:

$$H_\tau + \frac{\mathrm{Re}}{S}H^2H_X - \frac{5}{24}\mathrm{Re}(H^4H_\tau)_X - \frac{3}{40}\frac{\mathrm{Re}^2}{S}(H^6H_X)_X + \nabla\cdot\left\{H^3\nabla\left[\nabla^2F - \frac{1}{3}\frac{\mathrm{Re}\cot\beta}{S}F + \Pi(H)\right]\right\} - M\nabla\cdot\left\{H^2\nabla\left[\frac{1}{1+\mathrm{Bi}(H+L\kappa/\kappa_s)}\right]\right\} = 0 \tag{1}$$

where

$$\mathrm{Re} = \frac{gh^{*3}}{\nu^2}\sin\beta, \quad S = \frac{\rho\sigma h^*}{3\mu^2}, \quad M = \frac{3}{2}\frac{\sigma_T(T_w - T_g)}{\sigma}$$

$$\mathrm{Bi} = \frac{\alpha h^*}{\kappa}, \quad H = \frac{h}{h^*}, \quad L = \frac{l}{h^*}, \quad F = H + L, \quad X = \frac{x}{h^*}, \quad Y = \frac{y}{h^*} \tag{2}$$

$$\tau = \frac{t\sigma}{3h^*\mu}, \quad \Pi = \frac{\tilde{\Pi}h^*}{\sigma}$$

In the above, g is the acceleration of gravity, κ_s is the thermal conductivity of the solid wall, α is a heat transfer coefficient between the film surface and the ambient gas, and ρ, κ, μ, and ν are the density, the liquid thermal conductivity, and the dynamic and kinematic viscosities, respectively. Re denotes the Reynolds number, S is an inverse Crispation number, M is the product of the Marangoni number and the Crispation number, and Bi denotes the Biot number. The function $F(X,Y,\tau)$ describes the interface position. The function $\tilde{\Pi}(h)$ (in dimensionless form $\Pi(H)$) describes the disjoining pressure [37].

Equation (1) is an extension of the long-wave evolution equation describing a quiescent film on a heated microstructured wall, which has been verified by comparison with the results of the full-scale direct volume-of-fluid simulations [31]. The additional

terms, including the term describing the disjoining pressure and the terms describing the gravity-driven flow, are routinely used in the framework of the long-wave theory [5,6,33].

The value of the disjoining pressure $\tilde{\Pi}(h)$ is negligibly small if the film thickness $h > \sim 100$ nm. The effect of the disjoining pressure becomes important in the vicinity of the contact line. The form of the disjoining pressure depends on the different contributions to the intermolecular forces acting in the system, including the long-range forces between neutral molecules and the ionic-electrostatic forces. Several forms of the disjoining pressure have been suggested in literature [38–41], some of them depending not only on the film thickness but also on the film slope [42]. The choice of disjoining pressure for any specific problem depends on the solid material and the liquid under study. Several methods for experimental and theoretical determination of this function are described in literature [26,37]. In the present work we did not concentrate on a particular solid-liquid combination but chose two widely accepted forms of the disjoining pressure function. It will be shown in Sec. 2.2 that Eq. (1) with the chosen forms of disjoining pressure describes an adsorbed liquid film covering apparently dry wall regions. The disjoining pressure can be chosen to model the fully wetting situation (zero contact angle) or the partial wetting situation with a prescribed contact angle.

The evolution of Eq. (1) can be easily extended to include the effect of the liquid evaporation. In this case a term describing the mass loss due to evaporation should be added to this equation. Moreover, the Biot number should be calculated accounting for the molecular-kinetic resistance at the liquid-gas interface. If the evaporation flux is very high, a term accounting for the vapor recoil should be added to the evolution equation [20].

2.2 Basic State of Rivulet. We first treat the basic (undisturbed) state of rivulet. In this basic state the film thickness depends on Y alone: $H=H_0(Y)$. Then the evolution equation (1) reduces to

$$H_0^3\left[F_{0YY} - \frac{1}{3}\frac{\mathrm{Re}\cot\beta}{S}F_0 + \Pi(H_0)\right]_Y - MH_0^2\left[\frac{1}{1+\mathrm{Bi}(H_0+L\kappa/\kappa_s)}\right]_Y = 0 \tag{3}$$

Generally, this equation should be solved numerically. In the following we treat analytically a special limiting case of isothermal wall ($\kappa/\kappa_s \to 0$), a small Biot number ($\mathrm{Bi} \ll 1$), a negligible hydrostatic pressure in comparison to surface tension ($\mathrm{Re}\cot\beta/S \to 0$), and a triangular groove shape, which far away from the groove bottom and from the groove crest can be described by the following equation:

$$L(Y) = B|Y| \tag{4}$$

Under the above simplifications, Eq. (3) reduces to

$$H_{0YY} + \Pi(H_0) + \mathrm{Bi}M\log H_0 = \gamma \tag{5}$$

where γ is the integration constant, depending on the groove angle. This equation has an analytical solution in terms of the local inclination of the film interface, $\Psi(H_0)=H_{0Y}$.

$$\Psi(H_0) = \pm\left\{2\int_{H_{\mathrm{ads}}}^{H_0}[-\Pi(H') - \mathrm{Bi}M\log H' + \gamma]dH'\right\}^{1/2} \tag{6}$$

The plus sign corresponds to the branch $Y<0$ of the groove described by Eq. (4), and the minus sign corresponds to the branch $Y>0$.

Equation (6) has been derived under an assumption that the local inclination of the film interface is equal to zero at $H_0 = H_{\mathrm{ads}}$, where H_{ads} is the still unknown dimensionless thickness of the adsorbed layer. The adsorbed layer is assumed to be flat, so that $H_{0YY}=0$. Then the thickness of the adsorbed layer can be determined from Eq. (5) with the skipped first term at the left hand side.

$$\Pi(H_{\mathrm{ads}}) + \mathrm{Bi}M\log H_{\mathrm{ads}} = \gamma \tag{7}$$

In the present work we consider two forms of the disjoining pressure. The first is given by

$$\Pi(H) = A_3H^{-3} \tag{8}$$

with the dimensionless Hamaker constant $A_3>0$. If the system is isothermal, then Eq. (7) with disjoining pressure (8) has a real solution only if $\gamma>0$. Since in this case far from the contact line $H_{0YY}=\gamma$ (see Eq. (5)), the solution for H_{ads} exists only for a grooved surface ($B>0$). This happens because the disjoining pressure described by Eq. (8) corresponds to a zero contact angle (full wetting). In this case no stable rivulet can exist on a flat surface. The thickness of the absorbed film in the case $\gamma>0$ is determined by the macroscopic rivulet geometry [6].

Another form of the disjoining pressure is the integrated Lennard-Jones potential [39]

$$\Pi(H) = -\frac{A_3}{H^3} + \frac{A_9}{H^9} \tag{9}$$

where both A_3 and A_9 are positive material constants. For all reasonable values of these constants, the adsorbed layer thickness is close to the zero of the function $\Pi(H)$, so that H_{ads} is practically independent from γ and M. The behavior of the local inclination of the film interface (see Eq. (6)) in the vicinity of the apparent contact line is dominated by the first term of the integrand in this equation. Therefore, the interface shape is determined by the functional form of the disjoining pressure. It is easy to show that the value of Ψ rapidly increases from zero to a value that is approximately equal to

$$\Psi_{\mathrm{ref}} = \left(-2\int_{H_{\mathrm{ads}}}^{\infty}\Pi(H')dH'\right)^{1/2} = \frac{\sqrt{3}}{2}A_3^{2/3}A_9^{-1/6} \tag{10}$$

This reference value can be interpreted as a tangent of the microscopic contact angle. This value can be defined for any type of disjoining pressure, for which the integral defined in Eq. (10) exists. This includes the disjoining pressure stemming from polar and apolar intermolecular interactions, as well as the disjoining pressure stemming from simultaneous action of the attractive long-range and repulsive short-range intermolecular forces [33].

2.3 Stability Analysis. We perform a linear stability analysis of the basic rivulet state $H_0(Y)$ by applying a small harmonic disturbance [5,6,33], so that the disturbed film thickness is given by

$$H(X,Y,\tau) = H_0(Y) + \delta_0\varphi(Y)\exp[\Omega\tau + iKX] \tag{11}$$

where K is a dimensionless disturbance wave number in the X direction, Ω is a dimensionless number determining the disturbance growth rate and the disturbance propagation speed, δ_0 is a small parameter, and $\varphi(Y)$ is an unknown amplitude function. If the real part of Ω, or the disturbance growth rate Ω_R, is negative, the disturbance decays with time, and if it is positive, the disturbance grows exponentially and the flow is unstable.

Substitute the expression for the film thickness (11) in the evolution of Eq. (1) and linearize this equation around the basic solution $H_0(Y)$ for small values of δ_0. This results in a linear fourth-order equation for $\varphi(Y)$, which together with appropriate boundary conditions substitutes an eigenvalue problem for determination of Ω as a function of the wave number K. In the present work we consider only the axisymmetric disturbances of the rivulet. Therefore, we pose the symmetric boundary conditions for the function $\varphi(Y)$ at $Y=0$. At the adsorbed layer we pose the following boundary conditions: $\varphi=0$ and $\varphi_{YY}=0$. The first of them

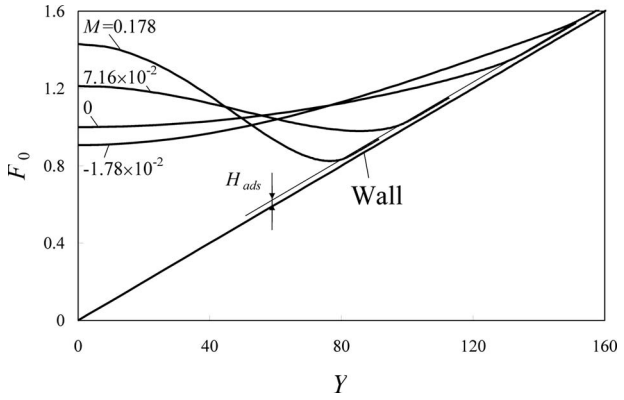

Fig. 2 Basic rivulet shapes for B=0.01, Bi=2.59×10^{-3}, $\kappa/\kappa_s \to 0$, and Re cot $\beta/S \to 0$. M=0.178 corresponds to $\Delta T = T_w - T_g$=50 K for water, and M=−1.78×10^{-2} corresponds to $\Delta T = T_w - T_g$=−5 K.

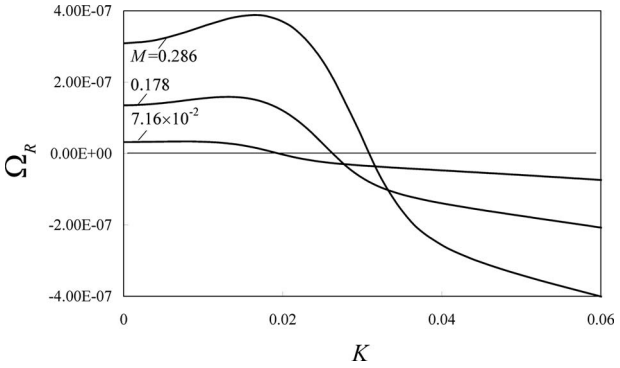

Fig. 3 Disturbance growth rate for the thermocapillary instability of rivulet in the absence of gravity. Parameters: B=0.01, Bi=2.59×10^{-3}, $\kappa/\kappa_s \to 0$, Re=0, A_3=2.46×10^{-8}, and A_9=9.82×10^{-18} (or Ψ_{ref}=5.0×10^{-3} and H_{ads}=2.7×10^{-2}).

means that the thickness of the adsorbed layer stays constant. The second means that the curvature of the adsorbed film is zero.

3 Results and Discussion

3.1 Basic State of Rivulet. Figure 2 shows the basic interface shape of a rivulet inside a triangular groove with B=0.01 at Bi =2.59×10^{-3} (corresponding to α=10 W/(m^2 K), h^*=150 μm, and κ=0.58 W/(m K)), A_3=2.46×10^{-8}, and A_9=9.82×10^{-18}. For these values of the parameters the microscopic contact angle is equal to Ψ_{ref}=5.0×10^{-3}, and the adsorbed layer thickness is equal to H_{ads}=2.7×10^{-2}. The values of the parameters A_3 and A_9 are uniquely determined by Ψ_{ref} and H_{ads}. Our numerical experiments have shown that for H_{ads}<0.05 the value of H_{ads} does not affect the computational results on the rivulet shape and on its stability. Therefore, we set H_{ads}=2.7×10^{-2} for all our calculations. The value of Ψ_{ref} has been varied under constraint $\Psi_{ref} \ll 1$, which is essential for applicability of the long-wave theory.

In the above the maximal film thickness of the isothermal rivulet has been chosen as the film thickness scale h^*. If the wall is hotter than the gas, the liquid-gas interface temperature at the groove trough, where the film thickness is maximal, is lower than that near the contact lines. The thermocapillary stresses act on the liquid at the interface in the direction of increasing surface tension, or decreasing temperature, i.e., toward the groove trough. The meniscus deforms in such a way that the film thickness in the vicinity of the groove trough further increases. The interface shape changes from convex in the middle of the rivulet to concave at the periphery. The wetted wall area decreases compared with the isothermal case. The interface deformation increases with an increase in the temperature difference between the wall and the ambient gas. If the wall is colder than the ambient gas (case M =−1.78×10^{-2} or $\Delta T = T_w - T_g$=−5 K in Fig. 2), the liquid-gas interface is colder near the contact lines. Then the liquid at the interface flows from the groove trough toward the periphery, so that the film thickness at the groove trough becomes lower than that in the isothermal case. The wetted wall area increases, the film thickness in the middle of the rivulet decreases, and the rivulet becomes fully convex.

3.2 Long-Wave Marangoni Instability. We analyze the long-wave Marangoni instability of a static rivulet in the absence of the gravity. Figure 3 illustrates the typical behavior of the disturbance growth rate at different Marangoni numbers.

As expected, the rivulet becomes more unstable as the temperature difference between the wall and the surrounding gas, expressed by the parameter M, increases. First, the cut-off wave number K_c, or the wave number corresponding to zero disturbance growth rate, increases with increasing M. This means that the region of the decaying disturbances decreases. Second, the growth rate of the disturbances increases with an increase in M. The wave number, corresponding to the maximal disturbance growth rate K_m, also increases with an increase in the driving temperature difference. Note that the disturbances with the wave number K >0 correspond to the rivulet deformations in the direction of the rivulet axis X. The growth of such disturbances leads to the rivulet splitting into droplets as a result of the long-wave Marangoni instability. The size of the droplets is determined by the fastest growing disturbance. This size is of the order $2\pi/K_m$, and it decreases with an increase in the parameter M. Note that the disturbance growth rate is positive also for K=0. This corresponds to the disturbances in the y-direction, which are uniform over the whole rivulet length. The growth of such disturbances may lead to the rivulet splitting into two or more thinner rivulets. If the maximal growth of disturbance occurs at K=0, which is the case at the smallest value of M shown on the graph (M=7.16×10^{-2} or $\Delta T = T_w - T_g$=20 K), the splitting of rivulet into several thinner rivulets is the preferred mode of the rivulet evolution. However, exact predictions of the rivulet dynamics can be done only on the basis of solution of the nonlinear evolution equation (1).

3.3 Kinematic-Wave Instability. Figure 4 illustrates the effect of the microscopic contact angle on the disturbance growth rate for an isothermal rivulet flowing down a vertical film inside a triangular groove with B=0.01. Different curves correspond to different values of Ψ_{ref}. The basic rivulet shapes for the nonzero contact angles have been calculated using the integrated Lennard-Jones potential (Eq. (9), A_3>0 and A_9>0), whereas the basic

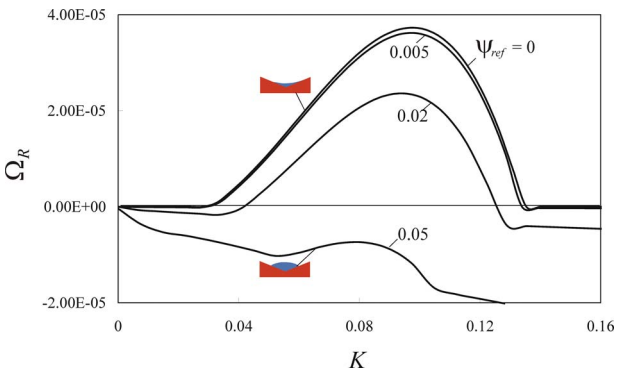

Fig. 4 Disturbance growth rate for the kinematic-wave instability of isothermal rivulet for B=0.01, $\beta=\pi/2$, and Re$^2/S$ =0.298

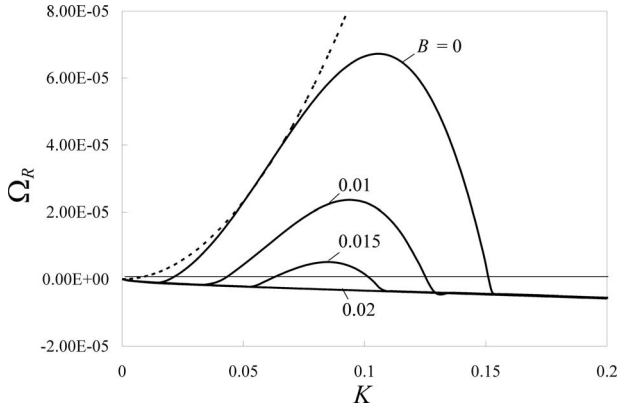

Fig. 5 Disturbance growth rate for the kinematic-wave instability of isothermal rivulet for $\Psi_{ref}=0.02$, $\beta=\pi/2$, and $Re^2/S=0.298$. Dashed line: asymptotic solution of Weiland and Davis [13] for fixed contact line position, flat surfaces, and small values of K.

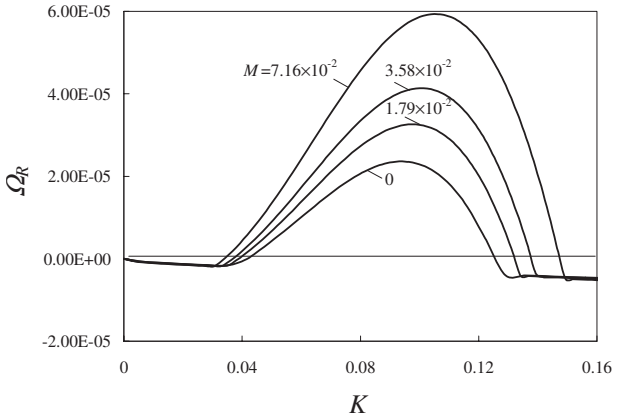

Fig. 6 Disturbance growth rate for the simultaneous action of gravity and thermocapillarity on the rivulet instability. Parameters: $\Psi_{ref}=0.02$, $B=0.01$, $\beta=\pi/2$, and $Re^2/S=0.298$.

rivulet shape for the case $\Psi_{ref}=0$ has been calculated using the standard h^{-3} disjoining pressure (Eq. (8), $A_3>0$). It should be noted that the difference between the curves $\Psi_{ref}=0$ and $\Psi_{ref}=5.0\times10^{-3}$ is rather small. We also found that the rivulet stability characteristics depend on the parameter Ψ_{ref} rather than on the specific choice of the parameters A_3 and A_9.

The behavior of the disturbance growth rate depicted in Fig. 4 is qualitatively different from that of a continuous film on a flat or a microstructured substrate. In the case of continuous falling films the value of Ω_R is 0 at $K=0$, positive for $0<K<K_c=(2Re^2/15S)^{1/2}$ and negative for $K>K_c$. In contrast, the kinematic-wave instability of a rivulet can be completely suppressed (see the curve corresponding to $\Psi_{ref}=0.05$, where the contact angle is maximal). For the smaller microscopic contact angles, the disturbance growth rate is negative for the small values of the disturbance wave number K. In a certain range of the disturbance wave numbers (for example, for the curve $\Psi_{ref}=0$ this range is approximately $0.03<K<0.13$) the value of Ω_R first drastically increases, reaches a maximal value, and then decreases again.

Figure 5 illustrates the dependence of the rivulet stability characteristics on the groove angle. The results corresponding to $B=0$ (flat wall) are compared with an asymptotic solution of Ref. [13] for a fixed contact line position and small values of the wave number K. The agreement is rather good. This means that in the present configuration our model describes the fixed contact line. It is clearly seen that the rivulet becomes more stable as the value of B increases (the groove angle decreases). If the value of B is large enough, the kinematic-wave instability is completely suppressed.

3.4 Rivulet Instability Under Simultaneous Action of Gravity and Thermocapillarity. Figure 6 represents the simultaneous influence of gravity and thermocapillarity on the stability of rivulet on a vertical wall for $\Psi_{ref}=0.02$, $B=0.01$, and $Re^2/S=0.298$. The results are compared with the isothermal case (see the curve $M=0$). Obviously, the thermocapillarity leads to an increase in the disturbance growth rate in comparison to the isothermal rivulet. This trend is similar to that reported for the continuous films [3,36]. The range of the disturbance wave numbers, corresponding to the positive growth rates, is also increased on heated surface. At the same time, the behavior of the Ω_R versus K curves is qualitatively the same for the isothermal and for the heated surfaces.

4 Conclusions

The flow of rivulets can be modeled in the framework of the long-wave theory using the disjoining pressure and the concept of adsorbed film.

The long-wave thermocapillary instability may lead to splitting of the rivulet into drops or into slender rivulets, depending on the driving temperature difference.

The computed disturbance growth rate corresponding to the kinematic-wave instability of a rivulet on a flat wall agrees with the growth rate calculated for a rivulet with a fixed contact line at small wave numbers.

The disturbance growth rate corresponding to the kinematic-wave instability increases with an increase in the groove angle and with a decrease in the contact angle. The kinematic-wave instability can be completely suppressed in the case of the rivulet flow in a groove, depending on the Reynolds and Crispation numbers, as well as the groove angle and the contact angle.

The rivulets on heated vertical walls are more unstable in comparison to the rivulets on isothermal vertical walls.

The results of the stability analysis can be used as a basis for the future simulations of the rivulet evolution.

Acknowledgment

The authors acknowledge the support of the German Science Foundation (DFG) through the Emmy Noether Program.

Nomenclature

A_3, A_9 = parameters of the dimensionless Lennard-Jones potential
B = parameter defining the groove angle
Bi = Biot number
g = acceleration of gravity, m/s^2
H = dimensionless film thickness
H_0 = dimensionless film thickness in the undisturbed state
h = film thickness, m
h^* = characteristic film thickness, m
K = dimensionless disturbance wave number
K_c = dimensionless cut-off wave number
K_m = dimensionless wave number corresponding to the maximal disturbance growth rate
L = dimensionless wall topography function
l = function describing the wall topography, m
M = product of the Marangoni number and Crispation number
Re = Reynolds number
S = inverse Crispation number

T = temperature, K
t = time, s
X, Y, Z = dimensionless coordinates
x, y, z = coordinates, m

Greek Symbols

α = heat transfer coefficient, $W/(m^2\,K)$
β = wall inclination angle
Ψ = tangent of the local film inclination
μ = dynamic viscosity of the liquid, $kg/(m\,s)$
ν = kinematic viscosity of the liquid, m^2/s
Π = dimensionless disjoining pressure
$\tilde{\Pi}$ = disjoining pressure, Pa
ρ = density of the liquid, kg/m^3
σ = surface tension of the liquid, N/m
Ω = dimensionless disturbance growth rate
τ = dimensionless time variable

References

[1] Davis, S. H., 1980, "Moving Contact Lines and Rivulet Instabilities. Part 1: The Static Rivulet," J. Fluid Mech., **98**(2), pp. 225–242.
[2] Hartley, D. E., and Murgatroyd, W., 1964, "Criteria for the Break-Up of Thin Liquid Layers Flowing Isothermally Over Solid Surfaces," Int. J. Heat Mass Transfer, **7**, pp. 1003–1015.
[3] Joo, S. W., Davis, S. H., and Bankoff, S. G., 1996, "A Mechanism for Rivulet Formation in Heated Falling Films," J. Fluid Mech., **321**, pp. 279–298.
[4] Faghri, A., 1995, *Heat Pipe Science and Technology*, Taylor & Francis, London.
[5] Gambaryan-Roisman, T., and Stephan, P., 2003, "Analysis of Falling Film Evaporation on Grooved Surfaces," J. Enhanced Heat Transfer, **10**(4), pp. 369–381.
[6] Gambaryan-Roisman, T., and Stephan, P., 2003, "Falling Films in Micro- and Minigrooves: Heat Transfer and Flow Stability," Therm. Sci. Eng., **11**(6), pp. 43–50.
[7] Gregorig, R., 1954, "Hautkondensation in Feingewelten Oberflächen bei Berüksichtigung der Oberflächenspannungen," Z. Angew. Math. Phys., **5**, pp. 36–49.
[8] Chamra, L. M., Webb, R. L., and Randlett, M. R., 1996, "Advanced Micro-Fin Tubes for Condensation," Int. J. Heat Mass Transfer, **39**(9), pp. 1839–1846.
[9] Potash, M., Jr., and Wayner, P. C., Jr., 1972, "Evaporation From a Two-Dimensional Extended Meniscus," Int. J. Heat Mass Transfer, **15**, pp. 1851–1863.
[10] Stephan, P., and Busse, C. A., 1992, "Analysis of Heat Transfer Coefficient of Grooved Heat Pipe Evaporator Walls," Int. J. Heat Mass Transfer, **35**, pp. 383–391.
[11] Stephan, P., and Brandt, C., 2004, "Advanced Capillary Structures for High Performance Heat Pipes," Heat Transfer Eng., **25**(3), pp. 78–85.
[12] Chinnov, E. A., Sharina, I. A., and Kabov, O. A., 2004, "Intensification of Heat Transfer in a Downward Liquid-Film Flow," J. Appl. Mech. Tech. Phys., **45**(5), pp. 705–711.
[13] Weiland, R. H., and Davis, S. H., 1981, "Moving Contact Lines and Rivulet Instabilities. Part 2: Long Waves on Flat Rivulets," J. Fluid Mech., **107**, pp. 261–280.
[14] Young, G. W., and Davis, S. H., 1987, "Rivulet Instabilities," J. Fluid Mech., **176**, pp. 1–31.
[15] Schmuki, P., and Laso, M., 1990, "On the Stability of Rivulet Flow," J. Fluid Mech., **215**, pp. 125–143.
[16] Myers, T. G., Liang, H. X., and Wetton, B., 2004, "The Stability and Flow of a Rivulet Driven by Interfacial Shear and Gravity," Int. J. Non-Linear Mech., **39**, pp. 1239–1249.
[17] Yih, C.-S., 1963, "Stability of Liquid Flow Down an Inclined Plane," Phys. Fluids, **6**(3), pp. 321–334.
[18] Alekseenko, S. V., and Nakoryakov, V. E., 1995, "Instability of a Liquid Film Moving Under the Effect of Gravity and Gas Flow," Int. J. Heat Mass Transfer, **38**(11), pp. 2127–2134.
[19] Davis, S. H., 1987, "Thermocapillary Instabilities," Annu. Rev. Fluid Mech., **19**, pp. 403–435.
[20] Burelbach, J. P., Bankoff, S. G., and Davis, S. H., 1988, "Nonlinear Stability of Evaporating/Condensing Liquid Film," J. Fluid Mech., **195**, pp. 463–494.
[21] Wilson, S. K., and Duffy, B. R., 1998, "On the Gravity-Driven Draining of Rivulet of Viscous Fluid Down a Slowly Varying Substrate With Variation Transverse to the Direction of Flow," Phys. Fluids, **10**(1), pp. 13–22.
[22] Holland, D., Duffy, B. R., and Wilson, S. K., 2001, "Thermocapillary Effects on a Thin Viscous Rivulet Draining Steadily Down a Uniformly Heated or Cooled Slowly Varying Substrate," J. Fluid Mech., **441**, pp. 195–221.
[23] Wilson, S. K., and Duffy, B. R., 2005, "When is it Energetically Favorable for a Rivulet of Perfectly Wetting Fluid to Split?," Phys. Fluids, **17**, p. 078104.
[24] Gibbs, J. W., 1948, *Collected Works*, Vol. 1, Yale University Press, New Haven, CT.
[25] Dussan, V. E. B., and Davis, S. H., 1974, "On the Motion of Fluid-Fluid Interface Along a Solid Surface," J. Fluid Mech., **65**, pp. 71–95.
[26] Derjaguin, B. V., 1955, "Definition of the Concept of and Magnitude of the Disjoining Pressure and Its Role in the Statics and Kinetics of Thin Layers of Liquid," Kolloidn. Zh., **17**, pp. 191–197.
[27] Blake, T. D., 1975, "Investigation of Equilibrium Wetting Films of n-Alkanes on α-Alumina," J. Chem. Soc., Faraday Trans. 1, **71**, pp. 192–208.
[28] Gokhale, S. J., Plawsky, J. L., and Wayner, P. C., Jr., 2005, "Spreading, Evaporation, and Contact Line Dynamics of Surfactant-Laden Microdrops," Langmuir, **21**, pp. 8188–8197.
[29] Gambaryan-Roisman, T., Alexeev, A., and Stephan, P., 2005, "Effect of the Microscale Wall Topography on the Thermocapillary Convection Within a Heated Liquid Film," Exp. Therm. Fluid Sci., **29**, pp. 765–772.
[30] Kabova, Y. O., Alexeev, A., Gambaryan-Roisman, T., and Stephan, P., 2005, "Thermocapillarity-Induced Vortexes and Liquid Film Dynamics on Structured Heated Walls," J. Non-Equilib. Thermodyn., **30**(3), pp. 225–241.
[31] Kabova, Y. O., Alexeev, A., Gambaryan-Roisman, T., and Stephan, P., 2006, "Marangoni-Induced Deformation and Rupture of a Liquid Film on a Heated Microstructured Wall," Phys. Fluids, **18**, p. 012104.
[32] Gambaryan-Roisman, T., and Stephan, P., 2004, "Evaporation of Gravity- and Gas Flow-Driven Thin Liquid Films in Micro- and Minigrooves." Proceedings of the Second International Conference on Microchannels and Minichannels, Rochester, NY, Jun. 17–19, pp. 551–558.
[33] Oron, A., Davis, S. H., and Bankoff, S. G., 1997, "Long-Scale Evolution of Thin Liquid Films," Rev. Mod. Phys., **69**(3), pp. 931–980.
[34] Stillwagon, L. E., and Larson, R. G., 1990, "Leveling of Thin Films Over Uneven Substrates During Spin Coating," Phys. Fluids A, **2**, pp. 1937–1944.
[35] Gramlich, C. M., Kalliadasis, S., Homsy, G. M., and Messer, C., 2002, "Optimal Leveling of Flow Over One-Dimensional Topography by Marangoni Stresses," Phys. Fluids, **14**, pp. 1841–1850.
[36] Gambaryan-Roisman, T., and Stephan, P., 2005, "Film Flow Down Vertical and Inclined Microstructured Heated Walls: Hydrodynamics, Heat Transfer and Stability," Proceedings of the Third International Berlin Workshop—IBW3 on Transport Phenomena With Moving Boundaries, Berlin, Germany, Oct. 6–7, pp. 184–196.
[37] Israelachvili, J. N., 1992, *Intermolecular and Surface Forces*, 2nd ed., Academic, London.
[38] Teletzke, G. F., Davis, H. T., and Scriven, L. E., 1988, "Wetting Hydrodynamics," Rev. Phys. Appl., **23**, pp. 989–1007.
[39] Mitlin, V. S., and Petviashvili, N. V., 1994, "Nonlinear Dynamics of Dewetting: Kinetically Stable Structures," Phys. Lett. A, **192**, pp. 323–326.
[40] Jameel, A. T., and Sharma, A., 1994, "Morphological Phase Separation in Thin Liquid Films," J. Colloid Interface Sci., **164**, pp. 416–427.
[41] Glasner, K. B., and Witelski, T. P., 2003, "Coarsening Dynamics of Dewetting Films," Phys. Rev. E, **67**, p. 016302.
[42] Wu, Q., and Wong, H., 2004, "A Slope-Dependent Disjoining Pressure for Non-Zero Contact Angles," J. Fluid Mech., **506**, pp. 157–185.

Nanofluids: Synthesis, Heat Conduction, and Extension

Liqiu Wang[1]
e-mail: lqwang@hku.hk

Xiaohao Wei

Department of Mechanical Engineering,
The University of Hong Kong,
Pokfulam Road, Hong Kong

We synthesize eight kinds of nanofluids with controllable microstructures by a chemical solution method (CSM) and develop a theory of macroscale heat conduction in nanofluids. By the CSM, we can easily vary and manipulate nanofluid microstructures through adjusting synthesis parameters. Our theory shows that heat conduction in nanofluids is of a dual-phase-lagging type instead of the postulated and commonly used Fourier heat conduction. Due to the coupled conduction of the two phases, thermal waves and possibly resonance may appear in nanofluid heat conduction. Such waves and resonance are responsible for the conductivity enhancement. Our theory also generalizes nanofluids into thermal-wave fluids in which heat conduction can support thermal waves. We emulsify olive oil into distilled water to form a new type of thermal-wave fluids that can support much stronger thermal waves and resonance than all reported nanofluids, and consequently extraordinary water conductivity enhancement (up to 153.3%) by adding some olive oil that has a much lower conductivity than water. [DOI: 10.1115/1.3056597]

Keywords: nanofluids, synthesis, heat conduction, thermal-wave fluids, dual-phase-lagging, thermal waves, thermal resonance, emulsion

1 Introduction

Choi [1] coined the term "nanofluids" for the fluids with nanoparticles suspended in them. Recent experiments on nanofluids have shown substantial increases in thermal conductivity and convective heat transfer coefficient with low particle volume concentrations compared with liquids without nanoparticles or with larger particles, strong temperature dependence of thermal conductivity, and substantial increases in critical heat flux (CHF) in boiling heat transfer [2–9]. These characteristics make them very attractive for a large number of industries such as transportation, electronics, defense, space, nuclear systems cooling, and biomedicine.

Efforts to synthesize nanofluids have often employed either a single-step physical method that simultaneously makes and disperses the nanoparticles into base fluids [10–15] or a two-step approach that first generates nanoparticles and subsequently disperses them into base fluids [2,3,6]. In addition to the challenge of how to effectively prevent nanoparticles from agglomerating or aggregating, the key issue in either of these two approaches is the lack of effective means for synthesizing nanofluids with various microstructures and properties due to either the limitation of available nanoparticle powers in the two-step method or the limitation of the system used in the single-step physical method. For creating nanofluids by design (the ultimate goal of all nanofluid research and development), it is thus crucial to develop effective techniques for synthesizing various nanofluids.

A relatively intensified effort has been made on determining nanofluid thermal conductivity from experiments, particularly for the nanofluids with spherical nanoparticles or nanotubes. While the data from these experiments have enabled some trends to be identified, there is still no consensus on the effects of some parameters such as particle size, shape, distribution, and additives in the nanofluids [2–7,16]. There also exist wide discrepancies and inconsistencies in the reported conductivity data due to a limited understanding of the precise nature of heat conduction in nanofluids, the poor microstructure characterization, and the unavailability of nanofluids with various microstructures [2–7,16–19]. In many cases the microstructural parameters were not measured by the experimenters themselves but rather taken from the powder manufacturers' nominal information. To reconcile these discrepancies and inconsistencies and to lay the foundations for better and more efficient designs of nanofluids, it is essential to generate nanofluids of various microstructures, characterize their microstructures by state-of-the-art instrumentation, and develop precise heat-conduction model for nanofluids.

Suggested reasons for the significant conductivity enhancement are the nanoparticle Brownian motion effect [20–25], the liquid layering effect at the liquid-particle interface [26–31], the nanoparticle cluster/aggregate effect [32,33], the nature of heat transport in the nanoparticle [34], and the nature of macroscale heat conduction in nanofluids [35,36]. As generally accepted [2–7], however, no conclusive explanation is available. Often, the explanation by one research group is confronted by others. Also, the theoretical work on macroscale heat conduction of nanofluids, which is more relevant to the thermal conductivity, is very limited. Therefore, it is critical to determine the precise nature of heat conduction in nanofluids.

We attempt to address the issues of (i) unavailability of nanofluids with controllable and tailor-designed microstructures and (ii) a limited understanding of the precise nature of heat conduction in nanofluids by using solution chemistry to synthesize nanofluids and by rigorously studying heat conduction in nanofluids. Such a study also leads to a substantial extension of nanofluid research.

2 Synthesis

The strength of the solution chemistry for synthesizing nanofluids lies in its ability to manipulate atoms and molecules in the liquid phase, thereby providing a powerful arsenal for synthesis of tailor-designed nanofluids using a bottom-up approach. Therefore, we propose to develop this technique for synthesis of nanofluids with various microstructures.

Figure 1 shows the flowchart of the CSM. The reaction between reactants A (e.g., Cu^{2+}) and B (e.g., OH^-) in the liquid phase yields the solution or colloid containing the precursor C (e.g., $Cu(OH)_2$). The additives (e.g., ammonium citrate or cetyltrimethyl ammonium bromide) are then added into the solution/

[1]Corresponding author.

Contributed by the Heat Transfer Division of ASME for publication in the JOURNAL OF HEAT TRANSFER. Manuscript received January 30, 2008; final manuscript received May 5, 2008; published online January 13, 2009. Review conducted by Robert D. Tzou. Paper presented at the 2008 International Conference on Micro/Nanoscale Heat Transfer (MNHT2008), Tainan, Taiwan, January 6–9, 2008.

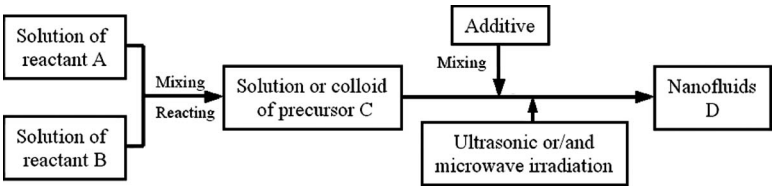

Fig. 1 CSM for synthesis of nanofluids: flowchart

colloid. Finally the solution/colloid of the precursor C transforms into nanofluid D (e.g., CuO/water) under ultrasonic or/and microwave irradiation.

Precursor C normally exists in the form of solution or colloid and is not, in general, the nanoparticle in the nanofluid D. Its solution or colloid can directly transform into the required nanofluids with the help of additives and external fields such as ultrasonic and microwave irradiation. Both the additives and the external fields are used to prevent nanoparticles from agglomeration and growth and thus control nanofluid microstructures.

By this method, we can synthesize nanofluids with various microstructures by adjusting synthesis parameters. Here the microstructure refers to nanoparticle size, size distribution, shape, morphology, liquid-particle interfacial property, and agglomerating/aggregating structure in nanofluids. The synthesis parameters include temperature, acidity, ultrasonic and microwave irradiation, types and concentrations of reactants and additives, and the order in which the additives are added to the solution.

We have applied the CSM to synthesize eight kinds of nanofluids. Figure 2 illustrates some transmission electron microscope (TEM) images of them:

(1) spherical Fe_3O_4 nanoparticles in water or various oils (Fig. 2(a))
(2) elliptic Cu nanorods in ethylene glycol (EG) or EG/water mixtures (Fig. 2(b))
(3) needlelike CuO nanoparticles in water or various oils (Fig. 2(c))
(4) octahedral Cu_2O nanoparticles in water or water/EG mixtures (Fig. 2(d))
(5) $CePO_4$ nanofibers in water, ethanol, EG, and their mixtures (Fig. 2(e))
(6) hollow Cu or CuS nanoparticles in water, ethanol, EG, and their mixtures (Fig. 2(f))
(7) hollow and wrinkled Cu_2O nanoparticles in EG or EG/water mixtures (Fig. 2(g))
(8) Cu_2O(core)/CuS(shell) nanoparticles in water (Fig. 2(h))

The last seven types of nanofluids appear new and are very likely to possess some unique properties.

These preliminary results appear very encouraging and seem to suggest that the CSM is very effective in fabricating nanofluids with controllable and tailor-designed microstructures. However, the detailed relation between synthesis parameters and microstructures of nanofluids is still not adequately understood. Further work is required to correlate synthesis parameters optimally or even ideally with microstructures and thermal conductivities of nanofluids.

Figure 3 shows the variation of conductivity ratio k/k_w with reactant concentration and nanofluid temperature for the $CePO_4$-nanofibers/water nanofluids in Fig. 2(e). Here k and k_w are

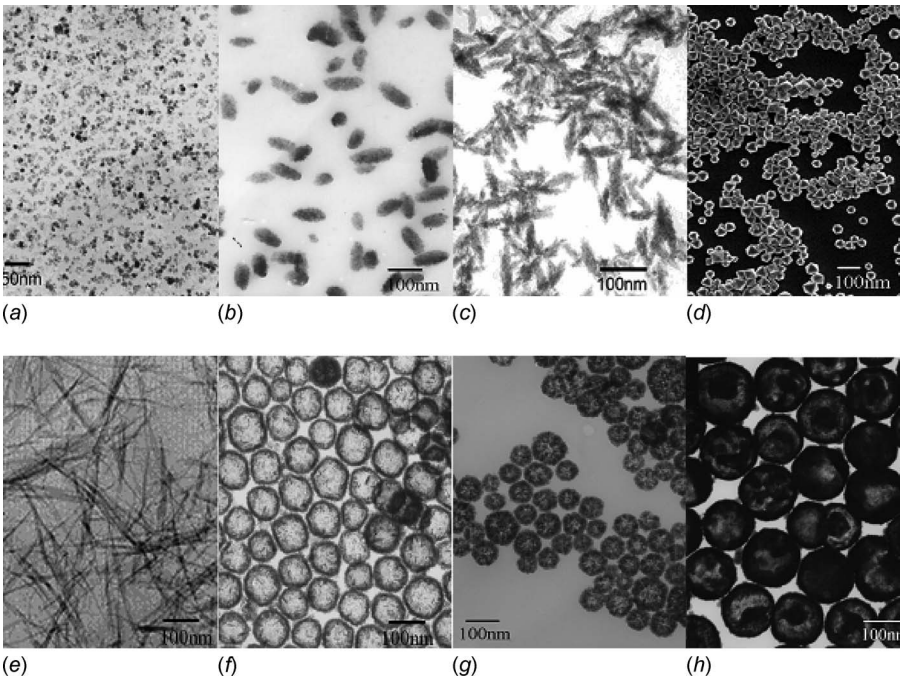

Fig. 2 TEM images of some nanoparticles from "drying" samples of nanofluids synthesized by the CSM ((*a*) spherical Fe_3O_4 nanoparticles, (*b*) elliptic Cu nanorods, (*c*) needlelike CuO nanoparticles, (*d*) octahedral Cu_2O nanoparticles, (*e*) $CePO_4$ nanofibers, (*f*) hollow CuS nanoparticles, (*g*) hollow and wrinkled Cu_2O nanoparticles, and (*h*) Cu_2O(core)/CuS(shell) nanoparticles)

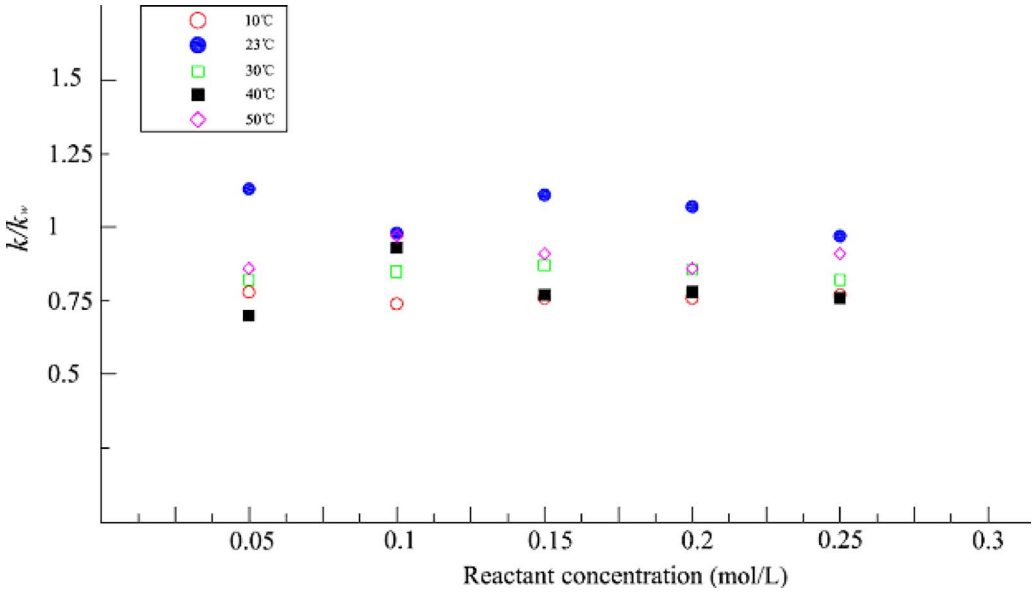

Fig. 3 Variation of k/k_w with reactant concentration and temperature for $CePO_4$-nanofibers/water nanofluids in Fig. 2(*e*) (k: nanofluids thermal conductivity; k_w: water thermal conductivity)

the thermal conductivity of the nanofluid and the water, respectively, measured by the standard transient hot-wire method (KD2, Therm Test Inc., Canada). The accuracy of the KD2 system has been verified by a careful calibration before experiments through measuring thermal conductivities of water and various oils and comparing with those well documented in literature. We observe a nonlinear dependence of k/k_w on both the reactant concentration and the temperature. The conductivity enhancement appears at 23°C with a ceiling value of 13%, but not at the other temperature values tested.

3 Heat Conduction in Nanofluids

The study of nanofluids is still in its infancy. The precise nature and mechanism of the significant improvement of thermal conductivity are still not known. There is also a lack of agreement between experimental results and between theoretical models. The fact that the conductivity enhancement comes from the presence of nanoparticles has directed research efforts nearly exclusively toward thermal transport at nanoscale. The classical heat-conduction equation has been postulated as the macroscale model but without adequate justification. Note that thermal conductivity is a macroscale phenomenological characterization of heat conduction, and the measurements are not performed at the nanoscale, but rather at the macroscale. Therefore, interest should focus not only on what happens at the nanoscale but also on how the presence of nanoparticles affects the heat transport at macroscale.

In order to isolate the mechanism responsible for the thermal conductivity enhancement, we develop a macroscale heat-conduction model in nanofluids by scaling up the microscale model for the heat conduction in the nanoparticles and in the base fluids. The approach for scaling-up is the volume averaging with the help of multiscale theorems [37–39]. The microscale model for the heat conduction in the nanoparticles and in the base fluids comes from the first law of thermodynamics and the Fourier law of heat conduction.

Consider heat conduction in nanofluids with the base fluid and the nanoparticle denoted by β- and σ-phases, respectively. By the first law of thermodynamics and the Fourier law of heat conduction [40], we have the microscale model for heat conduction in nanofluids (Fig. 4)

$$(\rho c)_\beta \frac{\partial T_\beta}{\partial t} = \nabla \cdot (k_\beta \nabla T_\beta) \quad \text{in the } \beta\text{-phase} \tag{1}$$

$$(\rho c)_\sigma \frac{\partial T_\sigma}{\partial t} = \nabla \cdot (k_\sigma \nabla T_\sigma) \quad \text{in the } \sigma\text{-phase} \tag{2}$$

$$T_\beta = T_\sigma \quad \text{at the } \beta\text{-}\sigma \text{ interface } A_{\beta\sigma} \tag{3}$$

$$\mathbf{n}_{\beta\sigma} \cdot k_\beta \nabla T_\beta = \mathbf{n}_{\beta\sigma} \cdot k_\sigma \nabla T_\sigma \quad \text{at the } \beta\text{-}\sigma \text{ interface } A_{\beta\sigma} \tag{4}$$

Here T is the temperature. ρ, c, and k are the density, specific heat, and thermal conductivity, respectively. Subscripts β and σ refer to the β- and σ-phases, respectively. $A_{\beta\sigma}$ represents the area of the β-σ interface, $\mathbf{n}_{\beta\sigma}$ is the outward-directed surface normal from the β-phase toward the σ-phase, and $\mathbf{n}_{\beta\sigma} = -\mathbf{n}_{\sigma\beta}$ (Fig. 4).

A macroscale model equivalent to the microscale behavior can be readily obtained by the method of volume averaging [37,38]. Consider a representative elementary volume (REV) in Fig. 4, the smallest differential volume resulting in statistically meaningful local average properties. Averaging Eqs. (1)–(4) over REV and applying the multiscale theorems [39] yield the macroscale model of heat conduction [41,42], as follows:

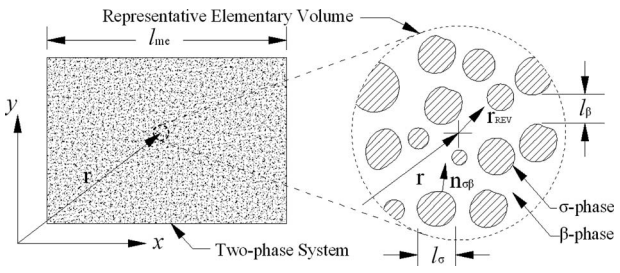

Fig. 4 Nanofluids and representative elementary volume (REV)

$$\gamma_\beta \frac{\partial \langle T_\beta \rangle^\beta}{\partial t} = \nabla \cdot \{\mathbf{K}_{\beta\beta} \cdot \nabla \langle T_\beta \rangle^\beta + \mathbf{K}_{\beta\sigma} \cdot \nabla \langle T_\sigma \rangle^\sigma\} + h a_v (\langle T_\sigma \rangle^\sigma - \langle T_\beta \rangle^\beta) \tag{5}$$

and

$$\gamma_\sigma \frac{\partial \langle T_\sigma \rangle^\sigma}{\partial t} = \nabla \cdot \{\mathbf{K}_{\sigma\sigma} \cdot \nabla \langle T_\sigma \rangle^\sigma + \mathbf{K}_{\sigma\beta} \cdot \nabla \langle T_\beta \rangle^\beta\} - h a_v (\langle T_\sigma \rangle^\sigma - \langle T_\beta \rangle^\beta) \tag{6}$$

where

$$\langle T_\beta \rangle^\beta = \frac{1}{V_\beta} \int_{V_\beta} T_\beta dV \tag{7}$$

and

$$\langle T_\sigma \rangle^\sigma = \frac{1}{V_\sigma} \int_{V_\sigma} T_\sigma dV \tag{8}$$

V_β and V_σ are the volumes of β- and σ-phases in REV, respectively. $\gamma_\beta = (1-\varphi)(\rho c)_\beta$ and $\gamma_\sigma = \varphi(\rho c)_\sigma$ are the β-phase and σ-phase effective thermal capacities, respectively. φ is the volume fraction of the σ-phase defined by $\varphi = V_\sigma / V_{\mathrm{REV}}$ (V_{REV} is the volume of REV). h and a_v come from modeling of the interfacial flux and are the film heat transfer coefficient and the interfacial area per unit volume, respectively [39,41]. $\mathbf{K}_{\beta\beta}$, $\mathbf{K}_{\sigma\sigma}$, $\mathbf{K}_{\beta\sigma}$, and $\mathbf{K}_{\sigma\beta}$ are the effective thermal conductivity tensors, and the coupled thermal conductivity tensors are equal

$$\mathbf{K}_{\beta\sigma} = \mathbf{K}_{\sigma\beta}$$

When the system is isotropic and the physical properties of the two phases are constant, Eqs. (5) and (6) reduce to

$$\gamma_\beta \frac{\partial \langle T_\beta \rangle^\beta}{\partial t} = k_\beta \Delta \langle T_\beta \rangle^\beta + k_{\beta\sigma} \Delta \langle T_\sigma \rangle^\sigma + h a_v (\langle T_\sigma \rangle^\sigma - \langle T_\beta \rangle^\beta) \tag{9}$$

and

$$\gamma_\sigma \frac{\partial \langle T_\sigma \rangle^\sigma}{\partial t} = k_\sigma \Delta \langle T_\sigma \rangle^\sigma + k_{\sigma\beta} \Delta \langle T_\beta \rangle^\beta - h a_v (\langle T_\sigma \rangle^\sigma - \langle T_\beta \rangle^\beta) \tag{10}$$

where k_β and k_σ are the effective thermal conductivities of the β- and σ-phases, respectively, and $k_{\beta\sigma} = k_{\sigma\beta}$ is the cross effective thermal conductivity of the two phases.

Rewrite Eqs. (9) and (10) in their operator form, as follows:

$$\begin{bmatrix} \gamma_\beta \frac{\partial}{\partial t} - k_\beta \Delta + h a_v & -k_{\beta\sigma} \Delta - h a_v \\ -k_{\beta\sigma} \Delta - h a_v & \gamma_\sigma \frac{\partial}{\partial t} - k_\sigma \Delta + h a_v \end{bmatrix} \begin{bmatrix} \langle T_\beta \rangle^\beta \\ \langle T_\sigma \rangle^\sigma \end{bmatrix} = 0 \tag{11}$$

We then obtain an uncoupled form by evaluating the operator determinant such that

$$\left[\left(\gamma_\beta \frac{\partial}{\partial t} - k_\beta \Delta + h a_v \right) \left(\gamma_\sigma \frac{\partial}{\partial t} - k_\sigma \Delta + h a_v \right) - (k_{\beta\sigma} \Delta + h a_v)^2 \right] \langle T_i \rangle^i = 0 \tag{12}$$

where the index i can take β or σ. Its explicit form reads, after dividing by $h a_v (\gamma_\beta + \gamma_\sigma)$,

$$\frac{\partial \langle T_i \rangle^i}{\partial t} + \tau_q \frac{\partial^2 \langle T_i \rangle^i}{\partial t^2} = \alpha \Delta \langle T_i \rangle^i + \alpha \tau_T \frac{\partial}{\partial t} (\Delta \langle T_i \rangle^i) + \frac{\alpha}{k} \frac{k_{\beta\sigma}^2 - k_\beta k_\sigma}{h a_v} \Delta^2 \langle T_i \rangle^i \tag{13}$$

where

$$\tau_q = \frac{\gamma_\beta \gamma_\sigma}{h a_v (\gamma_\beta + \gamma_\sigma)}, \quad \tau_T = \frac{\gamma_\beta k_\sigma + \gamma_a k_\beta}{h a_v (k_\beta + k_\sigma + 2 k_{\beta\sigma})}$$

$$k = k_\beta + k_\sigma + 2 k_{\beta\sigma}, \quad \alpha = \frac{k_\beta + k_\sigma + 2 k_{\beta\sigma}}{\gamma_\beta + \gamma_\sigma} \tag{14}$$

This can be regarded as a dual-phase-lagging (DPL) heat-conduction equation with $((k_{\beta\sigma}^2 - k_\beta k_\sigma)/h a_v) \Delta^2 \langle T_i \rangle^i$ as the DPL source-related term $F(\mathbf{r},t) + \tau_q (\partial F(\mathbf{r},t)/\partial t)$ and with τ_q and τ_T as the phase lags of the heat flux and the temperature gradient, respectively [41,43]. Here, $F(\boldsymbol{r},t)$ is the volumetric heat source. k, ρc, and α are the effective thermal conductivity, capacity, and diffusivity of nanofluids, respectively. The dual-phase-lagging heat-conduction equation originates from the first law of thermodynamics and the dual-phase-lagging constitutive relation of heat flux density [41,43]. It is developed in examining energy transport involving high-rate heating in which the nonequilibrium thermodynamic transition and the microstructural effect become important associated with a shortening of the response time. In addition to its application for ultrafast pulse-laser heating, the dual-phase-lagging heat-conduction equation also describes and predicts phenomena such as the propagation of temperature pulses in superfluid liquid helium, nonhomogeneous lagging responses in porous media, thermal lagging in amorphous materials, and the effects of material defects and thermomechanical coupling [43]. Furthermore, the dual-phase-lagging heat-conduction equation forms a generalized unified equation with the wave equation, the potential equation, the classical parabolic heat-conduction equation, the hyperbolic heat-conduction equation, the energy equation in the phonon scattering model, and the energy equation in the phonon-electron interaction model as its special cases [41,43]. This, with the rapid growth of microscale heat conduction of high-rate heat flux, has attracted the recent research effort on the dual-phase-lagging heat-conduction equations [41,43].

Therefore, the presence of nanoparticles shifts the Fourier heat conduction in the base fluid into the dual-phase-lagging heat conduction in nanofluids at the macroscale. This finding is significant because all results regarding dual-phase-lagging heat conduction can thus be applied to study heat conduction in nanofluids.

The presence of nanoparticles gives rise to variations of thermal capacity, conductivity, and diffusivity, which are given by, in terms of ratios over those of the base fluid,

$$\frac{\rho c}{(\rho c)_\beta} = (1 - \varphi) + \varphi \frac{(\rho c)_\sigma}{(\rho c)_\beta} \tag{15}$$

$$\frac{k}{k_\beta} = 1 + \frac{k_\sigma}{k_\beta} + 2 \frac{k_{\beta\sigma}}{k_\beta} \tag{16}$$

$$\frac{\alpha}{\alpha_\beta} = \frac{k}{k_\beta} \frac{(\rho c)_\beta}{\rho c} \tag{17}$$

Therefore, $\rho c / (\rho c)_\beta$ depends *only* on the volume fraction of nanoparticles and the nanoparticle-fluid capacity ratio. However, both k/k_β and α/α_β are affected by the geometry of the nanoparticle-fluid interface due to the term $k_{\beta\sigma}/k_\beta$. This dependency causes the most difficulty because it is the least precisely known feature of a nanofluid. The future research effort should thus focus on $k_{\beta\sigma}/k_\beta$ to develop predicting models of thermophysical properties for nanofluids.

Equation (16) predicts that k/k_β increases as k_σ/k_β, which agrees with all experimental data [1–7]. To show the possibility of conductivity enhancement, consider

$$\frac{\tau_T}{\tau_q} = 1 + \frac{\gamma_\beta^2 k_\sigma + \gamma_\sigma^2 k_\beta - 2 \gamma_\beta \gamma_\sigma k_{\beta\sigma}}{\gamma_\beta \gamma_\sigma (k_\beta + k_\sigma + 2 k_{\beta\sigma})} \tag{18}$$

It can be large, equal, or smaller than 1 depending on the sign of $\gamma_\beta^2 k_\sigma + \gamma_\sigma^2 k_\beta - 2 \gamma_\beta \gamma_\sigma k_{\beta\sigma}$. Therefore, by the condition for the existence of thermal waves that requires $\tau_T / \tau_q < 1$ [41,44], we may have thermal waves in nanofluid heat conduction when

Fig. 5 Oil/water emulsion (oil volume fraction from 0.5 vol % to 16.7 vol %)

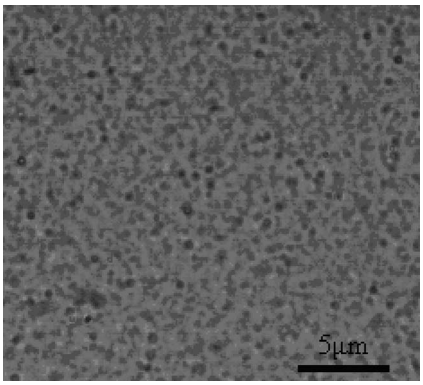

Fig. 6 Oil/water emulsion under microscope (oil volume fraction=3.33%; temperature=50°C; oil droplet mean diameter of 192.1 nm with a coefficient of variation (CV) of 4.99%)

$$\gamma_\beta^2 k_\sigma + \gamma_\sigma^2 k_\beta - 2\gamma_\beta \gamma_\sigma k_{\beta\sigma} < 0$$

Note also that for heat conduction in nanofluids there is a time-dependent source term $F(\boldsymbol{r},t)$ in the dual-phase-lagging heat conduction (Eq. (13)). Therefore, the resonance can also occur. These thermal waves and possibly resonance are believed to be the driving force for the conductivity enhancement. When $k_{\beta\sigma}=0$ so that τ_T/τ_q is always larger than 1, thermal waves and resonance would not appear. The coupled conductive terms in Eqs. (9) and (10) are thus responsible for thermal waves and resonance in nanofluid heat conduction. It is also interesting to note that although each τ_q and τ_T is ha_v-dependent, the ratio τ_T/τ_q is not. Therefore the evaluation of τ_T/τ_q will be much simpler than τ_q or τ_T.

4 Extension: Thermal-Wave Fluids

The present analysis of heat conduction nature in the last section is not limited to nanofluid heat conduction but is valid for heat conduction in all two-phase systems. It can also be extended to heat conduction in a system involving more than two phases. Therefore, all multiphase fluids are candidates of thermal-wave fluids in which heat conduction can support thermal waves and possibly resonance. The presence of such waves and resonance may enhance heat conduction processes, and consequently thermal conductivity significantly.

Thermal waves have been observed in casting sand experiments by two independent groups [43]. Substantial increases in thermal conductivity have also been confirmed experimentally for the porous-media fluids [45] and nanofluids [7]. However, the reported data of effective thermal conductivity are all in between those of two phases so that the k_β-enhancement appears only at $k_\sigma > k_\beta$. On the other hand, our theory shows that the k_β-enhancement can occur for all cases with $k_{\beta\sigma} > -k_\sigma/2$ (Eq. (14)). Therefore, it is possible to have some thermal-wave fluids that can support very strong thermal waves and resonance such that their conductivities are higher than those of two phases. We report here one of such thermal-wave fluids for the first time.

Our thermal-wave fluid is formed by emulsifying olive oil into distilled water with a small amount of cetyltrimethyl ammonium bromide under ultrasonic disruption (Ultrasonic Cell Processor, Haishu Kesheng Ultrasonic Equipment Ltd.). Loadings of olive oil droplets from 0.5 vol % to 16.7 vol % are synthesized and tested. Figure 5 shows the picture of the synthesized thermal-wave fluid with 12 values of oil volume fractions three months after its preparation. The fluid is very stable, and no bulk phase separation has been observed. Note that microemulsions are generally thermodynamically stable; their free energy is even lower than in the unmixed system [46,47]. Furthermore, the microemulsions are also freeze/thaw recoverable [48].

Figure 6 typifies the distribution of oil droplets in the emulsion, showing relatively monodispersed droplets uniformly distributed in the emulsion. The image analysis by using IMAGE PRO PLUS gives a mean droplet diameter of 192.1 nm with a coefficient of variation (CV) of 4.99%. Here CV is defined by $\mathrm{CV}=\sigma_d/d_m$ where σ_d is the standard derivation of the diameter and d_m is its mean value.

The conductivity ratio k/k_w measured by the standard transient hot-wire method (KD2, Therm Test Inc., Canada) is shown in Fig. 7 as a function of oil volume fraction and fluid temperature. Here k and k_w are the thermal conductivity of the thermal-wave fluid and the water, respectively. The prediction by the Maxwell model is also plotted in Fig. 7 for comparison [7,49]. Remarkably, an extraordinary conductivity enhancement—up to a 153.3% increase at the oil volume fraction of 3.3% and the fluid temperature of 30°C—is obtained in the fluid after adding some oil with lower thermal conductivity. For most tested cases, an extraordinary increase (rather than decrease) in thermal conductivity is achieved.

The oil/water emulsion conductivity predicted by using the Maxwell model shows a linear decrease with the increase in oil volume fraction and a negligible effect of emulsion temperature (Fig. 7). The measured conductivity shows a strong sensitivity and a high nonlinearity to both the oil volume fraction and the temperature and is consistent with the theory of thermal waves and resonance [41,43].

5 Concluding Remarks

Nanofluids can be synthesized by using solution chemistry. The ability to manipulate atoms and molecules in the liquid phase provides a powerful arsenal for synthesis of tailor-designed nanofluids using a bottom-up approach.

The presence of nanoparticles shifts the Fourier heat conduction in the base fluid into the dual-phase-lagging heat conduction in nanofluids at the macroscale. The coupled conduction of the two phases results in thermal waves and possibly resonance in nanofluid heat conduction. Such waves and resonance are responsible for the conductivity enhancement.

Our theory of nanofluid heat conduction also generalizes nanofluids into thermal-wave fluids and leads to the first experiment of extraordinary fluid conductivity enhancement (up to 153.3%) by adding some fluid even with lower conductivity. Such new thermal-wave fluids also have long-term stability and can be produced in large quantities. Therefore they can improve fluid conductivity and convective heat transfer more effectively than recently proposed nanofluids.

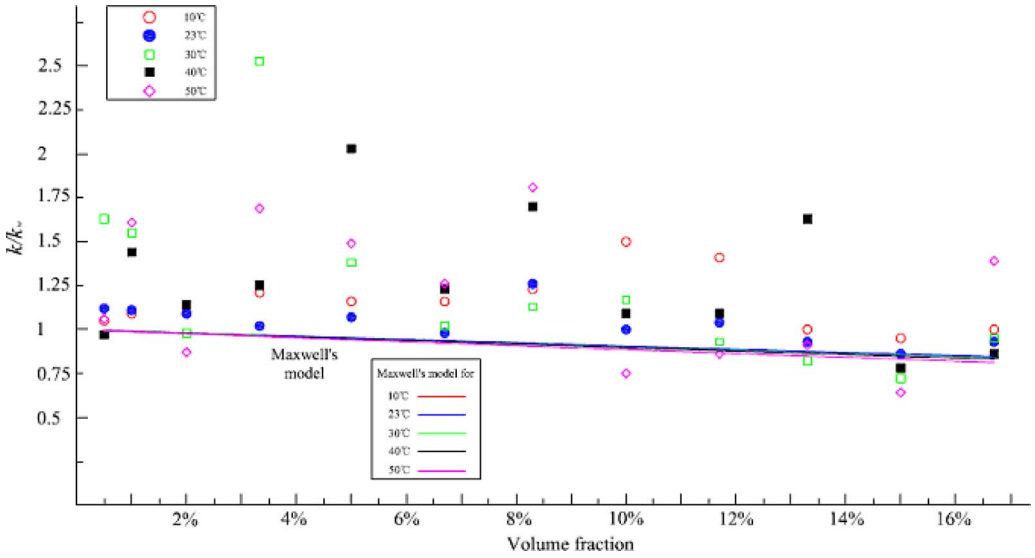

Fig. 7 Variation of k/k_w with oil volume fraction and emulsion temperature (k: emulsion thermal conductivity; k_w: water thermal conductivity)

Acknowledgment

The authors are indebted to Dr. H. T. Zhu for his contribution to the synthesis of nanofluids in Fig. 2. The financial support from the Research Grants Council of Hong Kong (GRF717508) is also gratefully acknowledged.

Nomenclature

a_v = interfacial area per unit volume, m^{-1}
$A_{\beta\sigma}$ = area of the β-σ interface, m^2
c = specific heat, J kg^{-1} K^{-1}
d_m = mean diameter, m
h = film heat transfer coefficient, W m^{-2} K^{-1}
k = thermal conductivity, W m^{-1} K^{-1}
k_β = effective thermal conductivity of the β-phases, W m^{-1} K^{-1}
k_σ = effective thermal conductivity of the σ-phases, W m^{-1} K^{-1}
$k_{\beta\sigma}$ = cross effective thermal conductivity of the β- and σ-phases, W m^{-1} K^{-1}
$\mathbf{K}_{\beta\beta}$ = effective thermal conductivity tensor associated with $\nabla\langle T_\beta\rangle^\beta$ in the β-phase equation, W m^{-1} K^{-1}
$\mathbf{K}_{\beta\sigma}$ = effective thermal conductivity tensor associated with $\nabla\langle T_\sigma\rangle^\sigma$ in the β-phase equation, W m^{-1} K^{-1}
$\mathbf{K}_{\sigma\sigma}$ = effective thermal conductivity tensor associated with $\nabla\langle T_\sigma\rangle^\sigma$ in the σ-phase equation, W m^{-1} K^{-1}
$\mathbf{K}_{\sigma\beta}$ = effective thermal conductivity tensor associated with $\nabla\langle T_\beta\rangle^\beta$ in the σ-phase equation, W m^{-1} K^{-1}
$\mathbf{n}$ = outward unit normal vector
$\mathbf{n}_{\beta\sigma}$ = $-\mathbf{n}_{\sigma\beta}$ outward unit normal vector pointing from the β-phase toward the σ-phase
t = time, s
T = temperature, K
V = volume measure, volume of integration, m^3
V_{REV} = volume of REV, m^3
V_α = the portion of the REV occupied by the α-phase and its volume, m^3
V_β = the portion of the REV occupied by the β-phase and its volume, m^3

Greek Symbols

α = thermal diffusivity, m^2 s^{-1}
φ = volume fraction of the σ-phase
γ = thermal capacity, J m^{-3} s^{-1} K^{-1}
γ_β = β-phase effective thermal capacity, J m^{-3} s^{-1} K^{-1}
γ_α = α-phase effective thermal capacity, J m^{-3} s^{-1} K^{-1}
ρ = density, kg m^{-3}
τ_q = phase-lag of heat flux vector, s
τ_T = phase-lag of temperature gradient, s

Other Mathematical Symbols

$\langle\ \rangle$ = averaging operator
∇ = gradient operator, m^{-1}
Δ = Laplacian, m^{-2}

Subscripts and Superscripts

i = general index qualifier
o = oil
w = water
α = α-phase
$\alpha\beta$ = entity qualifier for an interface between the α- and β-phase
β = β-phase
σ_d = standard derivation of the diameter, m

References

[1] Choi, S. U. S., 1995, "Enhancing Thermal Conductivity of Fluids With Nanoparticles," *Developments and Applications of Non-Newtonian Flows*, D. A. Singer and H. P. Wang, eds., ASME, New York, **FED 231**, pp. 99–105.
[2] Choi, S. U. S., Zhang, Z. G., and Keblinski, P., 2004, "Nanofluids," *Encyclopedia of Nanoscience and Nanotechnology*, H. S. Nalwa, ed., Vol. 6, American Scientific Publishers, New York, pp. 757–773.
[3] Eastman, J. A., Phillpot, S. R., Choi, S. U. S., and Keblinski, P., 2004, "Thermal Transport in Nanofluids," Annu. Rev. Mater. Res., **34**, pp. 219–246.
[4] Keblinski, P., Eastman, J. A., and Cahill, D. G., 2005, "Nanofluids for Thermal Transport," Mater. Today, **8**(6), pp. 36–44.
[5] Phelan, P. E., Bhattacharya, P., and Prasher, R. S., 2005, "Nanofluids for Heat Transfer Applications," Annu. Rev. Heat Transfer, **14**, pp. 255–275.
[6] Peterson, G. P., and Li, C. H., 2006, "Heat and Mass Transfer in Fluids With Nanoparticle Suspensions," Adv. Heat Transfer, **39**, pp. 257–376.

[7] Das, S. K., Choi, S. U. S., Yu, W. H., and Pradeep, T., 2008, *Nanofluids: Science and Technology*, Wiley, Hoboken, NJ.
[8] Jang, S. P., and Choi, S. U. S., 2007, "Effects of Various Parameters on Nanofluid Thermal Conductivity," ASME J. Heat Transfer, **129**(5), pp. 617–623.
[9] Buongiorno, J., 2006, "Convective Transport in Nanofluids," ASME J. Heat Transfer, **128**(3), pp. 240–250.
[10] Choi, S. U. S., and Eastman, J. A., 2001, "Enhanced Heat Transfer Using Nanofluids," U.S. Patent No. 6,221,275 B1.
[11] Eastman, J. A., Choi, S. U. S., Li, S., Yu, W., and Thompson, L. J., 2001, "Anomalously Increased Effective Thermal Conductivities of Ethylene Glycol-Based Nanofluids Containing Copper Nanoparticles," Appl. Phys. Lett., **78**(6), pp. 718–720.
[12] Kostic, M. M., 2006, "Critical Issues and Application Potentials in Nanofluids Research," *Proceedings of Multifunctional Nanocomposites*, Paper No. MN2006-17036.
[13] Chang, H., Tsung, T. T., Chen, L. C., Yang, Y. C., Lin, H. M., Lin, C. K., and Jwo, C. S., 2005, "Nanoparticle Suspension Preparation Using the Arc Spray Nanoparticle Synthesis System Combined With Ultrasonic Vibration and Rotating Electrode," Int. J. Adv. Manuf. Technol., **26**(5–6), pp. 552–558.
[14] Lo, C. H., Tsung, T. T., Chen, L. C., Su, C. H., and Lin, H. M., 2005, "Fabrication of Copper Oxide Nanofluid Using Submerged Arc Nanoparticle Synthesis System (SANSS)," J. Nanopart. Res., **7**(2–3), pp. 313–320.
[15] Lo, C. H., Tsung, T. T., and Chen, L. C., 2005, "Shaped-Controlled Synthesis of Cu-Based Nanofluid Using Submerged Arc Nanoparticle Synthesis System (SANSS)," J. Cryst. Growth, **277**(1–4), pp. 636–642.
[16] Kim, S. H., Choi, S. R., and Kim, D., 2007, "Thermal Conductivity of Metal-Oxide Nanofluids: Particle Size Dependence and Effect of Laser Irradiation," ASME J. Heat Transfer, **129**(3), pp. 298–307.
[17] Rusconi, R., Rodari, E., and Piazza, R., 2006, "Optical Measurements of the Thermal Properties of Nanofluids," Appl. Phys. Lett., **89**(26), p. 261916.
[18] Putnam, S. A., Cahill, D. G., Braun, P. V., Ge, Z. B., and Shimmin, R. G., 2006, "Thermal Conductivity of Nanoparticle Suspensions," J. Appl. Phys., **99**, p. 084308.
[19] Eapen, J., Williams, W. C., Buongiorno, J., Hu, L. W., and Yip, S., 2007, "Mean-Field Versus Microconvection Effects in Nanofluid Thermal Conduction," Phys. Rev. Lett., **99**, p. 095901.
[20] Xuan, Y. M., Li, Q., Zhang, X., and Hu, W., 2003, "Aggregation Structure and Thermal Conductivity of Nanofluids," AIChE J., **49**(4), pp. 1038–1043.
[21] Koo, J., and Kleinstreuer, C., 2004, "A New Thermal Conductivity Model for Nanofluids," J. Nanopart. Res., **6**(6), pp. 577–588.
[22] Jang, S. P., and Choi, S. U. S., 2004, "Role of Brownian Motion in the Enhanced Thermal Conductivity of Nanofluids," Appl. Phys. Lett., **84**(21), pp. 4316–4318.
[23] Bhattacharya, P., Saha, S. K., Yadav, A., Phelan, P. E., and Prasher, R. S., 2004, "Brownian Dynamics Simulation to Determine the Effect Thermal Conductivity of Nanofluids," J. Appl. Phys., **95**, pp. 6492–6494.
[24] Prasher, R., Bhattacharya, P., and Phelan, P. E., 2005, "Thermal Conductivity of Nanoscale Colloidal Solutions (Nanofluids)," Phys. Rev. Lett., **94**, p. 025901.
[25] Prasher, R., Bhattacharya, P., and Phelan, P. E., 2006, "Brownian-Motion-Based Convective-Conductive Model for the Effective Thermal Conductivity of Nanofluids," ASME J. Heat Transfer, **128**(6), pp. 588–595.
[26] Yu, W., and Choi, S. U. S., 2003, "The Role of Interfacial Layers in the Enhanced Thermal Conductivity of Nanofluids: A Renovated Maxwell Model," J. Nanopart. Res., **5**(1–2), pp. 167–171.
[27] Yu, W., and Choi, S. U. S., 2004, "The Role of Interfacial Layers in the Enhanced Thermal Conductivity of Nanofluids: A Renovated Hamilton-Crosser Model," J. Nanopart. Res., **6**(4), pp. 355–361.
[28] Xue, L., Keblinski, P., Phillpot, S. R., Choi, S. U. S., and Eastman, J. A., 2004, "Effect of Liquid Layering at the Liquid-Solid Interface on Thermal Transport," Int. J. Heat Mass Transfer, **47**(19–20), pp. 4277–4284.
[29] Xie, H., Fujii, M., and Zhang, X., 2005, "Effect of Interfacial Nanolayer on the Effective Thermal Conductivity of Nanoparticle-Fluid Mixture," Int. J. Heat Mass Transfer, **48**(14), pp. 2926–2932.
[30] Ren, Y., Xie, H., and Cai, A., 2005, "Effective Thermal Conductivity of Nanofluids Containing Spherical Nanoparticles," J. Phys. D, **38**(21), pp. 3958–3961.
[31] Leong, K. C., Yang, C., and Murshed, S. M. S., 2006, "A Model for the Thermal Conductivity of Nanofluids: The Effect of Interfacial Layer," J. Nanopart. Res., **8**(2), pp. 245–254.
[32] Wang, B. X., Zhou, L. P., and Peng, X. F., 2003, "A Fractal Model for Predicting the Effective Thermal Conductivity of Liquid With Suspension of Nanoparticles," Int. J. Heat Mass Transfer, **46**(14), pp. 2665–2672.
[33] Prasher, R., Phelan, P. E., and Bhattacharya, P., 2006, "Effect of Aggregation Kinetics on the Thermal Conductivity of Nanoscale Colloidal Solutions (Nanofluid)," Nano Lett., **6**(7), pp. 1529–1534.
[34] Chen, G., 2001, "Balistic-Diffusive Heat-Conduction Equations," Phys. Rev. Lett., **86**(11), pp. 2297–2300.
[35] Vadasz, J. J., Govender, S., and Vadasz, P., 2005, "Heat Transfer Enhancement in Nanofluids Suspensions: Possible Mechanisms and Explanations," Int. J. Heat Mass Transfer, **48**(13), pp. 2673–2683.
[36] Vadasz, P., 2006, "Heat Conduction in Nanofluid Suspensions," ASME J. Heat Transfer, **128**(5), pp. 465–477.
[37] Whitaker, S., 1999, *The Method of Volume Averaging*, Kluwer, Dordrecht, p. 219.
[38] Wang, L. Q., 2000, "Flows Through Porous Media: A Theoretical Development at Macroscale," Transp. Porous Media, **39**(1), pp. 1–24.
[39] Wang, L. Q., Xu, M. T., and Wei, X. H., 2008, "Multiscale Theorems," Adv. Chem. Eng., **34**, pp. 175–468.
[40] Wang, L. Q., 1994, "Generalized Fourier Law," Int. J. Heat Mass Transfer, **37**(17), pp. 2627–2634.
[41] Wang, L. Q., Zhou, X. S., and Wei, X. H., 2008, *Heat Conduction: Mathematical Models and Analytical Solutions*, Springer-Verlag, Berlin.
[42] Wang, L. Q., and Wei, X. H., 2008, "Equivalence Between Dual-Phase-Lagging and Two-Phase-System Heat Conduction Processes," Int. J. Heat Mass Transfer, **51**(7–8), pp. 1751–1756.
[43] Tzou, D. Y., 1997, *Macro-to Microscale Heat Transfer: The Lagging Behavior*, Taylor & Francis, Washington, D.C.
[44] Xu, M. T., and Wang, L. Q., 2002, "Thermal Oscillation and Resonance in Dual-Phase-Lagging Heat Conduction," Int. J. Heat Mass Transfer, **45**(5), pp. 1055–1061.
[45] Aichlmayr, H. T., and Kulacki, F. A., 2006, "The Effective Thermal Conductivity of Saturated Porous Media," Adv. Heat Transfer, **39**, pp. 377–460.
[46] Hoar, T. P., and Schulman, J. H., 1943, "Transparent Water-in-Oil Dispersions: The Oleopathic Hydro-Micelle," Nature (London), **152**, pp. 102–103.
[47] Kumar, P., and Mittal, K., 1999, *Handbook of Microemulsion Science and Technology*, CRC, Boca Raton, FL.
[48] Yang, B., and Han, Z. H., 2006, "Thermal Conductivity Enhancement in Water-in-FC72 Nanoemulsion Fluids," Appl. Phys. Lett., **88**(26), p. 261914.
[49] Maxwell, J. C., 1904, *A Treatise on Electricity and Magnetism*, Oxford University Press, Cambridge.

Modeling Micro Mass and Heat Transfer for Gases Using Extended Continuum Equations

Manuel Torrilhon
Seminar for Applied Mathematics,
ETH Zurich,
Zurich 8092, Switzerland
e-mail: matorril@math.ethz.ch

Henning Struchtrup
Department of Mechanical Engineering,
University of Victoria,
PO Box 3055 STN CSC,
Victoria BC V8W 3P6, Canada
e-mail: struchtr@uvic.ca

This paper presents recent contributions to the development of macroscopic continuum transport equations for micro gas flows and heat transfers. Within the kinetic theory of gases, a combination of the Chapman–Enskog expansion and the Grad moment method yields the regularized 13-moment equations (R13 equations), which are of high approximation order. In addition, a complete set of boundary conditions can be derived from the boundary conditions of the Boltzmann equation. The R13 equations are linearly stable, and their results for moderate Knudsen numbers stand in excellent agreement with direct simulation Monte Carlo (DSMC) method simulations. We give analytical expressions for heat and mass transfer in microchannels. These expressions help to understand the complex interaction of fluid variables in microscale systems. Additionally, we compare interesting analogies such as a mass flux and energy Knudsen paradox. In particular, the R13 model is capable of predicting and explaining the detailed features of Poiseuille microflows. [DOI: 10.1115/1.3056598]

Keywords: continuum models, Poiseuille flow, moment method, kinetic gas theory

1 Introduction

Processes in microscale flows of gases or, equivalently, in rarefaction situations are well described by the Boltzmann equation [1], which describes the evolution of the particle distribution function in phase space, i.e., on the microscopic level.

The relevant scaling parameter to characterize processes in microflow gases is the Knudsen number Kn, defined as the ratio between the mean free path of a particle and a relevant length scale. If the Knudsen number is small, the Boltzmann equation can be reduced to simpler models, which allow faster solutions. Indeed, if the Knudsen number is small ($\mathrm{Kn} < 0.01$), the hydrodynamic equations, the laws of Navier–Stokes and Fourier (NSF), can be derived from the Boltzmann equation, e.g., by the Chapman-Enskog method [2]. The NSF equations are macroscopic equations for mass density ρ, velocity v_i, and temperature T and thus pose a mathematically less complex problem than the Boltzmann equation.

Macroscopic equations for rarefied gas flows at Knudsen numbers above 0.01 promise to replace the Boltzmann equation with simpler equations that still capture the relevant physics. The Chapman–Enskog expansion is the classical method to achieve this goal, but the resulting Burnett and super-Burnett equations are unstable [3]. To fix these problems in the framework of the Chapman–Enskog expansion is cumbersome [4,5]. Nevertheless, in some cases Burnett equations could be used for simulations of nonequilibrium gases [6–8].

A classical alternative is Grad's moment method [9], which extends the set of variables by adding deviatoric pressure tensor $\sigma_{ij} := p_{\langle ij \rangle}$ (stress), heat flux q_i, and possibly higher moments of the velocity distribution function (phase density) of the particles. The resulting equations are stable but lead to spurious discontinuities in shocks [10]. Nevertheless, some successes have been obtained with moment methods, and popularity is rising (see Refs. [11–15]). However, for a given value of the Knudsen number, it is not clear what set of moments one would have to consider [2].

Struchtrup and Torrilhon [16,17] combined both approaches by performing a Chapman–Enskog expansion around a nonequilibrium phase density of Grad type, which resulted in the "regularized 13-moment equations" (R13 equations), which form a stable set of equations for the 13 variables $(\rho, v_i, T, \sigma_{ij}, q_i)$ of super-Burnett order, i.e., of third order in the Knudsen number when asymptotically expanded. Section 2 gives a review of this original derivation. An alternative approach to the problem was presented by Struchtrup in Refs. [18,19], partly based on an earlier work by Müller et al. [20]. This order-of-magnitude method is based on a rigorous asymptotic analysis of the infinite hierarchy of the moment equations. A brief outline is also given in Sec. 2.

One of the biggest problems for all models beyond NSF is to prescribe suitable boundary conditions for the extended equations, which should follow from the boundary conditions for the Boltzmann equation. This task was recently tackled in Ref. [21], and the general solution to the problem [22] will be discussed after the derivation of the equations when we present boundary conditions for the R13 equations.

The second part of this paper will survey the properties of the R13 equations, which are linearly stable, obey an H-theorem for the linear case, contain the Burnett and super-Burnett equations asymptotically, predict phase speeds and damping of ultrasound waves in excellent agreement with experiments, yield smooth and accurate shock structures for all Mach numbers, and exhibit Knudsen boundary layers and the Knudsen minimum of channel flow in excellent agreement with direct simulation Monte Carlo (DSMC) method simulations. This paper reviews detailed information about the performance of R13 for Poiseuille flow in microchannels and discusses how microvariables enter and influence the classical fluid dynamical relations. The interested reader is referred to the cited literature, including the monograph [2].

2 Derivation of R13

The derivation of the regularized 13-moment equations has been done in two ways. Both ways give specific insight into the structure and properties of the theory.

2.1 Based on Pseudo-Time-Scales. The original derivation

Contributed by the Heat Transfer Division ASME for publication in the JOURNAL OF HEAT TRANSFER. Manuscript received February 10, 2008; final manuscript received August 16, 2008; published online January 13, 2009. Review conducted by Robert D. Tzou. Paper presented at the 2008 International Conference on Micro/Nanoscale Heat Transfer (MNHT2008), January 6–9 2008, Tainan, Taiwan.

[16] develops an enhanced constitutive theory for Grad's moment equations. The closure procedure of Grad is too rigid and needs to be relaxed. The new theory can be summarized in three steps:

1. Identify the set of variables U and higher moments V that need a constitutive relation in Grad's theory.
2. Formulate evolution equations for the difference $R=V-V^{(\mathrm{Grad})}(U)$ of the constitutive moments and their Grad relation.
3. Perform an asymptotic expansion of R alone while fixing *all* variables U of Grad's theory.

This procedure can, in principle, be performed on any system obtained by Grad's moment method; i.e., any number of moments can be considered as a basic set of variables. For the derivation of R13 the first 13-moment density, velocity, temperature, stress deviator, and heat flux have been considered in accordance with the classical 13-moment case of Grad.

In the classical Grad approach, the difference R is considered to be zero: All constitutive moments follow from lower moments by means of Grad's distribution $V=V^{(\mathrm{Grad})}(U)$. This rigidity causes hyperbolicity as well as artifacts such as subshocks and poor accuracy. However, the evolution equation for R is, in general, not an identity. Instead it describes possible deviations of Grad's closure. The constitutive theory of R13 takes these deviations into account.

The evolution equation for R cannot be solved exactly because it is influenced by even higher moments. Hence, an approximation is found by asymptotic expansion. In doing this, step 3 requires a modeling assumption about a scaling cascade of the higher order moments. In the asymptotic expansion of R, we fix lower moments, that is, density, velocity, and temperature, as well as nonequilibrium quantities such as stress and heat flux. The assumption is a pseudo-time-scale such that the higher moments R follow a faster relaxation. The expansion can also be considered as an expansion around a nonequilibrium (pseudo-equilibrium). A similar idea has been formulated in Ref. [23] based solely on distribution functions.

The result for R after one expansion step is a relation that couples R to gradients of the variables U; in R13 these are gradients of stress and heat flux. The gradient terms enter the divergences in the equations for stress and heat flux and produce dissipative second order derivatives. The final system is a regularization of Grad's 13-moment equations. The procedure resembles the derivation of the NSF system. Indeed the NSF equations can be considered as a regularization of Euler equations (i.e., Grad's five-moment system).

2.2 Based on Order of Magnitude. The order-of-magnitude method [18,19] considers the infinite system of moment equations resulting from Boltzmann's equation. It does not depend on Grad's closure relations and does not directly utilize the result of asymptotic expansions. The method finds the proper equations with the order of accuracy λ_0 in the Knudsen number by the following three steps:

1. determination of the order of magnitude λ of the moments
2. construction of moment set with a minimum number of moments at order λ
3. deletion of all terms in all equations that would lead only to contributions of orders $\lambda>\lambda_0$ in the conservation laws for energy and momentum

Step 1 is based on a Chapman–Enskog expansion where a moment φ is expanded according to $\varphi=\varphi_0+\mathrm{Kn}\varphi_1+\mathrm{Kn}^2\varphi_2+\cdots$, and the leading order of φ is determined by inserting this ansatz into the complete set of moment equations. A moment is said to be of leading order λ if $\varphi_\beta=0$ for all $\beta<\lambda$. This first step agrees with the ideas of Ref. [20]. Alternatively, the order of magnitude of the moments can be found from the principle that a single term in an equation cannot be larger in size by one or several orders of magnitude than all other terms [24].

In step 2, new variables are introduced by a linear combination of the moments originally chosen. The new variables are constructed such that the number of moments at a given order λ is minimal. This step gives an unambiguous set of moments at order λ.

Step 3 follows from the definition of the order of accuracy λ_0: A set of equations is said to be accurate of order λ_0 when stress and heat flux are known within the order $\mathcal{O}(\mathrm{Kn}^{\lambda_0})$.

The order-of-magnitude method gives the Euler and NSF equations at zeroth and first orders and thus agrees with the Chapman–Enskog method in the lower orders [18]. The second order equations turn out to be Grad's 13-moment equations for Maxwell molecules [18] and a generalization of these for molecules that interact with power potentials [2,19]. At third order, the method was only performed for Maxwell molecules, where it yields the R13 equations [18]. It follows that R13 satisfies some optimality when processes are to be described with third order accuracy.

Note that the derivation based on pseudo-time-scales above requires an unphysical assumption, namely, strongly different relaxation times for different moments. Such a cascading does not exist since all moments relax on roughly the same time scale proportional to Kn. The order-of-magnitude approach does not rely on such an assumption. Instead of different relaxation times, this method induces a structure on the set of nonequilibrium moments based on size, that is, order of magnitude, and justifies different closed systems of moment equations.

2.3 Result. Here, we display the original R13 equations from Ref. [16], which are build from the general conservation laws for a monatomic gas with mass density ρ, velocity v_i, and temperature θ in energy units,

$$\frac{\partial \varrho}{\partial t}+\frac{\partial \varrho v_k}{\partial x_k}=0 \tag{1}$$

$$\varrho\frac{\partial v_i}{\partial t}+\varrho v_k\frac{\partial v_i}{\partial x_k}+\frac{\partial p}{\partial x_i}+\frac{\partial \sigma_{ik}}{\partial x_k}=0 \tag{2}$$

$$\frac{3}{2}\varrho\frac{\partial \theta}{\partial t}+\frac{3}{2}\varrho v_k\frac{\partial \theta}{\partial x_k}+\frac{\partial q_k}{\partial x_k}+(p\delta_{ij}+\sigma_{ij})\frac{\partial v_i}{\partial x_j}=0 \tag{3}$$

where δ_{ij} is the Kronecker symbol or identity matrix. For the pressure p we assume the ideal gas law $p=\rho\theta$. We use Cartesian index notation with $i,j,k,l\in\{1,2,3\}$ and summation convention. The additional evolution equations that close the system are given by

$$\frac{\partial \sigma_{ij}}{\partial t}+\frac{\partial \sigma_{ij}v_k}{\partial x_k}+\frac{4}{5}\frac{\partial q_{\langle i}}{\partial x_{j\rangle}}+2p\frac{\partial v_{\langle i}}{\partial x_{j\rangle}}+2\sigma_{k\langle i}\frac{\partial v_{j\rangle}}{\partial x_k}+\frac{\partial m_{ijk}}{\partial x_k}=-\frac{p}{\mu}\sigma_{ij} \tag{4}$$

for the stress deviator σ_{ij} and

$$\frac{\partial q_i}{\partial t}+\frac{\partial q_i v_k}{\partial x_k}+p\frac{\partial(\sigma_{ik}/\rho)}{\partial x_k}+\frac{5}{2}(p\delta_{ik}+\sigma_{ik})\frac{\partial \theta}{\partial x_k}-\frac{\sigma_{ij}}{\varrho}\frac{\partial \sigma_{jk}}{\partial x_k}+\left(m_{ijk}+\frac{6}{5}q_{(i}\delta_{jk)}+q_k\delta_{ij}\right)\frac{\partial v_j}{\partial x_k}+\frac{1}{2}\frac{\partial \hat{R}_{ik}}{\partial x_k}=-\frac{2p}{3\mu}q_i \tag{5}$$

for the heat flux q_i with μ the viscosity of the gas. Round brackets give the symmetric part of a tensor, while angular brackets around indices denote the symmetric deviatoric part, e.g., $A_{\langle ij\rangle}=A_{(ij)}-\frac{1}{3}A_{kk}\delta_{ij}=\frac{1}{2}(A_{ij}+A_{ji})-\frac{1}{3}A_{kk}\delta_{ij}$, and analogously for three indices, see Ref. [2].

Note that these equations include the classical laws of Navier–Stokes and Fourier for stress deviator and heat flux. They can be

formally recovered by setting σ_{ij}, q_i, m_{ijk}, and $\hat{R}_{ij}$ to zero on the left hand side only. The additional terms in the equations beyond the classical laws allow for inertial effects and nongradient transport. That is, stress and heat flux are no longer slaved to the thermodynamic fluxes, velocity gradient, and temperature gradient.

The remaining quantities m_{ijk} and $\hat{R}_{ij}$ represent higher moments, and as such they form fluxes of stress and heat flux. These are zero in the Grad case, but the R13 theory provides the gradient expressions

$$m_{ijk} = -2\mu \frac{\partial(\sigma_{\langle ij}/\rho)}{\partial x_{k\rangle}} + \frac{8}{10p} q_{\langle i} \sigma_{jk\rangle}^{(\mathrm{NSF})} \tag{6}$$

$$R_{ij} = -\frac{24}{5}\mu \frac{\partial(q_{\langle j}/\rho)}{\partial x_{j\rangle}} + \frac{32}{25p} q_{\langle i} q_{j\rangle}^{(\mathrm{NSF})} + \frac{24}{7\rho} \sigma_{k\langle i} \sigma_{j\rangle k}^{(\mathrm{NSF})} \tag{7}$$

$$R = -12\mu \frac{\partial(q_k/\rho)}{\partial x_k} + \frac{8}{p} q_k q_k^{(\mathrm{NSF})} + \frac{6}{\rho} \sigma_{ij} \sigma_{ij}^{(\mathrm{NSF})} \tag{8}$$

with $\hat{R}_{ij} = R_{ij} + \frac{1}{3} R \delta_{ij}$ and the abbreviations

$$\sigma_{ij}^{(\mathrm{NSF})} = -2\mu \frac{\partial v_{\langle i}}{\partial x_{j\rangle}}, \quad q_i^{(\mathrm{NSF})} = -\frac{15}{4}\mu \frac{\partial \theta}{\partial x_i} \tag{9}$$

In total the R13 system is given by nonlinear parabolic-hyperbolic partial differential equations with relaxation. In that sense it resembles the mathematical structure of the NSF equations.

3 Boundary Conditions for R13

The computation of boundary conditions for the R13 equations is based on Maxwell's model for boundary conditions for the Boltzmann equation [1,2,25], which states that a fraction χ of the particles hitting the wall are thermalized, while the remaining $1-\chi$ particles are specularly reflected. Boundary conditions for moments follow by taking moments of the boundary conditions of the Boltzmann equation. To produce meaningful boundary conditions, one needs to obey the following rules:

1. *Continuity*: In order to have meaningful boundary conditions for all accommodation coefficients $\chi \in [0,1]$, only boundary conditions for tensors with an odd number of normal components should be considered [21].
2. *Consistency*: Only boundary conditions for fluxes that actually appear in the equations should be considered [22].
3. *Coherence*: The same number of boundary conditions should be prescribed for the linearized and the nonlinear equations [22].

The application of rules 1 and 2 is straightforward and yields the following set of kinetic boundary conditions (t and n denote tangential and normal tensor components, respectively) for moments:

$$\begin{aligned}
\sigma_{tn} &= -\beta\left(PV_t + \tfrac{1}{2} m_{tnn} + \tfrac{1}{5} q_t\right) \\
q_n &= -\beta\left(2P\Delta\theta + \tfrac{5}{28} R_{nn} + \tfrac{1}{15} R + \tfrac{1}{2}\theta\sigma_{nn} - \tfrac{1}{2} PV_t^2\right) \\
R_{tn} &= \beta\left(P\theta V_t - \tfrac{1}{2}\theta m_{tnn} - \tfrac{11}{5}\theta q_t - PV_t^3 + 6P\Delta\theta V_t\right) \\
m_{nnn} &= \beta\left(\tfrac{2}{5} P\Delta\theta - \tfrac{1}{14} R_{nn} + \tfrac{1}{75} R - \tfrac{7}{5}\theta\sigma_{nn} - \tfrac{3}{5} PV_t^2\right) \\
m_{ttn} &= -\frac{m_{nnn}}{2} - \beta\left(\frac{1}{14}\left(R_{tt} + \frac{R_{nn}}{2}\right) + \theta\left(\sigma_{tt} + \frac{\sigma_{nn}}{2}\right) - PV_t^2\right)
\end{aligned} \tag{10}$$

where $\Delta\theta = \theta - \theta_W$, $V_t = v_t - v_t^W$, and

$$P := \rho\theta + \frac{\sigma_{nn}}{2} - \frac{R_{nn}}{28\theta} - \frac{R}{120\theta} \tag{11}$$

The properties of the wall are given by its temperature θ_W and velocity v_t^W and the modified accommodation coefficient

$$\beta = \chi/(2-\chi)\sqrt{2/(\pi\theta)} \tag{12}$$

In extrapolation of the theory of accommodation, these coefficients that occur in every equation of Eq. (10) could be chosen differently. So far, most results have been obtained with only one accommodation coefficient in accordance with the Maxwell model. Clearly, the Maxwell model is a strong reduction of the wall properties, and in many realistic cases more parameters are required to model wall interactions. Different accommodation coefficients of the single moment fluxes, e.g., shear or heat flux, could be used to model detailed wall properties. However, more investigations and comparisons are required for such an approach.

The first condition above is the slip condition for the velocity, while the second equation is the jump condition for the temperature. They come in a generalized form, with the essential part given by $\sigma_{tn} \sim V_t$ and $q_n \sim \Delta\theta$. In a manner of speaking, the other conditions can be described as jump conditions for higher moments, which again relate fluxes and respective variables. In perfect analogy to the usual slip and jump conditions, the essential part is given by $R_{tn} \sim q_t$ and $m_{nnn} \sim \sigma_{nn}$. The additional terms in Eq. (10) are off-diagonal terms coupling all even (in index n) moments in the boundary conditions.

When the R13 equations are considered for channel flows in their original form, it turns out that a different number of boundary conditions is required to solve the fully nonlinear and the linearized equations. Since this would not allow a smooth transition between linear and nonlinear situations, we formulated the third rule as given above.

Asymptotic analysis shows that some terms can be changed without changing the overall asymptotic accuracy of the R13 equations. This leads to the algebraization of several nonlinear terms in the partial differential equations, which, after some algebra, leads to algebraic relations, termed as bulk equations, between the moments that serve as additional boundary conditions for the nonlinear equations [22],

$$m_{tnn} = \frac{32}{45p} \sigma_{tn} q_n \tag{13}$$

$$\hat{R}_{nn} = \frac{136}{25p} q_n^2 - \frac{72}{35\rho} \sigma_{tn}^2 \tag{14}$$

These equations have a special interpretation. The possibility to prescribe kinetic boundary conditions as in Eq. (10) for moments is related to the ability of the moments to produce a so-called Knudsen layer. The Knudsen layer is a boundary layer that occurs close to the wall in high Knudsen number flows, for example, in microchannels. The kinetic boundary condition specifies the amplitude of the boundary layer. In the R13 system some variables, for instance, parallel heat flux, and normal stresses, are able to produce a Knudsen layer, while the higher moments $\hat{R}_{nn}$ and m_{tnn} cannot. This is due to the finite number of moments considered. In the infinite moment hierarchy, all moments exhibit Knudsen layers (see Ref. [26]).

Due to the lack of a Knudsen layer, kinetic boundary conditions may not be used for the moments $\hat{R}_{nn}$ and m_{tnn}. Instead, we assume that the boundary layer is relaxed infinitely fast to an interior solution—the bulk relation given in Eq. (13). The analysis shows that relation (13) is valid not only at the boundary but also at some distance from it where the flow has shear flow character. In that sense the bulk relations are consistency requirements and not only boundary conditions. They are algebraic relations required by the R13 equations, and the values for $\hat{R}_{nn}$ and m_{tnn} at the wall need to be consistent. Correspondingly, Eq. (13) should be

prescribed at the wall. Hence, the bulk solution turns out to be the natural boundary conditions for Knudsen-layer-less variables. Details of this interpretation can be found in Ref. [22].

4 Achievements With R13

We summarize the most important features of the R13 equations, which result from analytical considerations and from analytical and numerical solutions. The results of R13 have been compared with experimental data as well as to direct simulation results obtained by DSMC [27].

The R13 equations

- are derived in a rational manner by means of the order-of-magnitude method [18,19] or from a Chapman–Enskog expansion around nonequilibrium [16,17], as described above
- are of third order in the Knudsen number [2,16–19] when expanded in an asymptotic expansion and compared with the full expansion of Boltzmann's equation
- are linearly stable for initial and boundary value problems [16,17] (that is, amplitudes of linear sound and heat waves are not amplified)
- contain Burnett and super-Burnett asymptotically in the linear [16] and nonlinear [17] cases (however, higher order contributions stabilize the R13 system)
- predict phase speeds and damping of sound waves with high frequencies and short wavelengths in excellent agreement with experiments [16]
- give smooth shock structures without subshocks for all Mach numbers, with quantitatively very good agreement with DSMC simulations for $\mathrm{Ma} \lesssim 3$ [17]
- are accompanied by a complete set of boundary conditions [22] based on the most commonly used accommodation model in kinetic theory
- obey an entropy and H-theorem for the linear case, including the boundaries [28], which can also be used to derive the equations as such
- exhibit the Knudsen paradox, i.e., the minimum of the mass flow rate for channel flows (see Sec. 5) [22,28]
- exhibit Knudsen boundary layers for temperature and velocity profiles as well as other moments in good agreement with DSMC [29,30]
- are easily accessible to numerical simulations in multiple space dimensions based on finite volume methods [31] or pressure-correction schemes [21]
- predict dynamic form factors [32] in accordance with experiments of light scattering spectra measuring small scale density fluctuations

We proceed with presenting the details of microchannel flows.

5 Microchannel Flows

To approach microchannel flows, we study a special class of steady shear flows that include steady Couette or Poiseuille flows. For the R13 system, shear flow is a multidimensional phenomenon in the sense that it produces a fully multidimensional reaction for the stress tensor and heat flux. Introducing $x_i \hat{=} (x,y,z)$, we consider shear flow, which is homogeneous in the z-direction, and define the remaining nonvanishing parts of stress tensor and heat flux as

$$\sigma = \begin{pmatrix} \sigma_{xx} & \sigma_{xy} & 0 \\ \sigma_{yx} & \sigma_{yy} & 0 \\ 0 & 0 & \sigma_{zz} \end{pmatrix}, \quad \mathbf{q} = (q_x, q_y, 0) \tag{15}$$

where $\sigma_{xy} = \sigma_{yx}$ and $\sigma_{zz} = -(\sigma_{xx} + \sigma_{yy})$ since σ must be trace free. For the velocity we assume $v_y = v_z = 0$ and

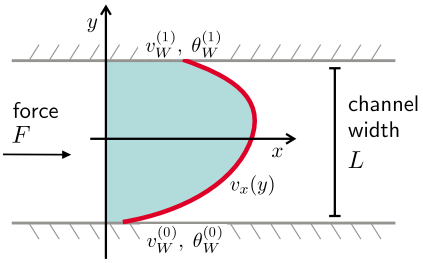

Fig. 1 General setting for shear flow between two infinite plates. The plates are moving and may be heated.

$$\mathbf{v}(x,y,z) = (v_x(y), 0, 0) \tag{16}$$

The force acts only in the x-direction, $\mathbf{f} = (F,0,0)$ and enters the momentum balance (2) but no other equation. This setting is valid for channel flows, as displayed in Fig. 1. The gas is confined between two infinite plates at distance L and moves solely in the x-direction. The walls are moving with x-velocities $v_W^{(0,1)}$ and may be heated with different temperatures $\theta_W^{(0,1)}$. The Knudsen number $\mathrm{Kn} = \lambda / L$ with mean free path $\lambda = \mu / (\rho \sqrt{\theta})$ is based on the width of the channel.

In this setting we have eight independent variables in the R13 equations, namely, $\{\rho, v_x, p, \sigma_{xx}, \sigma_{yy}, \sigma_{xy}, q_x, q_y\}$. Optionally, the pressure p can be replaced by the temperature θ. The five remaining relevant constitutive quantities are $\{m_{xxy}, m_{xyy}, m_{yyy}, \hat{R}_{xy}, \hat{R}_{yy}\}$. Systems (1)–(9) reduces to 13 first order nonlinear ordinary differential equations in the space variable y. The equations uncover a striking simplicity by decomposing into three linearly decoupled blocks. The coupling is displayed by writing the vector of variables in the form

$$\mathbf{U} = \{v_x, \sigma_{xy}, q_x, m_{xyy}, R_{xy} | \theta, q_y, \sigma_{yy}, \hat{R}_{yy}, m_{yyy} | \rho, \sigma_{xx}, m_{xxy}\} \tag{17}$$

The first block describes the velocity part with the balances of v_x, σ_{xy}, and q_x and higher moments m_{xyy} and $\hat{R}_{xy}$; the second block describes the temperature part with the balances of θ, q_y, and σ_{yy} and higher moments $\hat{R}_{yy}$ and m_{yyy}. Both parts are governed dominantly by two classical variables, (v_x, σ_{xy}) and (θ, q_y), respectively, which behave essentially in an intuitive way. In NSF the second variable is related to the gradient of the first. The third variable in both parts, q_x and σ_{yy}, respectively, is given by a seemingly classical variable, which, however, plays a nonintuitive role. It represents a *heat flux produced by a velocity shear* in the first block and a *normal stress due to temperature difference* in the second. Both are typical rarefaction effects in microflows of gases. Through these variables the classical variables velocity and temperature are coupled to the high order internal quantities, m_{xyy} and $\hat{R}_{xy}$, and $\hat{R}_{yy}$ and m_{yyy}, respectively. From tensorial considerations, the first block can be identified with mixed normal/tangential variables (shear), while the second block couples the purely normal variables (temperature). The last block combines the density and purely tangential tensorial variables and exhibits only a minor influence.

5.1 Linear Equations and Knudsen Layers. One of the most important advantages of continuum models is the possibility to gain understanding in micro gas dynamics through analytical expressions. The mathematical structure of the equations provides a general insight into new physics and may teach intuition about complex processes.

Here, we demonstrate the rise of Knudsen layers and microscale variables, i.e., nongradient heat fluxes and normal stresses. Similar calculations can be found in Refs. [29,30].

5.1.1 Velocity Part. As mentioned above, the equations split into a velocity and a temperature part in the linear case. The

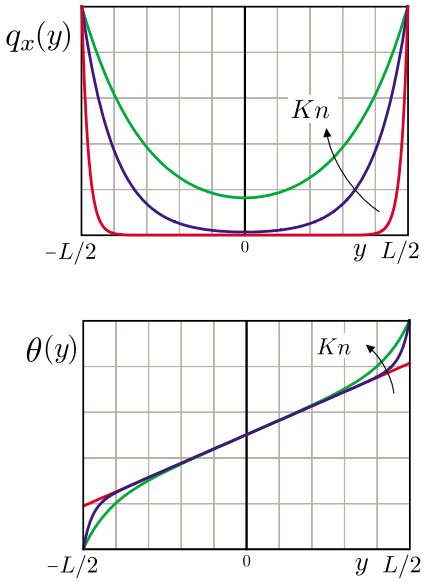

Fig. 2 R13 predicts exponential Knudsen layers for, e.g., parallel heat flux. The upper plot shows a schematic picture for *F*=0, Kn=0.01, 0.1, and 0.5. These functions lead to typical s-shaped profiles for, e.g., temperature; see the schematic lower plot with Kn=0.01, 0.1, and 0.2.

velocity part is governed by the momentum balance and an equation for shear stress, which are given by Eq. (2) with force term and the xy-component of Eq. (4) and read

$$\partial_y \sigma_{xy} = \rho F \tag{18}$$

$$\sigma_{xy} = -\mu \partial_y v_x - \frac{2}{5}\frac{\mu}{p}\partial_y q_x \tag{19}$$

with constant density, pressure, and viscosity μ. Obviously, shear stress is given by the velocity gradient and by a microscale contribution from the heat flux q_x parallel to the walls. This heat flux satisfies Eq. (5),

$$\frac{\mu}{\rho}\partial_y \sigma_{xy} + \frac{1}{2}\frac{\mu}{p}\partial_y R_{xy} = -\frac{2}{3}q_x \tag{20}$$

$$R_{xy} = -\frac{12}{5}\frac{\mu}{p}\partial_y q_x \tag{21}$$

with higher order flux R_{xy} given by Eq. (7). In particular, the parallel heat flux is independent of a temperature gradient. It is triggered from the shear stress and boundary conditions. Elimination of R_{xy} leads to a second order ordinary differential equation for q_x with solution (assuming symmetry),

$$q_x(y) = -\frac{3}{2}\mu F + C_1 \sinh\left(\frac{\sqrt{5}}{3}\frac{1}{\mathrm{Kn}}\frac{y}{L/2}\right) \tag{22}$$

using the Knudsen number[1]

$$\mathrm{Kn} = \frac{\mu\sqrt{\theta}}{pL} \tag{23}$$

The hyperbolic sine function has the shape of a boundary layer, as can be seen in Fig. 2. This boundary layer is superimposed on a bulk solution $\sim \mu F$ in q_x. Finally, the parallel heat flux enters the velocity solution (assuming symmetry)

$$v_x(y) = C_2 + \frac{\rho F}{2\mu}\left(\left(\frac{L}{2}\right)^2 - y^2\right) - \frac{2}{5p}q_x(y) \tag{24}$$

inheriting the Knudsen layer. Hence, the velocity consists of a bulk solution given by the classical parabolic profile and a layer contribution from the parallel heat flux.

Note that the boundary layers grow quickly with the Knudsen number and fill out the channel already at Kn=0.5 (see Fig. 2). At these Knudsen numbers, the bulk and layer in Eq. (24) cannot be distinguished anymore, and the solution will show a quality in its own right with no resemblance to classical solutions.

5.1.2 Temperature Part. Remarkably, the temperature part of the linear R13 equations shows identical mathematical structures. The two basic equations are now given by the energy balance (Eq. (3)) and the equation for normal heat flux q_y (Eq. (5)), which together read

$$\partial_y q_y = 0 \tag{25}$$

$$q_y = -\kappa \partial_y \theta - \frac{2}{5}\frac{\kappa}{\rho}\partial_y \sigma_{yy} \tag{26}$$

with constant density, pressure, and heat conductivity $\kappa = \frac{15}{4}\mu$ (temperature in energy units). Again, the first term on the right hand side describes Fourier's law, but the second shows the influence of normal stress σ_{yy} as a microscale variable. This normal stress is determined by Eq. (4),

$$\frac{\kappa}{p}\partial_y q_y + \frac{2}{9}\frac{\kappa}{p}\partial_y m_{yyy} = -\frac{5}{6}\sigma_{yy} \tag{27}$$

$$m_{yyy} = -\frac{8}{25}\frac{\kappa}{p}\partial_y \sigma_{yy} \tag{28}$$

with higher order flux m_{yyy} given by relation (7). Note the perfect analogy to the equations of the velocity part above. Consequently, the normal stress is given by a hyperbolic sine function (assuming antisymmetry),

$$\sigma_{yy}(y) = C_3 \sinh\left(\sqrt{\frac{5}{6}}\frac{1}{\mathrm{Kn}}\frac{y}{L/2}\right) \tag{29}$$

exhibiting boundary layer character again with the Knudsen number as the scaling parameter. This boundary layer enters the profile of the temperature,

$$\theta(y) = C_4 + \frac{C_5}{\kappa}\frac{y}{L/2} - \frac{2}{5p}\sigma_{yy}(y) \tag{30}$$

and leads to a typical s-shape, as seen in Fig. 2. The bulk solution of σ_{yy} is zero, while the bulk solution of the temperature is the classical linear function.

The integration constants C_i have to be fixed by boundary conditions, as given in Eq. (10). Similar to the equations, the boundary conditions also decouple into a velocity and a temperature part when linearized.

5.2 Mass Flux Knudsen Paradox. Gas flow through a channel is known to exhibit a paradoxical behavior known as the Knudsen paradox [33]. When reducing the Knudsen number in the experiment, the normalized mass flow rate

$$J = \int_{-1/2}^{1/2} v(y)dy \tag{31}$$

through the channel reaches a minimum and afterward starts to increase for larger Knudsen numbers.

To model this, we consider Poiseuille flow given by acceleration-driven channel flow with walls at rest and identical

[1]This definition is most suitable for dimensionless moment equations. Other definitions differ only by factors, e.g., $\widetilde{\mathrm{Kn}}$ in Ref. [3] or [6], which is $\widetilde{\mathrm{Kn}} = (4/5)\sqrt{(8/\pi)}(\mu\sqrt{\theta}/p) \approx 1.277\ \mathrm{Kn}$, or k used in Ref. [21], which is $k = (4/5)\sqrt{2}(\mu\sqrt{\theta}/p) \approx 1.13\ \mathrm{Kn}$.

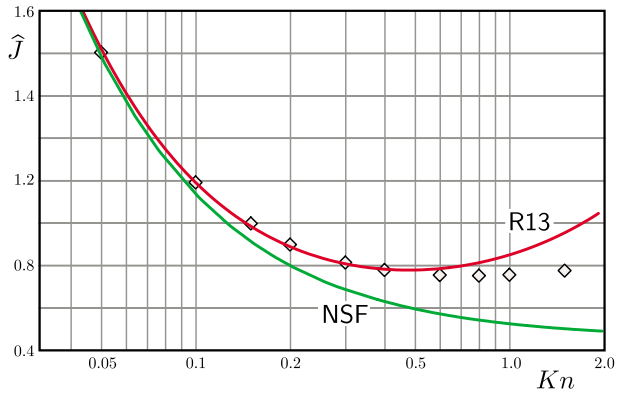

Fig. 3 Averaged mass flow rate in acceleration-driven channel flow. The R13 equations predict the Knudsen paradox.

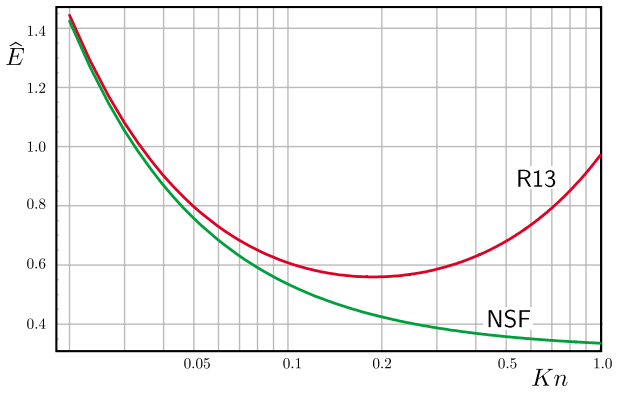

Fig. 4 R13 predicts an energy Knudsen paradox: The normalized total energy content of an externally heated channel shows a nonintuitive minimum when plotted against the Knudsen number. Standard NSF does not show this minimum.

temperatures. The channel is considered to be infinitely long such that a steady velocity profile has developed from the viscous boundary layers. The given acceleration can be interpreted as a homogeneous pressure gradient.

Given the analytical result for the channel flow of the linear R13 system above, it is easy to determine an explicit function for the mass flow rate. After integration we find

$$J = \frac{\gamma_1}{\mathrm{Kn}} + \gamma_2 \mathrm{Kn} + \gamma_3$$

where $\gamma_{1,2,3}$ depend on the coefficients in the equations and boundary conditions, essentially, viscosity and accommodation factor. The functional dependence on the Knudsen number is valuable information. In general, the coefficients could also be calibrated to measurements.

Figure 3 shows the dimensionless mass flow rate obtained from R13 as a function of Kn. The curve clearly shows a minimum and thus correctly predicts a Knudsen paradox. The figure also shows the mass flow rate obtained with NSF and standard slip boundary conditions, which clearly fails to produce a Knudsen minimum. In Ref. [34] the mass flow rate has been calculated based on the linearized Boltzmann equation, and those results are given in Fig. 3 as symbols. The mass flow for R13 follows the Boltzmann result fairly accurately until $\mathrm{Kn} \lesssim 1.0$ and then lifts off too quickly. At these high Knudsen numbers, the assumptions of the theory are not valid anymore.

The Knudsen paradox is essentially a boundary effect, as explained below. Hence, it is possible to tweak the NSF system to exhibit a Knudsen minimum as well when using second order slip (see, e.g., Ref. [35]). However, when comparing different models for second order slip with the R13 result, it turns out that the R13 curve gives a better fit to the Boltzmann result (see Ref. [36]). Additionally, the fields of flow variables temperature and heat flux in microchannel flows show a very interesting behavior correctly reproduced only by extended models beyond NSF (see Sec. 5.4).

Intuitively one would expect a decreasing mass flow for a smaller channel. The explanation for the minimum is the following: For very small Knudsen numbers, viscosity is almost vanishing, and a fully developed flow would exhibit a huge velocity profile, hence a very large mass flow rate. When viscosity is increased, this profile shrinks; however in the other extreme of large Knudsen numbers a different effect takes over. The interaction between the particles and the wall becomes so small due to lack of collisions that the particles merely accelerate and fall through the channel. Again, a fully developed flow of "accelerated freely falling" particles leads to an infinite mass flux. Between these two extrema, there must be a minimum. In summary, at a certain microscale the friction inside the gas becomes small and the growing slip velocity at the wall dominates the mass flow rate.

5.3 Energy Knudsen Paradox. We have seen above that the channel flow separates the R13 equations into two different systems of equations: one part for the velocity and shear and another part for the temperature and normal heat flux. The two parts exhibit mathematical identical structures in the linearized setting and allow us to transfer the specific behavior of shear flows to the analogous behavior of heat transfer.

This leads us to the prediction of an energy Knudsen paradox for heat transfer in the following sense. Let a resting monatomic gas between the two plates in Fig. 1 be heated by a constant volume source, e.g., radiation r. That is, the steady energy balance has the form $\partial_y q = r$. The total energy content between the plates is essentially the integral of the temperature θ

$$E = \frac{3}{2}\int_{-1/2}^{1/2} \theta(y)\,dy \tag{32}$$

when written in dimensionless form. When normalized with the energy input r, the energy content depends on the Knudsen number and the R13 theory predicts a paradoxical behavior when changing the width of the channel. When increasing the Knudsen number and decreasing the channel width, the energy content decreases, but only up to a certain Knudsen number. For a very small width, the total energy increases with Kn, which is nonintuitive.

Figure 4 shows the respective plot that compares the normalized total energy content $\hat{E}$, as predicted by R13 and NSF with first order jump conditions. As before, the standard NSF model without second order jump conditions does not show a minimum. R13 predicts an energy minimum, which is at smaller Knudsen numbers than the Knudsen minimum for the mass flux in Fig. 3.

To our knowledge there are no experimental or DSMC data to verify this prediction. However, it is very likely that such data would unveil an approximation quality of R13 similar to that of Fig. 3.

5.4 Full Solution for Poiseuille Flow. In the linear setting, the dissipation term in the energy balance is neglected and any velocity profile does not lead to a temperature rise. To see the temperature profile, the nonlinear equations have to be solved. Apart from arithmetic complexity, this is not a problem with the R13 model.

We solve the full nonlinear R13 system in forms (1)–(9) for a Poiseuille flow, as described above with kinetic boundary condition (10)–(14) for various Knudsen numbers. The mass flow rate is only a rough property of microflows, and the R13 result gives much more insight when considering the fields of the moments. Figures 5 and 6 display some fields obtained by R13 for Knudsen numbers $\mathrm{Kn} = 0.068$, 0.15, 0.4, and 1.0. The figures show the con-

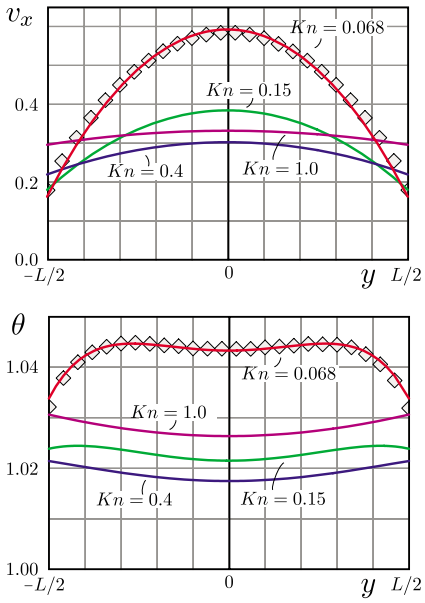

Fig. 5 Velocity and temperature profiles in acceleration-driven channel flow for various Knudsen numbers. The symbols in the case Kn=0.068 represent a DSMC result.

servation variables velocity v_x and temperature θ, as well as the microscale variables tangential heat flux q_x and normal stress σ_{yy}. Note that the channel flow produces a significant parallel heat flux q_x even though the temperature is homogeneous along x. Similarly, the temperature field triggers a normal stress even though $\partial_y v_y = 0$. This is a microscale effect. Higher Knudsen numbers show stronger nonequilibrium, as indicated by larger magnitudes of q_x and σ_{yy}. Interestingly, the temperature profile starts to invert for higher Knudsen numbers. Note also that the Knudsen paradox can be observed in the results of the R13 system in Fig. 5. The velocity profile becomes flatter, but the slip increases and the velocity curve for Kn=1.0 lies above the curve of Kn=0.4.

The simulations were obtained with a dimensionless acceleration force fixed at $F=0.23$, such that Knudsen number Kn =0.068 corresponds to the case of Poiseuille flow calculated in Ref. [37] (see also Ref. [38]) by DSMC. These results are shown in Figs. 5 and 6 as symbols. R13 gives good agreement with the DSMC result.

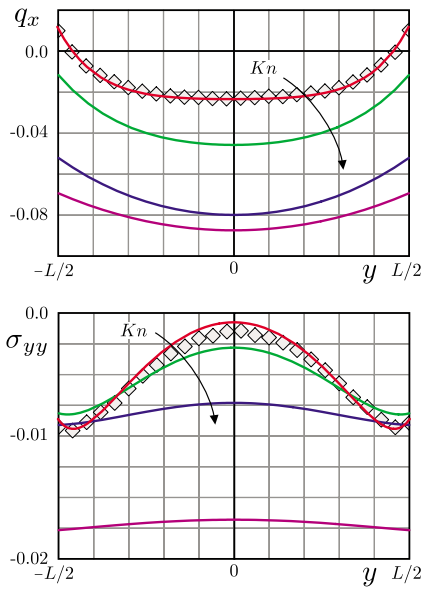

Fig. 6 Microscale effects, such as parallel heat flux q_x and normal stresses σ_{yy}, in microchannels as predicted by R13 for various Knudsen numbers. The symbols in the case Kn =0.068 represent a DSMC result.

Comparison with NSF. While the Knudsen minimum can be reproduced with the lower order system of Navier–Stokes and Fourier using higher order boundary conditions, many details of the channel flow shown above are out of scope for NSF. The temperature profile in NSF is a purely convex function with no dip and no tendency to invert for higher Knudsen numbers. NSF is also unable to predict the micro effects of parallel heat flux q_x and normal stresses σ_{yy}. Both quantities are identically zero in NSF for all Knudsen numbers because there is no temperature gradient in the x-direction and no velocity divergence.

Comparison with Ohwada et al. Ohwada et al. [34] computed Poiseuille flow results based on the linearized Boltzmann equation. They gave field curves for velocity and parallel heat flux for Kn=0.088, which are in good agreement with the R13 results and corresponding DSMC above. Especially, the parallel heat flux shows positive and negative values at this lower Knudsen number identical to the curve in 6. Unfortunately, no other fields, for example, temperature, are given in Ref. [34].

6 Conclusions and Challenges

With these properties and features, the R13 equations must be considered as the most successful continuum model for gas microflows. In contrast to direct simulations or molecular dynamics, such a model gives valuable insight into physical effects by identifying effects inside equations. The application of the R13 equations to a wider variety of microflow problems is planned for the future.

In spite of the success, the R13 equations face plenty of open challenges. From the modeling point of view, extensions to mixtures and polyatomic gases are necessary. Some ideas for such moment systems exist in the literature where internal energy variables and multiple species distribution functions are added to the kinetic description. The regularized moment approach can be applied to these settings. The current R13 equations still exhibit loss of hyperbolicity of the flux part, which leads to problems when calculating high speed flows (see Ref. [31]). The development of a globally hyperbolic flux for higher order moments is a long standing open problem. Multidimensional simulations require suitable numerical methods. Existing approaches such as those in Ref. [31] or [21] need to be refined. For slow flows as in microchannels, the hybrid numerical methods that combine classical incompressible simulation tools with compressible features caused by rarefaction effects are needed.

Interesting problems to simulate with R13 are thermal creep phenomena, for instance, in Knudsen pumps. Also, microcavity flows such as those in Refs. [39,40] are important applications.

Acknowledgment

H.S. acknowledges support by the Natural Sciences and Engineering Research Council of Canada (NSERC). M.T. acknowledges support through the EURYI award of the European Science Foundation (ESF).

References

[1] Cercignani, C., 1988, *The Boltzmann Equation and Its Applications*, Applied Mathematical Sciences Vol. 67, Springer, New York.
[2] Struchtrup, H., 2005, *Macroscopic Transport Equations for Rarefied Gas Flows*, Interaction of Mechanics and Mathematics, Springer, New York.
[3] Bobylev, A. V., 1982, "The Chapman-Enskog and Grad Methods for Solving the Boltzmann Equation," Sov. Phys. Dokl., **27**, pp. 29–31.
[4] Bobylev, A. V., 2006, "Instabilities in the Chapman-Enskog Expansion and Hyperbolic Burnett Equations," J. Stat. Phys., **124**(2–4), pp. 371–399.
[5] Jin, S., and Slemrod, M., 2001, "Regularization of the Burnett Equations Via Relaxation," J. Stat. Phys., **103**(5–6), pp. 1009–1033.
[6] Agarwal, R. K., Yun, K.-Y., and Balakrishnan, R., 2001, "Beyond Navier–

Stokes: Burnett Equations for Flows in the Continuum-Transition Regime," Phys. Fluids, **13**, pp. 3061–3085.
[7] Agarwal, R. K., Yun, K.-Y., and Balakrishnan, R., 2002, "Erratum: "Beyond Navier–Stokes: Burnett Equations for Flows in the Continuum-Transition Regime" [Phys. Fluids 13, 3061 (2001)]," Phys. Fluids, **14**, p. 1818.
[8] Lockerby, D. A., and Reese, J. M., 2003, "High-Resolution Burnett Simulations of Micro Couette Flow and Heat Transfer," J. Comput. Phys., **188**(2), pp. 333–347.
[9] Grad, H., 1949, "On the Kinetic Theory of Rarefied Gases," Commun. Pure Appl. Math., **2**, pp. 331–407.
[10] Weiss, W., 1995, "Continuous Shock Structure in Extended Thermodynamics," Phys. Rev. E, **52**, pp. R5760–R5763.
[11] Müller, I., and Ruggeri, T., 1998, *Rational Extended Thermodynamics*, Springer Tracts in Natural Philosophy Vol. 37, 2nd ed., Springer, New York.
[12] Au, J. D., Torrilhon, M., and Weiss, W., 2001, "The Shock Tube Study in Extended Thermodynamics," Phys. Fluids, **13**(8), pp. 2423–2432.
[13] Levermore, C. D., 1996, "Moment Closure Hierarchies for Kinetic Theories," J. Stat. Phys., **83**(5–6), pp. 1021–1065.
[14] Eu, B.-C., 1980, "A Modified Moment Method and Irreversible Thermodynamics," J. Chem. Phys., **73**(6), pp. 2958–2969.
[15] Myong, R.-S., 2001, "A Computational Method for Eu's Generalized Hydrodynamic Equations of Rarefied and Microscale Gas Dynamics," J. Comput. Phys., **168**(1), pp. 47–72.
[16] Struchtrup, H., and Torrilhon, M., 2003, "Regularization of Grad's 13-Moment-Equations: Derivation and Linear Analysis," Phys. Fluids, **15**(9), pp. 2668–2680.
[17] Torrilhon, M., and Struchtrup, H., 2004, "Regularized 13-Moment-Equations: Shock Structure Calculations and Comparison to Burnett Models," J. Fluid Mech., **513**, pp. 171–198.
[18] Struchtrup, H., 2004, "Stable Transport Equations for Rarefied Gases at High Orders in the Knudsen Number," Phys. Fluids, **16**(11), pp. 3921–3934.
[19] Struchtrup, H., 2005, "Derivation of 13 Moment Equations for Rarefied Gas Flow to Second Order Accuracy for Arbitrary Interaction Potentials," Multiscale Model. Simul., **3**(1), pp. 221–243.
[20] Müller, I., Reitebuch, D., and Weiss, W., 2003, "Extended Thermodynamics—Consistent in Order of Magnitude," Continuum Mech. Thermodyn., **15**(2), pp. 113–146.
[21] Gu, X., and Emerson, D., 2007, "A Computational Strategy for the Regularized 13 Moment Equations With Enhanced Wall-Boundary Conditions," J. Comput. Phys., **225**, pp. 263–283.
[22] Torrilhon, M., and Struchtrup, H., 2008, "Boundary Conditions for Regularized 13-Moment-Equations for Micro-Channels," J. Comput. Phys., **227**, pp. 1982–2011.
[23] Karlin, I. V., Gorban, A. N., Dukek, G., and Nonnenmacher, T. F., 1998, "Dynamic Correction to Moment Approximations," Phys. Rev. E, **57**(2), pp. 1668–1672.
[24] Struchtrup, H., 2006, "Scaling and Expansion of Moment Equations in Kinetic Theory," J. Stat. Phys., **125**, pp. 565–587.
[25] Maxwell, J. C., 1879, "On Stresses in Rarefied Gases Arising From Inequalities of Temperature," Philos. Trans. R. Soc. London, **170**, pp. 231–256.
[26] Struchtrup, H., 2003, "Grad's Moment Equations for Microscale Flows," AIP Conf. Proc., **663**, pp. 792–799.
[27] Bird, G. A., 1998, *Molecular Gas Dynamics and the Direct Simulation of Gas Flows*, 2nd ed., Oxford University Press, New York.
[28] Struchtrup, H., and Torrilhon, M., 2007, "H-Theorem, Regularization, and Boundary Conditions for Linearized 13 Moment Equations," Phys. Rev. Lett., **99**, p. 014502.
[29] Struchtrup, H., 2005, "Failures of the Burnett and Super-Burnett Equations in Steady State Processes," Continuum Mech. Thermodyn., **17**(1), pp. 43–50.
[30] Struchtrup, H., and Thatcher, T., 2007, "Bulk Equations and Knudsen Layers for the Regularized 13 Moment Equations," Continuum Mech. Thermodyn., **19**(3–4), pp. 177–189.
[31] Torrilhon, M., 2006, "Two-Dimensional Bulk Microflow Simulations Based on Regularized 13-Moment-Equations," Multiscale Model. Simul., **5**(3), pp. 695–728.
[32] Torrilhon, M., 2006, "Regularized 13-Moment-Equations," 25th International Symposium on Rarefied Gas Dynamics, St. Petersburg, Russia.
[33] Knudsen, M., 1909, "Die Gesetze der Molekularströmung und der inneren Reibungsströmung der Gase durch Röhren," Ann. Phys. (Leipzig), **333**, pp. 75–130.
[34] Ohwada, T., Sone, Y., and Aoki, K., 1989, "Numerical Analysis of the Poiseuille and Thermal Transpiration Flows Between Two Parallel Plates on the Basis of the Boltzmann Equation for Hard-Sphere Molecules," Phys. Fluids A, **1**(12), pp. 2042–2049.
[35] Hadjiconstantinou, N. G., 2003, "Comment on Cercignani's Second-Order Slip Coefficient," Phys. Fluids, **15**, pp. 2352–2354.
[36] Struchtrup, H., and Torrilhon, M., 2008, "Higher-Order Effects in Rarefied Channel Flows," Phys. Rev. E, **78**, p. 046301.
[37] Zheng, Y., Garcia, A. L., and Alder, J. B., 2002, "Comparison of Kinetic Theory and Hydrodynamics for Poiseuille Flow," J. Stat. Phys., **109**, pp. 495–505.
[38] Xu, K., and Li, Z.-H., 2004, "Microchannel Flow in the Slip Regime: Gas-Kinetic BGK-Burnett Solutions," J. Fluid Mech., **513**, pp. 87–110.
[39] Mizzi, S., Gu, X.-J., Emerson, D. R., Barber, R. W., and Reese, J., 2008, "Application of a High-Order Macroscopic Approach to Force-Driven Poiseuille Flow in the Slip and Transition Regimes," First International Conference on Micro- and Nano-Heat Transfer, Tainan, Taiwan, Paper No. MNHT2008-52203.
[40] Taheri, P., Torrilhon, M., and Struchtrup, H., 2008, "Couette and Poiseuille Flows in Micro-Channels: Analytical Solutions for Regularized 13-Moment Equations," in press.

S. V. Nedea[1]
Department of Mechanical Engineering,
Energy Technology,
Eindhoven University of Technology,
P. O. Box 513,
5600 MB, Eindhoven, The Netherlands
e-mail: s.v.nedea@tue.nl

A. J. Markvoort
Department of Biomedical Engineering,
BioModeling and BioInformatics,
Eindhoven University of Technology,
P. O. Box 513,
5600 MB, Eindhoven, The Netherlands

A. A. van Steenhoven
Department of Mechanical Engineering,
Energy Technology,
Eindhoven University of Technology,
P. O. Box 513,
5600 MB, Eindhoven, The Netherlands

P. A. J. Hilbers
Department of Biomedical Engineering,
BioModeling and BioInformatics,
Eindhoven University of Technology,
P. O. Box 513,
5600 MB, Eindhoven, The Netherlands

Heat Transfer Predictions for Micro-/Nanochannels at the Atomistic Level Using Combined Molecular Dynamics and Monte Carlo Techniques

The thermal behavior of a gas confined between two parallel walls is investigated. Wall effects such as hydrophobic or hydrophilic wall interactions are studied, and the effect on the heat flux and other characteristic parameters such as density and temperature is shown. For a dilute gas, the dependence on gas-wall interactions of the temperature profile between the walls for the incident and reflected molecules is obtained using molecular dynamics (MD). From these profiles, the effective accommodation coefficients for different interactions and different mass fluid/wall ratio are derived. We show that Monte Carlo (MC) with Maxwell boundary conditions based on the accommodation coefficient gives good results for heat flux predictions when compared with pure molecular dynamics simulations. We use these effective coefficients to compute the heat flux predictions for a dense gas using MD and MC with Maxwell-like boundary conditions. [DOI: 10.1115/1.3056592]

Keywords: molecular dynamics, Monte Carlo simulations, heat transfer, gas-wall interactions

1 Introduction

Heat transfer at the atomistic level is one of the most important issues within many application fields. One important application is in microchannel cooling. As a lot of electronic components produce heat when operating, cooling these devices is essential for the long lifetime of these components. These devices can be cooled locally where the power is produced using a gas or fluid flow through the microchannels. As these electronic components become smaller and smaller [1] and produce relatively more power, new models for temperature and heat flux predictions are necessary.

Conventional approaches used to study heat flow range from continuum to molecular techniques. Continuum represented by the Navier–Stokes equations breaks down when the size of these devices decreases or when the flow becomes more dilute [2,3]. The governing equation of the heat flow changes from Navier–Stokes to Boltzmann equation. This equation involves molecular velocities instead of macroscopic properties. To solve this equation is very difficult since the number of independent variables contains both those of velocity and of physical space. The alternative is to use particle simulation methods to study heat transfer in micro-/nanochannels, such as direct simulation Monte Carlo (DSMC) [2] or molecular dynamics (MD) [4].

Many studies have been made for analysis of rarefied gas flows using DSMC [5–8] and different boundary conditions were used to represent the gas-solid interface [9–12]. These boundary conditions are crucial for heat predictions as the transport properties of gases at the gas-solid interface can play a very important role in the overall behavior of the channel. A lot of effort has been concentrated on studying the gas-surface interface. In most cases of these analyses, a simplified boundary condition for reflected molecules at a solid surface has been used. This boundary condition called diffuse reflection assumes that the reflected molecules are completely accommodated with the wall surface and their velocity distribution is given by the Maxwellian distribution with the wall quantities. However, when the molecules have high energy, the diffuse reflection is not applicable, and the scattered flux shows preferred directions (e.g., specular ray direction) [13,14].

Other Maxwell-type boundary conditions are based on the assumption that a fraction $(1-\alpha)$ of molecules is reflected specular from the surface, while α is re-emitted diffusely with Maxwell distribution at wall conditions. α is called the accommodation coefficient and is taken to be that of the tangential momentum or of the energy of the molecules according to the flow situation [15]. A more elaborated model was proposed by Cercignani and Lampis [11] and developed by Lord [10], and includes two parameters: one coefficient of the tangential momentum accommodation parallel to the surface and one of energy accommodation normal to the surface.

An alternative is to use MD, allowing for the simulation of both wall, gas, and wall-gas interactions explicitly. The interaction of monoatomic gas molecules with solid molecules by MD method was studied by Wachman [9] and Matsui and Matsumoto [16]. They all computed the behavior of reflection or adsorption of the incident gas molecules, while Yamanishi and Matsumoto [17] constructed a gas-surface interaction model by developing a multistage collision between molecules based on the analysis of MD. Various other MD studies have been reported for specific gas-solid and fluid-solid interfaces [18,19].

In our previous work [20], we used a MD approach to study the wettability effect on heat and particle flow in nanochannels. The results on the heat flux predictions of the particles sticking to the

[1]Corresponding author.

Contributed by the Heat Transfer Division of ASME for publication in the JOURNAL OF HEAT TRANSFER. Manuscript received September 25, 2007; final manuscript received September 15, 2008; published online January 21, 2009. Review conducted by Satish G. Kandlikar. Paper presented at the Fifth International Conference on Nanochannels, Microchannels and Minichannels (ICNMM2007), Puebla, Mexico, June 18–20, 2007.

wall (attractive wall interactions) were given, showing that the relevant parameter is the gas-wall interaction strength, whereas gas-gas is of much less importance on the resulting heat flux. Particles were selected according to their velocities in the fluxes of particle going to the left ($V_x<0$, from the cold to the warm wall) and to the right ($V_x>0$, from the warm to the cold wall). In the gas-surface interface, these molecular fluxes correspond to the incident and reflected molecular fluxes.

To study the impact on the heat fluxes of gas-surface interactions in realistic channels (microchannels) is computationally very expensive. The idea is to combine MD and MC to cover larger time and length scales. Hybrid methods are such techniques used to study gas-surface interface using molecular dynamics and flow region with MC. These techniques are very accurate, but to simulate the MD region taking into account explicitly the walls and the fluid in the surface region is still computationally very demanding. Previously we have introduced a hybrid simulation approach combining MD and MC simulations to study dense and dilute gases in nanochannels [21]. Yamamoto et al. [15] used another hybrid approach combining MD and DSMC for the motion of molecules between two walls and investigating the characteristics of the reflected Ni gas molecules at a Pt surface [15,22]. Based on their results on the observed trajectories of gas molecules, the gas molecules bounce on the surface (once, twice, or many times), and eventually return. In some cases, the molecules are adsorbed on the surface, and leave after a while. From the trajectories they could not deduce that the Maxwell-type distribution function consisting of the specular and diffuse reflections well describes the distribution function of the reflected molecules, but the global velocity is well described by this distribution if the accommodation coefficient involved is chosen properly. Based on this result, we investigate the gas-surface interface for a gas confined between two parallel walls [20], and we compute the accommodation coefficient for a dilute gas from a MD simulation with explicit and different wall interactions (attractive and repulsive). Also the influence of the ratio between the mass of the wall molecules and fluid molecules on the accommodation coefficient α and on the heat flux q_x is shown. We then introduce these coefficients into a MC simulation based on Maxwell-type boundary conditions. The temperature and density distributions of incident and reflected molecules are shown and the effect on the heat flux is discussed.

Considering that each individual molecule is accommodated by the wall during the collision with a factor depending only on the interaction strength $\varepsilon_{G\text{-}S}$ between the gas molecule and wall molecule, we extend these gas-wall characteristics to study the heat flux predictions for denser gases in the channel. Thus, we transfer the accommodation coefficients computed for dilute gas to study heat flux in the microchannel for a dense gas and we accurately compute the enhanced collisions with the wall and in the wall vicinity. These accommodation coefficients are computed from the temperature profiles of the dilute gas next to the wall boundary and used in a Maxwell-type boundary condition for a MC simulation based on Enskog equation [5,23]. We compare the heat fluxes computed using the two approaches, MD and MC with Maxwell-type boundary conditions based on α. In the end, effective values of α established confronting the MD q_x results with a map of MC q_x results for different accommodation coefficients are investigated and compared with previously computed accommodation coefficients. The differences in the heat flux predictions are shown and explained.

2 The Physical Model

Our model to study the one-dimensional heat flow in a microchannel consists of two parallel plates of length L_y at a distance L_x apart from each other and of gas molecules confined between these two walls. Both plates have their own temperature, T_1 and T_2, respectively, where this temperature is uniform on the plate surface and constant in time, and $T_2/T_1=1/2$. The gas consists of spherical particles of diameter a and mass m, at temperature T. The density of the gas can be expressed as n, being the number of particles per unit of volume, or using a reduced density η, which also takes the particle sizes into account and is related to the number density as $\eta=\pi na^3/6$ [23]. The mean free path of the gas particles is related to this reduced density. For a relatively dense gas with $\eta=0.1$, the mean free path $\lambda=1/\sqrt{2}\pi a^3 nY(\eta)$ and the molecular diameter a have the same order of magnitude. The $Y(\eta)$ factor is the pair correlation function at contact [5,23]. The distance L_x between the plates, in the x-direction, is always such that both plates are only a few mean free paths apart. The walls can be modeled explicitly (based on a MD model) or using boundary conditions (Maxwell or Maxwell-like boundary conditions in a MC model). Two situations were considered: (a) a dilute gas confined between the walls with the reduced density $\eta=0.005$ and $L_x=1.39\lambda=32.0a$, and (b) a dense gas with $\eta=0.2$ and $L_x=95\lambda=46.9a$.

In MD, the Lennard-Jones (LJ) potential is used to model the interactions between the gas-gas, gas-wall, and wall-wall molecules [20]. As it is a generic system we are interested in and not in one specific system, the Lennard-Jones potential serves our purpose of studying the dependency of the accommodation coefficient on the gas-wall interactions. This Lennard-Jones potentials are especially appropriate for noble gases but it captures also the essence of all systems and can thus in principle be used for metals [24,25]. Of course, more realistic potential for metals are available taking into account many-atom interactions but because LJ capture the essence of all systems and we are not directly interested in one particular metal, this potential suffices for investigating the problem we are interested in of modeling hydrophilic and hydrophobic wall interactions and study the thermal behavior in the micro-/nanochannel.

The Lennard-Jones potential is given by the relation

$$V_{\mathrm{LJ}}=\varepsilon\left[\left(\frac{2R_{\mathrm{vdW}}}{r}\right)^{12}-2\left(\frac{2R_{\mathrm{vdW}}}{r}\right)^{6}\right] \tag{1}$$

where ε is the interaction strength and R_{vdW} is the van der Waals radius, a measure of the particle size. In order to simulate hard-sphere-like interactions using MD, truncated shifted Lennard-Jones (tsLJ) potentials were used for the interactions between gas molecules. This potential is defined as

$$V_{\mathrm{tsLJ}}=\begin{cases}V_{\mathrm{LJ}}(r)-V_{\mathrm{LJ}}(r_c) & \text{if } r\le r_c\\ 0 & \text{if } r>r_c\end{cases} \tag{2}$$

where r_c is the cut-off radius. This tsLJ is used to keep only the repulsive contribution as a model for hard-sphere molecules. The walls are kept together by a relatively strong interaction strength $\varepsilon=6.0$ in the LJ potential. The gas-wall interactions can be hydrophilic (attractive) or hydrophobic (repulsive) wall interactions. Attractive wall interactions are modeled by LJ with ε between 0.10 and 0.5, and repulsive wall interactions by tsLJ with $\varepsilon=1.0$. A figure of the potentials used in the simulations is given in Fig. 1.

Because we are not directly interested in one specific system, but in the dependency of the accommodation coefficient on the gas-wall interaction, the parameters used in our model are expressed in reduced units. The system consists of the following reduced units: the unit for length σ^*, the unit for mass m^*, and the unit for energy ε^*. Other units can be derived out of these choices [4,20]. The two walls consisting of 18,000 particles each forming a face centered cubic (fcc) lattice are placed in a box of size $95.0\lambda\times139.49\lambda\times139.49\lambda$ in case (a) and in a box of size $1.39\lambda\times2.03\lambda\times2.03\lambda$ in case (b), and are separated from each other in x-direction. For $\eta=0.2$, the ratio $\lambda/\sigma=0.3362$ and for $\eta=0.005$, the ratio is $\lambda/\sigma=23.0215$. We name one wall warm (W) and the other one cold (C). The total number of gas particles in the box in case (a) is 55,998 corresponding to a number density $n_0=0.4\sigma^{*-3}$ simulated, and 1300 corresponding to a number density $n_0=0.01\sigma^{*-3}$ simulated. The temperature of the two plates can be

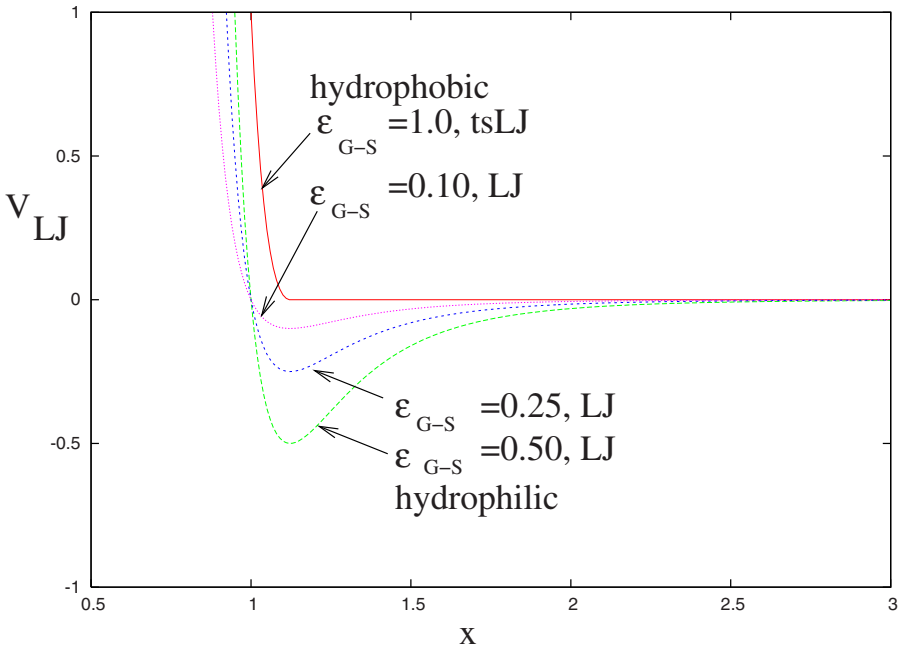

Fig. 1 Hydrophilic wall interactions modeled by Lennard-Jones potential with $\varepsilon=0.10$, 0.20, 0.50 and hydrophobic wall interactions modeled by truncated shifted Lennard-Jones with $\varepsilon=1.0$

controlled by coupling them to a heat bath. The mass and the size of wall particles are taken as follows: $m_2=1m^*$ and $\sigma=1\sigma^*$. The size for both type of particles (gas and wall) is σ for this paper. The mass of the gas varies in our simulations as a fraction of the wall mass: $m_1/m_2=\frac{1}{1}$, $m_1/m_2=\frac{1}{2}$, $m_1/m_2=\frac{1}{4}$, and $m_1/m_2=\frac{1}{8}$. Every simulation, both MC and MD, consists of two parts. In the first part the system is run until equilibrium is reached, and in the second part the macroscopic quantities such as density, temperature, and heat flux profiles are obtained. These simulations consist of 5,000,000 iterations and were executed on 8 CPUs of an AMD Athlon 1800+ Beowulf cluster.

3 Effective Accommodation Coefficients for a Dilute Gas

Boundary conditions have a strong effect on transport properties and heat transfer in microchannels. Wettability and hydrophilic and hydrophobic surface effects need to be studied in detail on molecular level as they have a strong impact on the heat flow in systems and devices. As explained, MD simulations for such large systems are computationally not possible. With the approach presented in this section we have the benefit that the accommodation coefficients (alpha) for the boundary conditions are computed on molecular level reflecting thus the dependency of these boundaries on molecular properties such as $(\varepsilon_{G\text{-}S}, m_1/m_2, T)$. In this section the dependency on $\varepsilon_{G\text{-}S}$ and m_1/m_2 (gas/wall mass ratio) is shown. The Maxwell-like boundary conditions based on α derived from MD simulations can be used then to reproduce the correct heat flux predictions and properties in the microchannel.

Thus, in Ref. [20], we have seen that at low densities, density peaks depending on the attractive gas-wall interaction potential are present and that this effect is reflected in increased gradients in the temperature near the wall interface. As a result of particles sticking to the wall, their velocity is adapted much more to the wall temperature, such that the higher the attraction, the higher the difference in temperature between gas particles going to the left (impinging) and particles moving to the right (reflected). We use MD with explicit wall interactions to get the temperature and density profiles averaged over time of the particles moving from the cold to the warm wall (C-W), from the warm to the cold wall (W-C), and the profiles of the total temperature and number of particles, as these properties change with the gas-wall interactions. As a result of the MD simulations, we could see that there are more particles going from the C to the W wall, than from the W to the C wall for more attractive walls, and that the numbers are almost equal for repulsive wall interactions. The reason for this is that the warm particles move faster than the cold particles. Thus, it takes longer for particles to move from the cold to the warm wall than from the warm to the cold wall and this results then in more particles moving toward the warm wall. With other words, because total flow in both directions is constant at equilibrium, this results in less warm particles and more cold particles moving toward the warm wall. The slopes of these profiles in the channel vary with the gas-surface interaction strength, $\varepsilon_{G\text{-}S}$, and peaks are present in the temperature and density profiles when increasing $\varepsilon_{G\text{-}S}$.

The higher the slope in T next to the wall, the higher the thermal accommodation at the wall and the effective accommodation coefficient α based on the temperature of the incident and reflected molecules in the immediate vicinity of the wall can be computed (see Fig. 2). The high peaks correspond to the layer of particles adsorbed or sticking to the wall, and higher peaks determine increased α reflected also in the T slopes.

As already stated, we define the effective accommodation coefficient based on T as

$$\alpha = (T_{\text{in}} - T_{\text{out}})/(T_{\text{in}} - T_S)$$

where T_{in} is the temperature of the particles moving toward the wall (incident), T_{out} is the temperature of particles leaving the wall (reflected), and T_S is the temperature of the considered wall surface. We can compute all the α's from the MD temperature profiles for different $G\text{-}S$ interactions (attractive: LJ $\varepsilon=0.10, 0.25, 0.5$, and repulsive: tsLJ $\varepsilon=1.0$—see columns 1 and 2 of Table 1).

With the newly computed α for each ε, we can compute the heat fluxes between the walls using MC with Maxwell-like boundary conditions (BCs) based on α [15]. The values for α are found in Table 1 (column 1) where we can also compare the heat predictions from pure MD (column 3), MC with Maxwell (last

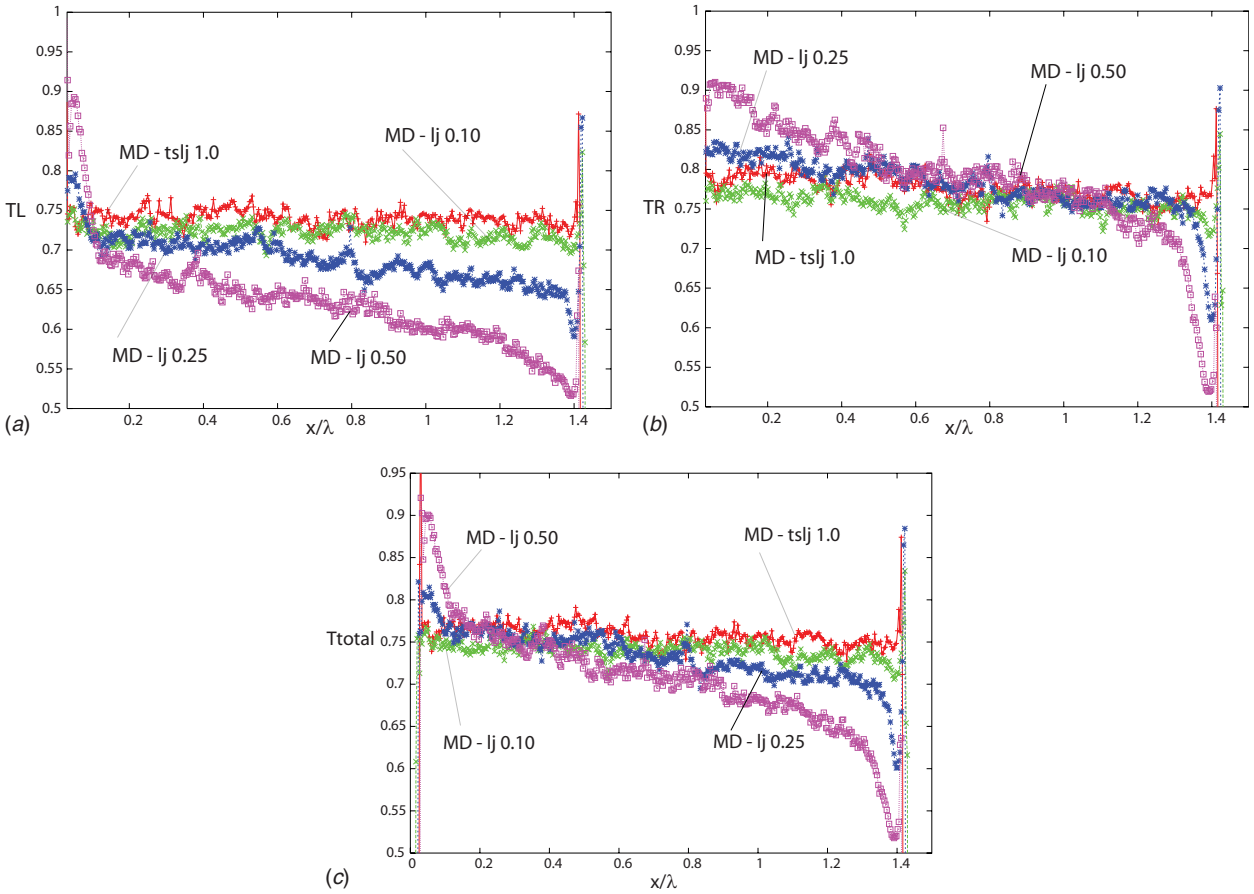

Fig. 2 (*a*) **MD results for the temperature of particles going to the left wall (cold-warm).** (*b*) **MD results for the temperature of particles going to the right wall (warm-cold).** (*c*) **MD results for the total temperature of particles between the walls. All the results are for a dilute gas with η=0.005.**

row), and MC with Maxwell-like BCs based on α (column 4). From this table we see that the α accommodation coefficients computed from the temperature profiles in MD simulations give better heat flux predictions in MC simulations when used in Maxwell-like BCs based on the accommodation coefficient α than the pure Maxwell BCs (α=1.0). For example, for hydrophilic wall interactions (LJ=0.25), MD predicts q_x=0.00087[$\varepsilon^*/(\sigma^{*2}\tau)$] and α=0.25 from the temperature profiles of the impinging and reflected molecules. MC with Maxwell-like BCs with α=0.25 predicts the heat flux q_x=0.00232[$\varepsilon^*/(\sigma^{*2}\tau)$], which is 2.6 times the correct MD heat flux predictions. Quantitative support for the deviations of the combined diffusive-specular boundary conditions from the pure Maxwell can also be seen in Figs. 3 and 4, where the profiles for the total temperature, and temperature of impinging and of reflected molecules can be compared using pure Maxwell boundary conditions, combined diffusive-reflective (Maxwell-like based on an accommodation coefficient α), and explicit MD wall boundary conditions.

Table 1 Heat fluxes using MD and MC with Maxwell-like boundary conditions based on the accommodation coefficient α. A dilute gas was considered with η=0.005. Column 1 contains the gas-wall interaction strength for the LJ potential, column 2 contains the accommodation coefficient for each interaction, and columns 3 and 4 contain the MD and MC heat predictions.

MD	α	MD q_x	MC q_x
tsLJ 1.0	0.14	0.00046	0.00025
LJ 0.10	0.12	0.00047	0.00021
LJ 0.25	0.25	0.00087	0.00070
LJ 0.50	0.58	0.00124	0.00119
	1.0		0.00232

We analyze how the profiles of the total temperature and temperature profiles of particles moving toward and from the wall change depending on the wall properties from Maxwell to Maxwell-type based on α, when compared with the MD profiles.

In Fig. 3 we see that the total T profiles have the same slope as MD when Maxwell-type BCs are used. Figure 3 shows also that MD and MC Maxwell-type based on α get closer to MC Maxwell predictions for higher values of ε, while at lower ε, the slopes are very much different. MD and MC (Maxwell-α based) are on the other side in very good agreement. To analyze the accommodation coefficient we study the behavior of the incident and reflected molecules to the wall. From the MD simulations we see that the number of molecules going from the W-C wall is smaller than the number of molecules going from the C to the W wall and they become equal for a lower ε. The reason for this is that warm particles move faster than the cold particles. Because total flow in both directions is constant at equilibrium, this results in less warm particles and more particles moving toward the warm wall. Also, the higher the ε, the better the agreement with Maxwell predictions. From the results of these temperature profiles from the C to the W and from the W to the C wall in Fig. 4, we have already computed the accommodation coefficients based on the MD results in Table 1.

Computing α from the T profiles next to the wall for high ε's becomes difficult due to the enhanced clustering effect next to the

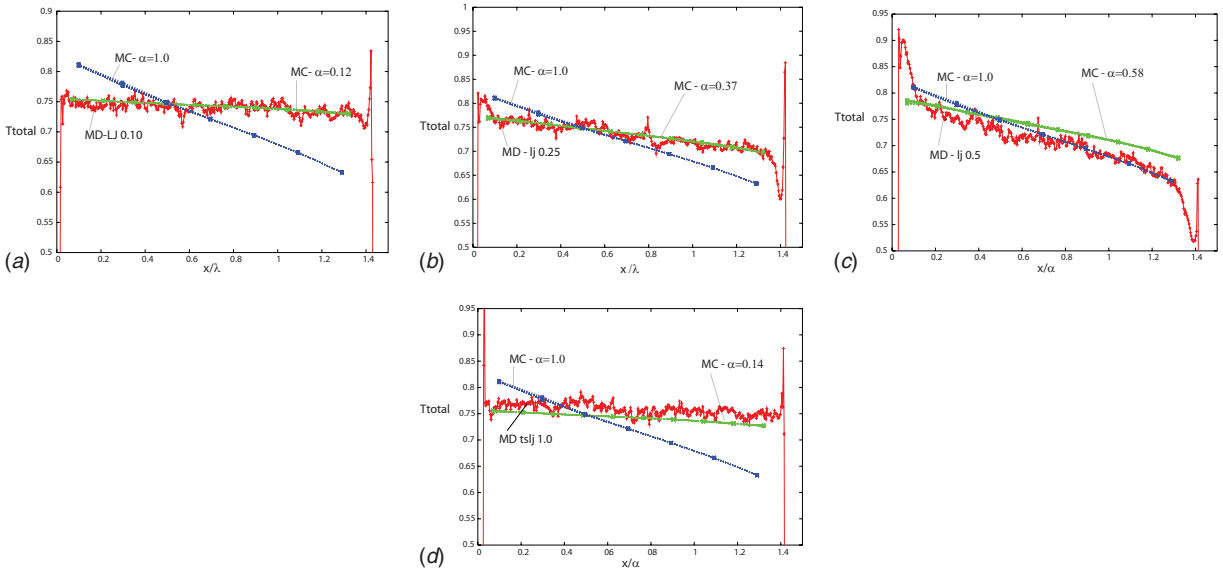

Fig. 3 Time average of the temperature profiles of particles going to the left wall (cold-warm) and to the right wall using MD and MC. The parameters for the MD and MC simulations are (*a*) MC: α=0.12, MC: α=1.0, and MD: ε_{LJ}=0.10; (*b*) MC: α=0.37, MC: α=1.0, and MD: ε_{LJ}=0.25; (*c*) MC: α=0.58, MC: α=1.0, and MD: ε_{LJ}=0.50; and (*d*) MC: α=0.14, MC: α=1.0, and MD: ε_{tsLJ}=1.0. All the results are for a dilute gas with η=0.005.

cold wall and due to the shifted bulk temperature value in MC when compared with MD, caused by the fact that MC cannot predict the increased peaks near the wall.

That is why, in order to predict accurately α, a map is given in Fig. 5. In this map, for a certain heat flux prediction in MD, we can get the effective value of the α coefficient from the MC heat flux predictions with Maxwell-like BC function on the accommodation coefficient α. The α values measured from the temperature MD profiles, for the four values of ε used until now for the gas-wall interactions, are plotted also in Fig. 5 and show good agreement with the map. For lower values of ε, the prediction is a bit lower due to higher statistical error in this case.

Table 2 shows the average number of particles, n, and average temperature T of particles going to the left (cold-warm) and to the right (warm-cold), using MD, MC with Maxwell-like BC based on α, and MC with fully accommodating walls (α=1). We see also from these measurements that the density and temperature of

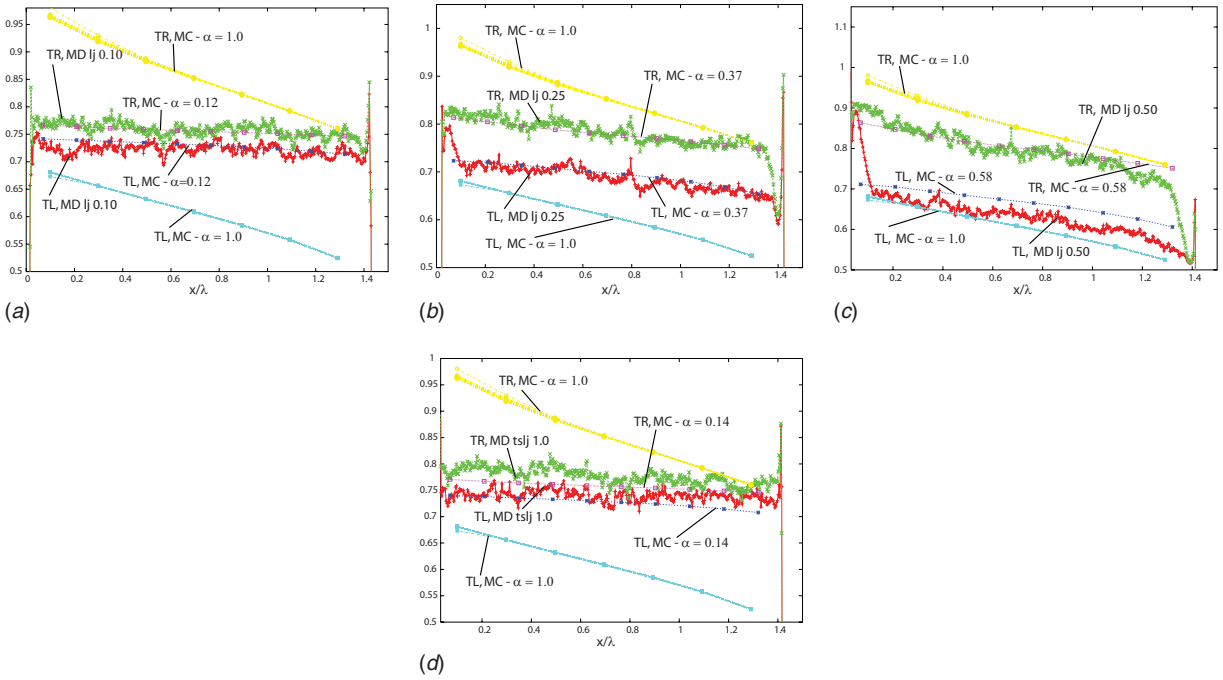

Fig. 4 Time average of the temperature profiles of the total particles between the two walls. The parameters for the MD and MC simulations are (*a*) MC: α=0.12, MC: α=1.0, and MD: ε_{LJ}=0.10; (*b*) MC: α=0.37, MC: α=1.0, and MD: ε_{LJ}=0.25; (*c*) MC: α=0.58, MC: α=1.0, and MD: ε_{LJ}=0.50; and (*d*) MC: α=0.14, MC: α=1.0, and MD: ε_{tsLJ}=1.0. All the results are for a dilute gas with η=0.005.

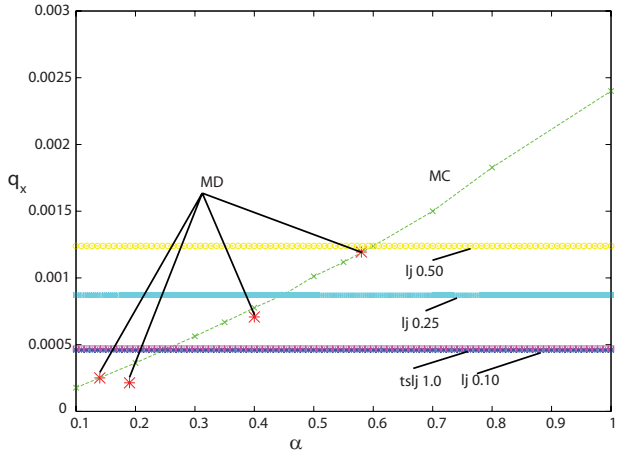

Fig. 5 MC heat flux predictions as a function of accommodation coefficient α (Maxwell-type boundary conditions) with continuous lines. Comparison with MD heat prediction (points) for different gas-wall interactions (ε_{LJ}=0.10, ε_{LJ}=0.25, ε_{LJ}=0.5, and ε_{tsLJ}=1.0). The results are reported for a dilute gas with η =0.005.

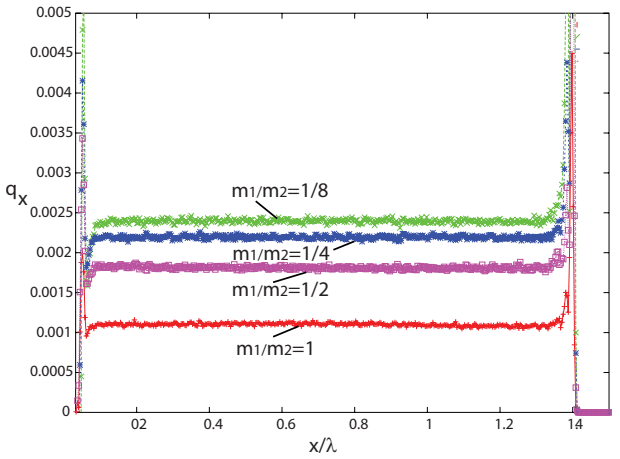

Fig. 6 MD heat flux profiles averaged in time for different fluid/wall mass ratios. From the bottom to the top are the heat flux lines for mass ratios $\frac{1}{1}$, $\frac{1}{2}$, $\frac{1}{4}$, and $\frac{1}{8}$. The results are for a dilute gas with η=0.005 and $\varepsilon_{G\text{-}S}$=0.50.

incident and reflected fluxes of molecules correspond very well for lower ε. At higher values of ε, the clustering next to the wall becomes important and large differences between the fluxes of particles and their T are registered when comparing MD with MC including Maxwell-like BCs based on α accommodation coefficient. This α is then one simple way to characterize the wall-gas interface at the immediate boundary but it is not able to predict the influence of the local effects in the wall vicinity.

We also looked at the dependency of the MD heat flux predictions on the molecular fluid/wall mass ratio. As we can see in Fig. 6, the heat flux q_x increases with decreasing mass ratio. The values of the heat fluxes on different mass ratios are shown in Table 3. The physical explanation for an increasing heat flux with decreasing mass ratio is the fact that for smaller masses of the gas, the gas particles move faster. This dependence of the mass ratio is given also by the Bird formula for the heat flux between a cold and a warm wall in case of a free molecular flow [2]. In the plots in Fig. 6, the deviations for the MD results for the total heat flux near the wall are caused because the interaction with the walls is not taken into account in the calculation of the heat flux. The values considered in the heat flux comparisons in the paper are the space averaged values for the middle of the channel.

The values of the accommodation coefficients α for different mass ratios and different wall interactions with the wall ($\varepsilon_{G\text{-}S}$) can be derived from the temperature profile from Fig. 7. The accommodation coefficients vary with ε and mass such that at low values of ε (e.g., ε=0.10), the mass ratio does not influence α and has values around 0.14. For higher values of ε (e.g., ε=0.25), α has almost the same value for mass ratios 1.0 (α=0.35) and 0.125 (α=0.32), but has higher values for mass ratios 0.25 and 0.5 (α =0.44). For very attractive walls (ε=0.5), α has the lowest value for mass ratio 0.125 (α=0.46), followed by the case with mass ratio 1.0 (α=0.58), and the same value for both mass ratios 0.25 and 0.5 (α=0.64). It is interesting to see that for more attractive walls, α for mass ratio 1.0 is always higher than the value for mass ratio 0.125, but lower than for 0.25 and 0.5. For repulsive walls, accommodation coefficient α is higher (0.2) for mass ratio 1.0 than for the other mass ratios 0.125, 0.25, and 0.5 (α=0.1).

4 Using the Effective Accommodation Coefficient for the Heat Flux Predictions for a Dense Gas

Assuming that the computed α for different gas-wall interactions ($\varepsilon_{G\text{-}S}$) in the MD model is a characteristic of the wall-gas interface, we use these effective values of the accommodation coefficient α to compute the heat flux of a dense gas between the two walls at different temperatures.

First we determine the heat flux q_x in a channel with wall separation L_x=95λ and η=0.2, for different wall-gas and gas-gas interactions. The results in Table 4 show that the gas-gas interactions become important, such that the higher the $\varepsilon_{G\text{-}G}$, the lower the heat flux. When walls are very attractive, the role of gas-gas interactions becomes less important.

We compute the heat flux predictions in a dense gas with η =0.2 from MC simulations with Maxwell-type BCs based on the effective α coefficient transferred from the gas-surface interface of a dilute gas, and we compare with MD results in the case when gas-gas interactions are considered hard-sphere (tsLJ). We see that these values are closer to MD results than MC heat predictions

Table 2 Average density and temperature of the particles going from the cold to the warm wall ($N_{C\text{-}W}$, $T_{C\text{-}W}$), and from the warm to the cold wall ($N_{C\text{-}W}$, $T_{C\text{-}W}$), using MD, MC with Maxwell-like boundary conditions based on α, and MC with Maxwell boundary conditions (α=1). Density is normalized with the reference density n_0=0.01 and temperature with T_0=T_2 (temperature of the cold wall), and η=0.005.

	MD				MC-Max (α)				MC-Max (α=1)			
	$N_{C\text{-}W}$	$T_{C\text{-}W}$	$N_{W\text{-}C}$	$T_{W\text{-}C}$	$N_{C\text{-}W}$	$T_{C\text{-}W}$	$N_{W\text{-}C}$	$T_{W\text{-}C}$	$N_{C\text{-}W}$	$T_{C\text{-}W}$	$N_{W\text{-}C}$	$T_{W\text{-}C}$
tsLJ 1.0	0.50	0.71	0.49	0.75	0.50	0.72	0.49	0.75	0.52	0.64	0.47	0.82
LJ 0.10	0.51	0.71	0.48	0.75	0.50	0.72	0.49	0.75				
LJ 0.25	0.51	0.68	0.48	0.77	0.51	0.69	0.48	0.77				
LJ 0.50	0.52	0.62	0.47	0.80	0.52	0.66	0.47	0.80				

Table 3 Average heat flux for different molecular fluid/wall mass ratios m_1/m_2, for a dilute gas with η=0.005 and ε_{G-S} =0.50

m_1/m_2	$\frac{1}{1}$	$\frac{1}{2}$	$\frac{1}{4}$	$\frac{1}{8}$
q_x	0.0010	0.0018	0.0022	0.0023

Table 4 Heat flux using MD with different wall-gas and gas-gas LJ interaction potentials, for a dense gas with η=0.2. The columns stand for the wall-gas interactions and the rows for the gas-gas interactions.

		G-W			
		tsLJ 1.0	LJ 0.10	LJ 0.25	LJ 0.50
G-G	tsLJ 1.0	0.015	0.014	0.016	0.017
	LJ 0.10	0.012	0.011	0.014	0.015
	LJ 0.25	0.012	0.011	0.0135	0.016
	LJ 0.50	0.009	0.009	0.012	0.016

with Maxwell BCs (α=1), especially for the hydrophobic wall interactions (small α). For attractive walls, even though better results are predicted than MC based on Maxwell BCs (α=1), the deviations are larger due to the overlapping of attractive walls and clustering effect (see Table 5).

5 Conclusions

In this paper, MD simulation including explicit walls were conducted to study the gas-surface interface, and to compute the effective accommodation coefficients to be used as boundary conditions in MC simulations. The dependence of heat flux predictions and accommodation coefficients on the wall properties (attractive and repulsive) and on the molecular fluid/wall ratio is shown and an effective map of the MC heat flux values depending on the generic accommodation coefficient is given. Confronting this map with the MD heat flux predictions, the effective accommodation coefficients that predict the same q_x in MD as well as in MC were found. These effective values for accommodation coefficients are computed for a dilute gas-surface interface and are transferred then to the MC simulation of a dense gas in a nanochannel. The MC heat flux results using these coefficients were compared with the MD heat predictions. Even though better results are registered compared with other boundary conditions, still large deviations are registered due to the overlapping effect of attractive/clustering next to the wall in the case of a dense gas in the nanochannel such that α cannot be simply transferred.

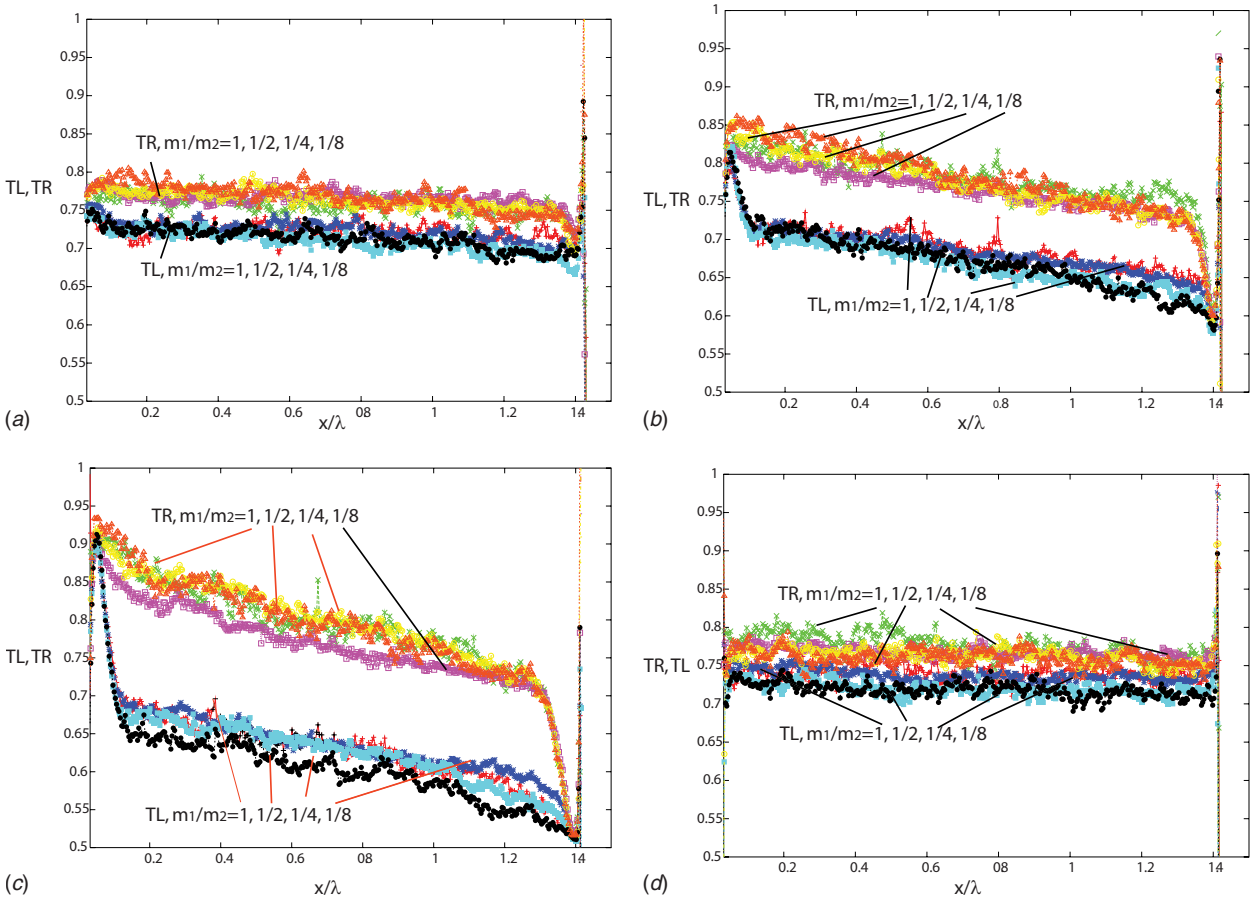

Fig. 7 Time average of the MD temperature profiles of particles going from the C-W wall (T_L) and from the W-C wall (T_R), for different mass ratios and ε: (*a*) $m_1/m_2=\frac{1}{1},\frac{1}{2},\frac{1}{4},\frac{1}{8}$ and ε_{LJ}=0.10, (*b*) $m_1/m_2=\frac{1}{1},\frac{1}{2},\frac{1}{4},\frac{1}{8}$ and ε_{LJ}=0.25, (*c*) $m_1/m_2=\frac{1}{1},\frac{1}{2},\frac{1}{4},\frac{1}{8}$ and ε_{LJ}=0.50, and (*d*) $m_1/m_2=\frac{1}{1},\frac{1}{2},\frac{1}{4},\frac{1}{8}$ and ε_{tsLJ}=1.0. All the results are for a dilute gas with η=0.005.

Table 5 Heat flux using MD and MC with Maxwell-like boundary conditions based on the effective accommodation coefficient α. A dense gas was considered with $\eta=0.2$. Column 1 contains the gas-wall interaction strength for the LJ or tsLJ potential. Column 2 contains the accommodation coefficient for each interaction case as evaluated at low density from MD simulations. Columns 3 and 4 contain the MD and MC heat predictions at high gas density.

MD	α	MD-q_x	MC-q_x
tsLJ 1.0	0.14	0.015	0.010
LJ 0.10	0.12	0.014	0.008
LJ 0.25	0.25	0.016	0.025
LJ 0.50	0.58	0.017	0.037
	1.0		0.057

References

[1] Schmidt, R. R., and Notohardjono, B., 2002, "'High and Server Low Temperature Cooling," IBM J. Res. Dev., **46**, pp. 739–751.

[2] Bird, G., 1994, *Molecular Gas Dynamics and the Direct Simulation of Gas Flows*, Clarendon, Oxford.

[3] Kucaba-Pietal, A., and Zbigniew Walenta, Z., 2004, "Size and Wall Effects in Water Flows in Nanochannels," International Journal Turbulence, **10**, pp. 77–81.

[4] Frenkel, D., and Smit, B., 1996, *Understanding Molecular Simulation*, Academic, San Diego, CA.

[5] Frezzotti, A., 1997, "A Particle Scheme for the Numerical Solution of the Enskog Equation," Phys. Fluids, **9**(5), pp. 1329–1335.

[6] Montanero, J., and Santos, A., 1996, "Monte Carlo Simulation Method for the Enskog Equation," Phys. Rev. E, **54**, pp. 438–444.

[7] Montanero, J., and Santos, A., 1997, "Simulation of the Enskog Equation A La Bird," Phys. Fluids, **9**, pp. 2057–2060.

[8] Nanbu, K., 1986, "Theoretical Basis of the Direct Simulation Monte Carlo Method," *Proceedings of the 15th International Symposium on RGD*, Vol. 1, V. Boffi and C. Cercignani, eds., pp. 369–383.

[9] Wachman, H. Y., 1993, "Thermal Accommodation Coefficient: The Contributions of Lloyd Brewster Thomas," *Progress in Astronautics and Aeronautics, Rarefied Gas Dynamics*, Vol. 158, A. R. Seebass, B. D. Shizgal, and D. P. Weaver, eds., AIAA, Washington, DC, p. 461.

[10] Lord, R. G., 1991, "Some Extensions to the Cercignani-Lampis Gas-Surface Scattering Model," Phys. Fluids A, **3**, pp. 706–710.

[11] Cercignani, C., and Lampis, M., 1971, "Kinetic Models for Gas-Surface Interactions," Transp. Theory Stat. Phys., **1**, pp. 101–114.

[12] Cieplak, M., Koplik, J., and Banavar, J., 1999, "Applications of Statistical Mechanics in Subcontinuum Fluid Mechanics," Physica A, **274**, pp. 281–293.

[13] Devienne, F., Souquet, J., and Roustan, J., 1966, "Study of the Scattering of High Energy Molecules by Various Surfaces," *Advanced in Applied Mechanics, Suppl. 3, Rarefied Gas Dynamics*, Vol. 2, J. H. Leeuw, ed., Academic, New York, p. 584.

[14] Gregory, J., and Peters, P., 1986, "A Measurement of the Angular Distribution of 5 eV Atomic Oxygen Scattered of a Solid Surface in Earth Orbit," *Rarefied Gas Dynamics*, Vol. 1, V. Boffi and C. Cercignani, eds., Academic, New York, p. 644.

[15] Yamamoto, K., Takeuchi, H., and Hyakutake, T., 2006, "Characteristics of Reflected Gas Molecules at a Solid Surface," Phys. Fluids, **18**, p. 046103.

[16] Matsui, J., and Matsumoto, Y., 1993, "Study of Scattering Process in Gas-Surface Interactions," *Progress in Astronautics and Aeronautics, Rarefied Gas Dynamics*, Vol. 158, A. R. Seebass, B. D. Shizgal, and D. P. Weaver, eds., AIAA, Washington, DC, p. 515.

[17] Yamanishi, N., and Matsumoto, Y., 1999, "The Multi-Stage Reflection Model for DSMC Calculations," *Rarefied Gas Dynamics*, Vol. 1, R. Brun, et al., eds., Cépaduès-Éditions, Toulouse, France, p. 421.

[18] Chirita, V., Pailthorpe, B., and Collins, R., 1993, "Molecular Dynamics Study of Low-Energy Ar Scattering by the Ni(001) Surface," J. Phys. D, **26**, pp. 133–142.

[19] Kimura, T., and Maruyama, S., 2002, "Molecular Dynamics Simulation of Water Droplet in Contact With Platinum Surface," 12th International Heat Transfer Conference, pp. 537–542.

[20] Markvoort, A., Hilbers, P., and Nedea, S., 2005, "Molecular Dynamics Study of the Influence of Wall-Gas Interactions on Heat Flow in Nanochannels," Phys. Rev. E, **71**, p. 066702.

[21] Nedea, S., Markvoort, A., Frijns, A., van Steenhoven, A., and Hilbers, P., 2005, "Hybrid Method Coupling Molecular Dynamics and Monte Carlo Simulations to Study the Properties of Gases in Micro and Nanochannels," Phys. Rev. E, **72**, pp. 016705.

[22] Yamamoto, K., Takeuchi, H., and Hyakutake, T., 2003, "Effect of Wall Characteristics on the Behaviors of Reflected Gas Molecules in a Thermal Problem," *Rarefied Gas Dynamics*, Vol. 663, A. D. Ketsdever and E. P. Muntz, eds., AIP, New York, p. 1008.

[23] Frezzotti, A., 1999, "Monte Carlo Simulation of the Heat Flow in a Dense Hard Sphere Gas," Eur. J. Mech. B/Fluids, **18**, pp. 103–119.

[24] Halicioğlu, T., and Pound, G. M., 1975, "Calculation of Potential Energy Parameters From Crystalline State Properties," Phys. Status Solidi A, **30**(2), pp. 619–623.

[25] Guan, P., McKenzie, D., and Pailthorpe, B., 1996, "MD Simulations of Ag Film Growth Using the Lennard-Jones Potential," J. Phys.: Condens. Matter, **8**, pp. 8753–8762.

Semiconductor Thin Films Combined With Metallic Grating for Selective Improvement of Thermal Radiative Absorption/Emission

C. J. Fu[1]
e-mail: cjfu@pku.edu.cn

W. C. Tan

LTCS and Department of Mechanics and Aerospace Engineering,
College of Engineering,
Peking University,
Beijing 100871, China

We propose in this work a structure of semiconductor thin films combined with a one-dimensional metallic grating, which allows for selective improvement of thermal radiative absorptivity (also emissivity) of the structure. Both shallow and deep gratings are considered in this work. Our numerical results obtained with a 2D rigorous coupled-wave analysis algorithm demonstrate that the proposed structure exhibits enhanced spectral absorptivity for photon energy slightly above the gap energy of the semiconductor (silicon in this work). Furthermore, the selectively improved absorptivity can be obtained in a wide range of incidence angles. As such, much smaller thickness of the semiconductor layer is required to absorb the same amount of high energy photons than in a conventional Si-based photovoltaic device. In addition, absorptivity for low energy photons in the new structure is lower due to the smaller semiconductor layer thickness. Therefore, the new structure may have potential applications in energy conversion devices. [DOI: 10.1115/1.3056599]

Keywords: grating, rigorous coupled-wave analysis, absorptivity, surface polariton, microcavity mode

1 Introduction

Structured materials and materials with surface microstructures, such as photonic crystals (PCs), multilayered thin films, and materials with surface gratings, have been shown to have significantly different optical and thermal properties compared with bulk materials [1]. The rapid development of micro-/nanoscience and technology in the past two decades has made it possible to fabricate such kinds of materials for applications of different purposes such as thermophotovoltaic (TPV) devices and coherent thermal emission sources [2–17]. PCs [2–6] were shown to be able to suppress thermal emission in the forbidden gap and enhance thermal emission near the gap edge. Therefore, PCs have the advantage to manipulate their thermal emission spectra by changing their composing constituents and geometry, which makes them very good candidates for use as the emitter of a TPV system. But challenges also exist in fabricating PCs especially of two dimensions and three dimensions for applications in the near infrared region. Materials with surface relief gratings [7–17] have been shown to be able to selectively improve the thermal emissivity due to excitation of surface polaritons or microcavity effect. Improved thermal emissivity resulting from excitation of surface polaritons (SPs) may be highly emission angle-dependent while that due to microcavity effect is angle-independent [13]. Thus, selective improvement of thermal emissivity due to microcavity effect is more appropriate for application in TPV devices while that highly angle-dependent is suitable for use in coherent thermal emission sources. Regardless of all these properties, grating structures previously studied for selective improvement of thermal radiative emission are ruled on the top surface of a material and are primarily considered for use as thermal radiators. No research has been conducted to study the thermal properties of structures with a grating sandwiched between different materials. On the other hand, such kind of structures may be applied as not only the emitter, but also the receiver in energy conversion devices.

In this work, we propose a structure of semiconductor thin films combined with a 1D metallic grating for selective improvement of thermal radiative absorption/emission. The purpose of selecting a semiconductor in the proposed structure is twofold: The new structure may not only be used as an emitter, but also as a receiver in energy conversion devices. Both shallow and deep gratings are considered in our work. We numerically calculate the absorptivity of the structure using a 2D rigorous coupled-wave analysis (RCWA) algorithm. The emissivity can be obtained from Kirchhoff's law. Our simulation results show that improved absorptivity of the structure for photon energy slightly higher than the semiconductor gap energy can be achieved using both shallow and deep gratings. Furthermore, the selectively improved absorptivity can be obtained in a wide range of incidence angles. As a result, much smaller thickness of the semiconductor layer is required to absorb the same amount of high energy photons than in a conventional Si-based photovoltaic device. In addition, absorptivity for low energy photons in the new structure is lower due to the smaller semiconductor layer thickness. Therefore, the new structure may have potential applications in energy conversion devices.

2 Analysis

The proposed structure is schematically shown in Fig. 1. For demonstrative purposes, we assume in this work that the metallic grating is one dimensional and is made of silver. The semiconductor thin film of thickness d_2 on top of the grating is silicon (Si). The grating has a period of Λ and a depth of d_3, and f is the filling

[1]Corresponding author.

Contributed by the Heat Transfer Division of ASME for publication in the JOURNAL OF HEAT TRANSFER. Manuscript received January 28, 2008; final manuscript received July 22, 2008; published online January 21, 2009. Review conducted by Robert D. Tzou. Paper presented at the 2008 International Conference on Micro/Nanoscale Heat Transfer (MNHT 2008), Tainan, Taiwan, January 6–9, 2008.

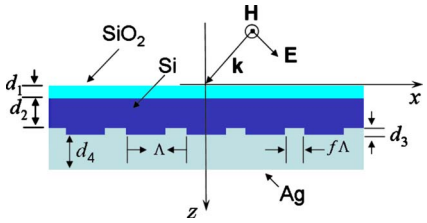

Fig. 1 Schematic of the proposed structure, also shown are the relative orientations of the electric field vector E, magnetic field vector H, and wave vector k

ratio such that $f\Lambda$ over a complete period of the grating is occupied by silver and $(1-f)\Lambda$ is occupied by Si. The SiO_2 thin film of thickness d_1 on top of the Si layer is used as an antireflection layer in this work. Note that this proposed structure is similar to a Si-based solar cell if the grating is not present. The z-axis of the coordinates is assumed vertically downward along the direction of the surface normal and the x-y plane is parallel to the surface. The structure is placed in air or vacuum and its lateral extension is assumed to be infinite. When a plane wave is incident on the surface of the antireflection layer, if the depth of the grating d_3 is zero or the filling ratio f is equal to one or zero, all the interfaces of the structure are flat and the conventional thin film optics formulas [18,19] can be used to calculate the thermal radiative properties of the structure. But if d_3 is nonzero and f is not equal to one or zero, the conventional thin film optics formulas are inapplicable. The RCWA method is employed in this work to study the thermal radiative properties of the structure. This method is a well-developed algorithm for analyzing wave scattering by gratings [20–23] and will not be discussed here. As for the structure shown in Fig. 1, each layer can be taken as a grating with period Λ. But the filling ratio for the two top layers and the silver layer of thickness d_4 is equal to 1. It should be noted that the above-mentioned absorptivity is actually termed spectral, directional absorptivity, but the two prefixed adjectives will be omitted throughout the paper for brevity. The emissivity of the structure is simply equal to the absorptivity of the same according to Kirchhoff's law and thus only the absorptivity needs to be considered below. Furthermore, we assume plane wave incidence of s- and p-polarizations, and the electromagnetic fields are independent of the y variable. Therefore, the problem is a two-dimensional problem.

3 Results and Discussion

In our simulations the dielectric constants of Si, SiO_2 (glass), and silver are taken from Ref. [24]. For comparison, we consider five cases of the proposed structure with the feature dimensions of each case listed in Table 1. But in order to verify that our RCWA codes are correct, we first calculate the diffraction efficiency of an asymmetric sawtoothlike grating. The grating (refractive index $n=2.04$) is a 15-layer stairstep with a step width of 1/16 of the grating period and a layer of 1/15 of the total depth of the structure. The calculated first-order transmissivity of the structure versus the grating depth up to five wavelengths is plotted in Fig. 2(a)

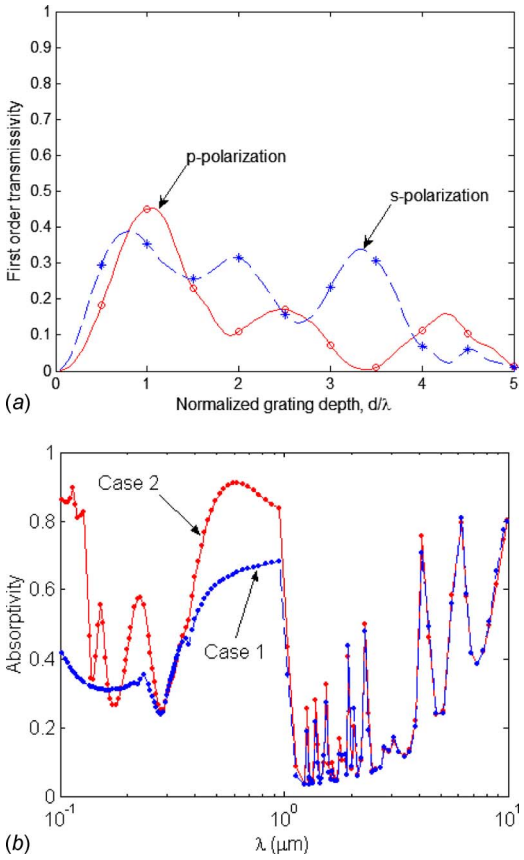

Fig. 2 (a) Comparison of the calculated first-order transmissivity (curves) of a sawtoothlike dielectric grating with published results (markers); (b) comparison of the calculated absorptivity of the proposed structure for normal incidence by the RCWA method (solid curves) and by the formulas of thin film optics (dots) when $d_3=0$

for incidence angle $\theta=10$ deg and compared with published results [22]. It can be seen that for both polarizations, our results (curves) agree exactly with the published results (markers). Second, we assume that the grating depth d_3 of the proposed structure equals zero such that the interface between Si and silver is flat (i.e., Cases 1, 2, and 4 in Table 1). The thermal radiative properties of such a multilayered structure with flat interfaces can readily be obtained using the formulas of thin film optics [18,19]. Figure 2(b) compares the frequency-dependent absorptivity of Cases 1 and 2 for plane waves at normal incidence calculated with the formulas of thin film optics and the RCWA method. The solid curves are the results calculated with the RCWA method and the dots correspond to the results calculated with the formulas of thin film optics. It is clear that the results obtained from the two methods are in excellent agreement, verifying the applicability and correctness of our codes.

Table 1 Feature dimensions of the structure studied in this work

	d_1 (μm)	d_2 (μm)	d_3 (μm)	Λ (μm)	f	d_4 (μm)
Case 1	0	250	0	—	—	2.5
Case 2	0.1	250	0	—	—	2.5
Case 3	0.1	54	0.03	0.25	0.25	2.5
Case 4	0.1	54	0	—	—	2.5
Case 5	0.1	54	2.5	0.25	0.25	2.5

From Fig. 2(*b*), the antireflection coating is advantageous to improving the absorptivity for wavelength less than 1 μm. The absorptivity drops abruptly around $\lambda=1$ μm, resulting in very low absorptivity at the edge of the energy gap (corresponding to a wavelength of 1.1 μm at room temperature). According to the principles of photoelectric energy conversion [25], it is desirable for the Si layer to have absorptivity of unity for photons with energy higher than the gap energy and zero absorptivity for photons with energy lower than the gap energy. This is, however, impossible in reality. Especially, the extinction coefficient of Si is so small for photons with energy slightly above the gap energy that the Si layer in conventional Si-based photovoltaic devices is usually made 200–400 μm thick in order to absorb as many photons transmitted into it with energy higher than the gap energy as possible. On the other hand, absorption of photons with energy lower than the gap energy may also increase in a thick Si layer, as can be seen in Fig. 2(*b*) where the Si layer thickness is taken to be 250 μm. However, these low energy photons can only add to heat dissipation and are not desired in energy conversion systems [5,25]. Therefore, techniques that can improve selectively the absorptivity of the Si layer for photon energy slightly above the gap energy will help to reduce the Si layer thickness as well as the absorption of low energy photons in the Si layer. We will investigate the possibility for selectively improving the absorptivity of the structure in the presence of a grating at the interface of Si and silver layers. A shallow grating case and a deep grating case will be considered separately.

3.1 Shallow Grating. The structure with a shallow grating has feature dimensions given in Table 1 as Case 3 (the values of d_3, Λ, and f are chosen to have optimized results in our calculations, thus representing optimized parameters of the grating). Note that the Si layer thickness in Case 3 is roughly only one-fifth of that in Case 2. Its calculated absorptivity for a plane wave of *p*-polarization (i.e., the magnetic field parallel to the groove of the grating) at normal incidence is shown in Fig. 3(*a*), wherein the corresponding result for Case 2 is also shown for comparison. Interestingly, it can be seen that the absorptivity of the structure around the Si energy gap edge is greatly enhanced when the grating is present though the thickness of the Si layer is much less than that in Case 2. On the other hand, the value of the absorptivity is smaller than that of Case 2 in the longer wavelength region. Furthermore, the two curves merge together when $\lambda<0.8$ μm, showing that the presence of the grating does not affect the absorptivity of the structure. This is because the penetration depth of Si for $\lambda<0.8$ μm is smaller than 12.7 μm so that thermal radiation wave in the Si layer can be completely absorbed before it can touch the grating. For verification, we also calculate the absorptivity of Case 4 and the result is also plotted in Fig. 3(*a*). Clearly, this curve merges with the other curves when λ is smaller than 0.8 μm. The absorptivity of this case is essentially lower than that with a shallow grating at longer wavelengths and the peak at $\lambda\approx0.95$ μm is due to wave interference in the Si layer. Plotted in Fig. 3(*b*) is the absorptivity of Case 3 for incidence angles equal to 30 deg and 60 deg, respectively. Enhanced absorptivity can be found to persist around the gap edge of Si while the absorptivity at longer wavelengths keeps at low values.

In order to get better insight into the phenomenon, we fix $\lambda=1.033$ μm, which is slightly shorter than the gap wavelength 1.1 μm, and calculate the absorptivity of Cases 2–4 as a function of θ, respectively. The results are shown in Fig. 4. Obviously, the presence of the grating can greatly enhance the absorptivity of the structure over a wide range of incidence angles such that the absorptivity of Case 3 is better than that of Case 2 and is much better than that of Case 4. The many peaks in curves of Cases 2 and 4 are caused by wave interference effect. However, the peaks in the curve of Case 3 result from different mechanisms, namely, excitation of SPs, wave interference, and interactions of multiple-order diffracted waves as will be discussed in detail below.

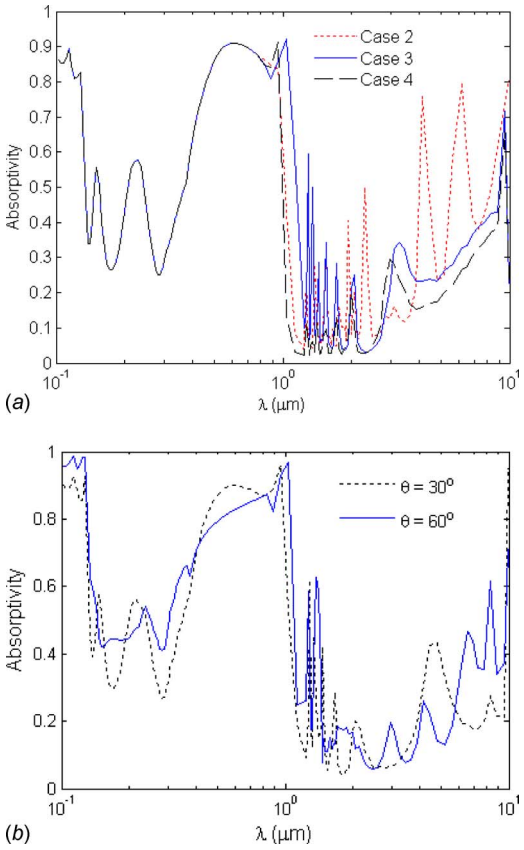

Fig. 3 (*a*) Calculated absorptivity of the structure at normal incidence for Cases 2–4 listed in Table 1; (*b*) calculated absorptivity of the structure at incidence angles equal to 30 deg and 60 deg, respectively, for Case 3

SPs are surface electromagnetic waves that originate from resonant movement of charged particles at the interface between two different media and propagate along the interface with the field amplitudes decaying exponentially away from the interface [12]. Only *p*-polarized SPs can be excited for naturally occurred materials and the excitation of SPs at the interface between two different media requires that the real parts of the two media's dielectric constants have opposite signs (assume their imaginary parts are negligibly small) and satisfy the following relation [10]:

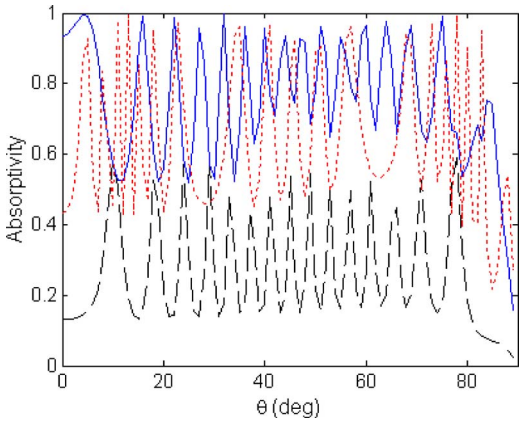

Fig. 4 Calculated absorptivity of the structure as a function of incidence angle at wavelength $\lambda=1.033$ μm for Cases 2 (dotted), 3 (solid), and 4 (dashed), respectively

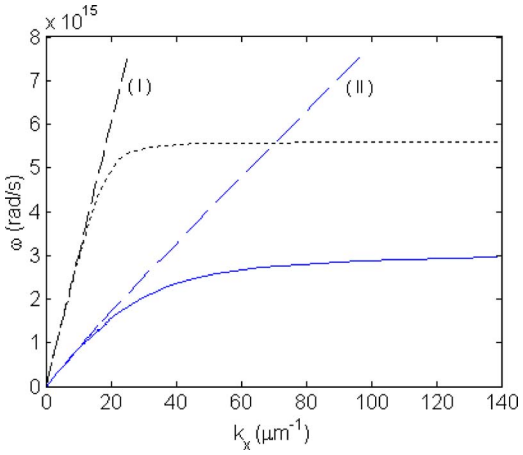

Fig. 5 The dispersion curves of SPs at the interface between silicon and silver (solid) and between vacuum and silver (dotted). The dashed curves (I) and (II) are, respectively, the dispersion curves for light propagating in vacuum and silicon.

$$\frac{k_{1z}}{\varepsilon_1}+\frac{k_{2z}}{\varepsilon_2}=0 \tag{1}$$

Here, ε_1 and ε_2 are, respectively, the dielectric constants of the two media and are real numbers, and $k_{1z}=\sqrt{\varepsilon_1 k^2-k_x^2}$ and $k_{2z}=\sqrt{\varepsilon_2 k^2-k_x^2}$, where k_x denotes wave vector of the electromagnetic surface wave. According to the dielectric constant data of silver from Ref. [24], the real part of the silver's dielectric constant is negative for 0.17 μm$<\lambda<$0.27 μm and $\lambda>$0.33 μm. Therefore, it is possible to excite SPs at the interface between silver and air (vacuum) up to frequencies in the ultraviolet and optical regions when Eq. (1) is satisfied. The dotted curve in Fig. 5 shows the dispersion relation of SPs excited at a flat interface between silver and air. The dashed curve (I) corresponds to the dispersion relation of light traveling in air. The dotted curve asymptotically approaches an angular frequency $\omega=5.6\times10^{15}$ rad/s, which corresponds to a wavelength of 0.3 μm. The solid curve in Fig. 5 is the dispersion relation of SPs excited at a flat interface between silver and Si and the dashed curve (II) is the corresponding dispersion relation of light traveling in Si. The whole solid curve is located below the dotted curve and asymptotically approaches an angular frequency $\omega=3.0\times10^{15}$ rad/s (i.e., $\lambda=0.63$ μm). In addition, the solid curve is much flatter than the dotted curve in the optical and near infrared regions so that SPs excited at the Si/silver interface is more angle-independent than at the air/silver interface. Note that SPs may be excited at longer wavelengths, but the loss in silver may deteriorate the SP effect. Note also that heavily doped Si grating alone can achieve selectively improved thermal radiative absorption/emission in the mid-infrared region [7,10], which is not suitable for applications in optical and near infrared regions.

The dotted and solid curves in Fig. 5 are located, respectively, to the right of the dashed curves (I) and (II), indicating that SPs cannot be excited at a flat interface directly by radiative waves [9]. With grating structure, radiative waves can be diffracted by the grating and the diffracted wave vectors can match the wave vectors of SPs, resulting in SP excitations. In other words, SPs can be excited if the incident wave vector k and the SP wave vector k_x satisfy the grating equation [9]

$$k_x=k\sin\theta+j\frac{2\pi}{\Lambda} \tag{2}$$

where θ is the angle of incidence and j is an integer. In order to verify the above analysis, we calculate the electromagnetic field distribution in the Si layer of Case 3 for a p-polarized plane wave

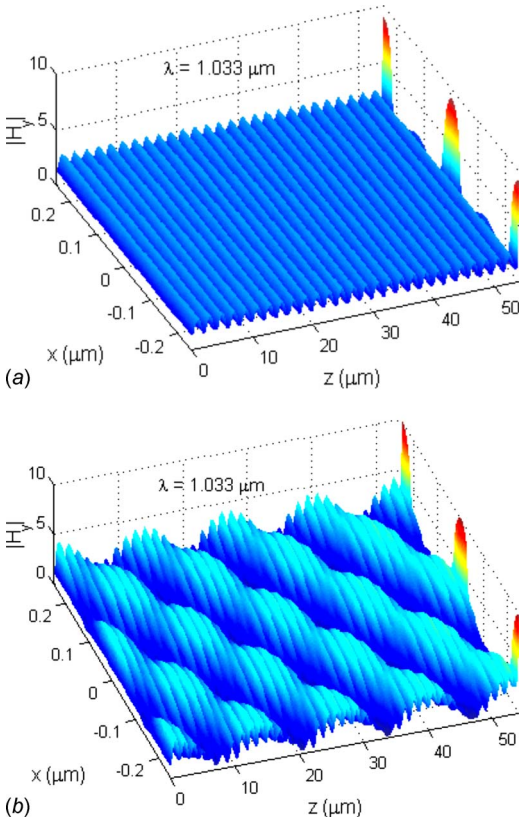

Fig. 6 Magnetic field amplitude distributions in the silicon layer of Case 3 for (*a*) $\theta=0$ deg and (*b*) $\theta=36$ deg; a very large field amplitude can be seen in the region close to the grating in both figures, but the field amplitude distribution in (*b*) is much more complicated compared with that in (*a*)

of $\lambda=1.033$ μm at normal incidence. The amplitude distribution of the magnetic field in the Si layer is plotted in Fig. 6(*a*). A very large field amplitude can be clearly seen in the vicinity of the grating, which is the signature of SP excitations. The field amplitude oscillation along the z-axis direction is due to wave interference effect in the Si layer. It should be noted that with normal incidence $\theta=0$ deg, the excited SP wave vector k_x can be obtained from Eq. (2) to be 25.13 μm^{-1} with $j=1$, which corresponds to $\omega=1.824\times10^{15}$ rad/s from the dispersion curve in Fig. 5. On the other hand, the corresponding angular frequency for $\lambda=1.033$ μm is equal to $\omega=1.825\times10^{15}$ rad/s, which is in excellent agreement with that obtained from the dispersion curve. Furthermore, since the dispersion curve is relatively flat near wavelength $\lambda=1.033$ μm and the variation of the tangential wave vector is not large when the incidence angle changes from 0 deg to 90 deg, the absorptivity is still high at oblique incidence. But the field amplitude distribution may be very different. The refractive index n of Si at $\lambda=1.033$ μm is equal to 3.56 [24], which means the wavelength in Si is $\lambda/n=0.29$ μm. Assuming β as the angle of diffraction from the grating, Eq. (2) can be rewritten as

$$\sin\beta=\frac{\sin\theta}{n}+\frac{j\lambda}{n\Lambda} \tag{3}$$

Therefore, it can be derived from Eq. (3) that at normal incidence ($\theta=0$ deg) only the zero-order ($j=0$) diffracted wave is propagating wave, and the others are all evanescent waves. However, as θ is greater than 35 deg, both the 0-order and -1-order diffracted waves are propagating, resulting in very complicated wave interactions in the Si layer. Figure 6(*b*) shows the amplitude distribution of the magnetic field (p-polarized wave) in the Si layer when the incidence angle $\theta=36$ deg. It can be seen that a very large

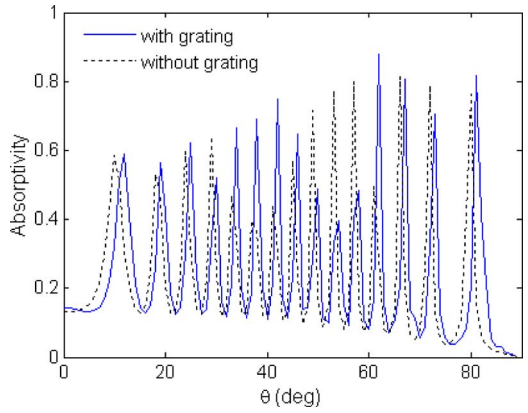

Fig. 7 Absorptivity of Case 3 (with grating) and Case 4 (without grating) for incidence of *s*-polarization versus the incidence angle θ

field amplitude still exists in the vicinity of the grating. But the field amplitude distribution in the x- and z-directions is much more complicated than that in Fig. 6(a), which is caused by the interactions of the 0-order and -1-order diffracted waves and wave interference effect in the Si layer.

We emphasize here that excitation of SPs to enhance thermal radiative absorption in the proposed structure is only possible for incidence of p-polarized wave since naturally occurred materials do not support SPs of s-polarization [9]. To clearly demonstrate this property, we also calculate the absorptivity of Cases 3 and 4 for incidence of s-polarization versus the incidence angle θ. The results plotted in Fig. 7 indicate that the absorptivity does not improve appreciably with the shallow grating; only the peaks have a slight shift toward a larger incidence angle.

3.2 Deep Grating. As the grating becomes deep, however, the situation is different compared with the case of shallow grating, i.e., Case 3. The grating depth in Case 5 is taken to be 2.5 μm while the other feature dimensions are the same as in Case 3, that is, the ratio of d_3/Λ is equal to 10. We calculate the absorptivity of Case 5 for normal incidence of s- and p-polarized plane waves as functions of the incidence wavelength λ. The results are plotted in Fig. 8 in which the corresponding result of Case 2 is also shown for comparison. It is interesting to find that the absorptivity around the Si gap edge is greatly enhanced for both s- and p-polarized waves of incidence in the presence of deep grating though the thickness of the Si layer is much smaller than that in Case 2. In order to see the absorptivity enhancement for wavelength of incidence slightly shorter than the Si gap wavelength at different incidence angles, we again fix $\lambda = 1.033$ μm and calculate the absorptivity of Cases 4 and 5 versus the incidence angle θ. The results are shown in Figs. 9(a) and 9(b) for s- and p-polarized plane waves, respectively. It can be seen that the absorptivity enhancement can be achieved at virtually any angle of incidence for both s- and p-polarizations by employing the deep grating. Though not shown here, we have checked that the absorptivity of Case 5 at $\lambda = 1.033$ μm is better than that of Case 2 for both polarizations.

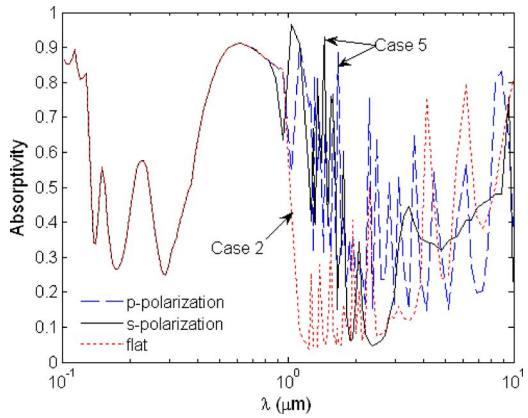

Fig. 8 Calculated absorptivity of Case 5 compared with that of Case 2 for plane wave at normal incidence

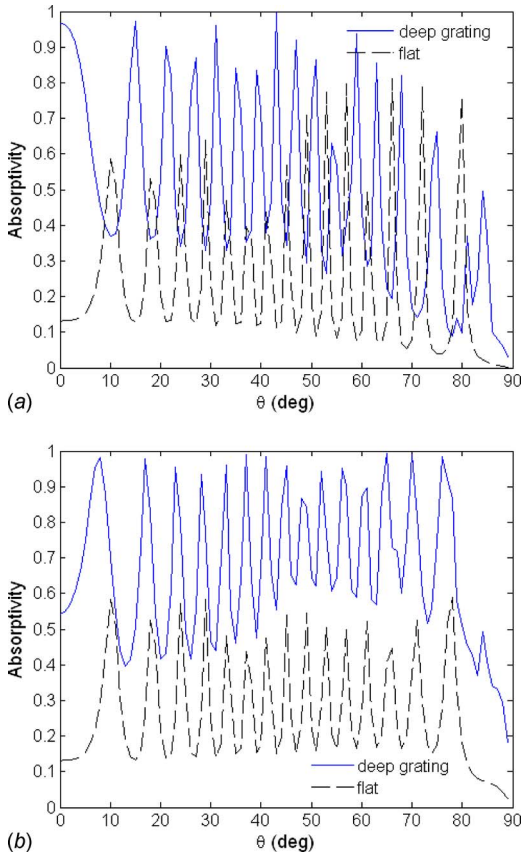

Fig. 9 Comparison of absorptivity of Case 5 to that of Case 4 at wavelength $\lambda = 1.033$ μm and various incidence angles: (*a*) *s*-polarization and (*b*) *p*-polarization

The mechanism for the selective improvement of thermal radiative absorption in Case 5 cannot be simply explained as the result of SP excitations, since the improvement is achieved for both polarizations. In order to investigate the mechanism for the absorptivity improvement, we calculate the electromagnetic fields inside the Si layer and the grating region for plane wave of $\lambda = 1.033$ μm at normal incidence. The electric field amplitude distribution in part of the Si layer and the grating region for s-polarization is shown in Fig. 10(a). It can be seen that the electric field amplitude in the grating region has distinct characteristics compared with that in the Si layer in that it is almost confined in the grooves of the grating (i.e., the space occupied by Si). Furthermore, the electric field amplitude distribution in the grating region is plotted separately in Fig. 10(b), which indicates a series of alternating peaks and valleys in the direction of the grating depth and is similar to the electric field in a microcavity. This is termed the microcavity mode excitation [7,13]. Figures 10(c) and 10(d) are the corresponding energy flux (i.e., the z-component of the Poynting vector) distributions. The energy flux decreases very slowly in the Si layer, indicating weak absorption wherein. However, as is clearly shown in Fig. 10(d), the absorption in the grooves of the gating is so strong that the energy flux is almost zero at the bottom of grooves. Similar phenomenon can be ob-

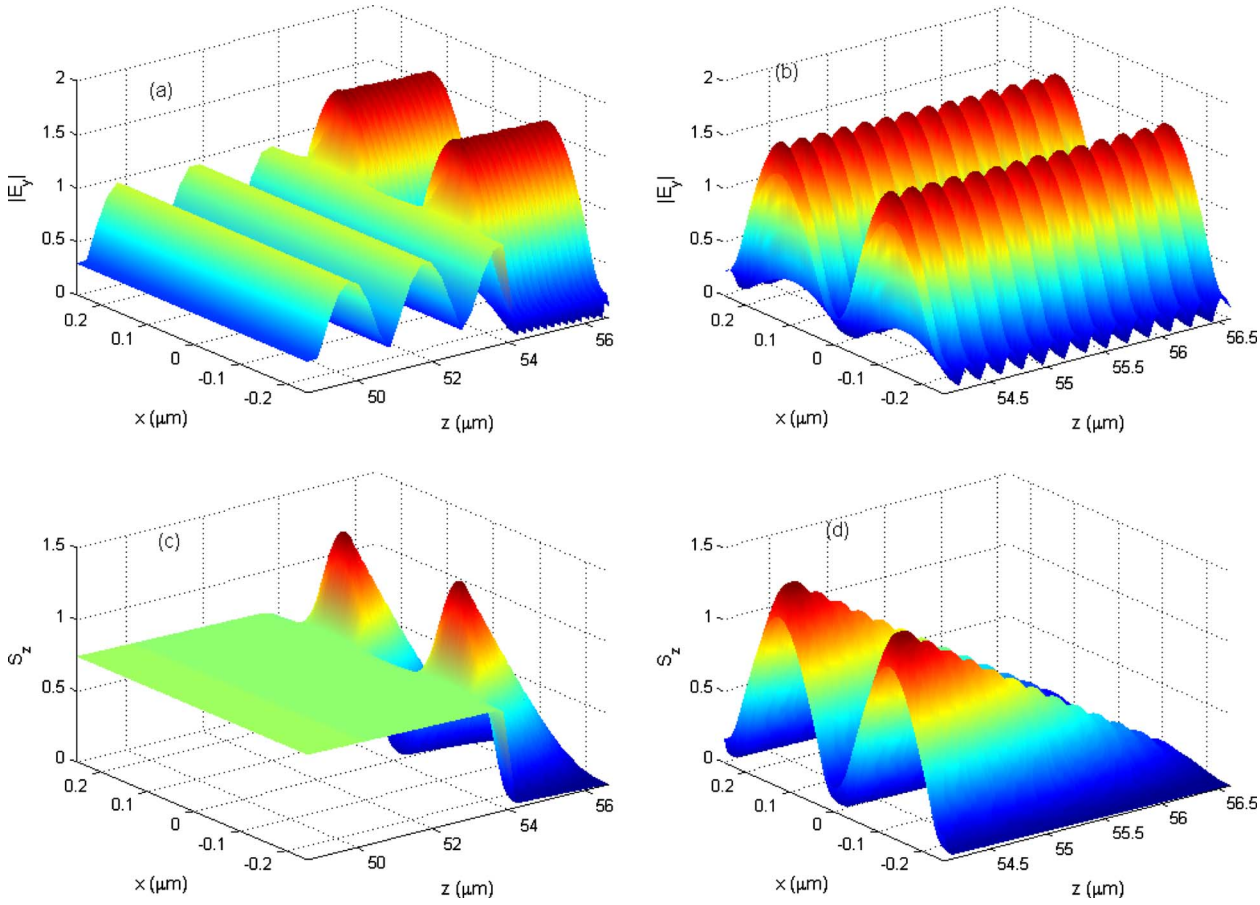

Fig. 10 Calculated (*a*) electric field amplitude distribution and (*c*) energy flux in the Si layer and the grating region of Case 5 for *s*-polarized plane wave at normal incidence. (*b*) and (*d*) show, respectively, enlarged electric field amplitude distribution and energy flux in the grating region.

served for incidence at different angles. Therefore, we conclude that the enhanced absorption in the structure is facilitated by the excitation of microcavity modes for incidence of *s*-polarization. In the case of *p*-polarization, however, extra phenomenon can be observed. The magnetic field and energy flux in the Si layer and the grating region for a *p*-polarized plane wave incident at $\theta = 8$ deg are calculated and the results are shown in Fig. 11. It can be seen from Figs. 11(*a*) and 11(*b*) that, similar to Fig. 6, a very large magnetic field amplitude is localized at the top and bottom edges of the grating, which is caused by SP excitations. On the other hand, the magnetic field distribution in the grooves of the grating also exhibits the characteristics of microcavity modes, indicating excitations of microcavity modes in the grooves. From the energy flux shown in Figs. 11(*c*) and 11(*d*), one finds that energy absorption in the grooves of the grating is greatly enhanced with the excitations of SPs and microcavity modes.

It deserves to be noted that the grooves are too shallow for microcavity modes to be excited in Case 3 discussed above, and the energy absorbed in the grooves is negligibly small. In this case, though not shown here, large absorption is in the ridges of the grating when SPs are excited. This is different from the case of deep grating. In addition, the above discussion is true for the emissivity of the proposed structure since the emissivity is equal to the absorptivity according to Kirchhoff's law. Therefore, the proposed structure can also achieve selectively enhanced emissivity by employing the grating so that it might also be used as an emitter for other purposes.

4 Conclusion

We propose a structure of semiconductor thin films combined with a one-dimensional metallic grating in this work, which can achieve selective improvement of thermal radiative absorption (also emission). We numerically demonstrate with a 2D RCWA algorithm that the proposed structure exhibits enhanced spectral absorptivity for photon energy slightly above the gap energy of the semiconductor (Si in this work) while the absorptivity in the longer wavelength region keeps at low values. The enhanced absorptivity in the case of shallow grating is attributed to excitations of SPs and is possible only for incidence of *p*-polarization. In the case of deep grating, microcavity modes (for *s*- and *p*-polarizations) and SPs (for *p*-polarization) can be excited in the grating region so that enhanced absorptivity can be achieved for both polarizations. Furthermore, the numerical results show that the enhanced absorptivity of the structure persists in a wide range of incidence angles. Because the proposed structure is similar to a conventional Si-based photovoltaic device and our results are obtained with the Si layer thickness much smaller than that in a conventional Si-based photovoltaic device, the proposed structure, especially the case with a deep grating, might help to reduce semiconductor material cost in photovoltaic energy conversion purposes. Finally, the proposed structure may be built with different semiconductors and metals for application at different wavelength regions.

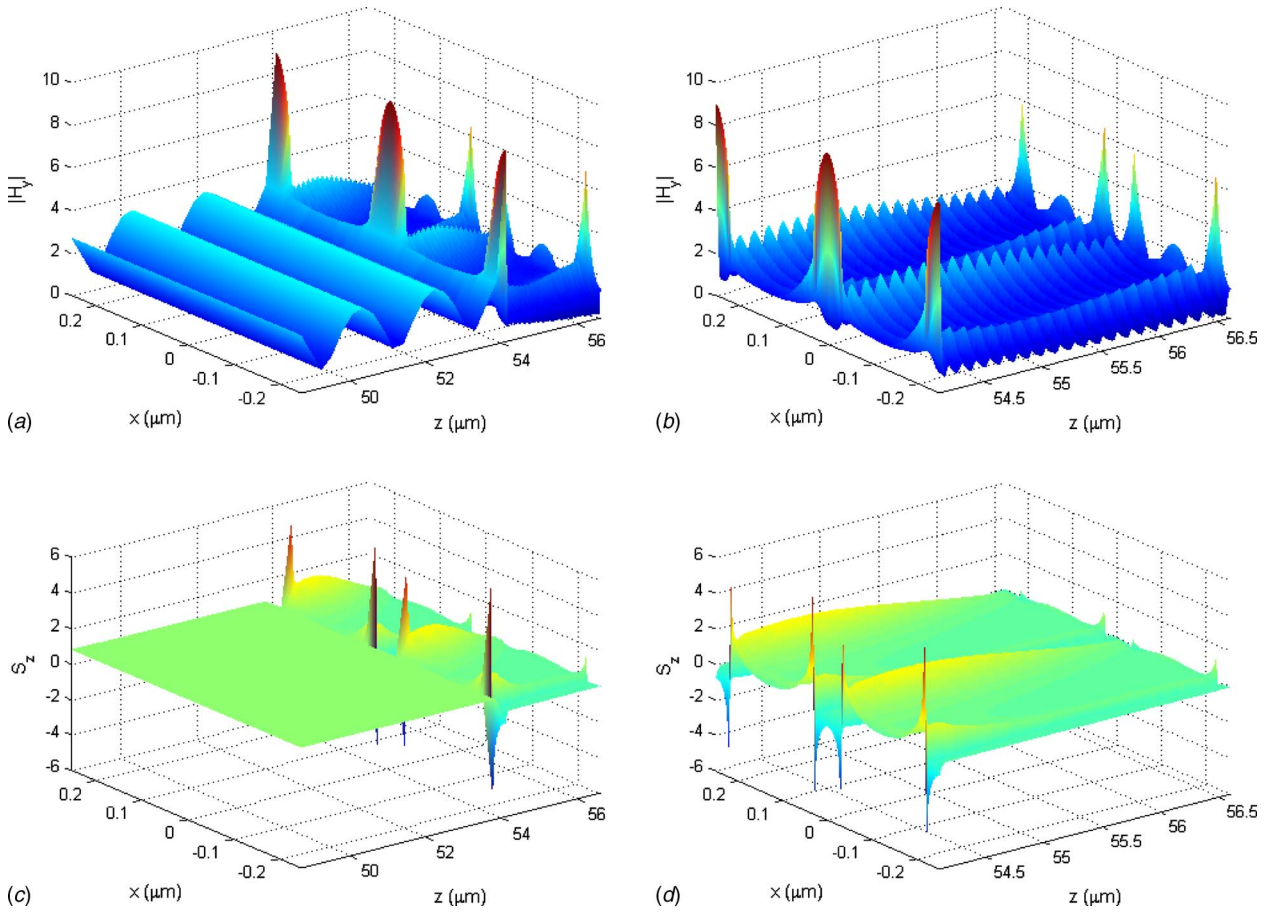

Fig. 11 Calculated (*a*) magnetic field amplitude distribution and (*c*) energy flux in the Si layer and the grating region of Case 5 for *p*-polarized plane wave at incidence angle of 8 deg. (*b*) and (*d*) show, respectively, enlarged magnetic field amplitude distribution and energy flux in the grating region.

Acknowledgment

C.J.F. thanks Professor Q.Z. Zhu and Professor Y.-B. Chen for valuable discussion on the RCWA analysis. This work is supported by the National Natural Science Foundation of China (Grant No. 50606001).

Nomenclature

d = thin film thickness (μm)
$\mathbf{E}$ = electric field vector (V/m)
$\mathbf{H}$ = magnetic field vector (A/m)
f = grating filling ratio
k = wave vector amplitude (μm^{-1})
n = refractive index

Greek Symbols

β = angle of diffraction (deg)
ε = dielectric constant
λ = electromagnetic wavelength in vacuum (μm)
Λ = grating period (μm)
θ = incidence angle (deg)
ω = angular frequency (rad/s)

Subscripts and Superscripts

j = order of diffraction/space harmonics
x = component in the x-direction
z = component in the z-direction

References

[1] Zhang, Z. M., 2007, *Nano/Microscale Heat Transfer*, McGraw-Hill, New York.
[2] Lin, S. Y., Fleming, J. G., Chow, E., Bur, J., Choi, K. K., and Goldberg, A., 2000, "Enhancement and Suppression of Thermal Emission by a Three-Dimensional Photonic Crystal," Phys. Rev. B, **62**, pp. R2243–R2246.
[3] Lin, S. Y., Fleming, J. G., and El-Kady, I., 2003, "Highly Efficient Light Emission at λ=1.5 μm by a Three-Dimensional Tungsten Photonic Crystal," Opt. Lett., **28**, pp. 1683–1685.
[4] Lin, S. Y., Moreno, J., and Fleming, J. G., 2003, "Three-Dimensional Photonic-Crystal Emitter for Thermal Photovoltaic Power Generation," Appl. Phys. Lett., **83**, pp. 380–382.
[5] Narayanaswamy, A., and Chen, G., 2004, "Thermal Emission Control With One-Dimensional Metallodielectric Photonic Crystals," Phys. Rev. B, **70**, p. 125101.
[6] Lee, B. J., and Zhang, Z. M., 2007, "Coherent Thermal Emission From Modified Periodic Multilayer Structures," ASME J. Heat Transfer, **129**, pp. 17–26.
[7] Hesketh, P. J., Zemel, J. N., and Gebhart, B., 1986, "Organ Pipe Radiant Modes of Periodic Micromachined Silicon Surfaces," Nature (London), **324**, pp. 549–551.
[8] Kreiter, M., Oster, J., Sambles, R., Herminghaus, S., Mittler-Neher, S., and Knoll, W., 1999, "Thermally Induced Emission of Light From a Metallic Diffraction Grating Mediated by Surface Plasmons," Opt. Commun., **168**, pp. 117–122.
[9] Greffet, J.-J., Carminati, R., Joulain, K., Mulet, J. P., Mainguy, S. P., and Chen, Y., 2002, "Coherent Emission of Light by Thermal Sources," Nature (London), **416**, pp. 61–64.
[10] Marquier, F., Joulain, K., Mulet, J. P., Carminati, R., and Greffet, J.-J., 2004, "Engineering Infrared Emission Properties of Silicon in the Near Field and the Far Field," Opt. Commun., **237**, pp. 379–388.
[11] Dahan, N., Niv, A., Biener, G., Kleiner, V., and Hasman, E., 2005, "Space-Variant Polarization Manipulation of a Thermal Emission by a SiO_2 Subwavelength Grating Supporting Surface Phonon-Polaritons," Appl. Phys. Lett., **86**, p. 191102.
[12] Marquier, F., Joulain, K., Mulet, J. P., Carminati, R., Greffet, J.-J., and Chen,

Y., 2004, "Coherent Spontaneous Emission of Light by Thermal Sources," Phys. Rev. B, **69**, p. 155412.
[13] Sai, H., Kanamori, Y., and Yugami, H., 2005, "Tuning of the Thermal Radiation Spectrum in the Near-Infrared Region by Metallic Surface Microstructures," J. Micromech. Microeng., **15**, pp. S243–S249.
[14] Chen, Y.-B., and Zhang, Z. M., 2007, "Design of Tungsten Complex Gratings for Thermophotovoltaic Radiators," Opt. Commun., **269**, pp. 411–417.
[15] Basu, S., Chen, Y.-B., and Zhang, Z. M., 2007, "Microscale Radiation in Thermophotovoltaic Devices—A Review," Int. J. Energy Res., **31**, pp. 689–716.
[16] Marquier, F., Laroche, M., Carminati, R., and Greffet, J.-J., 2007, "Anisotropic Polarized Emission of a Doped Silicon Lamellar Grating," ASME J. Heat Transfer, **129**, pp. 11–16.
[17] Chen, Y.-B., Zhang, Z. M., and Timans, P. J., 2007, "Radiative Properties of Patterned Wafers With Nanoscale Linewidth," ASME J. Heat Transfer, **129**, pp. 79–90.
[18] Heavens, O. S., 1965, *Optical Properties of Thin Solid Films*, Dover, New York.
[19] Fu, C. J., Zhang, Z. M., and Tanner, D. B., 2005, "Energy Transmission by Photon Tunneling in Multilayer Structures Including Negative Index Materials," ASME J. Heat Transfer, **127**, pp. 1046–1052.
[20] Chateau, N., and Hugonin, J.-P., 1994, "Algorithm for the Rigorous Coupled-Wave Analysis of Grating Diffraction," J. Opt. Soc. Am. A, **11**, pp. 1321–1331.
[21] Moharam, M. G., Grann, E. B., Pommet, D. A., and Gaylord, T. K., 1995, "Formulation for Stable and Efficient Implementation of the Rigorous Coupled-Wave Analysis of Binary Grating," J. Opt. Soc. Am. A, **12**, pp. 1068–1076.
[22] Moharam, M. G., Pommet, D. A., Grann, E. B., and Gaylord, T. K., 1995, "Stable Implementation of the Rigorous Coupled-Wave Analysis for Surface-Relief Gratings: Enhanced Transmittance Matrix Approach," J. Opt. Soc. Am. A, **12**, pp. 1077–1086.
[23] Li, L. F., 1996, "Formulation and Comparison of Two Recursive Matrix Algorithms for Modeling Layered Diffraction Gratings," J. Opt. Soc. Am. A, **13**, pp. 1024–1035.
[24] E. D. Palik, ed., 1998, *Handbook of Optical Constants of Solids*, Academic, San Diego, CA.
[25] Nelson, J., 2003, *The Physics of Solar Cells*, Imperial College Press, UK.

Nanofluids: From Vision to Reality Through Research

Stephen U. S. Choi
Department of Mechanical and Industrial Engineering,
University of Illinois at Chicago,
Chicago, IL 60607
e-mail: suschoi@uic.edu
e-mail: suschoi7@yahoo.com

Nanofluids are a new class of nanotechnology-based heat transfer fluids engineered by dispersing and stably suspending nanoparticles with typical length on the order of 1–50 nm in traditional heat transfer fluids. For the past decade, pioneering scientists and engineers have made phenomenal discoveries that a very small amount (<1 vol %) of guest nanoparticles can provide dramatic improvements in the thermal properties of the host fluids. For example, some nanofluids exhibit superior thermal properties such as anomalously high thermal conductivity at low nanoparticle concentrations, strong temperature- and size-dependent thermal conductivity, a nonlinear relationship between thermal conductivity and concentration, and a threefold increase in the critical heat flux at a small particle concentration of the order of 10 ppm. Nanofluids are of great scientific interest because these unprecedented thermal transport phenomena surpass the fundamental limits of conventional macroscopic theories of suspensions. Therefore, numerous mechanisms and models have been proposed to account for these unexpected, intriguing thermal properties of nanofluids. These discoveries also show that nanofluids technology can provide exciting new opportunities to develop nanotechnology-based coolants for a variety of innovative engineering and medical applications. As a result, the study of nanofluids has emerged as a new field of scientific research and innovative applications. Hence, the subject of nanofluids is of great interest worldwide for basic and applied research. This paper highlights recent advances in this new field of research and shows future directions in nanofluids research through which the vision of nanofluids can be turned into reality. [DOI: 10.1115/1.3056479]

Keywords: nanofluids, thermal properties, mechanisms for enhanced thermal transport, nanotechnology-based coolants

1 What Are Nanofluids?

Nanofluids are the most recent approach in more than a century of work to improve the thermal conductivity of liquids. The low thermal conductivity of conventional heat transfer fluids (HTFs) is a serious limitation in improving the performance and compactness of engineering equipment. What began with millimeter-to-micrometer sized particles in the late 19th century has become a part of the modern adventure into the new realm of the very small: the world of nanoparticles. Specifically, nanofluids are a new class of nanotechnology-based heat transfer fluids that are engineered by stably suspending a small amount (1 vol % or less) of particles, fibers, or tubes with lengths on the order of 1–50 nm in traditional HTFs. The concept and the term were proposed by Choi in the early 1990s [1].

Unlike HTFs containing microparticles, nanofluids are both stable and dilute. The key to their success as engineered HTFs is the synergy—through mechanisms still poorly understood—between the solid and liquid materials. The result is a suite of remarkable thermal properties that have inspired students, scientists, and engineers around the world to undertake the challenge of exploring the possibilities of these fascinating fluids.

2 Historical Prologue: A New Field of Scientific Research

Table 1 summarizes the 15 year history of the emergence of nanofluids as a new field of inquiry. In 1991 I began developing a microchannel heat exchanger for the Advanced Photon Source, a 7 GeV synchrotron X-ray source at Argonne National Laboratory. That was the first step on my "downscaling" journey. In that project, I noted that the heat transfer would be excellent but at the cost of high pumping power. I wanted to find a new concept that enhanced heat transfer without a large pumping power increase. In 1993, I realized from reading an article in the Argonne publication *Logos* that Argonne had a unique capability to produce nanoparticles. Starting from the vision that it could be possible to break down the century-old technical barriers of conventional suspensions by exploiting the unique properties of nanoparticles, I conceived the concept of nanofluids. Thus, nanofluids technology came into being long before "nano" became a buzzword. The initial work reported in 1995 [1] raised the remarkable possibility of doubling convection heat transfer coefficients by using nanofluids, a result that would otherwise require a tenfold increase in pumping power (Fig. 1).

For the past decade, I and colleagues have built a network with industry and universities that is beginning to bear fruit. Research institutions worldwide have established research groups or interdisciplinary nanofluids centers, and several universities have graduated Ph.Ds in this new area. Small businesses and large multinational companies are working on nanofluids for their specific applications. In short, nanofluids is a new field of scientific research that has grown enormously in the past few years (Fig. 2). Still, it is a field in its adolescence, and there are a number of issues which have not been fully investigated. Despite recent advances, such as discoveries of unexpected thermal properties, proposed new mechanisms, and unconventional models proposed, the mysteries of nanofluids are unsolved. Nanofluids is an interdisciplinary ensemble of several fields of science and technology. Much work is necessary in every area of nanofluids, from fundamentals to formulation to large-scale production.

Contributed by the Heat Transfer Division of ASME for publication in the JOURNAL OF HEAT TRANSFER. Manuscript received March 15, 2008; final manuscript received June 6, 2008; published online January 21, 2009. Review conducted by Robert D. Tzou. Paper presented at the 2008 International Conference on Micro/Nanoscale Heat Transfer (MNHT2008), Tainan, Taiwan, January 6–9, 2008.

Table 1 Timeline of emergence of nanofluids

1981	D.B. Tuckerman introduces microchannel technology.
1985	Argonne National Laboratory starts program to develop advanced fluids.
1991	Choi develops a microchannel heat exchanger for the Advanced Photon Source at Argonne.
1992	Funding cut for Argonne advanced fluids program. Choi turns attention from micro to nano.
1993	Choi learns of Argonne capability for nanoparticle production. Choi conceived the concept of nanofluids. Thus, nanofluids technology came into being 12 years after Tuckerman introduced microchannel technology. Choi submits first nanofluid proposal in May, and a second later with J.A. Eastman.
1994–1997	A third proposal in 1994 leads to 3 years of funding for the first nanofluids project, with a focus on proof of concept.
1995	Choi presents a seminal paper on the concept of nanofluids at the American Society of Mechanical Engineers Winter Annual Meeting, San Francisco, CA, Nov. 12–17 [1].
1998–present	Argonne nanofluids research funded by U.S. Department of Energy (DOE) Office of Basic Energy Sciences (BES) and Office of Transportation Technologies to work on both fundamentals and applications of nanofluids.
1999	Choi's group publishes the first SCI article on nanofluids [10].
2000	President Clinton announces the United States' National Nanotechnology Initiative (NNI) at Caltech in January 2000. Choi serves as proposal reviewer for the DOE BES and National Science Foundation, including the first Nanoscale Science, Engineering and Technology proposals under the NNI.
2001	Choi's group publishes two papers in Applied Physics Letters [5,14].
2002–2003	The nanofluid work is named a top achievement by DOE's Office of Basic Energy Sciences in both 2002 and 2003.
2007	The first single-theme conference on nanofluids was held. Nanofluids: Fundamentals and Applications, Copper Mountain, CO, Sept. 16–20, 2007, The Engineering Conferences International. The first book on nanofluids, *Nanofluids: Science and Technology*, is published by Wiley.

3 Are Nanofluids Really New?

One could say that nanofluids are an old story—centuries old, in fact. From historical evidence, medieval artisans used them, probably without knowing their own secret. The artisans of stained glass for medieval cathedrals used a suspension of gold nanoparticles to give the windows their characteristic deep red color. Later, in the 15th century, potters in Italy used metallic nanoparticles dispersed in a liquid matrix to make luster pottery [2]. These artisans exploited the color and luster effects of nanoparticles without being aware of their size.

Nanofluids are a type of colloidal dispersion, though with some significant differences from the usual colloids. Someone asked a good question recently: Colloids have been known for decades, so why has not the abnormally high thermal conductivity been discovered before? The answer lies in the differences in the particle size, phase, major physical properties, basic processing steps, and

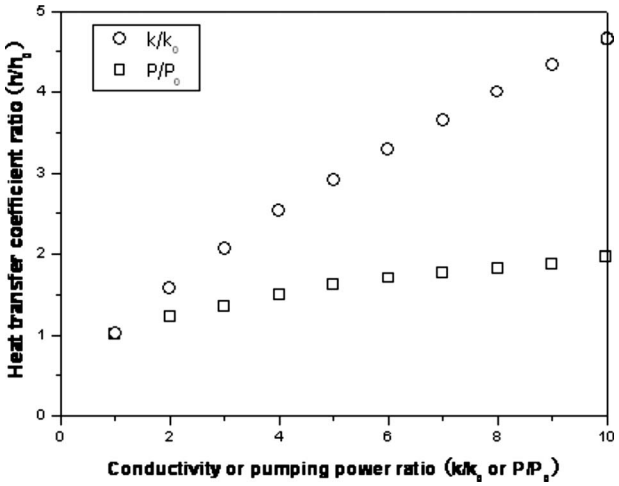

Fig. 1 Effects of thermal conductivity and pumping power on heat transfer

major applications. The particles in nanofluids are at dimensions of 1–100 nm, an order of magnitude smaller than colloid particles, which are in the size range of 10–1000 nm. With particles in this size range (particularly below 10 nm), unique and remarkable thermal phenomena are observed. A colloid in colloidal dispersions can be a solid, a liquid droplet, or a gas bubble, forming a suspension, an emulsion, or a foam, respectively. However, a nanoparticle in nanofluids is a solid, forming only a suspension. With respect to major physical properties, colloids have been studied primarily with a view to their rheological properties, but with the recent emergence of nanofluids the focus has shifted to thermal properties. In addition, the basic processing steps are different. Colloidal processing has five basic steps: powder synthesis, suspension preparation, consolidation, solvent removal, and densification at elevated temperatures. Nanofluids processing has one or two steps: powder synthesis and suspension preparation. The major applications are also different. Colloid science has led to technological advances in ceramics (films and bulk forms), coatings, paints, inks, drug delivery, and food processing. Nanofluids have recently emerged with new potential applications in cooling electronics, vehicle engines, nuclear reactors, energy efficiency enhancement, and biomedical. For these reasons, thermal engineers make a distinction between nanofluids and other composite

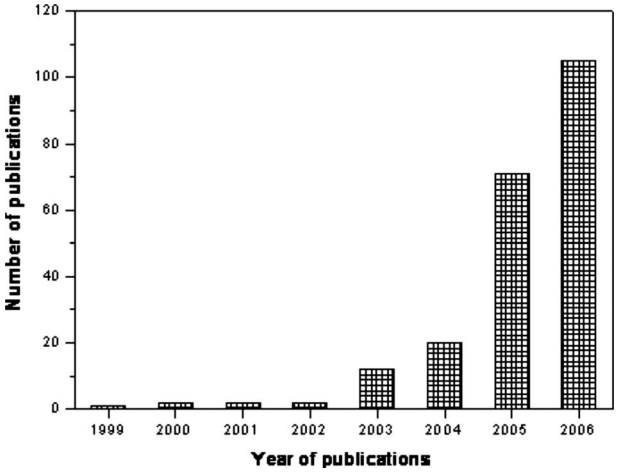

Fig. 2 Exponential increase in Science Citation Index (SCI) publications. Nanofluids now show one of the fastest growth rates in scientific papers in nanoscale science and technology.

materials (colloids and slurries). What the two fields share, however, is a need for an improved understanding of stability, as discussed later.

Nanofluids pose new challenges for thermal scientists and engineers because transport properties are "anomalously" high, surface and interface effects are dominant, and nanoparticle motion and interactions are vital. So in the end, these strange thermal properties of nanofluids do make them truly new.

4 The Cooling Challenge

One of the chief motivations in the initial development of nanofluids is the pressing need, in many industrial technologies, for better cooling systems. Heat rejection requirements are continually increasing for such devices as micro- and nanoelectromechanical systems (MEMS and NEMS), power electronics, light emitting diodes (LEDs), integrated circuits, and semiconductor lasers. For example, it is now widely accepted that the thermal management in nanosize devices plays a fundamentally critical role that controls their performance and stability. In electronics, as feature scaling and processing speeds cause the power density to double every 3 years [3], device temperatures are reaching levels that will prevent their reliable operation. At the macroscale, the problem is also acute for internal combustion engines. However, with extended-surface thermal control technologies (such as fins and microchannels) stretched to their limits, new technologies with potential to improve the thermal properties of cooling fluids are of great interest. Nanofluids offer a promising way forward to meet these cooling needs.

5 Size Matters in Nanofluids

Before diving into the specifics of the thermal properties of nanotechnology-based HTFs, it is important to understand the importance of particle size in creating practical nanofluids. First of all, particle size matters in making nanofluids stable. Dense nanoparticles can be suspended in liquids because the particles have an extremely high ratio of surface area to volume so that the interaction of the particle surface with the liquids is strong enough to overcome differences in density (i.e., the gravity effect is negligible). Furthermore, nanoparticles are charged and thus particle-particle interactions are not allowed.

Second, size matters in making nanofluids with novel properties. The very small particle size can affect transport mechanisms at the nanoscale. The properties of nanofluids are dominated not only by the characteristics of nanoscale surface/interface structures but also by nanoscale dynamics.

Finally, particle size matters in making nanofluids useful. For example, since the size of nanoparticles is similar to that of biomolecules, nanofluids can be used in biomedical applications such as drug delivery and nanofluids-based control of biological functions.

6 Making Nanofluids

Dispersing the nanoparticles uniformly and suspending them stably in the host liquid is critical in producing high-quality nanofluids. Good dispersion and stable suspension are prerequisites for the study of nanofluids properties and for applications. The key in producing extremely stable nanofluids is to disperse monosized nanoparticles before they agglomerate.

Many two-step and one-step physical and chemical processes have been developed for making nanofluids. These processes can be summarized as follows.

• *Two-step process.* In a typical two-step process, nanoparticles, nanotubes, or nanofibers are first produced as a dry powder by physical or chemical methods such as inert gas condensation and chemical vapor deposition. This step is followed by powder dispersion in the liquid. The major problem with two-step processes is aggregation of nanoparticles. Kwak and Kim [4] showed that particles, strongly aggregated before dispersion, are still in an aggregated state after dispersion in ethylene glycol and 9 h of sonication. Most researchers purchase nanoparticles in powder form and mix them with the base fluid. However, these nanofluids are not stable, although stability can be enhanced with *p*H control and/or surfactant addition. Some researchers purchase commercially available nanofluids. But these nanofluids contain impurities and nanoparticles whose size is different from vendor specifications. Although the two-step process works fairly well for oxide nanoparticles, it is not as effective for metallic nanoparticles.

• *One-step process.* In a one-step process, synthesis and dispersion of nanoparticles into the fluid take place simultaneously. For example, Argonne developed a one-step nanofluid production system in which nanoscale vapor from metallic source material can be directly dispersed into low-vapor-pressure fluids [5]. This novel one-step process was developed to overcome the van der Waals forces between the nanoparticles and produced stable suspensions of Cu nanoparticles without any dispersants. Another one-step physical process is wet grinding technology with bead mills [6]. One-step chemical methods for producing stable metallic nanofluids have been developed using a chemical reduction method [7,8]. Also, Ag-water nanofluids were produced using one-step optical laser ablation in liquid [9].

7 Characterizing Nanofluids

Good methods for characterizing nanofluids are critical to a correct understanding of their novel properties. Characterization of nanofluids includes determination of colloidal stability, particle size and size distribution, concentration, and elemental composition as well as measurements of thermophysical properties. For some applications, measurement of the electrical conductivity of nanofluids is required. Some of the most commonly used tools for characterization include transmission electron microscopy (TEM) imaging and dynamic light scattering (DLS). One of the most measured thermophysical properties is the thermal conductivity of nanofluids. Generally, three methods are used to measure the thermal conductivity of nanofluids: the transient hot wire method, the 3-ω method, and the laser flash method.

8 Novel Thermal Transport Phenomena

Several pioneering experiments with nanofluids showed that nanofluids have unprecedented thermal transport phenomena that show remarkable enhancement in thermal properties compared with the base fluid. These phenomena surpass the fundamental limits of macroscopic theories of suspensions and provide avenues to exciting new coolants for a variety of applications. The enhanced transport properties and heat transfer have been studied with varying degrees of thoroughness. Thermal conductivity has been extensively studied, as has two-phase heat transfer. Single-phase convection heat transfer is the subject of current extensive studies. Viscosity and mass diffusion have been occasionally studied.

8.1 High Thermal Conductivity at Low Concentrations. The early proof-of-concept experiments were conducted with oxide nanofluids produced by two-step methods. Although these fluids showed enhanced performance, the improvement could be predicted by existing models. Thus, oxide nanofluids failed to generate great interest. However, when copper nanofluids produced by a one-step method showed up to a 40% increase at a particle concentration of 0.3 vol % [5], researchers took notice! These results are shown in Fig. 3. This measured enhancement is anomalous, according to calculations with the weighted average model. This discovery is especially significant because the concentration is reduced by one order of magnitude at comparable enhancement compared with oxide nanofluids [10].

Liu et al. [8] synthesized Cu nanofluids using the chemical reduction method with no surfactant; in this study thermal conductivity was enhanced by up to 23.8% at 0.1 vol %. Jana et al. [11] showed that Cu-water nanofluids have a 74% increase in

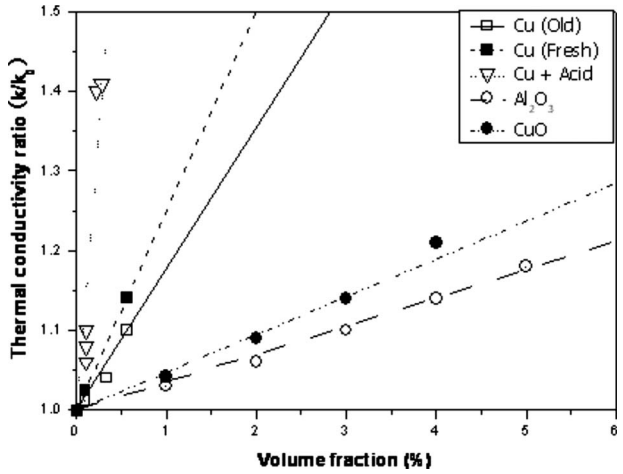

Fig. 3 The thermal conductivity of nanofluids depends on nanoparticle concentration and synthesis method

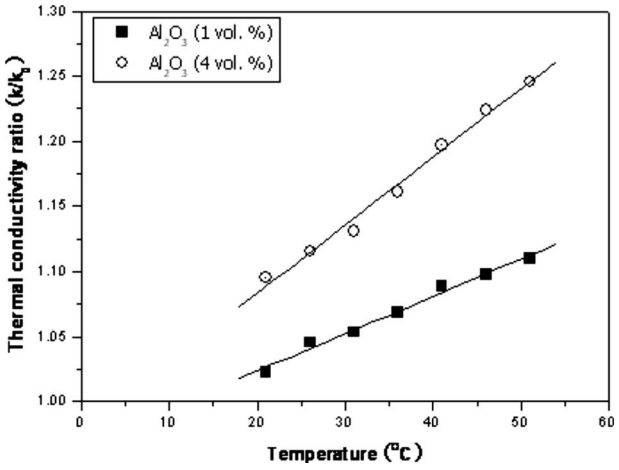

Fig. 5 The strong temperature dependence of thermal conductivity of nanofluids

conductivity at 0.3 vol %, far exceeding the previous record of 40%. However, Zhang et al. [12] and Putnam et al. [13] found no anomalous enhancement. These contradictory data highlight the need for more accurate characterization of nanofluids.

8.2 Nonlinear Increase in Conductivity With Nanoparticle Concentrations. Nanofluids have shown unexpected nonlinearity in several properties. Nonlinearity was first observed in the thermal conductivity of a fluid with carbon nanotubes (CNTs) dispersed in a matrix material, first prepared by Choi et al. [14]. CNTs, the most thermally conductive material known, yield the highest enhancement ever achieved in liquid (150% increase in conductivity of oil at ~1 vol %). The measured thermal conductivity is (1) an order of magnitude greater than predicted by existing models and (2) nonlinear with volume fraction, while predictions show a linear relationship (Fig. 4). Shaikh et al. [15] confirmed independently the largest increase in the thermal conductivity of the MWNT-PAO nanofluids Choi et al. reported six years ago [14]. This nonlinear behavior is not limited to CNTs with a high aspect ratio. Murshed et al. [16], Hong et al. [17], and Chopkar et al. [6] showed that nanofluids containing spherical nanoparticles also have strong nonlinear behavior.

8.3 Strongly Temperature-Dependent and Size-Dependent Conductivity. Das et al. [18] discovered that nanofluids have strongly temperature-dependent thermal conductivity (Fig. 5). The conductivity enhancement of Al_2O_3 or CuO nanofluids is twice to four times that of the base fluid over a small temperature range between 20°C and 50°C. Li and Peterson [19] found that the temperature effect is stronger compared with the data of Das et al. The discovery is significant because it raises an exciting possibility to develop smart nanocoolants that "sense" their thermal environment, making them a very attractive solution for preventing hot spots.

A similar trend was soon predicted [20] for nanoparticle size. Chopkar et al. [6] measured the thermal conductivity of $Al_{70}Cu_{30}$ nanofluids as a function of particle size to show strongly size-dependent conductivity. Chon et al. (in two studies) [21,22], Hong et al. [23], and Kim et al. [24] also showed size-dependent conductivity. Strong size effects in nanofluids are significant for practical applications.

These effects are so pronounced that strong temperature and size dependences of the thermal conductivity have been accepted as the criteria for classifying a given suspension as a nanofluid.

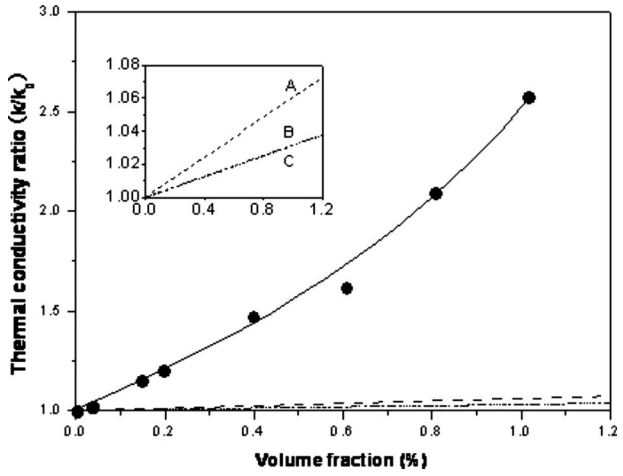

Fig. 4 Thermal behavior of first nanofluids containing carbon nanotubes

8.4 Nonlinear Rheological Properties. Das et al. [25] and Prasher et al. [26] showed linearity and Newtonian behavior; other investigators have reported nonlinearity with concentration [27–29]. A size factor may also need to be considered: Jang et al. [30] discovered that the viscosity of Al_2O_3 nanofluids not only increases nonlinearly with concentration but also depends on the size of nanoparticles relative to the tube size. Kwak and Kim [4] discovered that the zero shear viscosity of CuO-ethylene glycol nanofluids changes abruptly when particle volume fraction becomes larger than 0.2% (Fig. 6); hence this volume fraction is regarded as the dilute limit. Substantial enhancement in thermal conductivity is attainable only when particle concentration is below the dilute limit. For concentrations above the dilute limit, where both rotational and translational Brownian motions are restricted, there is no additional increase in conductivity beyond the predictions of effective medium theory. The viscosities of CuO-ethylene glycol nanofluid show that particles exist in aggregated form. It has a strong effect on both the viscosity and thermal conductivity of nanofluid.

8.5 Little or Modest Increase in Pressure Drop. Microparticle suspensions have much higher viscosity than their base fluids and require large pumping power to get the same thermal performance as their base fluids. Most nanofluids have flow properties similar to those of a single-phase base liquid and have little or modest increase in turbulent pressure drop [28,31]. This flow behavior is attractive for application engineers. An exception is the type of oxide nanofluids studied by Pak and Cho [32], which had high viscosities. To be successful in practical applications, nano-

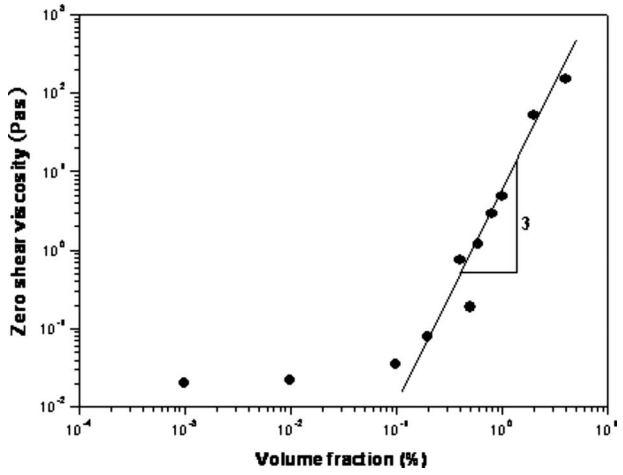

Fig. 6 Zero shear viscosity of CuO-ethylene glycol nanofluid as a function of particle volume fraction

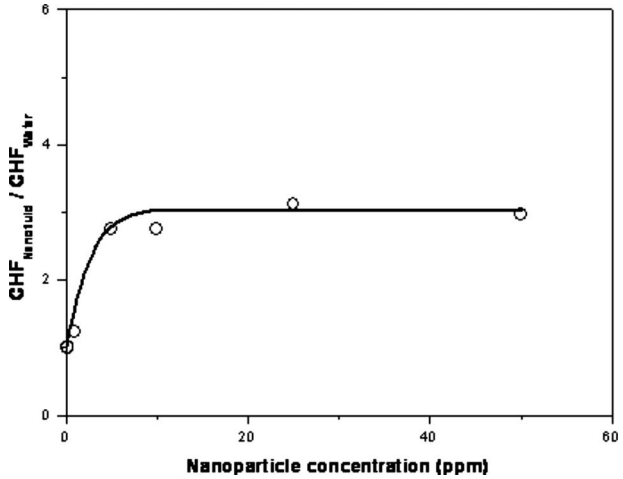

Fig. 7 Nanofluids can increase the pool boiling CHF by a factor of 3

fluids must be engineered to enhance heat transfer without much penalty in pressure drop. This requires an accurate selection of the particle shape, size, materials, and concentrations.

8.6 Single-Phase Convection Heat Transfer: Laminar Flow. Ding et al. [33] showed that the laminar heat transfer coefficient of CNT nanofluids increases rapidly at the highest values of the Reynolds number up to a 150% enhancement. They also showed that this coefficient increases with the nondimensional axial distance x/D. Faulkner et al. [34] showed that the laminar heat transfer coefficient of CNT nanofluids nearly doubled at the upper end of the Reynolds number range tested; it also decreased with increasing concentration in the concentration range from 1.1 vol % to 4.4 vol %.

8.7 Single-Phase Convection Heat Transfer: Turbulent Flow. Pak and Cho [32] studied heat transfer in oxide nanofluids and showed that, even though the Nusselt number increased, the turbulent heat transfer coefficient actually decreased by 3–12%. Xuan and Li [35] showed that the turbulent heat transfer coefficient of Cu-water nanofluids increased by ~40% at 2 vol %. The friction factor is not affected by the particle concentration for a given Reynolds number in both laminar and turbulent flow conditions. The MIT group [36] showed that, as far as single-phase convective heat transfer and pressure drop are concerned, their alumina-water and zirconia-water nanofluids behave like pure fluids, provided that the temperature and loading dependence of the thermophysical properties are measured and used in the Re, Pr, and Nu definitions.

8.8 Size-Dependent Single-Phase Convection Heat Transfer. He et al. [28] showed that the conductivity increases with decreasing particle size, but nanoparticle size (in the range of 95–210 nm) has a marginal effect on the heat transfer coefficient. However, recent work shows the opposite trend. This finding is consistent with recent results for turbulent flow by Nguyen et al. [37], who showed size-dependent heat transfer coefficients in turbulent forced convection. The discovery that nanofluids have size-dependent heat transfer coefficients in both laminar and turbulent flows is significant.

8.9 Pool Boiling Heat Transfer. Most experiments on the pool boiling of nanofluids show that nanoparticles deteriorate the boiling heat transfer coefficient [38,39]. However, Wen and Ding [40], using dilute nanofluids (<0.32 vol %), showed that alumina nanoparticles can enhance boiling heat transfer (by up to 40%). Furthermore, the enhancement increases with particle concentration. Interestingly, Nnanna [41] also showed that heat transfer in buoyancy-driven single-phase nanofluids is augmented for small volume fraction ($<2\%$) but suppressed for large volume fraction ($>2\%$). Therefore, the nanoparticle concentration is an important factor. Dilute nanofluids are desirable for both single phase, buoyancy-driven heat transfer and two-phase boiling heat transfer.

8.10 Threefold Increase in Critical Heat Flux. You et al. [42] were the first to show that nanofluids have a threefold increase in critical heat flux (CHF) over that of water at an Al_2O_3 concentration on the order of 10 ppm (Fig. 7). The enhancement of CHF was further confirmed with SiO_2 particles in water by Vassallo et al. [43]. Soon thereafter, Milanova and Kumar [44] showed that an increase in fluid pH increases the CHF by as much as 350%.

8.11 Flow Boiling CHF and Post-CHF. A group at MIT showed for the first time that nanofluids can significantly enhance the flow boiling CHF [45]. Hansson et al. [46] showed that nanofluids have a higher post-CHF (film boiling) heat transfer rate. These discoveries are significant because they could pave the way for making nuclear reactors safer. Furthermore, Liu et al. [47] showed that, in a miniature flat heat pipe, the heat transfer coefficient and CHF of CuO nanofluids increase greatly with decreasing pressure as compared with those of water.

9 Mechanisms and Models

Marvelous discoveries such as those described above show the fundamental limits of conventional models of heat conduction, convection, and boiling for solid/liquid suspensions. For example, various macroscopic models have been based on the assumption that heat conduction in suspensions occurs by diffusion. However, some nanofluids show greater thermal conductivity than predicted by Fourier heat conduction theory. Expecting that these discoveries could change the traditional understanding of energy transport in nanofluids, several investigators have searched for new concepts and mechanisms behind such dramatically enhanced properties. They have proposed both static (or structural) and dynamic mechanisms and models to account for the anomalously enhanced thermal properties. Hot debates are ongoing in the nanofluids community on the validity of proposed mechanisms and models of heat conduction in nanofluids. Some of these proposed approaches are discussed below.

9.1 Ordered Nanolayer of Liquid Molecules. Yu and Choi [48] proposed a new mechanism that, unlike in solid-solid composites, an ordered liquid layer (or nanolayer) acts as a thermal bridge between a nanoparticle and a bulk liquid. They developed a renovated Maxwell model to include the effect of this ordered

nanolayer. They further extended this structural model to nonspherical particles and renovated the Hamilton and Crosser model. However, their two static models do not predict the nonlinear behavior of nanofluid conductivity. Xue [49] was the first to model this nonlinear behavior. Although these models predict well the measured thermal conductivity data, both the thickness and conductivity of the liquid layer have to be assumed.

9.2 Percolationlike Behavior. Carbon nanotubes have extremely high aspect ratio. Foygel et al. [50] performed Monte Carlo simulations to show that the percolation regime starts at a surprisingly low critical concentration of 0.01 vol %. The new percolation theory accounts for the two features of the thermal conductivity data for CNT nanofluids, namely, the nonlinear increase with CNT concentration and the significant increase in thermal conductivity.

9.3 Interfacial Thermal Resistance. Experiments show that adding 1 vol % of CNTs to synthetic oil [14] or polymer epoxy [51] can increase the conductivity of the matrix material more than twofold. Huxtable et al. [52] used a pump-probe method to measure heat transfer across the particle-liquid interface. They showed that the exceptionally large interface thermal resistance, i.e., the Kapitza resistance, can significantly reduce the thermal conductivity of nanofluids. Nan et al. [53] developed a model for thermal conductivity enhancement in CNT composites by incorporating the Kapitza resistance in the effective medium approximation.

9.4 Brownian Motion of Nanoparticles. The static models, such as the liquid layering model and the interface thermal resistance model, cannot explain the strong temperature dependence of the conductivities of nanofluids. Effective medium theory models, such as the Maxwell–Garnett, Bruggeman, Hamilton–Crosser, and Jeffrey and Davis models, do not take particle motion into consideration. A nanofluid is a dynamic system because the nanoparticles are in motion even if the fluid is stationary. Several dynamic models have been developed in combination with static models.

Xuan et al. [31] developed a dynamic model that takes into account the effects of Brownian motion of nanoparticles and fractals. They showed, probably for the first time, that the conductivity of nanofluids increases with the square root of fluid temperature. However, their model did not predict the linear increase of thermal conductivity with temperature, as obtained by Das et al. [18].

9.5 Nanoconvection. All the static and dynamic models developed with conduction-based mechanisms still fail to predict the magnitude and trends of the experimental data. Nanoparticle diffusion, which is orders of magnitude slower than heat diffusion, has little effect on the k of nanofluids. Jang and Choi [20] proposed the concept of nanoconvection induced by Brownian motion of nanoparticles assuming that energy transport in nanofluids is by nanoscale flow of fluids around Brownian nanoparticles. They developed a theoretical model that takes into account nanoconvection. Though the new model makes simplifying assumptions, it generates useful results for interpreting experiments (Fig. 8). Whereas Maxwell-type theories fail to capture the temperature-dependent conductivity, calculations with the new model agree with temperature-dependent data and predict size-dependent conductivity.

Xuan et al. [54] developed, based on the Green–Kubo theorem, a conductivity model consisting of the static and dynamic terms. This model accounts for the Kapitza resistance and nanoconvection, nanoparticle size and concentration, and fluid temperature. Their model shows that the contribution of the nanoconvection effect increases rapidly when the nanoparticle size is smaller than 30 nm. Several other studies have considered various aspects of nanoconvection. Prasher et al. [55] extended the concept of nanoconvection by considering for the first time the effect of multiparticle convection. Koo and Kleinstreuer [56] developed a theoretical model that takes into account the effects of fluids dragged by nanoparticles and mixing. Patel et al. [57] developed a microconvection model for evaluation of conductivity of a nanofluid by taking into account nanoconvection induced by Brownian nanoparticles and the specific surface area of nanoparticles. Finally, Ren et al. [58] considered kinetic-theory-based microconvection and liquid layering in addition to liquid and particle conduction.

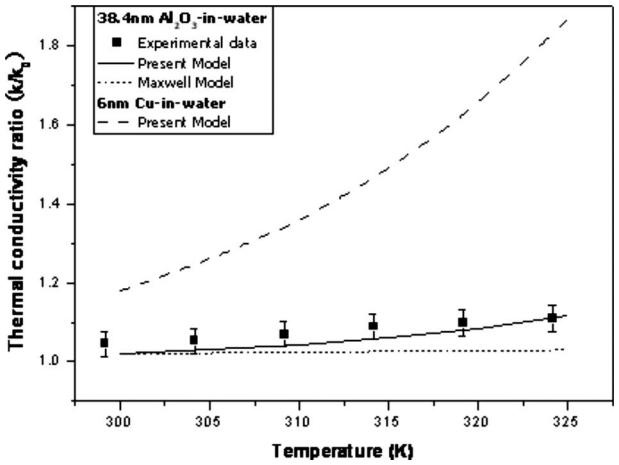

Fig. 8 Experimental data from Das et al. [18] and predictions from Jang and Choi's [20] new model based on nanoconvection induced by Brownian motion

Several other groups have questioned the importance and mechanisms of nanoconvection. For example, Evans et al. [59] and Vladkov and Barrat [60] conducted molecular dynamics simulations (MDS) of model nanofluids to show that the effect of nanoconvection is negligible. However, Sarkar and Selvam [61] also used MDS to show that the conductivity enhancement is mostly due to the increased movement of liquid atoms in the presence of nanoparticle. Most recently, Eapen et al. [62] measured the conductivity of silica and Teflon suspensions to show that microconvection does not influence the conductivity of their nanofluids. The debate over the role of Brownian nanoparticles in the enhanced conductivity of nanofluids will continue.

9.6 Surface Charge Model. Lee et al. [63] presented the surface charge state as a new key parameter for the anomalous enhancement of the conductivity of nanofluids. They showed that the effective thermal conductivity increases by a factor of 3 as pH decreases from 8 to 3.

9.7 Molecular-Level Mechanisms of Enhanced Conductivity. Eapen et al. [64] considered three fluctuation modes in the microscopic heat flux and showed a molecular-level mechanism for enhanced conductivity of nanofluids.

A number of mechanisms and models of enhanced conductivity have been proposed, but none has gained universal support.

9.8 Heat Transfer Models. Models of heat transfer in nanofluids come in three varieties at present.

- *Homogeneous flow.* Choi [1] assumed that traditional heat transfer correlations can be used for nanofluids, provided that their enhanced thermophysical properties are used.
- *Dispersion.* Xuan and Roetzel [65] were the first to employ the concept of thermal dispersion, assuming that velocity slip induces a velocity and temperature perturbation.
- *Particle migration.* Ding and Wen [66] were the first to use the concept of particle migration in nanofluids and developed a theoretical model to predict particle migration in pressure-driven laminar pipe flows of relatively dilute nanofluids.

- *Brownian diffusion and two-component nonhomogeneous equilibrium.* Buongiorno [67] was the first to show that Brownian diffusion and thermophoresis are important slip mechanisms in nanofluids. Based on this finding, he developed a two-component nonhomogeneous equilibrium model for mass, momentum, and heat transport in nanofluids. He explained that the abnormal heat transfer behavior of nanofluids is due to a significant decrease in viscosity within the boundary layer [67].

9.9 Mechanisms and Models of Viscosity. Ding and Wen [66] developed a theoretical model to examine particle migration in pressure-driven laminar pipe flows of nanofluids. The model considers particle migration due to spatial gradients in viscosity and shear rate and Brownian motion. The results show that particle migration can result in nonuniform particle concentration, thermal conductivity, and viscosity. However, nanofluids have Peclet numbers <10 (because $\mathrm{Pe} \sim dp^3$) and thus concentration and viscosity distributions are uniform over the pipe cross section. Most recently, Jang et al. [30] showed that, when nanoparticles have a nonzero slip velocity, the viscosity of Al_2O_3 nanofluids flowing through micro- and minitubes increases nonlinearly with concentration even in the range of 0.02–0.3 vol % and depends strongly on the nanoparticle diameter to the tube diameter ratio.

9.10 Pool Boiling Heat Transfer Mechanisms. Narayan et al. [68] observed that with a rough heater (Ra=524 nm), heat transfer is significantly enhanced by up to ~70% at 0.5 wt % and with a smooth heater (Ra=48 nm), heat transfer is significantly deteriorated by up to ~45% at 2 wt %. Furthermore, they observed that a new parameter, which is the ratio of average size of the particle to the average roughness value of the heater, can explain the reported controversy in the pool boiling behavior of nanofluids.

9.11 Mechanisms of Enhanced CHF. Because the transport and thermodynamic properties of very dilute nanofluids are nearly the same as those of a base fluid, the classic theory of CHF would predict no CHF enhancement. Bang and Chang [39] suggested that the enhanced CHF might be due to the surface coating effect by the deposition of nanoparticles. A MIT group demonstrated several important results that may help explain the unexpected CHF for nanofluids [69]. Upon boiling of nanofluids, nanoparticles precipitate on the heater surface and form a porous layer. The presence of the nanoparticle layer significantly improves the surface wettability. The change in the contact angle from ~70 deg to ~20 deg and high surface wettability can plausibly explain the CHF enhancement in nanofluids. A realistic model of CHF in nanofluids may thus be possible.

Kim et al. [70] also showed that a porous layer of nanoparticles significantly improves the surface wettability. However, they are the first to show that the effect of wettability alone cannot explain the additional increases in the CHF. Focusing on the role of capillarity in the CHF behavior of nanofluids they showed that, due to capillarity, the liquid rises on nanoparticle-coated surfaces. Kim and Kim [71] used capillarity to characterize a completely wetted nanoparticle-coated surface. They showed that the estimated heat flux gain due to capillary liquid supply along the porous layer was of the same order of magnitude as that due to the wettability enhancement. They concluded that the significant CHF enhancement of nanofluids during pool boiling is a consequence of not only increased surface wettability but also improved capillarity due to the surface deposition of nanoparticles.

10 Applications of Nanofluids

Nanofluids can be used in a wide range of applications wherever improved heat transfer or efficient heat dissipation is required. Major examples include electronics, automotive, and nuclear applications. The following examples give a picture of the versatility of this technology.

Nanofluids are a promising candidate for microelectronics cooling. Tsai et al. [72] used gold nanofluids as the working fluid for meshed circular heat pipe. Their results show that, at the same charge volume, there is a significant reduction (by as much as 37%) in the thermal resistance of the heat pipe with a nanofluid as compared with de-ionized water.

Nanofluids have a plethora of potential applications in many automotive parts and functions, including engine coolant, automatic transmission fluid, power steering fluid, fan clutches, engine oil, power electronics, brake fluid, gear lubrication, and greases. This research is being conducted at top research universities in conjunction with large multinational companies. The first commercial steps of nanofluids technology have been made in the automobile arena. Tzeng et al. [73] are the first to apply nanofluids in cooling a real-world automatic power transmission system. The results show that CuO nanofluids have the lowest temperature distribution and accordingly the best heat transfer performance.

Nuclear applications of nanofluids appear to be very promising—perhaps the most promising of currently envisaged uses. Nanofluids could be used in primary systems, emergency safety systems, and severe accident management systems, with resulting benefits such as power uprates in commercial pressurized water reactors (PWRs) and enhanced safety margins during design-basis events and severe accidents. In general, nanofluids could enhance economics and safety of nuclear reactors [74,75]. They also have great potential as a coolant for safer and smaller nuclear generators in the future.

Beyond these somewhat concrete possibilities lies a broad expanse of potential applications, wide open to the engineering imagination. A few ideas to provoke further thought include cooling and lubrication of drill bits for deep-hole drilling [76], drug delivery and nanofluids-based control of biological functions (because the size of nanoparticles is similar to that of biomolecules), process intensification in the chemical and metallurgical industry, efficiency optimization in the heating, ventilation and air conditioning (HVAC) industry, production of nanostructured materials, engineering of complex fluids, lubricant-based nanofluids (nanolubricants), and enhanced quenching performance.

11 Future Directions

11.1 Future Basic Research. The fundamental issue for basic research is that a general framework for nanofluid properties and heat transfer does not, as yet, exist. An important focus for future research should be determining the key energy transport mechanisms in nanofluids. The validity of most proposed still remains a subject of debate. Initial work should consider two distinct aspects: static mechanisms and dynamic mechanisms.

To understand the fundamental physics of energy transport in nanofluids, systematic experiments are needed, as are tools with a high spatial and temporal resolution. Another need is for comprehensive thermal conductivity models that consider transport mechanisms at multiscale levels. Theoretical predictions should be evaluated in terms of agreement with experiments regarding concentration, particle size, and temperature dependence.

11.2 Future Applied Research. Equally interesting challenges await the applied researcher who chooses to pursue questions related to nanofluids. The following are three of the most pressing issues.

- *Volume production.* Production of stable nanofluids with nonagglomerated nanoparticles is currently limited to laboratory-scale research. Future work should focus on identifying methods that provide volume production for commercial applications.
- *Stability.* Long-term physical and chemical stability of nanofluids is an important practical issue for commercialization of nanofluids.
- *Environmental issues.* Nanofluids offer compelling solutions for energy efficiency, but we also face public concerns about

their safety, both in production and in use. Nanofluids engineers would be prudent to pursue green designs by choosing nontoxic or biodegradable nanoparticles.

In summary, low-cost, high-volume production of stable green nanofluids is one of the most challenging directions for future applied research.

12 Conclusions

Nanofluids are an exciting new class of nanotechnology-based heat transfer fluids. Scientists and engineers are being challenged to discover the many unexpected thermal properties of these fluids, to propose new mechanisms and unconventional models to explain their behavior, and to explore innovative applications made possible by the fascinating features of nanofluids. In short, nanofluids have emerged as a new field of scientific research, especially in thermal sciences and engineering.

Despite recent advances, the mysteries of nanofluids are unsolved. Much more work is necessary in every area, from fundamentals to formulation to large-scale production. When the mysteries of nanofluids are solved we could imagine nanofluids designed to have novel properties. Consider what possibilities could open up if conductivity increased two- to threefold, effective specific heat increased two- to threefold, CHF increased three- to fourfold, and heat transfer coefficients increased two- to threefold. These are the kinds of visionary possibilities that can guide future research. However, the novel character of nanofluids demands not only new science but also a new approach to science, one that is uniquely interdisciplinary and collaborative. This point is especially important in considering the training of young scientists. To a greater degree than in other fields, the options for future research in this field will depend on the background gained by today's students. Perhaps the only path to master this field is a multidisciplinary one that includes both basic science and engineering knowledge.

Above all, the study of nanofluids is an interdisciplinary field that challenges researchers to consider the fundamentals of nanofluids from a more integrated perspective. The path to turn this new vision into reality demands what I call "iTEN R"—a special confluence of imagination and theoretical, experimental, and numerical research.

Acknowledgment

This paper is based on the works of pioneering scientists and engineers who have achieved important milestones in the research and development of nanofluids, including the novel concept, production methods, exceptional discoveries of unprecedented thermal transport phenomena, new mechanisms behind the enhanced thermal properties, unconventional models, and innovative potential applications of nanofluids.

I gratefully acknowledge more than a decade of support from the U.S. Department of Energy (DOE), beginning with the first nanofluids project in 1994. Special thanks to Dr. Bob Price of DOE's Office of Basic Energy Sciences and the late Dr. Sid Diamond of DOE's Office of Transportation Technologies, who shared my vision of nanofluids when few people realized the potential of nanofluids and provided strong encouragement and continuous financial support for basic and applied research in nanofluids.

Isaac Newton said, "If I have seen further than other men it is because I have stood on the shoulders of giants." Those pioneering scientists and engineers and prominent program managers acknowledged above are my giants.

Nomenclature

a = nanoparticle diameter (m)
D = tube diameter (m)
h = heat transfer coefficient (W/m^2 K)
k = thermal conductivity (W/m K)
P/P_o = pumping power ratio
T = temperature (C or K)

Greek Symbol

μ = viscosity (Pa s)

Subscript

o = base fluid

References

[1] Choi, S. U. S., 1995, "Enhancing Thermal Conductivity of Fluids With Nanoparticles," *Developments and Applications of Non-Newtonian Flows*, D. A. Siginer and H. P. Wang, eds., ASME, New York, FED-231/MD-66, pp. 99–105.
[2] Padovani, S., Sada, C., Mazzoldi, P., Brunetti, B., Borgia, I., Sgamellotti, A., Giulivi, A., D'Acapito, F., and Battaglin, G., 2003, "Copper in Glazes of Renaissance Luster Pottery: Nanoparticles, Ions, and Local Environment," J. Appl. Phys., **93**(12), pp. 10058–10063.
[3] Borkar, S., 1999, "Design Challenges of Technology Scaling," IEEE MICRO, **19**(4), pp. 23–29.
[4] Kwak, K., and Kim, C., 2005, "Viscosity and Thermal Conductivity of Copper Oxide Nanofluid Dispersed in Ethylene Glycol," Korea-Aust. Rheol. J., **17**(2), pp. 35–40.
[5] Eastman, J. A., Choi, S. U. S., Li, S., Yu, W., and Thomson, L. J., 2001, "Anomalously Increased Effective Thermal Conductivities of Ethylene Glycol Based Nanofluids Containing Copper Nanoparticles," Appl. Phys. Lett., **78**, pp. 718–720.
[6] Chopkar, M., Das, P. K., and Manna, I., 2006, "Synthesis and Characterization of Nanofluid for Advanced Heat Transfer Applications," Scr. Mater., **55**, pp. 549–552.
[7] Zhu, H., Zhang, C., Liu, S., and Tang, Y., 2006, "Effects of Nanoparticle Clustering and Alignment on Thermal Conductivities of Fe_3O_4 Aqueous Nanofluids," Appl. Phys. Lett., **89**, p. 023123.
[8] Liu, M. S., Lin, M. C. C., Tsai, C. Y., and Wang, C. C., 2006, "Enhancement of Thermal Conductivity With Cu for Nanofluids Using Chemical Reduction Method," Int. J. Heat Mass Transfer, **49**, pp. 3028–3033.
[9] Phuoc, T. X., Soong, Y., and Chyu, M. K., 2007, "Synthesis of Ag-Deionized Water Nanofluids Using Multi-Beam Laser Ablation in Liquids," Opt. Lasers Eng., **45**, pp. 1099–1106.
[10] Lee, S., Choi, S. U. S., Li, S., and Eastman, J. A., 1999, "Measuring Thermal Conductivity of Fluids Containing Oxide Nanoparticles," ASME J. Heat Transfer, **121**, pp. 280–289.
[11] Jana, S., Salehi-Khojin, A., and Zhong, W.-H., 2007, "Enhancement of Fluid Thermal Conductivity by the Addition of Single and Hybrid Nano-Additives," Thermochim. Acta, **462**, pp. 45–55.
[12] Zhang, X., Gu, H., and Fujii, M., 2006, "Effective Thermal Conductivity and Thermal Diffusivity of Nanofluids Containing Spherical and Cylindrical Nanoparticles," J. Appl. Phys., **100**(4), p. 044325.
[13] Putnam, S. A., Cahill, D. G., Braun, P. V., Ge, Z., and Shimmin, R. G., 2006, "Thermal Conductivity of Nanoparticle Suspensions," J. Appl. Phys., **99**, p. 084308.
[14] Choi, S. U. S., Zhang, Z. G., Yu, W., Lockwood, F. E., and Grulke, E. A., 2001, "Anomalous Thermal Conductivity Enhancement in Nanotube Suspensions," Appl. Phys. Lett., **79**, pp. 2252–2254.
[15] Shaikh, S., Lafdi, K., and Ponnappan, R., 2007, "Thermal Conductivity Improvement in Carbon Nanoparticle Doped PAO Oil: An Experimental Study," J. Appl. Phys., **101**, p. 064302.
[16] Murshed, S. M. S., Leong, K. C., and Yang, C., 2005, "Enhanced Thermal Conductivity of TiO2—Water Based Nanofluids," Int. J. Therm. Sci., **44**, pp. 367–373.
[17] Hong, T. K., Yang, H. S., and Choi, C. J., 2005, "Study of the Enhanced Thermal Conductivity of Fe Nanofluids," J. Appl. Phys., **97**, p. 064311.
[18] Das, S. K., Putra, N., Thiesen, P., and Roetzel, W., 2003, "Temperature Dependence of Thermal Conductivity Enhancement for Nanofluids," ASME J. Heat Transfer, **125**, pp. 567–574.
[19] Li, C. H., and Peterson, G. P., 2006, "Experimental Investigation of Temperature and Volume Fraction Variations on the Effective Thermal Conductivity of Nanoparticle Suspensions (Nanofluids)," J. Appl. Phys., **99**, p. 084314.
[20] Jang, S. P., and Choi, S. U. S., 2004, "Role of Brownian Motion in the Enhanced Thermal Conductivity of Nanofluids," Appl. Phys. Lett., **84**, pp. 4316–4318.
[21] Chon, C. H., Kihm, K. D., Lee, S. P., and Choi, S. U. S., 2005, "Empirical Correlation Finding the Role of Temperature and Particle Size for Nanofluid (Al_2O_3) Thermal Conductivity Enhancement," Appl. Phys. Lett., **87**, p. 153107.
[22] Chon, C. H., and Kihm, K. D., 2005, "Thermal Conductivity Enhancement of Nanofluids by Brownian Motion," ASME J. Heat Transfer, **127**, p. 810.
[23] Hong, K. S., Hong, T. K., and Yang, H. S., 2006, "Thermal Conductivity of Fe Nanofluids Depending on the Cluster Size of Nanoparticles," Appl. Phys. Lett., **88**, p. 031901.
[24] Kim, S. H., Choi, S. R., and Kim, D., 2007, "Thermal Conductivity of Metal-Oxide Nanofluids: Particle Size Dependence and Effect of Laser Irradiation," ASME J. Heat Transfer, **129**, pp. 298–307.

[25] Das, S. K., Putra, N., and Roetzel, W., 2003, "Pool Boiling Characteristics of Nano-Fluids," Int. J. Heat Mass Transfer, **46**, pp. 851–862.
[26] Prasher, R., Song, D., Wang, J., and Phelan, P., 2006, "Measurements of Nanofluid Viscosity and Its Implications for Thermal Applications," Appl. Phys. Lett., **89**, p. 133108.
[27] Wang, X., Xu, X., and Choi, U. S., 1999, "Thermal Conductivity of Nanoparticle-Fluid Mixture," J. Thermophys. Heat Transfer, **13**, pp. 474–480.
[28] He, Y., Jin, Y., Chen, H., Ding, Y., Cang, D., and Lu, H., 2007, "Heat Transfer and Flow Behavior of Aqueous Suspensions of TiO2 Nanoparticles (Nanofluids) Flowing Upward Through a Vertical Pipe," Int. J. Heat Mass Transfer, **50**, pp. 2272–2281.
[29] Murshed, S. M. S., Leong, K. C., and Yang, C., 2008, "Investigations of Thermal Conductivity and Viscosity of Nanofluids," Int. J. Therm. Sci., **47**, pp. 560–568.
[30] Jang, S. P., Lee, J. H., Hwang, K. S., and Choi, S. U. S., 2007, "Particle Concentration and Tube Size Dependence of Viscosities of Al_2O_3-Water Nanofluids Flowing Through Micro- and Minitubes," Appl. Phys. Lett., **91**, p. 243112.
[31] Xuan, Y., Li, Q., and Hu, W., 2003, "Aggregation Structure and Thermal Conductivity of Nanofluids," AIChE J., **49**, pp. 1038–1043.
[32] Pak, B., and Cho, Y. I., 1998, "Hydrodynamic and Heat Transfer Study of Dispersed Fluids With Submicron Metallic Oxide Particle," Exp. Heat Transfer, **11**, pp. 151–170.
[33] Ding, Y., Alias, H., Wen, D., and Williams, R. A., 2006, "Heat Transfer of Aqueous Suspensions of Carbon Nanotubes (CNT Nanofluids)," Int. J. Heat Mass Transfer, **49**, pp. 240–250.
[34] Faulkner, D. J., Rector, D. R., Davidson, J. J., and Shekarriz, R., 2004, "Enhanced Heat Transfer Through the Use of Nanofluids in Forced Convection," ASME Paper No. IMECE2004-62147.
[35] Xuan, Y., and Li, Q., 2003, "Investigation on Convective Heat Transfer and Flow Features of Nanofluids," ASME J. Heat Transfer, **125**, pp. 151–155.
[36] Williams, W. C., Buongiorno, J., and Hu, L. W., 2008, "Experimental Investigation of Turbulent Convective Heat Transfer and Pressure Loss of Alumina/Water and Zirconia/Water Nanoparticle Colloids (Nanofluids) in Horizontal Tubes," ASME J. Heat Transfer, **130**, p. 042412.
[37] Nguyen, C. T., Roy, G., Gauthier, C., and Galanis, N., 2007, "Heat Transfer Enhancement Using Al_2O_3-Water Nanofluid for an Electronic Liquid Cooling System," Appl. Therm. Eng., **27**, pp. 1501–1506.
[38] Das, S. K., Putra, N., and Roetzel, W., 2003, "Pool Boiling of Nano-Fluids on Horizontal Narrow Tubes," Int. J. Multiphase Flow, **29**, pp. 1237–1247.
[39] Bang, I. C., and Chang, S. H., 2005, "Boiling Heat Transfer Performance and Phenomena of Al2O3-Water Nano-Fluids From a Plain Surface in a Pool," Int. J. Heat Mass Transfer, **48**, pp. 2407–2419.
[40] Wen, D., and Ding, Y., 2005, "Experimental Investigation Into the Pool Boiling Heat Transfer of Aqueous Based Alumina Nanofluids," J. Nanopart. Res., **7**, pp. 265–274.
[41] Nnanna, A. G. A., 2007, "Experimental Model of Temperature-Driven Nanofluids," ASME J. Heat Transfer, **129**, pp. 697–704.
[42] You, S. M., Kim, J. H., and Kim, K. M., 2003, "Effect of Nanoparticles on Critical Heat Flux of Water in Pool Boiling of Heat Transfer," Appl. Phys. Lett., **83**, pp. 3374–3376.
[43] Vassallo, P., Kumar, R., and D'Amico, S., 2004, "Pool Boiling Heat Transfer Experiments in Silica-Water Nano-Fluids," Int. J. Heat Mass Transfer, **47**, pp. 407–411.
[44] Milanova, D., and Kumar, R., 2005, "Role of Ions in Pool Boiling Heat Transfer of Pure and Silica Nanofluids," Appl. Phys. Lett., **87**, p. 233107.
[45] Kim, S. J., McKrell, T., Buongiorno, J., and Hu, L. W., 2008, "Alumina Nanoparticles Enhance the Flow Critical Heat Flux of Water at Low Pressure," ASME J. Heat Transfer, **130**, p. 044501.
[46] Hansson, R., Park, H. S., Shiferaw, D., and Sehgal, B. R., 2005, "Spontaneous Steam Explosions in Subcooled Al_2O_3 Nanofluids," The 11th International Topical Meeting on Nuclear Reactor Thermal-Hydraulics (NURETH-11), Avignon, France, Oct. 2–6, Paper No. 464.
[47] Liu, Z. H., Xiong, J. G., and Bao, R., 2007, "Boiling Heat Transfer Characteristics of Nanofluids in a Flat Heat Pipe Evaporator With Micro-Grooved Heating Surface," Int. J. Multiphase Flow, **33**, pp. 1284–1295.
[48] Yu, W., and Choi, S. U. S., 2003, "The Role of Interfacial Layers in the Enhanced Thermal Conductivity of Nanofluids: A Renovated Maxwell Model," J. Nanopart. Res., **5**, pp. 167–171.
[49] Xue, Q.-Z., 2003, "Model for Effective Thermal Conductivity of Nanofluids," Phys. Lett. A, **307**, pp. 313–317.
[50] Foygel, M., Morris, R. D., Anez, D., French, S., and Sobolev, V. L., 2005, "Theoretical and Computational Studies of Carbon Nanotube Composites and Suspensions: Electrical and Thermal Conductivity," Phys. Rev. B, **71**, p. 104201.
[51] Biercuk, B. J., Llaguno, M. C., Radosavljevic, M., Hyun, J. K., and Johnson, A. T., 2002, "Carbon Nanotube Composites for Thermal Management," Appl. Phys. Lett., **80**, pp. 2767–2772.
[52] Huxtable, S. T., Cahill, D. G., Shenogin, S., Xue, L., Ozisik, R., Barone, P., Usrey, M., Strano, M. S., Siddons, G., Shim, M., and Keblinski, P., 2003, "Interfacial Heat Flow in Carbon Nanotube Suspensions," Nature Mater., **2**, pp. 731–734.
[53] Nan, C.-W., Liu, G., Lin, Y., and Li, M., 2004, "Interface Effect on Thermal Conductivity of Carbon Nanotube Composites," Appl. Phys. Lett., **85**, pp. 3549–3551.
[54] Xuan, Y., Li, Q., Zhang, X., and Fujii, M., 2006, "Stochastic Thermal Transport of Nanoparticle Suspensions," J. Appl. Phys., **100**, p. 043507.
[55] Prasher, R., Bhattacharya, P., and Phelan, P. E., 2005, "Thermal Conductivity of Nanoscale Colloidal Solutions (Nanofluids)," Phys. Rev. Lett., **94**, p. 025901.
[56] Koo, J., and Kleinstreuer, C., 2004, "A New Thermal Conductivity Model for Nanofluids," J. Nanopart. Res., **6**, pp. 577–588.
[57] Patel, H. E., Sundararajan, T., Pradeep, T., Dasgupta, A., Dasgupta, N., and Das, S. K., 2005, "A Micro-Convection Model for Thermal Conductivity of Nanofluid," Pramana, J. Phys., **65**, pp. 863–869.
[58] Ren, Y., Xie, H., and Cai, A., 2005, "Effective Thermal Conductivity of Nanofluids Containing Spherical Nanoparticles," J. Phys. D: Appl. Phys., **38**, pp. 3958–3961.
[59] Evans, W., Fish, J., and Keblinski, P., 2006, "Role of Brownian Motion Hydrodynamics on Nanofluid Thermal Conductivity," Appl. Phys. Lett., **88**, p. 093116.
[60] Vladkov, M., and Barrat, J.-L., 2006, "Modeling Transient Absorption and Thermal Conductivity in a Simple Nanofluid," Nano Lett., **6**, pp. 1224–1228.
[61] Sarkar, S., and Selvam, R. P., 2007, "Molecular Dynamics Simulation of Effective Thermal Conductivity and Study of Enhanced Thermal Transport Mechanism in Nanofluids," J. Appl. Phys., **102**, p. 074302.
[62] Eapen, J., Williams, W. C., Buongiorno, J., Hu, L.-W., and Yip, S., 2007, "Mean-Field Versus Microconvection Effects in Nanofluid Thermal Conduction," Phys. Rev. Lett., **99**, p. 095901.
[63] Lee, D., Kim, J.-W., and Kim, B. G., 2006, "A New Parameter to Control Heat Transport in Nanofluids: Surface Charge State of the Particle in Suspension," J. Phys. Chem. B, **110**, pp. 4323–4328.
[64] Eapen, J., Li, J., and Yip, S., 2007, "Mechanism of Thermal Transport in Dilute Nanocolloids," Phys. Rev. Lett., **98**, p. 028302.
[65] Xuan, Y., and Roetzel, W., 2000, "Conceptions for Heat Transfer Correlation of Nano-Fluids," Int. J. Heat Mass Transfer, **43**, pp. 3701–3707.
[66] Ding, Y., and Wen, D., 2005, "Particle Migration in a Flow of Nanoparticle Suspensions," Powder Technol., **149**, pp. 84–92.
[67] Buongiorno, J., 2006, "Convective Transport in Nanofluids," ASME J. Heat Transfer, **128**, pp. 240–250.
[68] Narayan, G. P., Anoop, K. B., and Das, S. K., 2007, "Mechanism of Enhancement/Deterioration of Boiling Heat Transfer Using Stable Nanoparticle Suspensions Over Vertical Tubes," J. Appl. Phys., **102**, p. 074317.
[69] Kim, S. J., Bang, I. C., Buongiorno, J., and Hu, L. W., 2006, "Effects of Nanoparticle Deposition on Surface Wettability Influencing Boiling Heat Transfer in Nanofluids," Appl. Phys. Lett., **89**, p. 153107.
[70] Kim, H. D., Kim, J., and Kim, M. H., 2007, "Experimental Studies on CHF Characteristics of Nano-Fluids at Pool Boiling," Int. J. Multiphase Flow, **33**, pp. 691–706.
[71] Kim, H. D., and Kim, M. H., 2007, "Effect of Nanoparticle Deposition on Capillary Wicking That Influences the Critical Heat Flux in Nanofluids," Appl. Phys. Lett., **91**, p. 014104.
[72] Tsai, C. Y., Chien, H. T., Ding, P. P., Chan, B., Luh, T. Y., and Chen, P. H., 2004, "Effect of Structural Character of Gold Nanoparticles in Nanofluid on Heat Pipe Thermal Performance," Mater. Lett., **58**, pp. 1461–1465.
[73] Tzeng, S.-C., Lin, C.-W., and Huang, K. D., 2005, "Heat Transfer Enhancement of Nanofluids in Rotary Blade Coupling of Four-Wheel-Drive Vehicles," Acta Mech., **179**, pp. 11–23.
[74] Buongiorno, J., Hu, L. W., Kim, S. J., Hannink, R., Truong, B., and Forrest, E., 2008, "Nanofluids for Enhanced Economics and Safety of Nuclear Reactors: An Evaluation of the Potential Features, Issues and Research Gaps," Nucl. Technol., **162**, pp. 80–91.
[75] Buongiorno, J., 2005, *Proceedings of the American Nuclear Society—International Congress on Advances in Nuclear Power Plants 2005, ICAPP'05 6*, pp. 3581–3585.
[76] Tran, P. X., 2007, "Nanofluids for Use as Ultra-Deep Drilling Fluids," Fact Sheet, National Energy Technology Laboratory, Office of Fossil Energy, U.S. Department of Energy, Jan., http://www.netl.doe.gov/publications/factsheets/rd/R&D108.pdf.

Pressure Drop During Two-Phase Flow of R134a and R32 in a Single Minichannel

Alberto Cavallini
e-mail: alcav@unipd.it

Davide Del Col
e-mail: davide.delcol@unipd.it

Marko Matkovic
e-mail: marko.matkovic@unipd.it

Luisa Rossetto
e-mail: luisa.rossetto@unipd.it

Dipartimento di Fisica Tecnica,
University of Padova,
Padova 35131, Italy

Condensation in minichannels is widely used in air-cooled condensers for the automotive and air-conditioning industry, heat pipes, and compact heat exchangers. The knowledge of pressure drops in such small channels is important in order to optimize heat transfer surfaces. Most of the available experimental work refers to measurements obtained within multiport smooth extruded tubes and deal with the average values over the number of parallel channels. In this context, the present authors have set up a new test apparatus for heat transfer and fluid flow studies in single minichannels. This paper presents new experimental frictional pressure gradient data, relative to single-phase flow and adiabatic two-phase flow of R134a and R32 inside a single horizontal minitube, with a 0.96 mm inner diameter and with not-negligible surface roughness. The new all-liquid and all-vapor data are successfully compared against predictions of single-phase flow models. Also the two-phase flow data are compared against a model previously developed by the present authors for adiabatic flow or flow during condensation of halogenated refrigerants inside smooth minichannels. Surface roughness effects on the liquid-vapor flow are discussed. In this respect, the friction factor in the proposed model is modified, in order to take into consideration also effects due to wall roughness. [DOI: 10.1115/1.3056556]

Keywords: minichannel, pressure drop, single phase, two phase, entrainment, roughness

1 Introduction

In this paper, following Ref. [1], minichannels are single tubes or multiport extruded aluminum channels with an inner hydraulic diameter in the range 0.2–3 mm. Two-phase flow in minichannels is affected by gravity, viscous shear, and surface tension. These forces influence flow regimes, pressure drops, and heat transfer.

The following researchers observed flow regimes during the condensation of R134a in minichannels, but no general flow regime map is available. Coleman and Garimella [2–4] reported flow patterns of R134a condensing in horizontal tubes and square minichannels with inner hydraulic diameters ranging from 1 mm to 4.9 mm. With mass velocities $G>150$ kg m^{-2} s^{-1} the authors observed annular, wavy, intermittent (slug, plug), and dispersed (bubble) flow patterns. At hydraulic diameters $D_h<1$ mm the wavy regime was not present, while at high flow rates and qualities annular film with mist core or mist flows were present. With R134a at 52 °C in square minichannels of diameter 1 mm or 2 mm mist flow was present for dimensionless gas velocity J_G larger than 10–15. While the hydraulic diameter was found to have a substantial effect on flow transitions, the tube shape was found to be less significant. Wang et al. [5] reported flow patterns for condensation of R134a at 35 °C in a multichannel of rectangular cross section with $D_h=1.46$ mm, at $75<G<350$ kg m^{-2} s^{-1}. They observed annular, wavy, and slug flow, while the flow was always annular for $J_G>2.5$. Kim et al. [6] observed annular, slug, and bubbly flow during condensation of R134a in a horizontal circular single tube with a diameter of 0.75 mm at 40 °C with $100<G<600$ kg m^{-2} s^{-1}.

Several researchers measured pressure drops during condensation or adiabatic flow in minichannels. Recent data are mostly relative to R134a, while few experiments have been undertaken at high reduced pressure and low reduced pressure conditions. Cavallini et al. [7,8] measured pressure drops during adiabatic flow at 40 °C of R134a, R236ea, and R410A inside a multiport minichannel having square cross section ports with a hydraulic diameter of 1.4 mm, a length of 1.13 m, and with mass velocities ranging from 200 kg m^{-2} s^{-1} to 1400 kg m^{-2} s^{-1}. The arithmetical mean deviation of the assessed profile *Ra* of the inner surface was *Ra* $=0.08$ μm, while the maximum height of profile *Rz* was equal to 0.43 μm. The three refrigerants were chosen because they present a wide range of reduced pressure at test conditions. In fact at 40 °C the reduced pressure p_R of R236ea is around 0.1, R134a has $p_R=0.25$, and R410A has $p_R=0.5$. The pressure drop in adiabatic conditions is obtained by measuring the saturation temperature drop in the tube, by means of one T-type thermopile, and two T-type thermocouples fixed to the aluminum tube. The thermopile used in the measurement presents an experimental uncertainty equal to ± 0.03 K, which leads to an experimental nominal uncertainty of ± 0.71 kPa m^{-1} for R134a, of ± 1.6 kPa m^{-1} for R410A and of ± 0.28 kPa m^{-1} for R236ea at the same average saturation temperature (40 °C). Coleman [9] measured pressure drop during the adiabatic and condensing flow of R134a at $p_R=0.37$ in channels with circular and square cross sections with $0.51\leq D_h \leq 1.52$ mm. Coleman estimated the relative roughness to be from 0.0001 to 0.0005 for the circular channels and 0.0009 for the square ones. Coleman [9] also measured pressure drop in multiport minichannels with triangular, barrel shape, N shape, and rectangular cross sections. For these channels the relative roughness was between 0.003 and 0.039. The pressure drop data of Zhang [10], Zhang and Webb [11], and Hirofumi and Webb [12] (reported in Ref. [10]) are relative to the adiabatic flow of R134a in circular and square cross section multiport channels and in a single minitube with plain inner surface. Reduced pressure for R134a was varied between 0.25 and 0.47. Hydraulic diameters varied between 0.96 mm and 3.25 mm. The data set of Jeong et al. [13] is relative to the adiabatic flow of R744 in square cross section channels, with a hydraulic diameter of 2 mm.

Contributed by the Heat Transfer Division of ASME for publication in the JOURNAL OF HEAT TRANSFER. Manuscript received April 14, 2008; final manuscript received August 29, 2008; published online January 21, 2009. Review conducted by Robert D. Tzou. Paper presented at the 2008 International Conference on Micro/Nanoscale Heat Transfer (MNHT2008), Tainan, Taiwan, January 6–9, 2008.

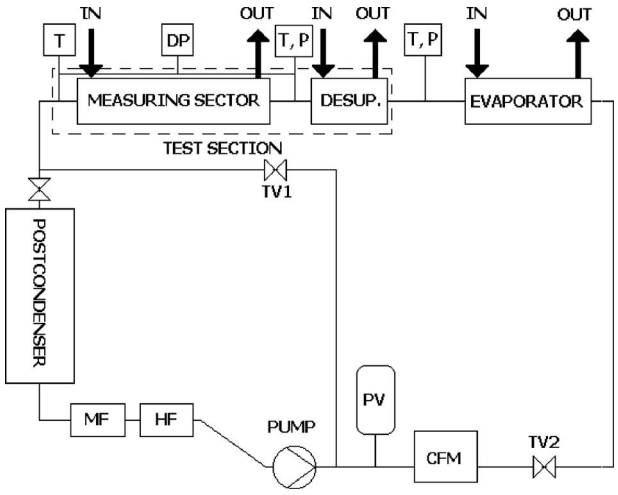

Fig. 1 Experimental test rig: desup=desuperheater, MF =mechanical filter, HF=dehumidifier, PV=pressure vessel, CFM=Coriolis-effect mass flow meter, P=pressure transducer, T=temperature transducer, DP=differential pressure transducer, and TV1 and TV2=throttling valves

Cavallini et al. [14] compared predictions from several models published in the open literature with experimental data by Cavallini et al. [8]. The models, either developed for conventional macrochannels or specifically developed for minichannels, were not able to predict the frictional pressure drop for flow in minichannels of high and low pressure fluids with a satisfactory agreement. Particularly no model seemed to be able to predict frictional pressure drops of R410A, while many models were not able to predict R236ea trends. Many correlations, on the contrary, were able to predict frictional pressure drops of R134a. A model for the frictional pressure gradient valid for adiabatic flow or for flow during condensation of halogenated refrigerants inside minichannels was then suggested by Cavallini et al. [15]. The model is suggested for smooth tubes since it is based on data taken in channels with negligible surface roughness and takes into account the effect of the entrainment rate of droplets from the liquid film. The model is applied to the annular, annular-mist, and intermittent flows, and it is also applied with success to horizontal macrotubes and to data for microfinned multiport minichannels by Webb and Ermis [16].

2 Experimental Tests in a Rough Single Minichannel

Surface roughness affects pressure drop during single-phase flow in macrochannels and minichannels, as shown by Taylor et al. [17]. The multiport minichannel tested by Cavallini et al. [7,8] is characterized by a square cross section and a low value of surface roughness (Ra=0.08 μm and Rz=0.43 μm), whose effect can thus be neglected. To investigate the effect of tube wall roughness and geometry of the channel on the two-phase frictional pressure gradient, the present authors report here the pressure drop measured during the condensation and adiabatic flow of R134a and R32 in a single circular section minitube with a much higher surface roughness as compared with the previously tested minichannel.

The test rig and experimental procedures used for measuring the pressure drop in the single round minichannel are fully described in Refs. [18,19]. The test rig arranged for heat transfer and pressure drop measurements during condensation is depicted in Fig. 1. It consists of the primary refrigerant loop and four auxiliary loops. The primary refrigerant loop is contaminant-free, since the circuit was cleaned and evacuated before filling it with refrigerant. The composition of the refrigerant was certified by the provider.

In the refrigerant loop, the subcooled refrigerant is sent through a filter and a dehumidifier into the gear pump coupled with a variable speed electric motor. It is then pumped through the Coriolis-effect mass flow meter into the evaporator where the fluid is heated up, vaporized, and superheated. There, the temperature and the pressure define the state of the vapor. The superheated vapor enters the test section (Fig. 2), which is composed of two countercurrent heat exchangers. The first one (desuperheater) is used to cool down the fluid to the saturation state at the inlet of the second heat exchanger, which is the actual measuring sector. During adiabatic two-phase tests, the vapor quality in the test tube is obtained from an energy balance on the water side in the desuperheater, before the refrigerant enters the measuring sector. During condensation tests, high values of the vapor quality are maintained at the inlet of the measuring sector, as determined from the thermal balance on the coolant side of the desuperheater. The saturation temperature is checked against the pressure in the two adia-

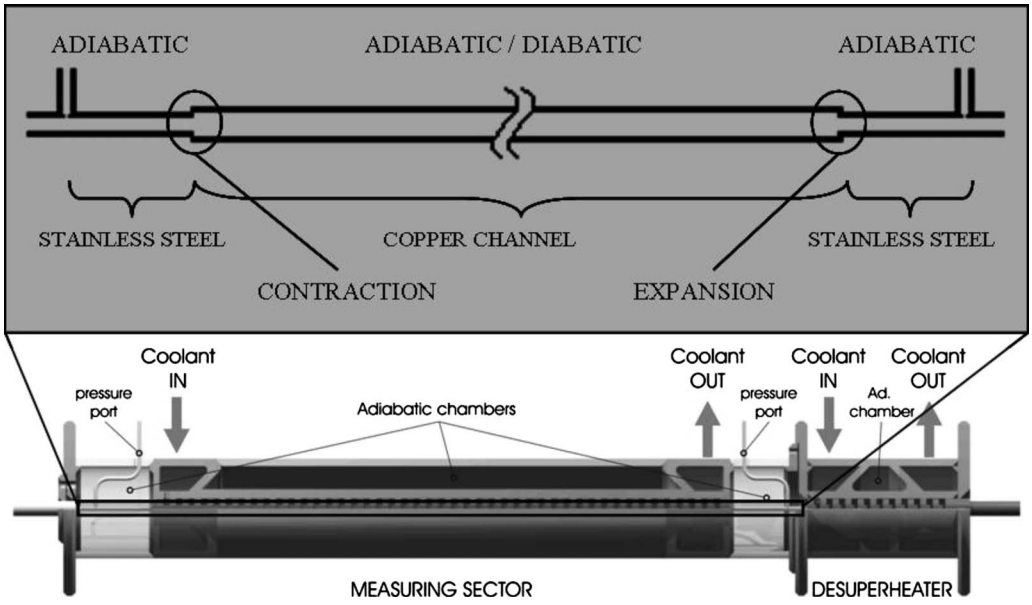

Fig. 2 The test section

batic sectors upstream and downstream of the measuring sector. There, the temperature is measured by means of adiabatic wall temperature measurement. Saturated refrigerant enters the measuring sector, where condensation is performed. The heat transfer in the two sectors is determined by measuring the coolant mass flow rates and temperatures in the annuli of the two sectors. Furthermore, the measuring sector is equipped with a substantial number of thermocouples, 15 set in the coolant flow and 13 set in the diabatic copper wall along the channel. Such facility permits the authors to measure vapor quality distribution all along the minitube; hence the local pressure gradient values are more feasible to be modeled. The refrigerant state is finally checked at the outlet of the measuring sector and closes the loop in the postcondenser, where it is condensed and subcooled. The temperatures and the flow rates of the secondary loops are controlled by a closed hot water loop, two thermal baths, and an additional resistance heater set in series at the inlet of the desuperheater. In this way, it is possible to independently control the temperatures of four different heat sinks or heat sources within the test rig.

The test tube is a commercial copper tube with an inner diameter of 0.96 mm and a length of 228.5 mm. The uncertainty associated to the diameter is equal to ± 0.02 mm. The arithmetical mean deviation of the assessed profile Ra of the inner surface is $Ra=1.3$ μm, the maximum height of profile Rz is 10 μm. These values are much higher than those of the multiport extruded aluminum channel tested by Cavallini et al. [7,8].

Before and after the copper test tube in the measuring sector, two stainless steel tubes are soldered to the copper minitube. The stainless steel tubes have a 0.762 mm inner diameter, $Ra=2.0$ μm, and $Rz=10.2$ μm. The inlet and outlet pressure ports are inserted in the two stainless steel tubes, 24 mm apart from the copper tube. The total frictional pressure drop is then the sum of the frictional pressure drop in the two stainless steel tubes, each 24 mm long, of the frictional pressure drop in the 228.5 mm long copper tube, and of the pressure variations due to abrupt enlargement (from 0.762 mm diameter to 0.96 mm diameter) and contraction (from 0.96 mm to 0.762 mm).

An absolute pressure transducer is connected to the pressure port at the inlet of the measuring sector; a differential pressure transducer is connected between the inlet and outlet. The experimental uncertainty is ± 0.1 kPa for the measured pressure difference, ± 3 kPa for the absolute pressure, and $\pm 0.2\%$ for the measured refrigerant flow rate.

The energy balance in the test section, desuperheater and measuring sector, has been checked at different refrigerant mass velocities over the entire vapor quality change, i.e., the heat transfer from inlet superheated vapor to outlet subcooled refrigerant has been checked against the thermal balance on the coolant side in the test section. The overall thermal balance has been found to be within 2%. Nevertheless, preliminary tests were performed to measure heat exchange to the external ambient and to quantify the effect of ambient temperature on the vapor quality.

First of all single-phase pressure drop experiments were performed to gain critical insight into the test section hydraulic performance. The frictional pressure drop in the copper tube is obtained from the total measured pressure drop by subtracting the local losses and the pressure loss in the stainless steel sectors

$$\Delta p_{\text{Cu tube}} = \Delta p_{\text{total}} - \sum \Delta p_{\text{local}} - \Delta p_{\text{SS tube}} \tag{1}$$

The abrupt enlargement and contraction pressure variations were estimated according to Ref. [20]. These calculated local values, which were less than 6% of the total measured value, were subtracted from the total experimental pressure drop.

The pressure variation in the stainless steel tube is calculated with the equation

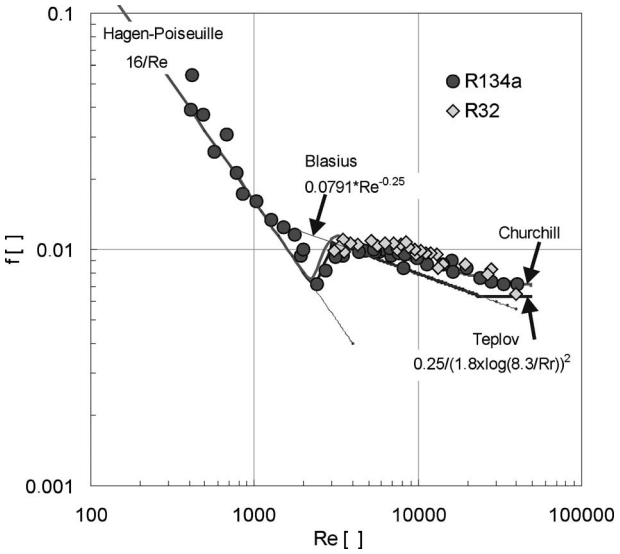

Fig. 3 Experimental and calculated friction factors for a 0.96 mm inner diameter circular single minichannel

$$\Delta p_{\text{SS tube}} = 2 f_{\text{SS}} \frac{L_{\text{SS}} G_{\text{SS}}^2}{D_{\text{SS}} \rho} \tag{2}$$

where the friction factor f_{SS} is estimated with the proper equation according to the corresponding Reynolds number, as reported in Appendix A (Eqs. (A1)–(A4)).

Figure 3 shows the calculated friction factor for the copper tube against the Reynolds number in the same tube, being the friction factor defined as

$$f_{\text{Cu tube}} = \Delta p_{\text{Cu tube}} \frac{D_{\text{Cu tube}} \rho}{2 L_{\text{Cu tube}} G_{\text{Cu tube}}^2} \tag{3}$$

Also in Fig. 3, equations for laminar flow and turbulent flow in smooth tubes and rough tubes are reported, as the ones by Hagen–Poiseuille, Blausius, Teplov for rough tubes, and Churchill [21]. The relative roughness of the tube has been assumed to be equal to $\text{RR}=2Ra/D$. The agreement between calculated and experimental values is satisfactory.

All the single-phase pressure drop experiments reported here refer to adiabatic flows. Low Reynolds number data are taken during subcooled liquid tests, whereas data at high Reynolds numbers were taken with superheated vapor. Nevertheless, diabatic single-phase pressure loss measurements were also performed in a wide range of test conditions. No significant difference in the frictional pressure gradient was found by comparing the diabatic experimental results to the adiabatic data.

After the single-phase tests, two-phase pressure drop tests were performed during adiabatic flow of R134a and R32 in the same test section, as described above. The same tests have also been repeated in different days to check repeatability of the measurements where no essential discrepancies in time have been found. Figures 4(*a*) and 4(*b*) show the total experimental pressure drop for R134a and R32 at 39–41 °C versus vapor quality, at different mass velocities (referred to the copper tube flow cross-sectional area): 400 kg m^{-2} s^{-1}, 600 kg m^{-2} s^{-1}, and 800 kg m^{-2} s^{-1} for R134a and 200 kg m^{-2} s^{-1}, 400 kg m^{-2} s^{-1}, 600 kg m^{-2} s^{-1}, 800 kg m^{-2} s^{-1}, and 1000 kg m^{-2} s^{-1} for R32. The total pressure drop reported in the graphs is the sum of pressure variations in the stainless steel tubes, in the copper tube, and in the two abrupt geometry changes. Error bars have been introduced for the vapor quality in Fig. 4. However, for the highest mass velocities, the error bars are too small to be read from the graphs. Moreover, experimental uncertainty of the measured pressure drop is not legible from the graphs either (± 0.1 kPa).

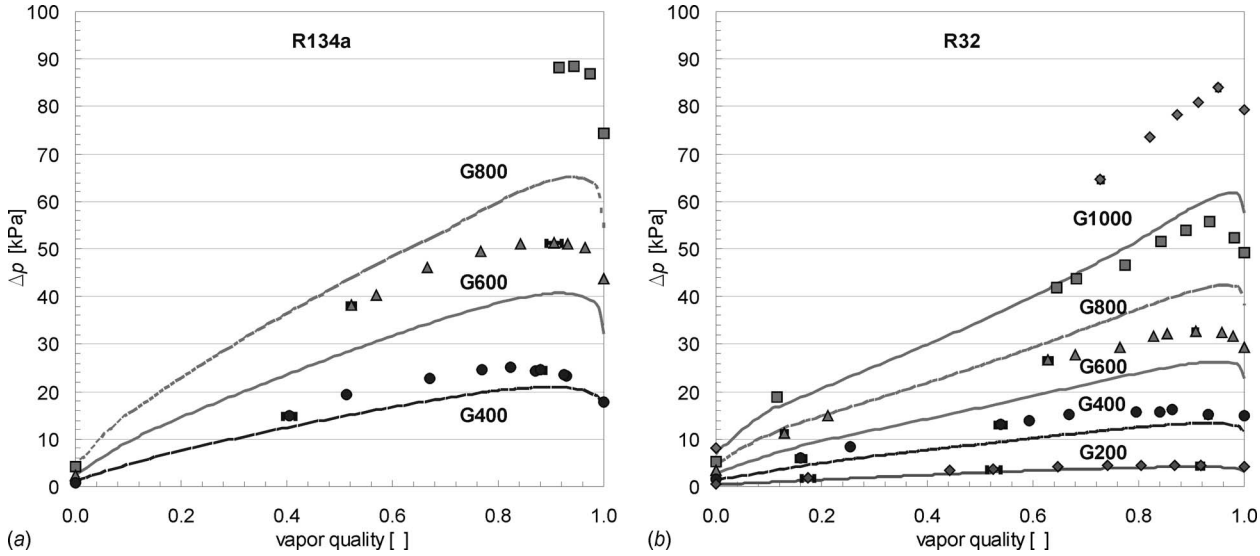

Fig. 4 Overall experimental pressure losses during adiabatic two-phase flow of R134a and R32 at 40°C saturation temperature and different mass velocities G (kg m^{-2} s^{-1}) in the 0.96 mm inner diameter circular single minichannel. Calculated trends (dashed lines) by the model, which do not consider surface roughness (Eq. (B1)–(B11)), are also reported.

Figures 4(*a*) and 4(*b*) show the comparison between the experimental Δp_{total} data and the calculated values at 40°C with the model of Cavallini et al. [15] (Eqs. (B1)–(B11) in Appendix B) for frictional losses and according to Paliwoda [22] for abrupt geometry changes. Pressure variations for geometry changes were around 10% of the overall calculated value. The Paliwoda [22] abrupt expansion equation was in good agreement with the Chalfi and Ghiaasiaan [23] model, while the Paliwoda abrupt contraction correlation agreed with Coleman [9] observations. The present model underestimates experimental pressure drops by 25%, as shown in Figs. 5(*a*) and 5(*b*), where experimental data are compared against calculated ones at the same saturation temperature.

First of all one must consider that the present test section is made of a single round channel, whereas most of the data used in developing the model of Cavallini et al. [15] refer to multiport tubes with square cross sections in some cases.

Besides, in comparison with the aluminum extruded tube tested by the present authors, the copper minitube presents a considerably higher surface roughness. Therefore, a possible explanation of the disagreement in Fig. 4 can be related to the surface roughness of the tube. In order to enlighten the effect of the roughness in the minichannel, one can calculate the liquid film thickness δ at the wall by using the model of Cavallini et al. [14] for condensation in minichannels during annular flow, based on the analysis of Kosky and Staub [24] for macrochannels

$$\delta = \frac{\delta^+ \cdot \nu_L}{u_\tau} = \frac{\delta^+ \cdot \nu_L}{\tau^{0.5}} \rho_L^{0.5} = \frac{\delta^+ \cdot \nu_L}{\left[\left(\frac{dp}{dz}\right)_f \frac{D}{4}\right]^{0.5}} \rho_L^{0.5} \tag{4}$$

with

$$\delta^+ = \left(\frac{\text{Re}_L}{2}\right)^{0.5}, \quad \text{Re}_L < 1145$$

$$\delta^+ = 0.0504\ \text{Re}_L^{7/8}, \quad \text{Re}_L > 1145$$

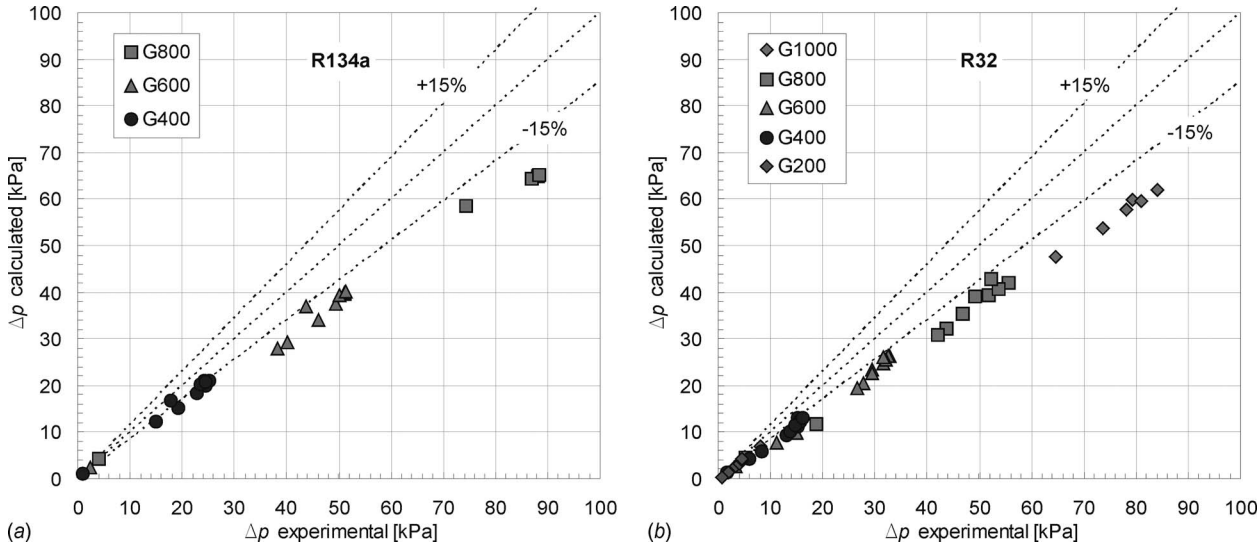

Fig. 5 Calculated (Eqs. (B1)–(B11)) versus experimental pressure drop

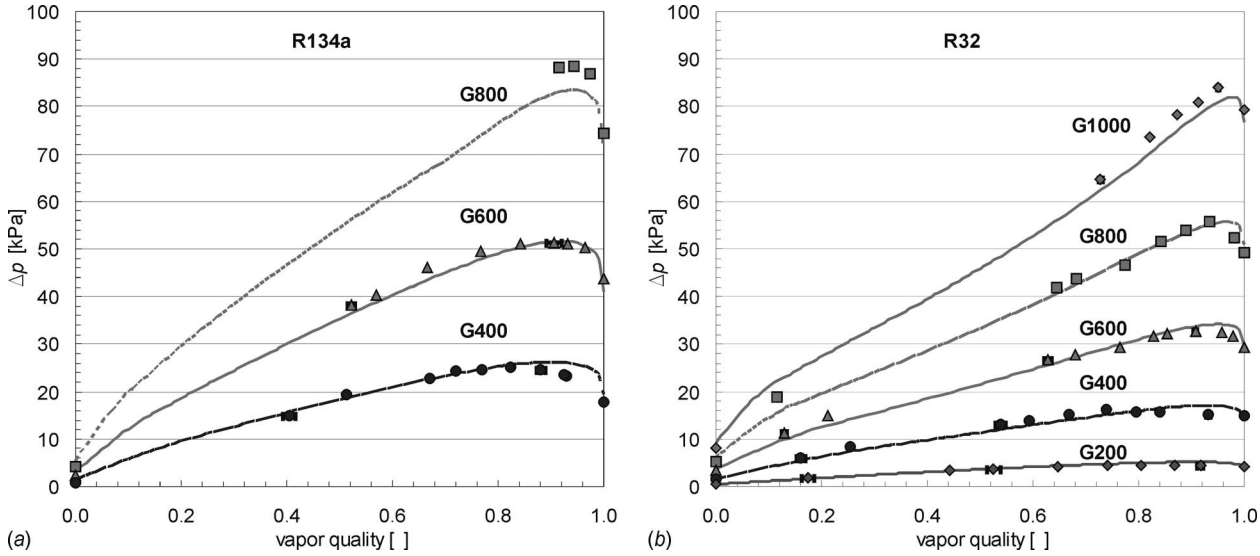

Fig. 6 Overall experimental pressure losses during adiabatic two-phase flow of R134a and R32 at around 40°C saturation temperature and different mass velocities G (kg m^{-2} s^{-1}) in the 0.96 mm inner diameter circular single minichannel. Calculated trends (dashed lines) by the model, modified for the surface roughness effect with Eq. (5), are also reported.

$$\mathrm{Re}_L = \frac{GD(1-x)(1-E)}{\mu_L}$$

and the frictional pressure gradient from Eqs. (B1)–(B11) in Appendix B.

Since most of the experimental data are relative to high vapor qualities ($x>0.7$), the dimensionless film thickness δ^+ calculated with the equations above, assuming no entrainment occurs, is less than 30, which means that the liquid film is laminar near the wall and in the transition to turbulent flow away from the wall. It corresponds to a liquid film $\delta<25$ μm, when $E=0$ and $x=0.75$. With entrainment calculated from Eqs. (B8) and (B9), the thickness of the liquid film at the wall is around 10–15 μm ($x=0.75$, $400\leq G\leq 800$ kg m^{-2} s^{-1}). Therefore, the surface roughness, with peaks up to 15 μm high, certainly affects the laminar and the laminar-turbulent transition sublayers. The liquid flow is influenced by both the vapor shear stress and the surface roughness.

At high mass velocities ($G\geq 400$ kg m^{-2} s^{-1}) the liquid laminar sublayer ($\delta^+<5$) has a thickness $\delta<8-10$ μm. When the peaks are higher than the liquid film thickness, the liquid film may also be influenced by the surface tension in the valleys between the peaks. All these effects are not present in the aluminum extruded tubes because of the lower surface roughness.

In the end, it can be concluded that the surface roughness affects the motion of the liquid film. There is no evidence that the liquid entrainment is affected by the surface roughness, except for the case when the peaks in the surface are in the same height range as the liquid film thickness.

With regard to the data presented above, it should also be considered that the geometry of the channel may play a role on the liquid entrainment: the presence of corners, in fact, should be in favor of a higher entrainment due to the combined effect of surface tension and shear stress. Unfortunately, the data available do not allow a clear detection of the effect of the geometry in minichannels and, with regard to data by the present authors, singling out the effect of roughness from the one due to the channel shape.

Properties of R134a and R32 have been calculated with REFPROP 7.0 by NIST [25].

3 Extension of the Model to Include the Effect of Surface Roughness

The above discussion points out the necessity to take into account surface roughness when calculating the frictional pressure gradient for two-phase flow in mini- and microchannels. Recently Agarwal and Garimella [26] also correlated the two-phase frictional pressure drops in minichannels with surface roughness. Besides this they suggested different coefficients for their different channel shapes.

In order to consider the effect of the tube wall roughness, the all-liquid friction factor of the model of Cavallini et al. [15] (Eq. (B2) in Appendix B) was corrected in the following way:

$$f^*_{\mathrm{LO}} = 0.046\,\mathrm{Re}_{\mathrm{LO}}^{-0.2} + 0.7\cdot \mathrm{RR} \quad \text{for} \quad \mathrm{RR} < 0.0027 \qquad (5)$$

The above friction factor is in good agreement with the Churchill curve in the range $3000<\mathrm{Re}_{\mathrm{LO}}<6000$. In Figs. 6 and 7 experimental values of the cumulative adiabatic two-phase pressure drops are compared with predicted values from the model modified with Eq. (5). Agreement is satisfactory, even if data are a little underestimated at high mass velocities and vapor qualities, suggesting channel shape effects or weakening of entrainment due to wall roughness.

Pressure drop measurements have also been performed during condensation of R134a and R32 in the copper minitube with an inner diameter 0.96 mm. Experiments have been carried out at three mass velocities: 400 kg m^{-2} s^{-1}, 600 kg m^{-2} s^{-1}, and 800 kg m^{-2} s^{-1} with vapor qualities varying from 0.95 to 0.10. In addition, two more mass velocities (1000 kg m^{-2} s^{-1} and 1200 kg m^{-2} s^{-1}) have been tested with the higher pressure fluid R32.

The total measured pressure variation during condensation tests is the sum of $\Delta p_{\mathrm{total}}$, as defined in Eq. (1) for adiabatic tests, and the pressure gain due to momentum change Δp_m. This last term can be estimated with the equation (derived in Appendix C)

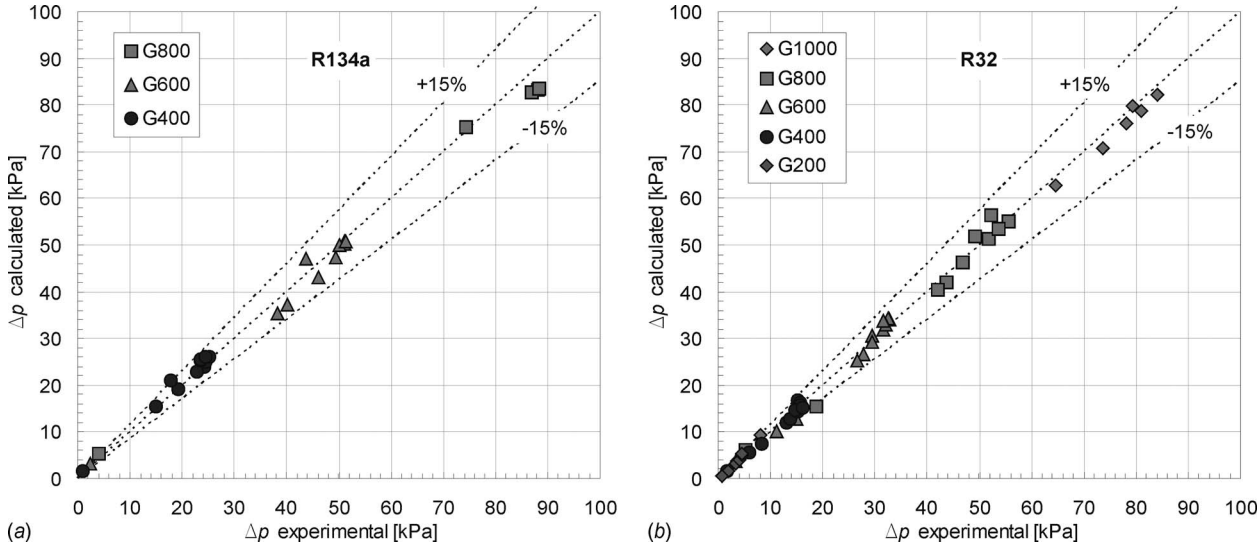

Fig. 7 Calculated (model modified with Eq. (5)) versus experimental pressure drop

$$(-\Delta p)_m = G^2\left[\frac{(1-x_{in})^2(1-E_{in})^2}{(\varepsilon_{in})\rho_L} + \frac{[x_{in}+(1-x_{in})E_{in}]^2}{(1-\varepsilon_{in})\cdot\rho_{GC,in}}\right] + - G^2\cdot\left[\frac{(1-x_{out})^2(1-E_{out})^2}{(\varepsilon_{out})\rho_L} + \frac{[x_{out}+(1-x_{out})E_{out}]^2}{(1-\varepsilon_{out})\cdot\rho_{GC,out}}\right] \quad (6)$$

with ε, the volume fraction of the liquid in the film at the wall, function of the liquid film thickness δ from Eq. (4), as

$$\varepsilon = 1 - \left(\frac{D-2\delta}{D}\right)^2$$

and ρ_{GC} the homogeneous gas core density from Eq. (B9) in Appendix B.

The comparison between the measured experimental values and predictions from the modified model give percentage deviations e_p of 3–26% for R134a and 1–16% for R32.

Finally, Fig. 8 shows the comparison between the measured values by Cavallini et al. [8] in a multiport tube and by Coleman [9] and predictions from the modified model.

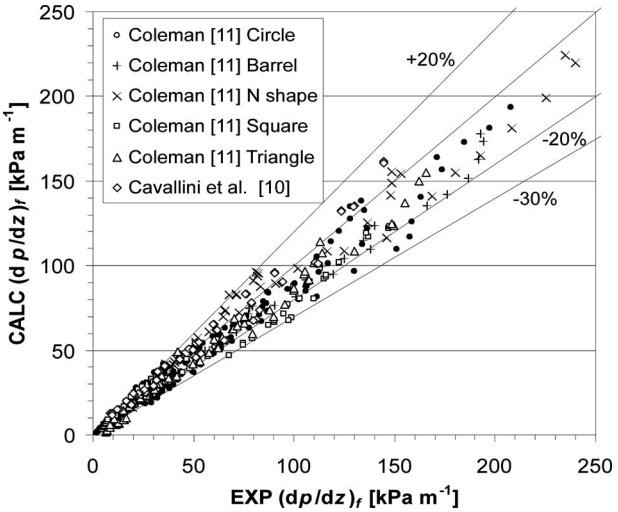

Fig. 8 Comparison between predictions from Cavallini et al. [15] model modified with Eq. (5) and experimental data by Cavallini et al. [8] and Coleman [9].

Data by Cavallini et al. [8] present a small relative roughness (RR=0.000114), while Coleman [9] declares for the channels considered in Fig. 8 a relative roughness varying between 0.0001 and 0.007. Agreement is within +20% and −30%. When the relative roughness is small, Eqs. (5) and (B2) give almost the same friction factor and predictions from the present model and the original analysis of Cavallini et al. [15] are comparable.

4 Conclusions

New pressure drop data taken inside a single minitube with not-negligible roughness have been presented. The surface roughness affects the single-phase pressure losses, when the flow is turbulent, and also the two-phase pressure losses in the tested minichannel.

The single-phase experimental measurements are well predicted by available models for macrotubes. The two-phase measurements are satisfactorily predicted by the model of Cavallini et al. [15], once a simple modification of the model is introduced to account for the effect of wall roughness.

A further improvement may be to investigate the dependence of the entrainment rate in minichannels on the channel shape and channel size.

Acknowledgment

The support of ESA through the ENCOM project and of MIUR through the PRIN program is gratefully acknowledged.

Nomenclature

D = tube inside diameter, m
e_p = percentage deviation $=100(\Delta p_{calc}-\Delta p_{exp})/\Delta p_{exp}$
e_R = average deviation $=(1/N_p)\Sigma e_p$
E = entrainment ratio
f = friction factor
F = parameter in Appendix B
g = gravitational acceleration, m s^{-2}
G = total mass velocity, kg m^{-2} s^{-1}
H = parameter in Appendix B
j_G = superficial gas velocity, m s^{-1}
J_G = dimensionless gas velocity $=xG/[gD_h\rho_G(\rho_L-\rho_G)]^{0.5}$
N_p = number of data points
p = pressure, Pa

p_R = reduced pressure $= p/p_c$
Ra = arithmetical mean deviation of the assessed profile (according to ISO 4287: 1997), μm
Re = Reynolds number
Re_L = $G(1-x)D_h/\mu_L$
$\mathrm{Re}_{\mathrm{LO}}$ = GD_h/μ_L
RR = relative roughness of the tube
Rz = maximum height of profile (according to ISO 4287: 1997), μm
T, t = temperature, K, °C
u_τ = friction velocity $=(\tau/\rho_L)^{0.5}$, m s^{-1}
x = thermodynamic vapor mass quality
W = parameter in Appendix B
z = axial coordinate oriented with the flow, m
Z = parameter in Appendix B

Greek Symbols

δ = liquid film thickness, m
Δp, Dp = pressure variation, Pa
ε = volume fraction of the liquid taking into consideration only the liquid in the film at the wall
Φ^2_{LO} = $(\mathrm{d}p/\mathrm{d}z)_f/(\mathrm{d}p/\mathrm{d}z)_{f,\mathrm{LO}}$
μ = dynamic viscosity, kg m^{-1} s^{-1}
ν = kinematic viscosity, m^2 s^{-1}
ρ = density, kg m^{-3}
σ = surface tension, N m^{-1}
τ = vapor shear stress on the liquid film, N m^{-2}

Subscripts and Superscripts

an = annular
c = critical
calc = calculated
exp = experimental
f = frictional
G = gas phase; gas with its actual mass flow rate
GC = gas core
h = hydraulic
in = at the inlet
L = liquid phase with its actual mass flow rate
LO = liquid phase with total mass flow rate
out = at the outlet
s = saturation
SS = stainless steel
w = tube wall

Appendix A

In detail, the friction factor f in single-phase flow in the stainless steel tube is estimated in laminar flow, for $\mathrm{Re} < 2300$, as

$$f_{\mathrm{laminar}} = \frac{16}{\mathrm{Re}_{\mathrm{SS}}} = \left(\frac{16\mu}{D_{\mathrm{SS}}G_{\mathrm{SS}}}\right) \tag{A1}$$

and in turbulent flow, for $\mathrm{Re} > 3000$, using the Blausius equation

$$f_{\mathrm{Blausius}} = 0.079\ \mathrm{Re}_{\mathrm{SS}}^{-0.25} = 0.079\left(\frac{\mu}{D_{\mathrm{SS}}G_{\mathrm{SS}}}\right)^{0.25} \tag{A2}$$

up to the intersection with the Teplov equation [20] for rough tubes

$$f_{\mathrm{Teplov}} = 0.25\left(\frac{1}{1.8\ \log(8.3/\mathrm{RR}_{\mathrm{SS}})}\right)^2 \tag{A3}$$

with $\mathrm{RR}_{\mathrm{SS}} = 2Ra_{\mathrm{SS}}/D_{\mathrm{SS}}$.

In the transition region, for $2300 \le \mathrm{Re} \le 3\,000$

$$f_{\mathrm{trans}} = \frac{f_{\mathrm{Blausius,Re=3000}} - f_{\mathrm{laminar,Re=2300}}}{3000-2300}(\mathrm{Re}_{\mathrm{SS}} - 2300) + f_{\mathrm{laminar,Re=2300}} \tag{A4}$$

Appendix B

Cavallini et al. [15] suggested Eqs. (B1)–(B9) to calculate the frictional pressure gradient during adiabatic flow or during condensation, when the dimensionless gas velocity $J_G > 2.5$

$$\left(\frac{\mathrm{d}p}{\mathrm{d}z}\right)_f = \Phi^2_{\mathrm{LO}}\left(\frac{\mathrm{d}p}{\mathrm{d}z}\right)_{f,\mathrm{LO}} = \Phi^2_{\mathrm{LO}} 2 f^*_{\mathrm{LO}} \frac{G^2}{D_h \rho_L} \tag{B1}$$

$$f^*_{\mathrm{LO}} = 0.046\ \mathrm{Re}_{\mathrm{LO}}^{-0.2} = 0.046\left(\frac{GD_h}{\mu_L}\right)^{-0.2} \quad \text{for any } \mathrm{Re}_{\mathrm{LO}} \tag{B2}$$

$$\Phi^2_{\mathrm{LO}} = Z + 3.595 \cdot F \cdot H \cdot (1-E)^W \tag{B3}$$

$$W = 1.398 p_R \tag{B4}$$

$$Z = (1-x)^2 + x^2 \frac{\rho_L}{\rho_G}\left(\frac{\mu_G}{\mu_L}\right)^{0.2} \tag{B5}$$

$$F = x^{0.9525}(1-x)^{0.414} \tag{B6}$$

$$H = \left(\frac{\rho_L}{\rho_G}\right)^{1.132}\left(\frac{\mu_G}{\mu_L}\right)^{0.44}\left(1-\frac{\mu_G}{\mu_L}\right)^{3.542} \tag{B7}$$

The entrainment ration E from Ref. [27]

$$E = 0.015 + 0.44 \cdot \log\left[\left(\frac{\rho_{\mathrm{GC}}}{\rho_L}\right)\left(\frac{\mu_L j_G}{\sigma}\right)^2 10^4\right]$$

$$\text{if } E \ge 0.95, \quad E = 0.95$$

$$\text{if } E \le 0, \quad E = 0 \tag{B8}$$

where the homogeneous gas core density ρ_{GC} is given by

$$\rho_{\mathrm{GC}} = \left(\frac{x + (1-x)E}{\dfrac{x}{\rho_G} + \dfrac{(1-x)E}{\rho_L}}\right)$$

$$\rho_{\mathrm{GC}} \approx \rho_G\left(1 + \frac{(1-x)E}{x}\right) \quad \text{for} \quad \rho_L \gg \rho_G \tag{B9}$$

The model, presented above, for the frictional pressure gradient can be extended to lower vapor qualities and mass velocities ($J_G < 2.5$), with the constraint to take the higher value between $(\mathrm{d}p/\mathrm{d}z)_f$ from Eqs. (B1)–(B9) and the all-liquid frictional pressure gradient $(\mathrm{d}p/\mathrm{d}z)_{f,\mathrm{LO}}$ for the considered channel geometry (Eqs. (B10) and (B11))

$$\left(\frac{\mathrm{d}p}{\mathrm{d}z}\right)_{f,\mathrm{LO}} = 2 f_{\mathrm{LO}} \frac{G^2}{D_h \rho_L} \tag{B10}$$

$$\text{for } \mathrm{Re}_{\mathrm{LO}} > 2000, \quad f_{\mathrm{LO}} = 0.046[GD_h/\mu_L]^{-0.2}$$

$$\text{for } \mathrm{Re}_{\mathrm{LO}} < 2000, \quad f_{\mathrm{LO}} = C/[GD_h/\mu_L] \tag{B11}$$

$C = 16$ for the circular section and $C = 14.3$ for the square section.

Appendix C

Assuming that the gas core and the entrained liquid flow with the same velocity, as suggested by Hewitt and Hall-Taylor [28], the vapor-liquid mixture in the core has density ρ_{GC} (Eq. (B9)) and velocity u_{GC} from

$$u_{\mathrm{GC}} = \frac{G[x + (1-x)E]}{(1-\varepsilon)\rho_{\mathrm{GC}}} \tag{C1}$$

The differential pressure gain due to momentum change is the sum of the term due to the liquid in the film at the wall and the quantity due to the liquid-vapor mixture in the core, as

$$(-dp)_m = G^2 d\left[\frac{(1-x)^2(1-E)^2}{(\varepsilon)\rho_L} + \frac{[x+(1-x)E]^2}{(1-\varepsilon)\cdot\rho_{GC}}\right] \quad \text{(C2)}$$

References

[1] Kandlikar, S. G., and Grande, W. J., 2003, "Evolution of Microchannel Flow Passages—Thermohydraulic Performance and Fabrication Technology," Heat Transfer Eng., **24**(1), pp. 3–17.

[2] Coleman, J. W., and Garimella, S., 1999, "Characterization of Two-Phase Flow Patterns in Small Diameter Round and Rectangular Tubes," Int. J. Heat Mass Transfer, **42**(15), pp. 2869–2881.

[3] Coleman, J. W., and Garimella, S., 2000, "Two-Phase Flow Regime Transitions in Microchannel Tubes: The Effect of Hydraulic Diameter," ASME Paper No. HTD-366-4.

[4] Coleman, J. W., and Garimella, S., 2000, "Visualization of Refrigerant Two-Phase Flow During Condensation," ASME Paper No. NHTC2000-12115.

[5] Wang, W.-W. W., Radcliff, T. D., and Christensen, R. N., 2002, "A Condensation Heat Transfer Correlation for Millimeter-Scale Tubing With Flow Regime Transition," Exp. Therm. Fluid Sci., **26**(5), pp. 473–485.

[6] Kim, M. H., Shin, J. S., Huh, C., Kim, T. J., and Seo, K. W., 2003, "A Study of Condensation Heat Transfer in a Single Mini-Tube and Review of Korean Micro- and Mini-Channel Studies," *Proceedings of the First International Conference on Microchannels and Minichannels*, Rochester, NY, ASME, New York, pp. 47–58.

[7] Cavallini, A., Del Col, D., Doretti, L., Matkovic, M., Rossetto, L., and Zilio, C., 2004, "Measurement of Pressure Gradient During Two-Phase Flow Inside Multi-Port Mini-Channels," *Proceedings of the Third International Symposium on Two-Phase Flow Modelling and Experimentation*, Pisa, Italy, Sep. 22–24.

[8] Cavallini, A., Del Col, D., Doretti, L., Matkovic, M., Rossetto, L., and Zilio, C., 2005, "Two-Phase Frictional Pressure Gradient of R236ea, R134a and R410A Inside Multi-Port Mini-Channels," Exp. Therm. Fluid Sci., **29**(7), pp. 861–870.

[9] Coleman, J. W., 2000, "Flow Visualization and Pressure Drop for Refrigerant Phase Change and Air-Water Flow in Small Hydraulic Diameter Geometries," Ph.D. thesis, Iowa State University, Ames, IA.

[10] Zhang, M., 1998, "A New Equivalent Reynolds Number Model for Vapor Shear-Controlled Condensation Inside Smooth and Micro-Fin Tubes," Ph.D. thesis, Pennsylvania State University.

[11] Zhang, M., and Webb, R. L., 2001, "Correlation of Two-Phase Friction for Refrigerants in Small-Diameter Tubes," Exp. Therm. Fluid Sci., **25**(3–4), pp. 131–139.

[12] Hirofumi, H., and Webb, R. L., 1995, "Condensation in Extruded Aluminium Tubes," Penn State Research Report, Showa Aluminum Corporation.

[13] Jeong, S., Cho, E., and Kim, H.-K., 2005, "Evaporative Heat Transfer and Pressure Drop of CO_2 in a Microchannel Tube," *Proceedings of the Third International Conference on Microchannels and Minichannels*, Jun. 13–15, Toronto, ON, ASME, New York.

[14] Cavallini, A., Doretti, L., Matkovic, M., and Rossetto, L., 2006, "Update on Condensation Heat Transfer and Pressure Drop in Minichannels," Heat Transfer Eng., **27**(4), pp. 74–87.

[15] Cavallini, A., Del Col, D., Matkovic, M., and Rossetto, L., 2008, ″Frictional Pressure Drop During Vapour-Liquid Flow in Minichannels: Modelling and Experimental Evaluation," Int. J. Heat Fluid Flow, doi: 10.1016/j.ijheatfluidflow.2008.09.003.

[16] Webb, R. L., and Ermis, K., 2001, "Effect of Hydraulic Diameter on Condensation of R-134a in Flat, Extruded Aluminum Tubes," J. Enhanced Heat Transfer, **8**(2), pp. 77–90.

[17] Taylor, J. B., Carrano, A. L., and Kandlikar, S. G., 2006, "Characterization of the Effect of Surface Roughness and Texture on Fluid Flow-Past, Present, and Future," Int. J. Therm. Sci., **45**(10), pp. 962–968.

[18] Cavallini, A., Del Col, D., Matkovic, M., and Rossetto, L., 2007, "Local Heat Transfer Coefficient During Condensation Inside a Single Minichannel," Sixth International Conference on Enhanced, Compact and Ultra-Compact Heat Exchangers: Science, Engineering and Technology, Postdam, Germany, Sept. 16–21.

[19] Matkovic, M., 2006, "Experimental Condensation Inside Minichannels," Ph.D. thesis, Università di Padova.

[20] Idelchik, I. E., 1996, *Handbook of Hydraulic Resistance*, 3rd ed., Begell House, New York.

[21] Churchill, S. W., 1977, "Friction Factor Equation Spans All Fluid-Flow Regimes," Chem. Eng. (New York, NY), **84**, pp. 91–92.

[22] Paliwoda, A., 1992, "Generalized Method of Pressure Drop Calculation Across Pipe Components Containing Two-Phase Flow of Refrigerants," Int. J. Refrig., **15**(2), pp. 119–125.

[23] Chalfi, T. Y., and Ghiaasiaan, S. M., 2008, "Pressure Drop Caused by Flow Area Changes in Capillaries Under Low Flow Conditions," Int. J. Multiphase Flow, **34**(1), pp. 2–12.

[24] Kosky, P. G., and Staub, F. W., 1971, "Local Condensing Heat Transfer Coefficients in the Annular Flow Regime," AIChE J., **17**(5), pp. 1037–1043.

[25] National Institute of Standard and Technology, NIST, 2002, REFPROP, Version 7.0, Boulder, CO.

[26] Agarwal, A., and Garimella, S., 2006, "Modeling of Pressure Drop During Condensation in Circular and Non-Circular Microchannels," ASME Paper No. IMECE2006-14672.

[27] Paleev, I. I., and Filippovich, B. S., 1966, "Phenomena of Liquid Transfer in Two-Phase Dispersed Annular Flow," Int. J. Heat Mass Transfer, **9**(10), pp. 1089–1093.

[28] Hewitt, G. F., and Hall-Taylor, N. S., 1970, *Annular Two-Phase Flow*, Pergamon, Oxford.

Multicomponent Energy Conserving Dissipative Particle Dynamics: A General Framework for Mesoscopic Heat Transfer Applications

Anuj Chaudhri
e-mail: chaudhri@seas.upenn.edu

Jennifer R. Lukes[1]
e-mail: jrlukes@seas.upenn.edu

Department of Mechanical Engineering and Applied Mechanics,
University of Pennsylvania,
Philadelphia, PA 19104

A multicomponent framework for energy conserving dissipative particle dynamics (DPD) is presented for the first time in both dimensional and dimensionless forms. Explicit definitions for unknown scaling factors that are consistent with DPD convention are found by comparing the present, general dimensionless governing equations to the standard DPD expressions in the literature. When the scaling factors are chosen based on the solvent in a multicomponent system, the system of equations reduces to a set that is easy to handle computationally. A computer code based on this multicomponent framework was validated, under the special case of identical components, for one-dimensional transient and one- and two-dimensional steady-state heat conduction in a random DPD solid. The results, which compare well with existing DPD works and with analytical solutions in one and two dimensions, show the promise of energy conserving DPD for modeling heat transfer at mesoscopic length scales. [DOI: 10.1115/1.3056602]

Keywords: DPD, constant energy, heat transfer, mesoscopic, micro-/nanoscale

1 Introduction

One of the key challenges in the micro-/nanoworld today is the understanding of thermal management in electronics cooling, heat exchangers, and materials processing [1]. Multicomponent complex fluids play a vital role in addressing these challenges. For example, liquid-vapor mixtures are the working fluid in boiling heat transfer electronics cooling applications, and nanofluids have attracted significant research interest for their potential for enhanced heat transfer. The contributions from the microstructure of these complex fluids can have a significant effect on their dynamic response, which can affect the macroscopic equilibrium and nonequilibrium transport properties [2]. The continuum methods used to model such fluids are based on averaged local properties such as density, velocity, and stress over a large number of atoms or molecules. Continuum theories can fail at regions such as contact lines, shocks, and interfaces where a molecular description of the system is required [3]. In many cases, constitutive equations are not available for a complete description and complex boundary conditions are difficult to handle with widely varying time and length scales [4]. Microscopic fluctuations are also important, which are difficult to incorporate in the already complex partial differential equations at the continuum level. Hence there is a need to look at methods where the microscopic physics of the system can be incorporated easily and predictions can be made about the micro-/macrobehavior.

Simulation methods such as molecular dynamics (MD) [5,6] can model systems from an atomistic perspective but are limited to short length (nanometers) and time (nanoseconds) scales. Colloidal suspensions such as nanofluids can have time and length scales that span over 15 orders of magnitude [7]. The relaxation times for such systems are usually on the order of a few nanoseconds to microseconds or more. These time and length scales cannot be probed using MD as one needs large system sizes and very long runs to be able to capture the physics. Consequently, mesoscale modeling and simulation techniques are required that are capable of capturing the right physics of these confined solids/fluids at the nano-/microscale and handling the disparate length and time scales involved in the process.

In mesoscopic modeling approaches, the fastest time and length scales of the system at the atomistic level are coarse grained to be able to probe larger relevant scales. These mesoscopic methods are mainly divided into two categories—particle based and grid based. The grid based methods include the lattice Boltzmann method (LBM) [8] and the lattice gas automata (LGA) [9]. The particle based methods include the Brownian dynamics (BD) [10], the Stokesian dynamics (SD) [11], the dissipative particle dynamics (DPD) [12], and the smoothed dissipative particle dynamics (SDPD) [13].

DPD is a meshless, coarse-grained, particle-based method used to simulate systems at mesoscopic length and time scales. The theoretical basis for DPD has been studied extensively and the equilibrium basis for isothermal situations has been identified [14,15]. DPD can be interpreted, loosely, as coarse-grained MD. Unlike BD, the solvent is modeled explicitly and includes the hydrodynamic interactions [16]. Essentially atoms, molecules, or monomers (denoted as "particles") are grouped together into mesoscopic clusters (denoted "beads") that are acted on by conservative, dissipative, and random forces. The interaction forces are pairwise in nature and act between bead centers. The link between the theoretical development and application of the method has been established subsequently [17,18] with applications to micelles and mesophages. The isothermal version of DPD has also been used to model a wide variety of systems as in the lipid bilayer membranes [19], vesicles [20], polymersomes [21], binary immiscible fluids [22], colloidal suspensions [23], and nanotube-polymer composites [24].

[1]Corresponding author.

Contributed by the Heat Transfer Division of ASME for publication in the JOURNAL OF HEAT TRANSFER. Manuscript received March 4, 2008; final manuscript received October 1, 2008; published online January 23, 2009. Review conducted by Robert D. Tzou. Paper presented at the 2008 International Conference on Micro/Nanoscale Heat Transfer (MNHT2008), Tainan, Taiwan, January 6–9, 2008.

The original formulation of DPD conserves linear and angular momentum but not energy [25]. To model heat flow in mesoscopic systems using DPD, an additional internal energy variable is introduced [26,27]. The internal energy variable represents the relaxed degrees of freedom of the particles that make up the bead. The mechanical energy dissipated due to velocity dependent forces is transformed into the internal energy of the beads. In addition to this, a model of heat conduction (HC) is also introduced to account for heat transfer processes that take place due to changes in internal energy. Since beads can have different internal energies, temperature gradients can easily be modeled. This model has been used to study one-dimensional heat conduction in a random "frozen" DPD solid [28,29] convection rolls [30] and has recently been used to study generalized hydrodynamics [31].

In studies [28–31], energy conserving DPD has been formulated for and applied to *single component* systems. As previously discussed, multicomponent and multiphase systems such as liquid-vapor mixtures, nanoparticle suspensions, nanoparticle composites, and emulsions are critically important in many heat transfer applications. To enable application of energy conserving DPD to such systems, a clear framework for modeling *multicomponent* systems with energy conserving DPD is needed but so far has not been published in the literature. For this reason, we present for the first time a multicomponent framework for energy conserving DPD that explicitly represents all components in the system. This framework, found in Sec. 2, is a generalization of the previous implementations of energy conserving DPD [26–31].

Additionally, the (single component) DPD expressions presented previously in the literature are typically given in dimensionless form. To relate DPD simulation results to real physical quantities, scaling factors linking dimensional and dimensionless quantities must be identified. Although scaling factors for quantities such as mass, length, and thermal energy have been defined previously [17], scaling factors for other quantities have not been explicitly defined. This makes it unclear as to how to compute dimensional physical properties in DPD. Our second new contribution in this work is to find explicit definitions for the unknown scaling factors. These definitions and details of how they were found are presented in Sec. 3. Briefly, we follow a nondimensionalization procedure similar to that used in our previous analysis of isothermal DPD [32]. In Secs. 4 and 5, we validate the framework, under the special case of identical components, for one-dimensional transient and one- and two-dimensional steady-state heat conduction in a random DPD solid. The results, which compare well with existing DPD works and with analytical solutions in one and two dimensions, show the promise of energy conserving DPD for modeling heat transfer at mesoscopic length scales.

2 Multicomponent Energy Conserving DPD: Governing Equations

2.1 Background. In *isothermal* DPD, bead positions, velocities, and forces are tracked and the state of a bead in the system is characterized by a set of position and momentum coordinates $\{\mathbf{r},\mathbf{p}\}$. In *energy conserving* DPD, an additional internal energy variable $\varepsilon_{i\alpha}$ is introduced [26,27]. This variable represents the relaxed degrees of freedom of the particles that make up the bead. It is assumed that the bead represents a local thermodynamic subsystem and that the internal degrees of freedom of the particles have fast relaxation time scales. In this way, the internal energy becomes a slow variable over the DPD time scale and changes can be tracked using an energy evolution equation. With this variable, the state of the system can now be characterized by the position, momentum, and energy coordinates $\{\mathbf{r}_{i\alpha},\mathbf{p}_{i\alpha},\varepsilon_{i\alpha}\}$ of all beads. Along with bead internal energy, bead temperature variable $T_{i\alpha}$ may be also be found through

$$T_{i\alpha} = \left[\frac{\partial S_{i\alpha}}{\partial \varepsilon_{i\alpha}}\right]^{-1} \tag{1}$$

provided that the equation of state linking internal energy, temperature, and bead entropy $S_{i\alpha}$ is known.

The significance of energy conserving DPD is that it is able to model heat flow in mesoscopic systems by allowing differences in bead energies and temperatures. The governing equations for multicomponent energy conserving DPD are discussed below. Key aspects of multicomponent isothermal DPD, which were discussed by us previously, have been introduced in abbreviated form below for clarity. For more details, we refer the reader to Ref. [32]. Here the main focus is on the additional governing equations required for the constant energy framework.

2.2 Review of Isothermal DPD. The DPD governing equations are stochastic ordinary differential equations (SODEs) that represent continuous Markov processes of the Langevin type [14]. The equations of motion for the ith bead of component α with position coordinate $\mathbf{r}_{i\alpha}$, velocity coordinate $\mathbf{v}_{i\alpha}$, and mass m_α are given by

$$\frac{d}{dt}[\mathbf{r}_{i\alpha}] = \mathbf{v}_{i\alpha} \tag{2}$$

$$m_\alpha \frac{d}{dt}[\mathbf{v}_{i\alpha}] = \mathbf{F}^C_{i\alpha} + \mathbf{F}^D_{i\alpha} + \mathbf{F}^R_{i\alpha} \tag{3}$$

where $\mathbf{F}^C_{i\alpha}$, $\mathbf{F}^D_{i\alpha}$, and $\mathbf{F}^R_{i\alpha}$ are the conservative, dissipative, and random forces acting on the ith bead of component α. These forces, which have been defined previously [32,15], are based on pairwise interactions between beads of type α and beads of type β. These interactions depend on bead-bead interaction parameters $a_{\alpha,\beta}$, $\gamma_{\alpha,\beta}$, and $\sigma_{\alpha,\beta}$, which govern the conservative, dissipative, and random force interactions between beads i and j of components α and β, respectively. Additionally, the forces depend on position, dimensionless position, and relative velocity vectors between beads $i\alpha$ and $j\beta$. These are defined as

$$\mathbf{r}_{i\alpha,j\beta} = \mathbf{r}_{i\alpha} - \mathbf{r}_{j\beta} \tag{4}$$

$$\hat{\mathbf{r}}_{i\alpha,j\beta} = \frac{\mathbf{r}_{i\alpha,j\beta}}{r_{i\alpha,j\beta}} \tag{5}$$

$$\mathbf{v}_{i\alpha,j\beta} = \mathbf{v}_{i\alpha} - \mathbf{v}_{j\beta} \tag{6}$$

and the magnitude of the position vector is given by

$$r_{i\alpha,j\beta} = |\mathbf{r}_{i\alpha,j\beta}| \tag{7}$$

The conservative, dissipative, and random forces also depend on arbitrary weight functions that vanish at the cutoff distance $r_{i\alpha,j\beta} = r^c_{\alpha,\beta}$. Typically the conservative and random weight functions $w^C_{i\alpha,j\beta}$ and $w^R_{i\alpha,j\beta}$ are chosen to be equal to each other. The two most commonly used weight functions used for these are the simple Groot/Warren function [17] and the Lucy function [28]. The dissipative weight function $w^D_{i\alpha,j\beta}$ is related to the random weight function; this relationship is discussed in Sec. 2.4. Finally, the random force depends on a normal random number $\psi_{i\alpha,j\beta}$ with zero mean and unit variance that is chosen independently for every pair of interacting beads in the system [17].

2.3 Energy Conserving DPD: Additional Equations. The additional governing equations required for the constant energy framework are based on the mechanical energy of the DPD system. For single component systems, the equation for changes in mechanical energy has been proposed in Refs. [26,27] and derived briefly in Ref. [33]. To be consistent with the notation introduced for a multicomponent system, the derivation is redone and described below. The total mechanical energy of the system is defined as the sum of potential and kinetic energies:

$$E_{\text{mech}} = \frac{1}{2}\sum_{\alpha}\sum_{\beta}\sum_{j\beta\neq i\alpha}^{N_\beta} V_{i\alpha,j\beta}(r_{i\alpha,j\beta}) + \frac{1}{2}\sum_{\alpha} m_\alpha[\mathbf{v}_{i\alpha}\bullet\mathbf{v}_{i\alpha}] \quad (8)$$

The change in mechanical energy can then be written as

$$d[E_{\text{mech}}] = d\left[\frac{1}{2}\sum_{\alpha}\sum_{\beta}\sum_{j\beta\neq i\alpha}^{N_\beta} V_{i\alpha,j\beta}(r_{i\alpha,j\beta})\right] + d\left[\frac{1}{2}\sum_{\alpha} m_\alpha[\mathbf{v}_{i\alpha}\bullet\mathbf{v}_{i\alpha}]\right] \quad (9)$$

The first term in Eq. (9) simplifies as

$$d\left[\frac{1}{2}\sum_{\alpha}\sum_{\beta}\sum_{j\beta\neq i\alpha}^{N_\beta} V_{i\alpha,j\beta}(r_{i\alpha,j\beta})\right] = -\frac{1}{2}\sum_{\alpha}\sum_{\beta}\sum_{j\beta\neq i\alpha}^{N_\beta} \mathbf{F}^{\text{C}}_{i\alpha,j\beta}\bullet\mathbf{v}_{i\alpha,j\beta}dt \quad (10)$$

For the second term, note that $\mathbf{v}_{i\alpha}$ is a stochastic variable and that E_{mech} is a function of this variable. The derivative of $d[\mathbf{v}_{i\alpha}\bullet\mathbf{v}_{i\alpha}]$ is given by a stochastic Taylor expansion of the function (Ito's formula) [34]. Applying this expansion to the second term on the right-hand side (RHS) of Eq. (9) gives

$$d\left[\frac{1}{2}\sum_{\alpha} m_\alpha[\mathbf{v}_{i\alpha}\bullet\mathbf{v}_{i\alpha}]\right] = \sum_{\alpha} m_\alpha[\mathbf{v}_{i\alpha}\bullet d[\mathbf{v}_{i\alpha}]] + \frac{1}{2}\sum_{\alpha}\sum_{\beta}\sum_{j\beta\neq i\alpha}^{N_\beta} m_a\frac{\sigma^2_{\alpha,\beta}[w^{\text{R}}_{i\alpha,j\beta}(r_{i\alpha,j\beta})]^2}{m^2_\alpha}dt \quad (11)$$

Using Eq. (3), the first term on the right-hand side of Eq. (11) can be simplified further. Equation (9) can then be simplified using Eqs. (10) and (11) and written as

$$d[E_{\text{mech}}] = -\frac{1}{2}\sum_{\alpha}\sum_{\beta}\sum_{j\beta\neq i\alpha}^{N_\beta} \mathbf{F}^{\text{C}}_{i\alpha,j\beta}\bullet\mathbf{v}_{i\alpha,j\beta}dt + \sum_{\alpha}\mathbf{v}_{i\alpha}\bullet[\mathbf{F}^{\text{C}}_{i\alpha} + \mathbf{F}^{\text{D}}_{i\alpha} + \mathbf{F}^{\text{R}}_{i\alpha}]dt + \sum_{\alpha}\sum_{\beta}\sum_{j\beta\neq i\alpha}^{N_\beta}\frac{m^{-1}_\alpha}{2}\sigma^2_{\alpha,\beta}[w^{\text{R}}_{i\alpha,j\beta}(r_{i\alpha,j\beta})]^2dt \quad (12)$$

By breaking the summation in the second term of Eq. (12) in terms of α and β and simplifying, we obtain

$$d[E_{\text{mech}}] = \frac{1}{2}\sum_{\alpha}\sum_{\beta}\sum_{j\beta\neq i\alpha}^{N_\beta}\mathbf{v}_{i\alpha,j\beta}\bullet[\mathbf{F}^{\text{D}}_{i\alpha,j\beta} + \mathbf{F}^{\text{R}}_{i\alpha,j\beta}]dt + \sum_{\alpha}\sum_{\beta}\sum_{j\beta\neq i\alpha}^{N_\beta}\frac{m^{-1}_\alpha}{2}\sigma^2_{\alpha,\beta}[w^{\text{R}}_{i\alpha,j\beta}(r_{i\alpha,j\beta})]^2dt \quad (13)$$

It is now assumed that the mechanical energy dissipated in Eq. (13) is invested in raising the internal energy $\varepsilon_{i\alpha}$ of the DPD beads in the system [26,27]. The mechanical energy dissipated due to velocity dependent forces is transformed into the internal energy of the beads. In addition to this, a model of heat conduction is also introduced to account for heat transfer processes that take place due to changes in internal energy. Since beads can have different internal energies, temperature gradients can easily be modeled.

The total internal energy change $d[\varepsilon_{i\alpha}]$ for a bead i of component α is given by

$$d[\varepsilon_{i\alpha}] = d[\varepsilon^{\text{VH}}_{i\alpha}] + d[\varepsilon^{\text{HC}}_{i\alpha}] \quad (14)$$

where energy changes arise from two sources. The first source is the change in mechanical energy, which leads to viscous heating (VH) in the system

$$d[E_{\text{mech}}] = -\sum_{i\alpha} d[\varepsilon^{\text{VH}}_{i\alpha}] \quad (15)$$

Using explicit definitions of forces from Ref. [32] in Eq. (13), the viscous heating term can be written as

$$d[\varepsilon^{\text{VH}}_{i\alpha}] = \frac{1}{2}\sum_{\beta}\sum_{j\beta\neq i\alpha}^{N_\beta}\gamma_{\alpha,\beta}w^{\text{D}}_{i\alpha,j\beta}(r_{i\alpha,j\beta})[\mathbf{v}_{i\alpha,j\beta}\bullet\hat{\mathbf{r}}_{i\alpha,j\beta}]^2dt - \frac{1}{2}\sum_{\beta}\sum_{j\beta\neq i\alpha}^{N_\beta}\sigma_{\alpha,\beta}w^{\text{R}}_{i\alpha,j\beta}(r_{i\alpha,j\beta})[\mathbf{v}_{i\alpha,j\beta}\bullet\hat{\mathbf{r}}_{i\alpha,j\beta}]dW_{i\alpha,j\beta} - \frac{m^{-1}_\alpha}{2}\sum_{\beta}\sum_{j\beta\neq i\alpha}^{N_\beta}\sigma^2_{\alpha,\beta}[w^{\text{R}}_{i\alpha,j\beta}(r_{i\alpha,j\beta})]^2dt \quad (16)$$

The second source of internal energy change arises from differences in internal energy content between the beads. This bead-bead transfer is modeled as a mesoscopic heat conduction (HC) term. This term is proposed [26,27] from the theory of irreversible thermodynamics to be

$$d[\varepsilon^{\text{HC}}_{i\alpha}] = \sum_{\beta}\sum_{j\beta\neq i\alpha}^{N_\beta}\text{K}^{\varepsilon}_{\alpha,\beta}\left[\frac{1}{T_{i\alpha}} - \frac{1}{T_{j\beta}}\right]w^{\varepsilon}_{i\alpha,j\beta}(r_{i\alpha,j\beta})dt + \sum_{\beta}\sum_{j\beta\neq i\alpha}^{N_\beta}\Lambda^{\varepsilon}_{\alpha,\beta}w^{\varepsilon\text{R}}_{i\alpha,j\beta}(r_{i\alpha,j\beta})dW^{\varepsilon}_{i\alpha,j\beta} \quad (17)$$

In Eq. (17), the first term corresponds to the transfer of heat due to differences in bead temperature (internal energy) and the second term corresponds to fluctuations due to a random heat flux. $\text{K}^{\varepsilon}_{\alpha,\beta}$ is a mesoscopic heat conduction term and $\Lambda^{\varepsilon}_{\alpha,\beta}$ determines the strength of the random heat flux in the system. The relation between $\Lambda^{\varepsilon}_{\alpha,\beta}$ and $\text{K}^{\varepsilon}_{\alpha,\beta}$ will be discussed in Sec. 2.4.

Equation (17) may be considered a mesoscopic constitutive law for heat conduction in which discrete beads exchange energy and undergo thermal fluctuations. However, it is important to note that the equation is not directly analogous to the Fourier law since no gradients or areas appear directly in the equation. Consequently, $\text{K}^{\varepsilon}_{\alpha,\beta}$ is similar to but not precisely the same as the macroscopic thermal conductivity.

As with the random force term discussed above, the random heat flux is modeled as a Weiner process $dW_{i\alpha,j\beta}$, which for computer simulations becomes

$$\frac{dW^{\varepsilon}_{i\alpha,j\beta}}{dt} = \frac{\psi^{\varepsilon}_{i\alpha,j\beta}dt^{1/2}}{dt} = \psi^{\varepsilon}_{i\alpha,j\beta}dt^{-1/2} \quad (18)$$

Again $\psi^{\varepsilon}_{i\alpha,j\beta}$ is a normal random number of zero mean and unit variance that is chosen independently for a pair of beads at each time step.

2.4 Considerations From Fluctuation: Dissipation Relations and Detailed Balance Conditions. The values of the DPD parameters and the functional form of the dissipative force weight functions introduced above are found through the fluctuation-dissipation (F-D) theorem and detailed balance conditions. The SODEs that govern the motion of DPD beads can be converted to an equivalent Fokker–Planck description of equations [34]. These equations give the evolution of probability distribution of the degrees of freedom of a given system. For the Fokker–Planck system to have an equilibrium distribution function, certain F-D relations have to be satisfied.

The weight functions used both in the momentum and energy equations satisfy the following relation:

$$w^{D}_{i\alpha,j\beta}(r_{i\alpha,j\beta}) = [w^{R}_{i\alpha,j\beta}(r_{i\alpha,j\beta})]^2 \quad (19)$$

$$w^{\varepsilon}_{i\alpha,j\beta}(r_{i\alpha,j\beta}) = [w^{\varepsilon R}_{i\alpha,j\beta}(r_{i\alpha,j\beta})]^2 \quad (20)$$

The friction parameter in the constant energy case is different from that of isothermal DPD, as it now depends on the individual fluctuating bead temperatures instead of the system temperature

$$\gamma_{\alpha,\beta} = \frac{\sigma_{\alpha,\beta}^2}{4k_B}\left[\frac{1}{T_{i\alpha}} + \frac{1}{T_{j\beta}}\right] \tag{21}$$

This property ensures that temperature gradients can be sustained in this version of DPD. The random heat flux parameter $\Lambda_{\alpha,\beta}^{\varepsilon}$ is related to the mesoscopic heat conduction term $K_{\alpha,\beta}^{\varepsilon}$ using the following F-D based expression:

$$[\Lambda_{\alpha,\beta}^{\varepsilon}]^2 = 2k_B K_{\alpha,\beta}^{\varepsilon} \tag{22}$$

Since the total mechanical energy E_{mech} is conserved, it follows that Eq. (17) is antisymmetric under particle exchange, i.e., the heat lost by a bead during heat conduction must be gained by the other bead. If the indices $(i\alpha, j\beta)$ are switched, the only way the antisymmetry will be maintained is by assuming that (1) the heat conduction term is symmetric under particle interchange

$$K_{\alpha,\beta}^{\varepsilon} = K_{\beta,\alpha}^{\varepsilon} \tag{23}$$

and (2) the increments of the random heat flux Weiner process have the following property:

$$dW_{i\alpha,j\beta}^{\varepsilon} = -dW_{j\beta,i\alpha}^{\varepsilon} \tag{24}$$

In addition, the system has to satisfy other properties known as detailed balance [33], which follow from the process being modeled as Markovian and the Fokker–Planck description of the system

$$\sigma_{\alpha,\beta} = \sigma_o[\varepsilon_{i\alpha} - \varepsilon_{j\beta}]^{n_1} \tag{25}$$

$$K_{\alpha,\beta}^{\varepsilon} = K_0 k_B\left[\frac{\varepsilon_{i\alpha} + \varepsilon_{j\beta}}{2}\right]^{n_2} \tag{26}$$

where σ_0 represents the strength of the noise level and K_0 is the heat collision frequency of the system. The exponents n_1 and n_2 control the temperature dependence of the noise and mesoscopic heat conduction terms, which is related to the energy in Eq. (1). As dimensional consistency requires that the units of $\sigma_{\alpha,\beta}$ and $K_{\alpha,\beta}^{\varepsilon}$ not vary based on the choice of n_1 and n_2, it follows that σ_0 and K_0 are not constants but are values whose units vary with n_1 and n_2. The precise form of this variation is shown in Eqs. (33) and (34) of Sec. 3.3, which give the (dimensional) scaling factors σ_0^* and K_0^*.

3 Nondimensionalization and Scaling Factors

3.1 Background. The multicomponent energy conserving DPD expressions introduced in Sec. 2 are in dimensional form. Importantly, the parameters in these expressions are also dimensional. The difficulty in performing dimensional DPD simulations, which are required for computation of real physical quantities and modeling real engineering processes, is that the appropriate dimensional parameters to use in these expressions are often not known. Although *dimensionless* values of all needed parameters are readily available in the literature, the scaling factors required to convert between the dimensional and dimensionless representations are not available for all parameters. This issue is addressed through the two-step procedure discussed below.

3.2 Dimensionless Equations From General Scaling Factors. Following Munson et al. [35], the governing equations are nondimensionalized using *general* scale factors that have *not* yet been defined in terms of the known parameters of the system. This is done for generality since the proper explicit definition of scale factors from such parameters depends on the dominant physical processes of the problem of interest and these are not necessarily the same for every DPD problem. As a related continuum fluid mechanics example, in high speed flows pressure is scaled by the product of density and the square of freestream velocity, while for very low speed flows it is scaled by viscous stress [36]. Thus, the scaling factor is problem dependent. Similarly for DPD, conservative forces in DPD are negligible for some types of fluids (e.g., ideal fluids), so universal use of the conservative force parameter as a scale factor would lead to poor scaling, e.g., nondimensional variables approaching infinity, for those fluids.

Table 1 Dimensionless quantities and scaling factors for parameters used in the DPD system

Length[a]	$\bar{\mathbf{r}} = \dfrac{\mathbf{r}}{r^*}$
Velocity[a]	$\bar{\mathbf{v}} = \dfrac{\mathbf{v}}{v^*}$
Time[a]	$\bar{t} = \dfrac{t}{t^*}$
Mass[a]	$\bar{m} = \dfrac{m}{m^*}$
Force[a]	$\bar{\mathbf{F}} = \dfrac{\mathbf{F}}{F^*}$
Conservative force parameter[a]	$\bar{a} = \dfrac{a}{a^*}$
Dissipative force parameter[a]	$\bar{\gamma} = \dfrac{\gamma}{\gamma^*}$
Random force parameter[a]	$\bar{\sigma} = \dfrac{\sigma}{\sigma^*}$
System volume[a]	$\bar{\Omega} = \dfrac{\Omega}{\Omega^*}$
Bead temperature	$\bar{T} = \dfrac{T}{T^*}$
Internal energy	$\bar{\varepsilon} = \dfrac{\varepsilon}{\varepsilon^*}$
Mesoscopic heat conduction parameter	$\bar{K}^{\varepsilon} = \dfrac{K^{\varepsilon}}{[K^{\varepsilon}]^*}$
Random heat flux parameter	$\bar{\Lambda}^{\varepsilon} = \dfrac{\Lambda^{\varepsilon}}{[\Lambda^{\varepsilon}]^*}$
Strength of noise level	$\bar{\sigma}_o = \dfrac{\sigma_o}{\sigma_o^*}$
Heat collision frequency	$\bar{K}_0 = \dfrac{K_0}{K_0^*}$

[a]For more details, Refer to Ref. [32].

The scaling factors for the DPD variables are denoted with an asterisk (*) and the dimensionless quantities are denoted with a bar, as shown in Table 1. These scaling factors define the DPD units used in the simulations. The scaling factors for variables used in Secs. 2.1 and 2.2 and the reduced equations that arise from this have been derived elsewhere [32]. For brevity, the dimensionless forms of only the energy equations (16) and (17) are shown below:

$$\begin{aligned}\frac{d[\bar{\varepsilon}_{i\alpha}^{\text{VH}}]}{d\bar{t}} = {} & \frac{1}{2}\sum_{\beta}\sum_{j\beta\neq i\alpha}^{N_\beta}\left[\frac{\gamma^*[v^*]^2 t^*}{\varepsilon^*}\right]\bar{\gamma}_{\alpha,\beta}\bar{w}_{i\alpha,j\beta}^{\text{D}}(\bar{r}_{i\alpha,j\beta})[\bar{\mathbf{v}}_{i\alpha,j\beta}\bullet\hat{\bar{\mathbf{r}}}_{i\alpha,j\beta}]^2 \\ & - \frac{1}{2}\sum_{\beta}\sum_{j\beta\neq i\alpha}^{N_\beta}\left[\frac{\sigma^* v^*[t^*]^{1/2}}{\varepsilon^*}\right]\bar{\sigma}_{\alpha,\beta}\bar{w}_{i\alpha,j\beta}^{\text{R}}(\bar{r}_{i\alpha,j\beta}) \\ & \times[\bar{\mathbf{v}}_{i\alpha,j\beta}\bullet\hat{\bar{\mathbf{r}}}_{i\alpha,j\beta}]\bar{\psi}_{i\alpha,j\beta}d\bar{t}^{-1/2} \\ & - \frac{\bar{m}_\alpha^{-1}}{2}\sum_{\beta}\sum_{j\beta\neq i\alpha}^{N_\beta}\left[\frac{[\sigma^*]^2 t^*}{m^*\varepsilon^*}\right]\bar{\sigma}_{\alpha,\beta}^2[\bar{w}_{i\alpha,j\beta}^{\text{R}}(\bar{r}_{i\alpha,j\beta})]^2\end{aligned} \tag{27}$$

$$\frac{d[\bar{\varepsilon}_{i\alpha}^{\mathrm{HC}}]}{d\bar{t}} = \sum_{\beta}\sum_{j\beta\neq i\alpha}^{N_\beta}\left[\frac{[\mathrm{K}^{\varepsilon}]^*t^*}{\varepsilon^*T^*}\right]\bar{\mathrm{K}}_{\alpha,\beta}^{\varepsilon}\left[\frac{1}{\bar{T}_{i\alpha}}-\frac{1}{\bar{T}_{j\beta}}\right]\bar{w}_{i\alpha,j\beta}^{\varepsilon}(\bar{r}_{i\alpha,j\beta}) + \sum_{\beta}\sum_{j\beta\neq i\alpha}^{N_\beta}\left[\frac{[\Lambda^{\varepsilon}]^*[t^*]^{1/2}}{\varepsilon^*}\right]\bar{\Lambda}_{\alpha,\beta}^{\varepsilon}\bar{w}_{i\alpha,j\beta}^{\varepsilon\mathrm{R}}(\bar{r}_{i\alpha,j\beta})\bar{\psi}_{i\alpha,j\beta}^{\varepsilon}d\bar{t}^{-1/2} \tag{28}$$

Two key points arise from the above expressions. The first point is that *all* parameters, including variables and material/system parameters, are nondimensionalized by DPD convention in such a way that the dimensionless parameter value is not equal to 1. For example, the dimensionless random ($\bar{\sigma}_{\alpha,\beta}$) force parameter commonly assumes the value 3 for water at room temperature [17].

3.3 Explicit Definition of Unknown Scaling Factors. The second point important point from Eqs. (27) and (28) is that the general scaling factors, which as of yet have not been defined, are grouped into square bracketed prefactor terms on the right-hand side of the equations. By direct term-by-term comparison to standard DPD equations in the literature [17], we are able to explicitly define the unknown scaling factors in a manner consistent with standard DPD practice. Specifically, the square bracketed terms must equal 1 to achieve such consistency. This sets the relationships between scaling factors and enables unknown factors to be found from known factors.

The model of Groot/Warren explicitly defined scaling factors for mass, length, and thermal energy but did not do so for several other important quantities in Table 1. In our previous work [32], we explicitly defined the remaining scaling factors for isothermal DPD. We use the same procedure here to extend it to the additional energy equations (27) and (28) required in energy conserving DPD. The scaling factors chosen here are based on the solvent in a multicomponent system, which has faster time scales compared with the suspended particles or monomers. The solvent component is denoted by the subscript (1) and solvent-solvent interactions are denoted by the subscript (1,1).

The explicit scaling factor definition is found by first recalling the internal energy and temperature scaling factors defined by Mackie et al. [30]. The bead internal energy scale is chosen as the thermal energy scale of the solvent

$$\varepsilon^* = [k_B T]_{(1)} \tag{29}$$

The bead internal temperature scale is set to be the same as the temperature of the solvent

$$T^* = T_{(1)} \tag{30}$$

Using the scaling factors from Ref. [32] and Eqs. (29) and (30) and setting the square bracketed terms in Eq. (27) ($[\gamma^*[v^*]^2t^*/\varepsilon^*]$, $[\sigma^*v^*[t^*]^{1/2}/\varepsilon^*]$, and $[[\sigma^*]^2t^*/m^*\varepsilon^*]$) and Eq. (28) ($[[K^{\varepsilon}]^*t^*/\varepsilon^*T^*]$ and $[\Lambda^*[t^*]^{1/2}/\varepsilon^*]$) equal to 1, we have the following definitions for the scaling factors for the mesoscopic heat conduction parameter and random heat flux parameter:

$$[K^{\varepsilon}]^* = \frac{T_{(1)}[k_B T]_{(1)}^{3/2}}{m_{(1)}^{1/2}r_{(1,1)}^{c}} \tag{31}$$

$$[\Lambda^{\varepsilon}]^* = \frac{[k_B T]_{(1)}^{5/4}}{m_{(1)}^{1/4}[r_{(1,1)}^{c}]^{1/2}} \tag{32}$$

Similarly, by casting Eqs. (25) and (26) in dimensionless form and setting the square bracketed terms to one, the scaling factors of σ_0^* and K_0^* become

$$\sigma_0^* = \frac{\sigma^*}{(\varepsilon^*)^{n_1}} \tag{33}$$

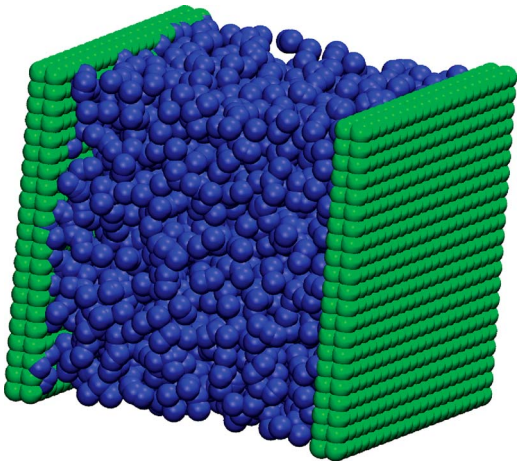

Fig. 1 Initial setup for one-dimensional heat conduction with N=3000 and N_{wall}=1764; figure rendered using VMD [39]

$$K_0^* = \frac{[K^{\varepsilon}]^*}{k_B(\varepsilon^*)^{n_2}} \tag{34}$$

Once all the dimensionless groupings and scaling factors have been identified, Eqs. (19)–(22) and (25)–(28) can be easily rewritten in reduced form. From this, we recover a multicomponent version of the standard dimensionless DPD equations [26,27,33]. An important consideration in DPD nondimensionalization is that no simplification (i.e., reduction in number of parameters) is achieved by scaling the DPD parameters. This is due to the convention in DPD of nondimensionalizing material parameters in such a way that the dimensionless parameter values are not equal to 1. The result is that the dimensionless variables appear in the equations instead of vanishing, leaving the number of dimensionless parameters the same as the number of dimensional parameters. In this sense, DPD nondimensionalization is different from the standard nondimensionalization approaches used in continuum fluid mechanics whereby assembling dimensional parameters into dimensionless groups leads to a reduction in the number of parameters necessary to specify a problem.

4 One Dimensional Steady: State and Transient Heat Conduction

As a first step in validating the multicomponent model formulated above, the heat conduction model in Eq. (28) is compared with analytical solutions for steady and unsteady heat conduction in one and two dimensions. Additionally validations are performed against existing work in the literature by Ripoll et al. [28,29,33]. To implement heat conduction, simulations were performed on a DPD solid with "frozen" beads randomly oriented with respect to cubic lattice sites. i.e., the beads are not allowed to move. This model serves as a particle-based counterpart for the fluctuating Fourier equation for heat conduction [26]. A simple Euler algorithm was used to march forward in time. The beads are enclosed with infinite walls in the z-direction (see Fig. 1). Periodic boundary conditions are imposed in the other two directions. Constant temperature boundary conditions are imposed on the two walls. The beads are set at an intermediate temperature initially. The parameters for the simulations are reported in Table 2. All simulations were performed using the Lucy function for the conservative and random weights:

$$\bar{w}_{i\alpha,j\beta}(\bar{r}_{i\alpha,j\beta}) = \frac{105}{6\pi}\left[1+3\frac{\bar{r}_{i\alpha,j\beta}}{\bar{r}_{\alpha,\beta}^{c}}\right]\left[1-\frac{\bar{r}_{i\alpha,j\beta}}{\bar{r}_{\alpha,\beta}^{c}}\right]^3 \tag{35}$$

The dissipative weights are found by squaring the Lucy function, following Eqs. (19) and (20) in Sec. 2.4.

Table 2 Value for parameters used in the heat conduction model

Parameter	Value
N	3000, 5184, 10125
N_{wall}	1764, 5954
$\bar{\Omega}=\bar{L}^3$	10^3, 12^3, 15^3
$\bar{r}^c_{(1,1)}$	1.0, 1.39, 1.71, 2.0, 2.19
$\bar{K}_0$	1e-04
$\bar{\varepsilon}_c$	1000.0
$\bar{T}_{\text{hot}}$	Range 2–25
$\bar{T}_{\text{cold}}$	1.0
$\bar{\rho}_{(1)}$	3, 8, 15, 24, 31.62
$N^m_{(1)}$	3
$\bar{m}_{(1)}$	1.0
$\Delta\bar{t}$	0.01
n_2	2

The volume is divided into bins and the bead temperature $\bar{T}_{i\alpha}$ is averaged in each bin. The relation between temperature and energy (Eq. (10)) was chosen to be the same as that of Ripoll et al. [28,29,33] in order to compare the present results to theirs. In this model, it is assumed that a simple linear law relates the bead internal energy and temperature

$$\varepsilon_{i\alpha} = C_v T_{i\alpha} \tag{36}$$

Here C_v is the heat capacity of the DPD beads and has the units of J/K. This simple equation of state is that of a perfect solid and is a good approximation for metals. Using the scaling factors in Eq. (36), this simplifies to

$$\bar{\varepsilon}_{i\alpha} = \bar{\varepsilon}_c \bar{T}_{i\alpha} \tag{37}$$

where $\bar{\varepsilon}_c = C_v/k_B$ is the dimensionless heat capacity. Using Eqs. (1) and (36), the entropy of the beads can be written as

$$S_{i\alpha} = C_v \ln\left[\frac{\varepsilon_{i\alpha}}{C_v}\right] \tag{38}$$

Ripoll et al. [28,29,33] used a value of $n_2=2$ in Eq. (34) so that the mesoscopic thermal conduction parameter would depend on energy (or temperature through Eq. (36)) in a quadratic manner. We use the same value in our simulations. Equation (33) does not feature in these simulations; it is used only in Eq. (27), which is not solved since the beads are frozen and have no momenta. Similarly parameters $\bar{a}, \bar{\gamma}, \bar{\sigma}$ are not used as they only appear in equations for momentum conservation and viscous heating. Therefore, no value of n_1 is needed in the present simulations. Ripoll et al. [28,29,33] observed that for very small values of dimensionless heat capacity $\bar{\varepsilon}_c < 10$, the random heat flux term produces a negative temperature in some beads. This violates the second law of thermodynamics by producing a flow of internal energy from a cold bead to a hot bead. Hence $\bar{\varepsilon}_c$ is chosen to have the numerical value of 1000 to ensure stability of the system. More generally, if real systems were to be modeled, the total heat capacity of the DPD system would have to be matched with the true heat capacity as

$$\frac{N\bar{\varepsilon}_c k_B}{\Omega} = \rho_{\text{real}} C_{v,\text{real}} \tag{39}$$

Simulations in this study were run for different densities $\bar{\rho}_{(1)}$ and at different temperature gradients defined as

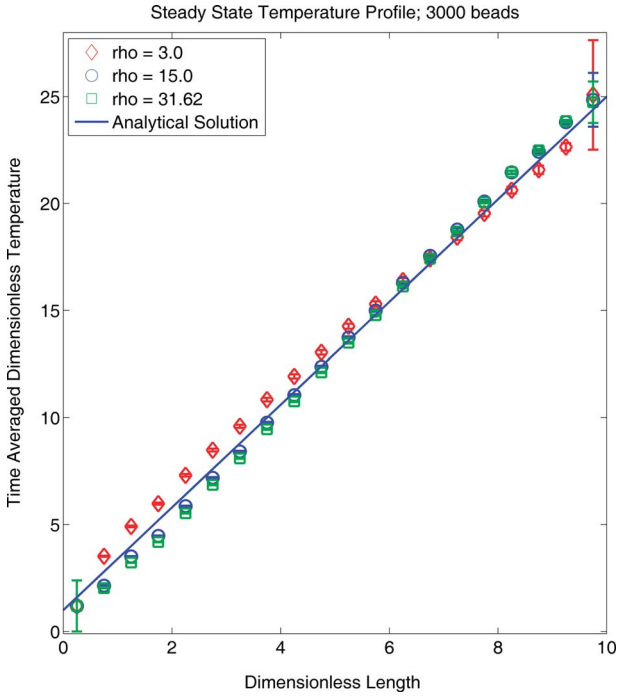

Fig. 2 Time averaged dimensionless steady-state temperature for a system with N=3000, $\bar{\rho}_{(1)}$=3.0,15.0,31.62

$$\bar{\nabla}\bar{T} = \frac{\bar{T}_{\text{hot}} - \bar{T}_{\text{cold}}}{\bar{L}} \tag{40}$$

The simulations were allowed to run for 400,000 iterations until a steady state was reached. The bead temperature was binned and recorded at each time step and averages were calculated over the next 100,000 iterations. For smaller temperature gradients, we observe that the temperature profile is not perfectly linear. This could be due to the fluctuations in the algorithm having a greater effect than the imposed temperature gradient. However, for larger temperature gradients and all densities simulated, the profile is close to linear, as shown in Fig. 2. The straight line in Fig. 2 corresponds to the steady state solution to the 1D continuum heat diffusion equation [37]. In Fig. 2, the ends have large error bars because there are fewer beads in those bins. The initial setup of the random lattice of DPD beads was first equilibrated using walls with a finite repulsion and is responsible for the fewer beads at the ends.

In Fig. 2, the slight deviation of the temperature profile at different densities from the analytical solution could be attributed to differences between the Fourier continuum model and the particle-based simulation method with a pair conduction interaction. The trend in Fig. 2 is similar to the results of Ripoll et al., which involved a large number density. Ripoll et al. [28] reported that the strength of the fluctuations in the model varies inversely with $\bar{\varepsilon}_c$. The heat capacity, being an extensive property, is a good measure of the size of the beads. For larger values of $\bar{\varepsilon}_c$, the size of the beads approaches continuum limits. Based on this idea, it is expected that larger values of $\bar{\varepsilon}_c$ compared with the one used here in the simulations would reduce fluctuations and reproduce Fourier's law of heat conduction more accurately. Also based on Ripoll's [33] work, it is expected that grid-based (beads arranged on a regular gridlike structure) lattices would reduce the deviations from linearity.

The transient instantaneous temperature profiles are shown in Fig. 3 for the particular case of N=5184, $\bar{\rho}_{(1)}$=3.0 along with the analytical solution [38]. The trends shown in Fig. 3 compare well with the results of Ripoll [33], which were for a significantly

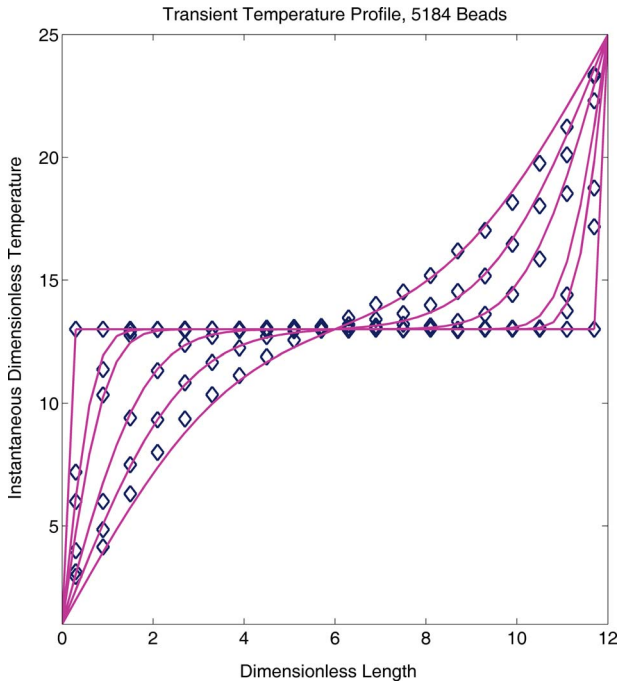

Fig. 3 Instantaneous dimensionless temperature profiles with increasing time for a system with N=5184, $\bar{\rho}_{(1)}$=3.0. The solid lines indicate the analytical temperature profiles and the points indicate the DPD simulation results.

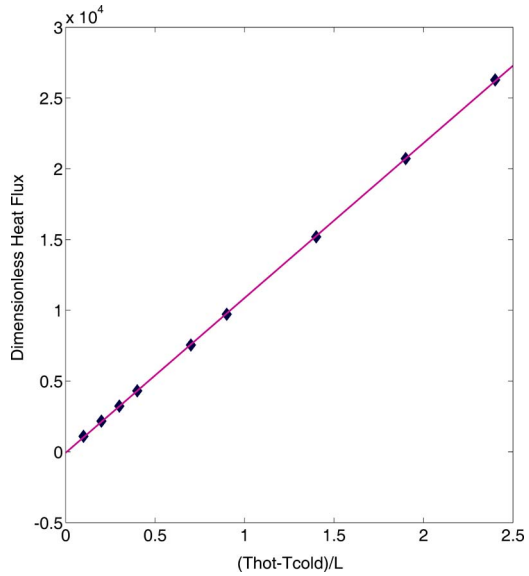

Fig. 4 Dimensionless time averaged heat flux as a function of imposed temperature gradient for a system with N=3000, $\bar{\rho}_{(1)}$ =31.62; the solid line is a linear fit to the simulation results.

higher number density and which were deterministic, as they only involved the first term of Eq. (28). Higher temperatures were sometimes observed in the instantaneous temperature profiles at the ends due to the stochastic nature of algorithm and the smaller number of beads in those regions.

Next a set of simulations was performed where the dimensionless mesoscopic heat flux is calculated using the following expression for different applied temperature gradients:

$$\bar{\mathbf{q}} = \frac{1}{\bar{\Omega}} \sum_{\alpha} \sum_{\beta} \sum_{j\beta \neq i\alpha}^{N_\beta} \bar{\mathrm{K}}^{\varepsilon}_{\alpha,\beta} \left[\frac{1}{\bar{T}_{i\alpha}} - \frac{1}{\bar{T}_{j\beta}} \right] \bar{w}^{\varepsilon}_{i\alpha,j\beta}(\bar{r}_{i\alpha,j\beta}) \bar{\mathbf{r}}_{i\alpha,j\beta} \quad (41)$$

Ripoll [33] defined a heat current that is the same as Eq. (41) without the volume term $\bar{\Omega}$. The heat flux is calculated at every time step and averaged over the last 100,000 time steps after the system has reached a steady state.

As per the macroscopic heat conduction law, the heat flux from the hot wall to the cold wall must be a constant at steady state. This is exactly what we observe in our simulations and is quantified by the very small error in the calculation of average heat flux. The ratio $error = std.dev/\sqrt{N_{steps}}$ was used to calculate the standard error in the mean heat flux and was found to be less than 1% in most cases.

Figure 4 shows the variation of dimensionless heat flux with dimensionless temperature gradient for a particular case of $\bar{\rho}_{(1)}$ =31.62. The linear dependence of heat flux on the imposed temperature gradient is very good and reproduces Fourier's law of heat conduction very well. Qualitatively the results compare very well with Ripoll. Quantitatively the value of the slope calculated using Fig. 4 is different from that of Ripoll. This is likely due to the differences in scaling parameters used for nondimensionalization, which are not very clear from Ripoll's work. Simulations for other densities given in Table 2 also show similar behavior.

The dimensionless thermal conductivity was calculated using the following expression:

$$\bar{\lambda}_{\mathrm{th}} = -\frac{\bar{q}_z}{\bar{\nabla}\bar{T}} \quad (42)$$

The thermal conductivity in Eq. (42) was calculated for a system with N=3000 beads and varying densities: $\bar{\rho}_{(1)}$=3.0–31.62. The results are shown in Fig. 5 as a function of the dimensionless density. The results given in Ref. [33] are presented in terms of thermal diffusivity, which is related to the thermal conductivity through the mass density and specific heat. Figure 5 indicates that thermal conductivity increases with increase in density as a power law as $\bar{\rho}_{(1)}^{1.65}$. Ripoll indicated that their thermal diffusivity results increases with the density as $\bar{\rho}_{(1)}^{2/3}$. However, the exact details of

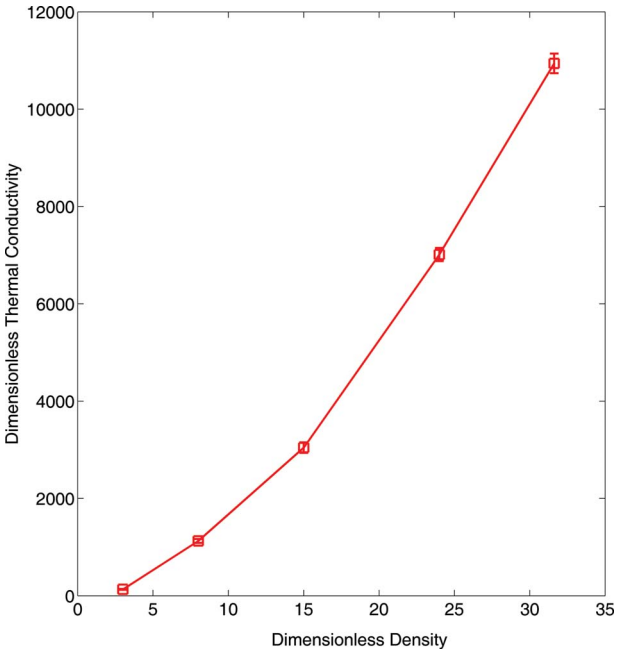

Fig. 5 Dimensionless thermal conductivity as a function of dimensionless density

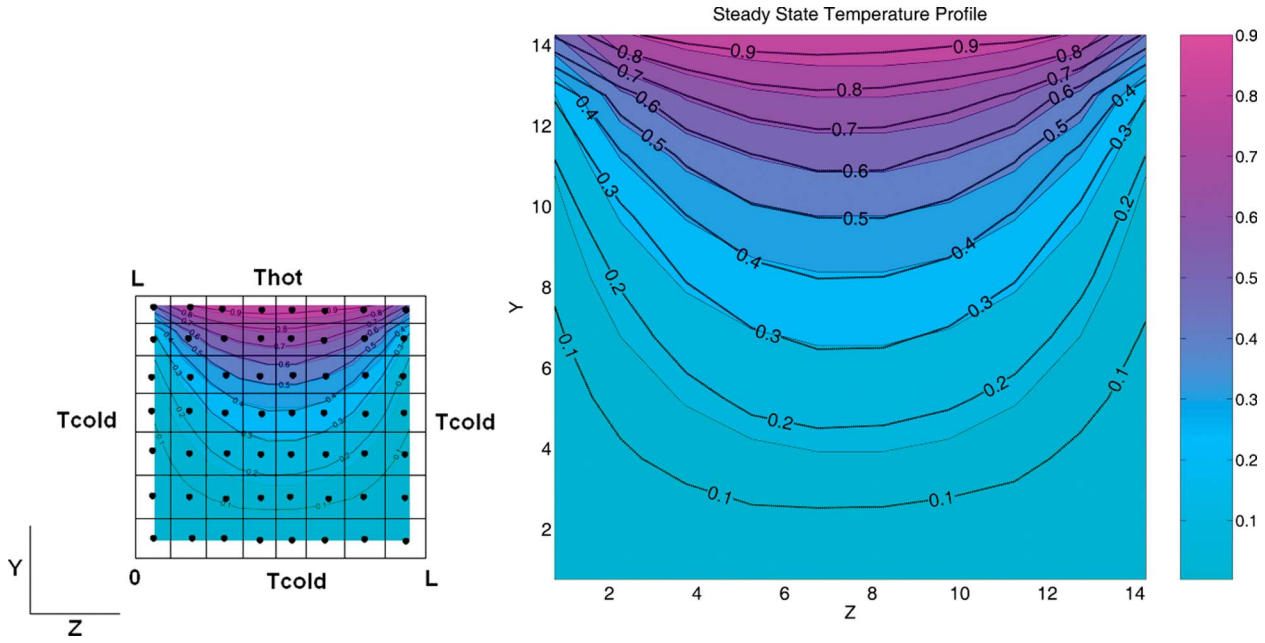

Fig. 6 Steady state isotherms for the two-dimensional heat conduction model; analytical solution [37] is shaded showing the variation in $\bar{\Theta}$ over the *yz* domain

the scaling factors used by Ripoll are not known; hence, the results in Fig. 5 are hard to compare directly to their results. However, increase in thermal conductivity with density is physically correct and the model does capture that effect.

5 Two-Dimensional Heat Conduction

To further strengthen the heat conduction model and its capabilities, we extended the one-dimensional model to two dimensions to compute the steady-state solution for which the analytical solution is well known. In this model, the frozen DPD beads are enclosed by walls in the *y*- and *z*-directions and periodic boundary conditions are applied in the *x*-direction.

The system parameters remain the same as given in Table 2, but only the $N=10125$, $\bar{\rho}=3.0$ case is presented here with $\bar{T}_{\text{hot}}=25.0$. For this model the analytical solution is given in Ref. [37]. The system was equilibrated for 400,000 iterations and the data were collected over the next 100,000 iterations. Bead temperature was recorded and averaged in the 2D *y*-*z* plane by dividing the area into 100 bins. Averages were also taken by taking slices of the plane along the *x*-direction. In Fig. 6, the analytical solution is plotted in the background and is shaded along with the DPD simulations shown as dark black isotherms. The data in Fig. 6 are presented in terms of the transformed variable $\bar{\Theta}=[\bar{T}-\bar{T}_{\text{cold}}]/[\bar{T}_{\text{hot}}-\bar{T}_{\text{cold}}]$. Both the analytical solution and simulation results were calculated at the bin centers shown in lower left hand corner of Fig. 6. For this reason alone, the isotherms do not seem to originate from the corners near the hot wall. As the resolution of the grid is changed and made finer, the isotherms would indeed become sharper close to the wall and merge into the corners next to the hot wall. For the grid resolution picked here, the DPD simulation isotherms seem to lie perfectly within the shaded regions predicted by the analytical solution. The agreement with theory is excellent.

6 Conclusions

A multicomponent framework of the energy conserving DPD model is presented. Explicit definitions for unknown scaling factors that are consistent with DPD convention are found by comparing the present general dimensionless governing equations to the standard DPD expressions in the literature. These factors will enable engineering calculation of real physical properties with DPD. The framework is validated for the special case of identical components in one and two dimensions. The steady one-dimensional heat conduction model is compared against the existing results and reproduces Fourier's law for cases shown here, and transient one-dimensional heat conduction also matches the analytical solution. The model is extended to a two-dimensional problem and also shows excellent agreement with analytical solutions. The general framework developed here will be useful for particle-based modeling of thermal transport in multicomponent systems.

Acknowledgment

This work was supported by the Office of Naval Research (Grant No. N00014-07-1-0665).

Nomenclature

a = conservative force parameter
C_v = specific heat capacity
E = energy of system
$\mathbf{F}$ = force acting at bead center
k_B = Boltzmann's constant
L = domain length
m = mass of bead
N = number of beads in system
N^m = number of particles per bead
$\mathbf{q}$ = heat flux vector
$\mathbf{r}$ = position vector of bead center
r_c = cutoff radius for bead-bead interaction
S = bead entropy
t = time
Δt = time step
T = bead temperature
T_{hot} = hot wall temperature
T_{cold} = cold wall temperature
$\mathbf{v}$ = velocity vector of bead center
V = potential energy
w = weight function
dW, dW^e = increments of the Weiner process

Greek Symbols

Ω = box volume
Φ = bead volume
γ = dissipative force parameter
σ = random noise parameter
σ_0 = strength of random noise parameter
ψ, ψ^{ε} = normal random number
ε = bead internal energy
K = mesoscopic heat conduction parameter
K_0 = strength of mesoscopic heat conduction parameter
Λ = random heat flux parameter
λ_{th} = thermal conductivity

Subscripts and Superscripts

α = type of component
β = type of component
i,j,k,l = bead numbers
(1) = component (1) with bead volume 90 $[A^0]^3$
C = conservative
D = dissipative
R = random
mech = mechanical
th = thermal
wall = wall

References

[1] Cahill, D. G., Ford, W. K., Goodson, K. E., Mahan, G. D., Majumdar, A., Maris, H. J., Merlin, R., and Phillpot, S. R., 2003, "Nanoscale Thermal Transport," J. Appl. Phys., **93**, pp. 793–818.
[2] Stickel, J. J., and Powell, R. L., 2005, "Fluid Mechanics and Rheology of Dense Suspensions," Annu. Rev. Fluid Mech., **37**, pp. 129–149.
[3] Koumoutsakos, P., 2005, "Multiscale Flow Simulations Using Particle," Annu. Rev. Fluid Mech., **37**, pp. 457–487.
[4] Español, P., Serrano, M., and Zuñiga, I., 1997, "Coarse-Graining of a Fluid and Its Relation With Dissipative Particle Dynamics and Smoothed Particle Dynamics," Int. J. Mod. Phys. C, **8**, pp. 899–908.
[5] Allen, M. P., and Tildesley, T. J., 1989, *Computer Simulation of Liquids*, Oxford University Press, New York.
[6] Haile, J. M., 1992, *Molecular Dynamics Simulation: Elementary Methods*, Wiley-Interscience, New York.
[7] Padding, J. T., and Louis, A. A., 2006, "Hydrodynamic Interactions and Brownian Forces in Colloidal Suspensions: Coarse-Graining Over Time and Length Scales," Phys. Rev. E, **74**, 031402.
[8] Succi, S., 2001, *The Lattice Boltzmann Equation: For Fluid Dynamics and Beyond*, Clarendon, Oxford.
[9] Rivet, J. P., and Boon, J. P., 2001, *Lattice Gas Hydrodynamics*, Cambridge University Press, Cambridge.
[10] Ermak, D. L., and McCammon, J. A., 1978, "Brownian Dynamics With Hydrodynamic Interactions," J. Chem. Phys., **69**, pp. 1352–1360.
[11] Brady, J. F., and Bossis, G., 1988, "Stokesian Dynamics," Annu. Rev. Fluid Mech., **20**, pp. 111–157.
[12] Hoogerbrugge, P. J., and Koelman, J. M. V. A., 1992, "Simulating Microscopic Hydrodynamic Phenomena With Dissipative Particle Dynamics," Europhys. Lett., **19**(3), pp. 155–160.
[13] Español, P., and Revenga, M., 2003, "Smoothed Dissipative Particle Dynamics," Phys. Rev. E, **67**, p. 026705.
[14] Español, P., and Warren, P., 1995, "Statistical Mechanics of Dissipative Particle Dynamics," Europhys. Lett., **30**, pp. 191–196.
[15] Coveney, P. V., and Español, P., 1997, "Dissipative Particle Dynamics for Interacting Multicomponent Systems," J. Phys. A, **30**, pp. 779–784.
[16] Español, P., 1995, "Hydrodynamics From Dissipative Particle Dynamics," Phys. Rev. E, **52**(2), pp. 1734–1742.
[17] Groot, R. D., and Warren, P. B., 1997, "Dissipative Particle Dynamics: Bridging the Gap Between Atomistic and Mesoscopic Simulation," J. Chem. Phys., **107**(11), pp. 4423–4435.
[18] Maiti, A., and McGrother, S., 2004, "Bead-Bead Interaction Parameters in Dissipative Particle Dynamics: Relation to Bead-Size, Solubility Parameter, and Surface Tension," J. Chem. Phys., **120**(3), pp. 1594–1601.
[19] Groot, R. D., and Rabone, K. L., 2001, "Mesoscopic Simulation of Cell Membrane Damage, Morphology Change and Rupture by Nonionic Surfactants," Biophys. J., **81**, pp. 725–736.
[20] Yamamoto, S., Maruyama, Y., and Hyodo, S., 2002, "Dissipative Particle Dynamics Study of Spontaneous Vesicle Formation of Amphiphilic Molecules," J. Chem. Phys., **116**, pp. 5842–5849.
[21] Ortiz, V., Nielsen, S. O., Discher, D. E., Klein, M. L., Lipowsky, R., and Shillcock, J., 2005, "Dissipative Particle Dynamics Simulations of Polymersomes," J. Phys. Chem. B, **109**, pp. 17708–17714.
[22] Coveney, P. V., and Novik, K. E., 1996, "Computer Simulations of Domain Growth and Phase Separation in Two-Dimensional Binary Immiscible Fluids Using Dissipative Particle Dynamics," Phys. Rev. E, **54**(5), pp. 5134–5141.
[23] Boek, E. S., Coveney, P. V., Lekkerkerker, H. N. W., and van der Schoot, P., 1997, "Simulating the Rheology of Dense Colloidal Suspensions Using Dissipative Particle Dynamics," Phys. Rev. E, **55**(3), pp. 3124–3133.
[24] Maiti, A., Wescott, J., and Kung, P., 2005, "Nanotube-Polymer Composites: Insights From Flory–Huggins Theory and Mesoscale Simulations," Mol. Simul., **31**, pp. 143–149.
[25] Marsh, C. A., Backx, G., and Ernst, M. H., 1997, "Static and Dynamic Properties of Dissipative Particle Dynamics," Phys. Rev. E, **56**(2), pp. 1676–1691.
[26] Avalos, J. B., and Mackie, A. D., 1997, "Dissipative Particle Dynamics With Energy Conservation," Europhys. Lett., **40**(2), pp. 141–146.
[27] Español, P., 1997, "Dissipative Particle Dynamics With Energy Conservation," Europhys. Lett., **40**(6), pp. 631–636.
[28] Ripoll, M., Español, P., and Ernst, M. H., 1998, "Dissipative Particle Dynamics With Energy Conservation: Heat Conduction," Int. J. Mod. Phys. C, **9**, pp. 1329–1338.
[29] Ripoll, M., and Español, P., 2000, "Heat Conduction Modeling With Energy Conservation Dissipative Particle Dynamics," Int. J. of Heat and Technology, **18**, pp. 57–61.
[30] Mackie, A., Bonet, D., Avalos, J., and Navas, V., 1999, "Dissipative Particle Dynamics With Energy Conservation: Modeling of Heat Flow," Phys. Chem. Chem. Phys., **1**, pp. 2039–2049.
[31] Ripoll, M., and Ernst, M. H., 2005, "Model System for Classical Fluids Out of Equilibrium," Phys. Rev. E, **71**, 041104.
[32] Chaudhri, A., and Lukes, J. R., 2008, "Multicomponent Dissipative Particle Dynamics: Formulation of a General Framework for Simulations of Complex Fluids," Int. J. Numer. Methods Fluids, in press.
[33] Ripoll, M., 2002, "Kinetic Theory of Dissipative Particle Dynamics Models," Ph.D. thesis, Universidad Nacional de Educación a Distancia, Madrid.
[34] Gardiner, C. W., 2004, *Handbook of Stochastic Methods for Physics, Chemistry and the Natural Sciences*, Springer-Verlag, Berlin.
[35] Munson, B. R., Young, D. F., and Okiishi, T. H., 2002, *Fundamentals of Fluid Mechanics*, 4th ed., Wiley, New York.
[36] Kundu, P. K., and Cohen, I. M., 2008, *Fluid Mechanics*, 4th ed., Academic, Amsterdam.
[37] Incropera, F. P., and DeWitt, D. P., 2002, *Fundamentals of Heat and Mass Transfer*, 5th ed., Wiley, Hoboken, NJ.
[38] Carslaw, H. S., and Jaeger, J. C., 1986, *Conduction of Heat in Solids*, 2nd ed., Oxford University Press, New York.
[39] Humphrey, W., Dalke, A., and Schulten, K., 1996, "VMD-Visual Molecular Dynamics," J. Mol. Graphics, **14**(1), pp. 33–38.

Heat Transfer Characterizations of Heat Pipe in Comparison With Copper Pipe

Chen-Ching Ting
Department of Mechanical Engineering,
National Taipei University of Technology,
No. 1, Sec. 3, Chung-Hsiao E. Road,
Taipei 10608, Taiwan
e-mail: chchting@ntut.edu.tw

Jing-Nang Lee[1]

Chien-Chih Chen

Graduate Institute of Manufacturing Technology,
National Taipei University of Technology,
No. 1, Sec. 3, Chung-Hsiao E. Road,
Taipei 10608, Taiwan

The article presents some significant experimental data for studying the heat transfer behavior of heat pipe, which will further help the cooling efficiency improvement of the heat pipe cooler. It is well known that the heat pipe owns the extreme large heat conductivity and is often integrated with cooling plates for CPU cooling. The heat pipe uses special heat transfer techniques to obtain extremely large heat conductivity, which are the inside liquid evaporation for heat absorption and the inside microstructural capillarity for condensation. These special techniques yield the instant heat transfer from the heat source to the remote side directly, but the special heat transfer behavior is changed due to the integration with cooling plates. The destroyed heat transfer behavior of the heat pipe causes the cooling efficiency of the heat pipe cooler to be not able to reach a predicted good value. To improve the cooling efficiency of the heat pipe cooler we recover the original heat transfer behavior of the heat pipe integrated with cooling plates. This work first built a CPU simulator in accordance with the ASTM standard for heating the heat pipe, then uses the color schlieren technique to visualize the sequent heat flux nearby the heat pipe and the infrared thermal camera for quantitative temperature measurements synchronously. The result shows that the heat flux first appears at the opposite side from the heat source and there exhibits also the highest temperature. This is different from the heat transfer behavior of the copper pipe. Another very interesting result is that the heat flux of the cooling plate nearest to the heat source is first viewed than the others, which is similar to the integration with the copper pipe. [DOI: 10.1115/1.3056571]

Keywords: heat transfer behavior, heat pipe, CPU cooling, microstructural capillarity

1 Introduction

Since 2004 the Intel company declared to produce the Intel CPU speed of computer up to its Prescott 3 GHz; the AMD company had the same decision later. The reason is that the overheat problem cannot be solved effectively. Beyond 3.0 GHz, practical cooling of the CPUs becomes a significant challenge. Up to 4.0 GHz of CPU speed in work, the generation of extremely large heat is until now without perfect solution. Figure 1 shows the development of thermal design power (TDP) for Intel P4 CPU [1].

A lot of technologies, e.g., thermal electric (TE) cooler, heat pipe, spray cooling, etc., have been discussed and in use, where the TE cooler is active and the heat pipe and the spray cooling are passive in principle [2]. Cooling methods are normally divided into two types, active and passive, by means of different applied principles, where the active cooling method uses the forced cooling technology to carry heat off and the passive cooling method uses the natural heat transfer. Passive cooling methods are further divided into the natural thermal conduction, the water cooling, and the air cooling in accordance with the applied transferring medium. A heat pipe is a passive cooling device with extremely high thermal conductivity, which is a heat transfer mechanism that can transport large quantities of heat with a tiny difference in temperature between the hot and the cold interfaces. While the general principle of the heat pipes using gravity dates back to the steam age, the benefits of employing capillary action were first noted by Grover at Los Alamos National Laboratory in 1963 and subsequently published in the Journal of Applied Physics in 1964 [3]. The application of heat pipe for cooling is a newly developed technique due to its extremely large thermal conductivity and normally integrated with the cooling plates, which is also named heat pipe cooler. The flow phenomenon between the cooling plates decides the cooling efficiency, and the cooling plates are normally built in microstructure [4].

Cotter [5] in 1984 first presented his technology of heat pipe using working fluid within the closing vacuum hollow copper tube and Lee [6] in 1998 described the spreading resistance in the heat pipe cooler. Nguyen et al. [7] used the module of the heat pipe cooler in the notebook to reduce the total heat resistance. According to the special technique, heat pipe has a positional discrete heat transfer property while the copper pipe is continuous. The nontraditional heat transfer property in the heat pipe causes its unexpected cooling efficiency. Theoretically, applying the heat pipe cooler should have a relative large cooling efficiency than the copper pipe cooler since the heat pipe has over 25 times thermal conductivity than the copper pipe, but the increasing value is actually not the same as expected [8]. The fact is that the heat transfer of the heat pipe cannot reach the end point after integration with cooling plates.

Whether cooling efficiency cannot reach the predicted value is the main question for the heat pipe cooler. Most of the studies on the heat pipe cooler ignored the considerations on the heat transfer behavior change in heat pipe and discussed only its integrating structure [9,10]. A standard application of heat pipe is in connection with cooling plates, but the integration of heat pipe cooler has changed the original heat transfer behavior of the heat pipe. Figure 2 shows the schema of the general heat pipe cooler.

The heat transfer behavior of the heat pipe is similar to the copper pipe due to its integration with cooling plates, which will reduce its cooling efficiency. Most of the publications on the topic of heat pipe cooler focused on the structural studies of cooling

[1]Also at Department of Refrigeration, Air-Conditioning, and Energy Engineering, National Chin-Yi University of Technology, Taiwan.

Contributed by the Heat Transfer Division of ASME for publication in the JOURNAL OF HEAT TRANSFER. Manuscript received June 9, 2008; final manuscript received October 20, 2008; published online January 23, 2009. Review conducted by Robert D. Tzou. Paper presented at the 2008 International Conference on Micro/Nanoscale Heat Transfer (MNHT2008), Tainan, Taiwan, January 6–9, 2008.

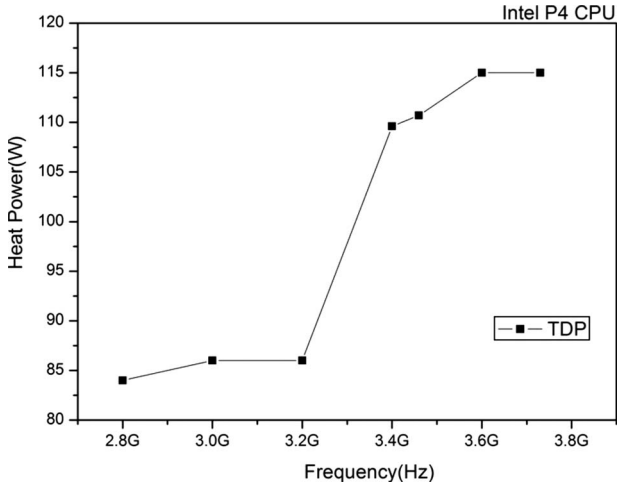

Fig. 1 TDP development of Intel P4 CPU [1]

plates for cooling improvement [9,10]. Studies on the heat transfer behavior inside the heat pipe are relatively few. This work discusses the inside heat transfer property change in heat pipe integrated with cooling plates using experimental methods. It was found that the change in heat transfer behavior in heat pipe integrated with cooling plates is the main reason for the lack cooling efficiency. The cooling plates far from the heat source cannot reach sufficient cooling efficiency. This work found also that a new structure of heat pipe for integration with cooling plates should be designed to keep the original heat transfer behavior of the heat pipe after integration with cooling plates.

2 Experimental Details

The applied technologies for measuring the time dependent change in surface temperature distribution on the heat and the copper pipes, as well as the visualization of heat flux nearby the heat and the copper pipes, use the infrared thermal photography and the color schlieren technique individually.

2.1 Infrared Thermal Photography. The infrared thermal camera can derive a two dimensional image with the surface temperature distribution of the object quantitatively and dynamically. Although the infrared thermal camera is convenient to do noncontact recording of the surface temperature distribution quantitatively, it has to adjust against the effect of the surroundings and the object surface. This work used the IRISYS infrared thermal camera, which has a 16×16 pixel resolution, 8 frames/s capturing speed, and the optical lens with a 30 cm built-in focal length. The measuring effect is equal to 256 sensors uniformly setup on a

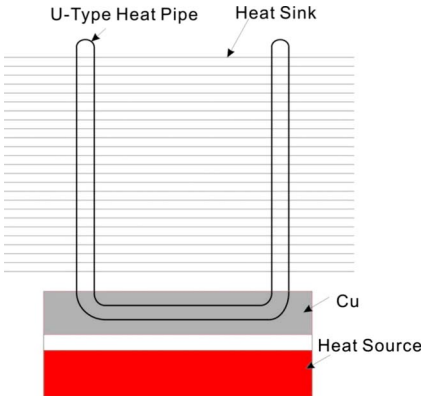

Fig. 2 Schema of the general heat pipe cooler

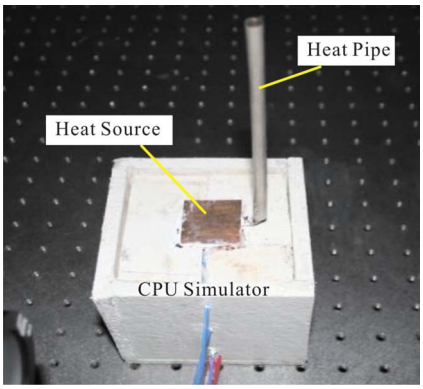

Fig. 3 Photo of the heat pipe built on the CPU simulator

13×13 cm^2 area, which has a standard measuring error ~2%. A calibration has been made using a thermocouple thermometer with deviation ~2% in the temperature range of 20–80°C.

Figure 3 exhibits a photo of the heat pipe built on the CPU simulator. A CPU simulator with the contact area 31×31 mm^2, in accordance with the ASTM D5470 standard including a T form copper block, some glass wool, fireproof board, two 150 W cartridge heaters, and a 300 W power supply, was built in the heat source for heating the copper and the heat pipes. In the experimental setup we use the IRISYS infrared thermal camera to record the time dependent change in the temperature distribution on the heated copper or heat pipes.

A $\phi_{out}=6$ mm, $\phi_{in}=5.4$ mm, $L=200$ mm copper tube was used in comparison with the heat pipe, where ϕ_{out} is the outer diameter, ϕ_{in} is the inner diameter, and L is the length of the copper tube. The used heat pipe has the same dimensions as the copper tube. It has the grooved wick structure and is often integrated with cooling plates for applications. The applied working fluid for the heat pipe is 4.51 mg water. Figure 4 shows the schematic cross section of the heat pipe.

The capturing screen of the infrared thermal camera shows 16×16 pixels corresponding to the 16×16 temperature sensors. Figure 5 represents the corresponding positions with the heated copper and heat pipes, which will be applied to the data evaluation in Sec. 3.

2.2 Color Schlieren Technique. Schlieren technique is often used to obtain the two dimensional refraction index gradient distribution within a transparent object [11,12]. Visualization of the heat flux nearby the copper and the heat pipes using the color schlieren technique with the standard setup of Z-arrangement is shown as a photo in Fig. 6.

Experimental performance used water as the visualized medium due to its larger Gladstone–Dale constant ($K_{water}=2.526$ cm^3/g) [13]. The thermal conductivity of water is 0.62 W/mK. The value is 20 times larger than air ($k=0.031$ W/mK), but water is also not

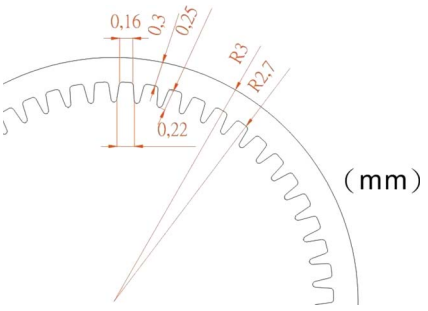

Fig. 4 Schematic cross section of the heat pipe

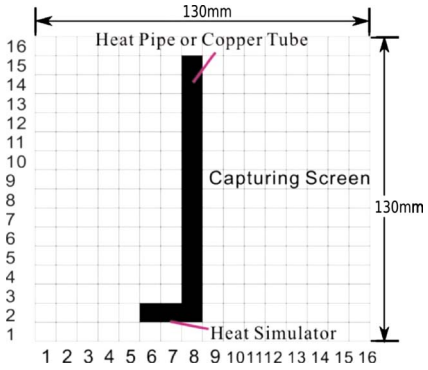

Fig. 5 Capturing screen of the infrared thermal camera corresponding to the position of the heated copper and heat pipes

a good thermal conductive medium in comparison with aluminum (k=230 W/mK) [14]. Visualization of heat flux in water will not change the original heat transfer behavior of the heat pipe, but it can help to view the sequent heat flux nearby the heat pipe much clearer. To visualize the heat flux nearby the copper and the heat pipes we insert the pipe in the water tank horizontally. This setup can reduce the self-disturbance of the heat flux and it does not change the results.

Another test object for characterization of the heat pipe integrated with cooling plates is schematically shown in Fig. 7. The integrated numbers of cooling plates are 1, 3, and 5 pieces separately. The visualization of the heat pipe coolers was carried out in the water tank.

3 Results and Discussion

The results and discussion focus on the time dependent change in the surface temperature distribution for the heat pipe in comparison with the copper pipe using the infrared thermal photography. Moreover, the direct observation of the heat transfer for the heat and copper pipes, as well as the heat pipe integrated with cooling plates by means of the visualization of heat flux using the color schlieren technique, is also carried out. Figures 8 and 9 show the time dependent change in the surface temperature distribution for the copper and heat pipes heated by the 300 W CPU simulator. The Arabic numerals shown in the figures represent the

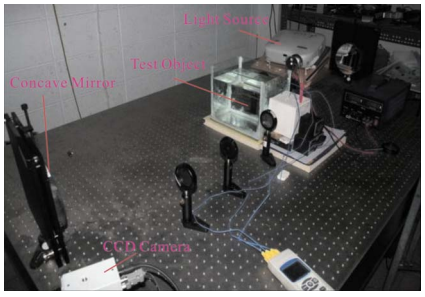

Fig. 6 Photo of the schlieren setup with typical *Z*-arrangement

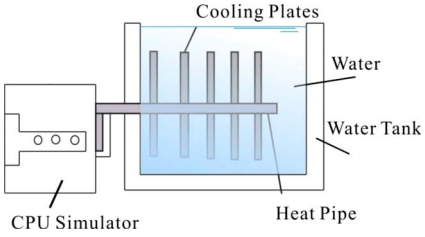

Fig. 7 Schematic setup of the heat pipe with the cooling plates

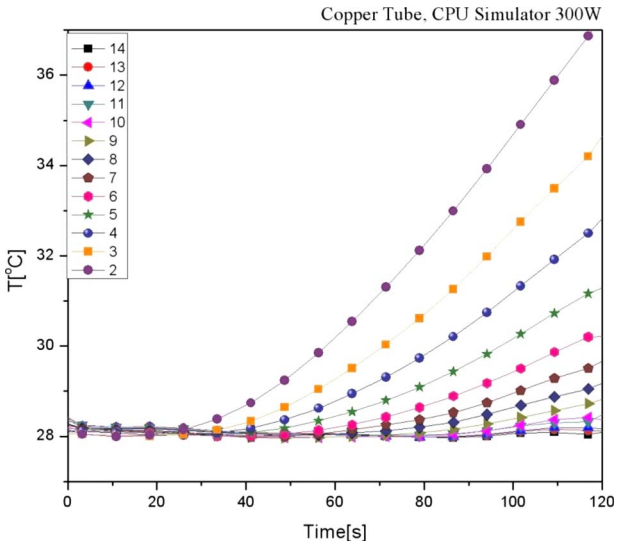

Fig. 8 The time dependent change in the surface temperature distribution for the copper pipe heated by the 300 W CPU simulator

measured positions, where the smaller value of the Arabic numerals corresponds to that nearer to the heat source (see Fig. 5).

Figure 8 indicates that the heat transfer behavior in copper pipe agrees with the traditional thermal conduction and satisfies Fourier's thermal conduction theorem [14]. The generated heat by the CPU simulator continuously transferred from near to far in the copper pipe. Figure 8 clearly shows that the surface temperature on the copper pipe nearby the heat source rises faster than the others due to the limitation of the copper's thermal conductivity. Comparison with the result of the heat pipe in Fig. 9 shows that the heat transfer in the heat pipe is opposite to the copper pipe. Figure 9 indicates that the surface temperature on the heat pipe nearby the heat source rises slower than the end point. Figure 10 zooms out the result at the point of time ~120 s. Figure 10 shows that the temperature on the end point of the heat pipe is higher than the near points. The middle insulating section of the heat pipe has the lowest temperature.

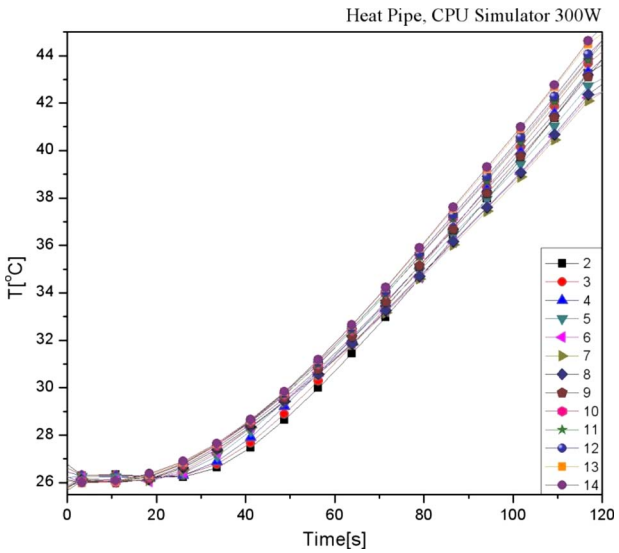

Fig. 9 The time dependent change in the surface temperature distribution for the heat pipe heated by the 300 W CPU simulator

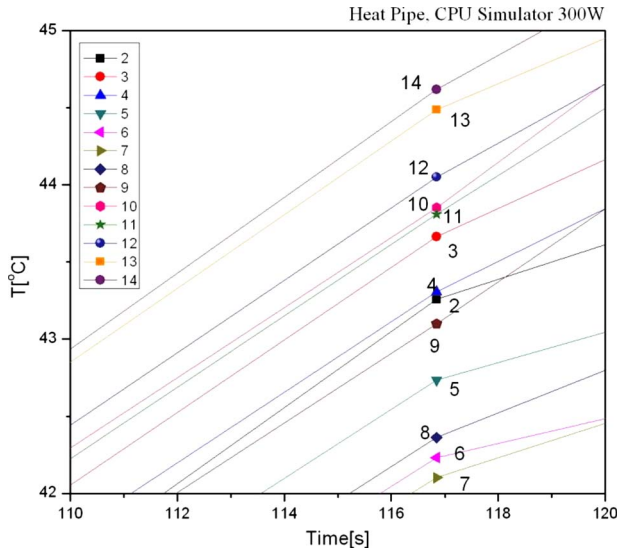

Fig. 10 The zoomed out result from Fig. 9 at the point of time ~120 s

Figure 11 exhibits the time sequent infrared thermal photographical images on the surface of the copper tube heated by the 300 W CPU simulator. The dashed line indicates the copper tube position. Figures 11(*b*) and 11(*c*) show that the temperature on the copper tube near the heat source rises faster than the others. The slow temperature rise is due to its smaller heat conductivity.

Figure 12 exhibits the time sequent infrared thermal photographical images on the surface of the heat pipe heated by the 300 W CPU simulator. The dashed line indicates the heat pipe position. Figure 12(*b*) shows that the temperature on the remote section rises faster than the middle insulating section and Fig. 12(*c*) indicates that the temperature reaches better constant at the heat pipe.

The reason is that the instant evaporized working fluid within the heat pipe transferred heat to the remote section directly and condensed on the remote section through the thermal convection with the surroundings. The instant vaporized working fluid absorbed and transferred heat to the remote section directly. This heat transfer behavior causes the temperature on the remote section to be higher than the other positions. At the same time, the heat source generated heat is also transferred away through the copper shell of the heat pipe with the thermal conduction. The condensed working fluid transferred heat back to the heat source direction through the capillary effect. This result shows that the heat transfer rate of the heat pipe through the thermal convection of the evaporation is faster than via the thermal conduction of the copper shell. The difference in the surface temperature distribution on the full heat pipe is small due to its extremely large thermal conductivity.

The special heat transfer behavior of the heat pipe is further described by the direct observation of the heat flux using the color schlieren technique. Figure 13 first represents the three time sequent images of 3 min, 4 min, and 5 min for the heat flux visualization on the copper pipe using the color schlieren technique heated by the 300 W CPU simulator. The left dark part in Fig. 13 is the heat source and the separating line between the top dark part and the center part is the water level. The horizontal dark bar in the middle is the copper pipe. The time of the captured image goes forward from the left to the right. The applied medium for visualization of the heat flux is water since it has a larger Gladstone–Dale constant. The heated copper pipe transferred the heat into the water and changed the density distribution of the water, which was visualized by the color schlieren technique. Figure 13(*c*) clearly exhibits that the heat flux appears only nearby the heat source on the copper pipe, whereas Figs. 13(*a*) and 13(*b*) are not

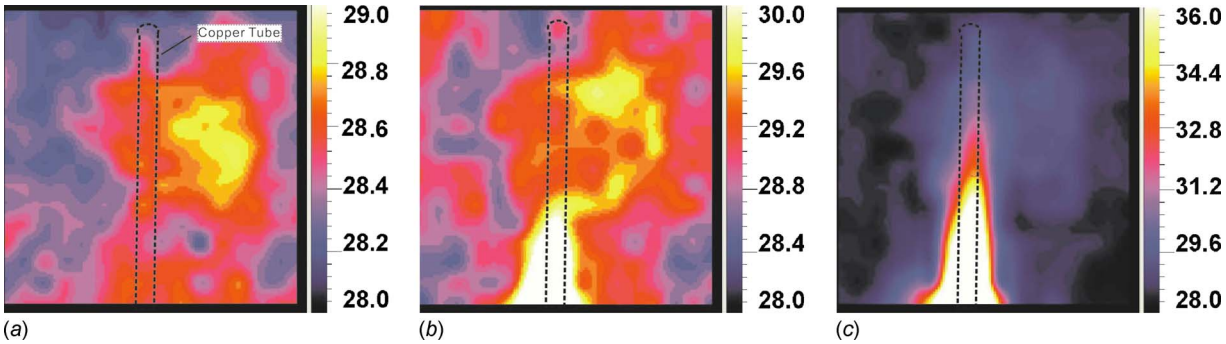

Fig. 11 The heat flux visualization of the copper pipe using the infrared thermal photography heated by the 300 W CPU simulator

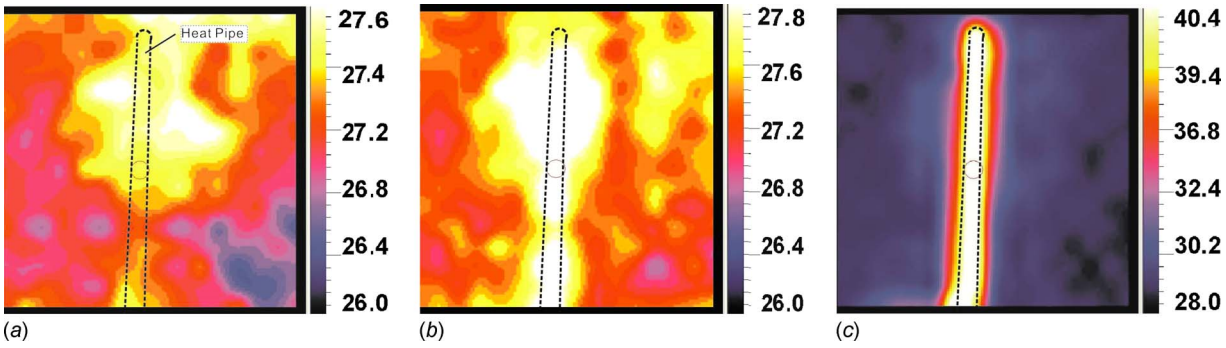

Fig. 12 The heat flux visualization of the heat pipe using the infrared thermal photography heated by the 300 W CPU simulator

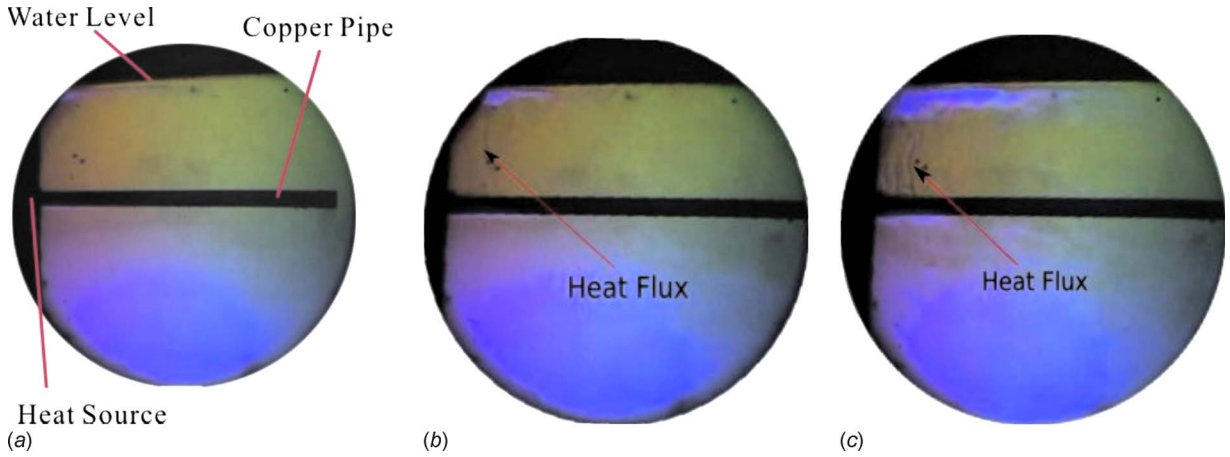

Fig. 13 The heat flux visualization of the copper pipe using the color schlieren technique heated by the 300 W CPU simulator

viewed clearly. According to the temporal series of the heat flux generation in water can determine the heat transfer behavior of the copper pipe. The result shows that the generated heat by the CPU simulator transferred from near to far in the copper pipe, which agrees with the result of temperature distribution measurements shown in Fig. 8.

Figure 14 exhibits the three time sequent images of 0 min, 2:30 min, and 3:57 min for the heat flux visualization of the heat pipe using the color schlieren technique heated by the 300 W CPU simulator. The experimental setup is the same as the copper pipe. The horizontal dark bar in the middle is the heat pipe. The time of the captured image goes forward from the left to the right. The heated heat pipe transferred the heat into the water and changed the density distribution of the water, which was visualized by the color schlieren technique. Figure 14(*b*) first shows that the heat flux appears only on the end point on the heat pipe, whereas Fig. 14(*a*) is not viewed. According to the temporal series of the heat flux generation in water can determine the heat transfer behavior of the heat pipe. The result shows that the generated heat by the CPU simulator transferred directly to the remote section, which agrees with the result of temperature distribution measurements shown in Fig. 9.

The comparison of the heat transfer behavior between the copper and the heat pipes shows the opposite result, which agrees with the theoretical prediction. The interesting result is about the heat pipe cooler. Figure 15 shows the time sequent heat flux visualization of the heat pipe integrated with one cooling plate using the color schlieren technique heated by the 300 W CPU simulator. Figure 15 shows that the cooling plate was first heated before the remote section. The heat transfer behavior in Fig. 15 is perhaps not clear enough. Further results integrated with more cooling plates are shown in Fig. 16. Figure 16 clearly shows that the cooling plate was first heated before the remote section. This result indicates that the heat transfer behavior of the heat pipe cooler is similar to the copper pipe cooler.

4 Conclusions

The measurements using the infrared thermal photography for the time dependent change in surface temperature distribution on the heat and the copper pipes, as well as the visualization of heat flux nearby the heat and the copper pipes using the color schlieren technique, are successfully carried out. The results show that the heat flux first appears at the opposite side from the heat source and exhibits also there the highest temperature. The discrete temperature distribution is different from the heat transfer behavior of the copper pipe. The result agrees with the theoretical trend completely. Whereas the heat pipe integrated with cooling plates yields the continuous heat transfer behavior, which is similar to the integration with copper pipe. The results indicate that the integration with cooling plates for the heat pipe has destroyed the original heat transfer behavior of the heat pipe. To improve the cooling efficiency of the heat pipe cooler we design a new struc-

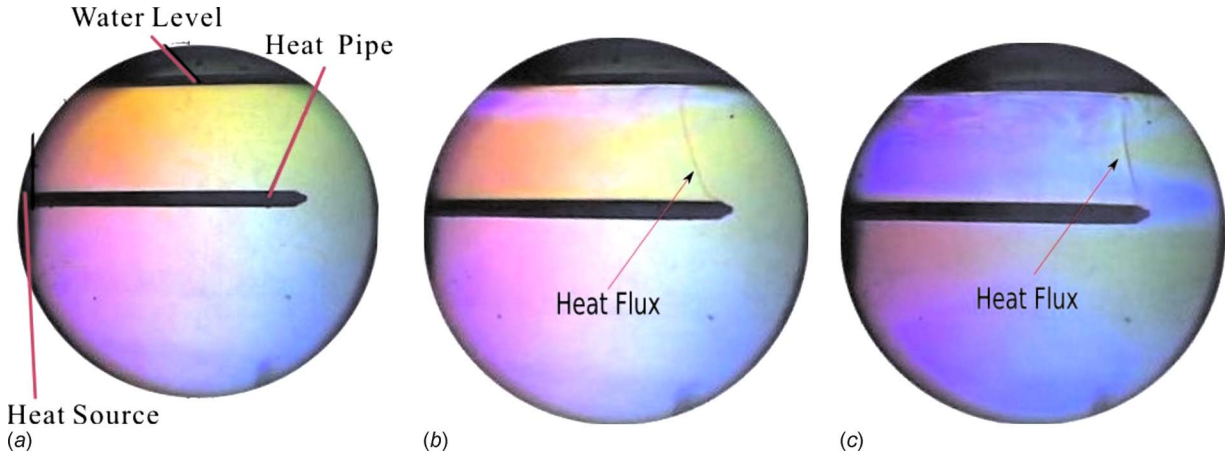

Fig. 14 The heat flux visualization of the heat pipe using the schlieren technique heated by the 300 W CPU simulator

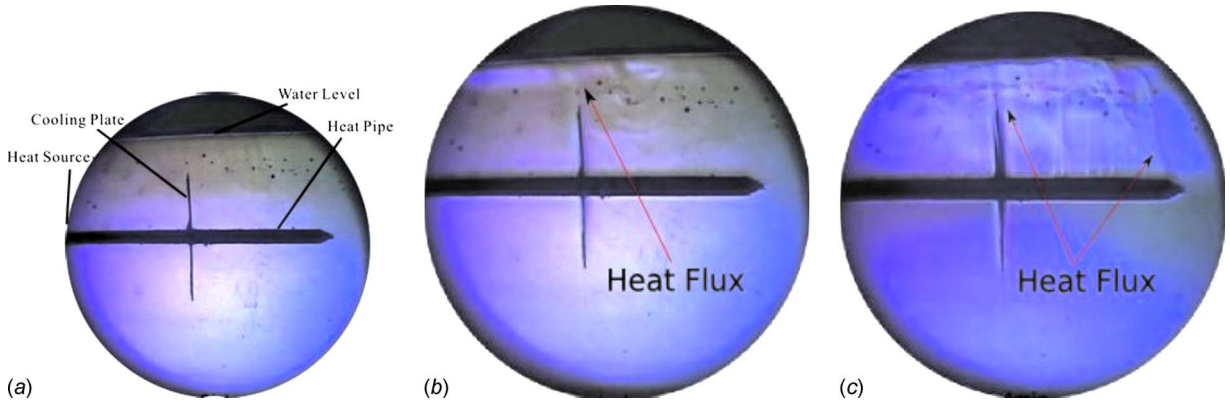

Fig. 15 The heat flux visualization of the heat pipe cooler with one cooling plate using the schlieren technique heated by the 300 W CPU simulator

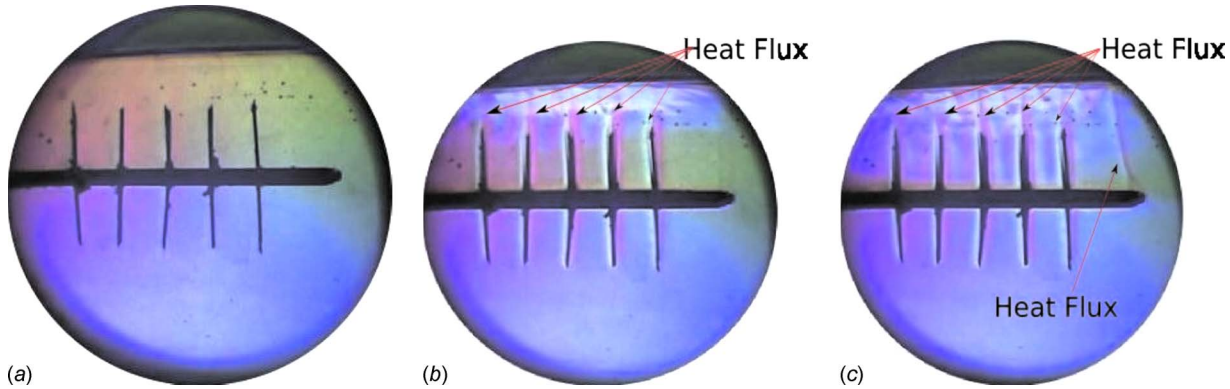

Fig. 16 The heat flux visualization of the heat pipe cooler with five cooling plates using the schlieren technique heated by the 300 W CPU simulator

ture of heat pipe to keep the original heat transfer behavior of the heat pipe after its integration with cooling plates.

Acknowledgment

The authors would like to acknowledge the financial support from the National Science Foundation of Taiwan under Grant No. NSC95-2622-E-027-041-CC3.

References

[1] http://www.intel.com/cd/channel/reseller/apac/zht/products/desktop/processor/pro cessors/core2extreme/tech/99346.htm#table%202.
[2] Tummala, R., 2002, *Fundamentals of Microsystems Packaging*, McGraw-Hill, New York.
[3] Grover, G. M., Cotter, T. P., and Erickson, G. F., 1964, "Structures of Very High Thermal Conductance," J. Appl. Phys., **35**(6), pp. 1990–1991.
[4] Li, J., Peterson, G. P., and Cheng, P., 2004, "Three-Dimensional Analysis of Heat Transfer in a Micro-Heat Sink With Single Phase Flow," Int. J. Heat Mass Transfer, **47**, pp. 4215–4231.
[5] Cotter, T. P., 1984, "Principles and Prospects for Micro Heat Pipes," *Proceedings of the Fifth International Heat Pipe Conference*, pp. 328–334.
[6] Lee, S., 1998, "Calculating Spreading Resistance in Heat Sinks," Electronics Cooling, **4**(1), pp. 30–33; see http://www.electronics-cooling.com/index.php
[7] Nguyen, T., Mochizuki, M., Mashiko, K., Saito, Y., Sauciuc, I., and Boggs, R., 2000, "Advanced Cooling System Using Miniature Heat Pipes in Mobile PC," IEEE Trans. Compon. Packag. Technol., **23**(1), pp. 86–90.
[8] Said, S.A. and Akash, B.A., 1999, "Experimental Performance of a Heat Pipe," Int. Commun. Heat Mass Transfer, **26**(5), pp. 679–684.
[9] Bejan, A., and Sciubba, E., 1992, "The Optimal Spacing of Parallel Plates Cooled by Forced Convection," Int. J. Heat Mass Transfer, **35**, pp. 3259–3264.
[10] Yeh, R. H., and Chang, M., 1995, "Optimum Longitudinal Convective Fin Arrays," Int. Commun. Heat Mass Transfer, **22**, pp. 445–460.
[11] Merzkirch, W., 1987, *Flow Visualisation*, 2nd ed., Academic, New York.
[12] Kleine, H., 1994, "Application and Limitation of a Schlieren System," Stosswellenlabor, RWTH-Aachen, Report No. WLS 12823.
[13] Swift, K. M., Schlie, L. A., and Rathge, R. D., 1988, "Dispersion of Gases in Atomic Iodine Lasers at 1.315 μm," Appl. Opt., **27**, pp. 4377–4384.
[14] Coulson, J. M., and Richardson, J. F., 1999, *Fluid Flow, Heat Transfer and Mass Transfer*, Butterworth-Heinemann Ltd., Oxford.

Li-Hsin Han

Wei Wang

Department of Mechanical Engineering,
University of Texas at Austin,
Austin, TX 78712

Yalin Lu

R. J. Knize

Physics Department,
Laser Optics Research Center,
USAF Academy,
Colorado Springs, CO 80840

Kitt Reinhardt
AFOSR/NE,
875 North Randolph Street, Suite 326,
Arlington, VA 22203

John Howell

Shaochen Chen[1]
e-mail: scchen@mail.utexas.edu

Department of Mechanical Engineering,
University of Texas at Austin,
Austin, TX 78712

Analytical and Experimental Investigations of Electromagnetic Field Enhancement Among Nanospheres With Varying Spacing

A modified Mie scattering theory was used to calculate the enhancement of electromagnetic (EM) field between gold nanospheres. The simulation result showed that the density of EM-energy in the space between neighboring nanospheres increases drastically as the interparticle space decreases. Simulated absorption-spectra also showed a peak-shifting from the visible to the infrared region when decreasing the nanosphere spacing. We used our previous experiment to verify the analytical results; the experiment was conducted by using a photodeformable microshell, which was coated with gold nanospheres. Made of photoshrinkable azobenzene polyelectrolytes, the microshells supported the gold nanospheres and gave the tunability of the interparticle spacing among the nanospheres. Upon irradiation of ultraviolet light, the microshells shrank and reduced the interparticle space. The absorption-spectra of the gradually shrinking microshells showed significant changes; a peak-broadening from the visible to the near-infrared region and a drastically enhanced water-absorption were observed in the experimental spectra. The experimental results confirmed the analytical analysis based on the modified scattering theory.
[DOI: 10.1115/1.3056574]

1 Introduction

Since the beginning of the last century, Mie scattering theory has become a very useful tool to analyze the enhancement of electromagnetic-wave by small particles [1,2]. Mie theory gives an exact solution to the distribution of electromagnetic field around one isolated, homogeneous, spherical object under the irradiation of a plane-wave. The solution successfully predicted the existence of multiple resonances, at which the scattering and absorption of the incident light by the sphere are maximized at specific wavelengths. In addition to conventional optics, the Mie scattering theory has brought important insight to many fields. For example, the electromagnetic resonance also induces a resonance of surface-electrons, which may trigger chemical reactions. For the case of metallic spheres for photocatalysis [3], the Mie theory was generally used to explain the formation of photo-electrons, which are responsible for the photochemical effects. Moreover, the Mie scattering theory was used for the study of photonic crystals [4] and photovoltaic devices [5].

For problems involving multiple-spheres, the original Mie model could lead to an approximated solution. The accuracy of the approximation, however, depends on the significance of the scattering effect among spheres, in which the light scattered by each sphere irradiates the whole system and becomes a part of the incident light. The intensity of multiple-scattering depends strongly on interparticle spacing. When the spacing is sufficiently large, the multiple-scattering effect becomes negligible and the scattering and absorption by the whole system are close to the linear combination of Mie's original solution for each individual sphere. In many real experiments, however, the particles are so concentrated that the multiple-scattering effect becomes important, and the linear combination approach becomes questionable. To solve the multiple-sphere problem, a modified Mie model was proposed decades ago to cover the multiple-scattering effects [6]. This modified theory differs from the original one by adding the scattering from each sphere $\vec{E}_s^i$ (which is unknown) to the incident wave. This model offers an exact solution for a multiple-sphere system, where the sphere size and optical property can be different from one to another. In the beginning, the application of this model was quite limited due to low computer-capacity [6]. In recent years, it has become possible to apply this model to a system of thousands of spheres. Surprisingly, however, little attention was paid to applying the modified Mie theory to real experiments that involve concentrated spheres. In this paper, we use the modified Mie scattering theory to simulate the electromagnetic-field enhancement by two gold nanospheres of varying spacing. We also develop an experiment to verify the simulation results. In the experiment, a photodeformable microshell coated with gold nanospheres is used to form a multiple-sphere-medium of tunable spacing. Upon irradiation with ultraviolet light, the microshells shrink gradually, leading to the decrease in the nanosphere spacing. The absorption-spectra of the microshells are measured to compare the simulation results.

[1]Corresponding author.

Contributed by the Heat Transfer Division of ASME for publication in the JOURNAL OF HEAT TRANSFER. Manuscript received July 11, 2008; final manuscript received October 7, 2008; published online January 23, 2009. Review conducted by Robert D. Tzou. Paper presented at the 2008 International Conference on Micro/Nanoscale Heat Transfer (MNHT2008), Tainan, Taiwan, January 6–9, 2008.

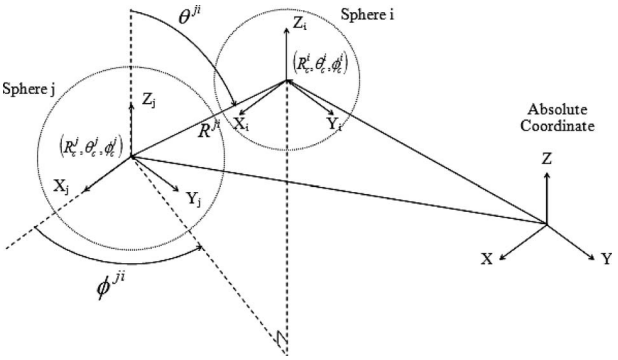

Fig. 1 A coordinate-system for the multiple-spheres. ($R^{ji}, \theta^{ji}, \phi^{ji}$) denotes the central point of sphere *i* with respect to the center of sphere *j*.

2 Analytical Analysis of the Electromagnetic Field in a Multisphere System

In the modified Mie theory, the electric field in the system $\vec{E}_{\text{total}}$ consists of the incident plane-wave $\vec{E}_0$ and the scattering by all particles $\vec{E}_s$, where $\vec{E}_s=\Sigma_{i=1}^{Ns}\vec{E}_s^i$. For linearization, the incident field $\vec{E}_i$ (typically a plane-wave), scattered field $\vec{E}_s$, and internal field $\vec{E}_1^i$ (the field inside a sphere) are expanded into polynomials of orthogonal vectors $\vec{M}_{mn}^{(j)}$ and $\vec{N}_{mn}^{(j)}$ as follows:

$$\vec{E}_0=\sum_{n=1}^{\infty}\sum_{m=-n}^{n}[p_{mn}\vec{N}_{mn}^{(1)}(r,\theta,\phi)+q_{mn}\vec{M}_{mn}^{(1)}(r,\theta,\phi)] \tag{1}$$

$$\vec{E}_s=\sum_{i=1}^{N_s}\sum_{n=1}^{\infty}\sum_{m=-n}^{n}[a_{mn}^i\vec{N}_{mn}^{(3)}(r^i,\theta^i,\phi^i)+b_{mn}^i\vec{M}_{mn}^{(3)}(r^i,\theta^i,\phi^i)]|_{R^i>a^i} \tag{2}$$

$$\vec{E}_1^i=\sum_{n=1}^{\infty}\sum_{m=-n}^{n}[d_{mn}^i\vec{N}_{mn}^{(1)}(m^ir^i,\theta^i,\phi^i)+c_{mn}^i\vec{M}_{mn}^{(1)}(m^ir^i,\theta^i,\phi^i)]|_{R^i<=a^i} \tag{3}$$

The derivation of these orthogonal vectors was given in Ref. [6]. Figure 1 illustrates the coordinate-system for the multiple-sphere problem. The spheres are numbered from 1 to N_s. The orthogonal vectors are calculated from $\vec{M}_{mn}^{(j)}=\nabla\times\vec{R}u_{mn}^{(j)}$ and $\vec{N}_{mn}^{(j)}=(1/k)\nabla\times M_{mn}^{(j)}$. $\vec{R}=(R,\theta,\phi)$ is a position with respect to the origin of a spherical coordinate-system. The r in the equations is a dimensionless radius derived from R, and $r=k\cdot R$, where k is the wave constant of the incident light in the surrounding media. (r^i,θ^i,ϕ^i) is the relative position with respect to the center of sphere i. $u_{mn}^{(j)}$ is the spherical harmonic function, where $u_{mn}^{(1)}=j_n(r)P_n^m(\cos\theta)e^{im\phi}$ and $u_{mn}^{(3)}=h_n(r)P_n^m(\cos\theta)e^{im\phi}$. P_n^m is a term of associated Legendre polynomial, $j_n(r)$ is the nth order spherical Bessel function, and $h_n(r)$ is the nth order spherical Hankel functions. a^i in Eq. (2) is the radius of sphere i. m^i in Eq. (3) is the relative dielectric constant of sphere i, $m^i=\sqrt{\varepsilon_s^i/\varepsilon_m}$.

To calculate the distribution of the electromagnetic field, we need to find the expansion coefficients p_{mn}, q_{mn}, c_{mn}^i, d_{mn}^i, a_{mn}^i, and b_{mn}^i. First, we need to transfer the origin of Eq. (1) to the center of each sphere i

$$\vec{E}_0=\sum_{n=1}^{\infty}\sum_{m=-n}^{n}[p_{mn}^i\vec{N}_{mn}^{(1)}(r^i,\theta^i,\phi^i)+q_{mn}^i\vec{M}_{mn}^{(1)}(r^i,\theta^i,\phi^i)] \tag{4}$$

For convenience, the direction of the electric field of the incident plane-wave $\vec{E}_0$ is set to be parallel to the x-direction of the absolute coordinate-system (see Fig. 1) and the wave vector $\vec{k}$ is parallel to the z-direction. That is, $\vec{E}_0=\hat{x}E_0\exp(ikR^0\cos\theta^0)$. Note that we denoted (R^0,θ^0,ϕ^0) as the absolute position in the space. With respect to the center of sphere i, $(R_c^i,\theta_c^i,\phi_c^i)$, the theory gives $p_{1n}^i=-\frac{1}{2}i^{n+1}E_0((2n+1)/n(n+1))\exp(ikR_c^i\cos\theta_c^i)$, $p_{-1n}^i=\frac{1}{2}i^{n+1}E_0(2n+1)\exp(ikR_c^i\cos\theta_c^i)$, $q_{1n}^i=p_{1n}^i$, $q_{-1n}^i=-p_{-1n}^i$, and $q_{mn}^i=p_{mn}^i=0$ for $|m|\neq 1$.

To calculate coefficients a_{mn}^i and b_{mn}^i, we use the continuity boundary condition at the surface of each sphere [7]. The tangential components of electric and magnetic fields are continuous across the boundary of the surface of each sphere

$$\left(\vec{E}_0+\sum_{i=1}^{N_s}\vec{E}_s^i-\vec{E}_1^i\right)\times\hat{e}_r|_{R^i=a^i}=0 \tag{5}$$

$$\left(\vec{H}_0+\sum_{i=1}^{N_s}\vec{H}_s^i-\vec{H}_1^i\right)\times\hat{e}_r|_{R^i=a^i}=0 \tag{6}$$

To solve a_{mn}^i and b_{mn}^i linearly, we need two more equations to relate the expansion vectors of sphere i, $\vec{N}_{mn}^{(1,3)}(r^i,\theta^i,\phi^i)$ and $\vec{M}_{mn}^{(1,3)}(r^i,\theta^i,\phi^i)$, to the expansion vectors of a different sphere j, $\vec{N}_{mn}^{(1,3)}(r^j,\theta^j,\phi^j)$ and $\vec{M}_{mn}^{(1,3)}(r^j,\theta^j,\phi^j)$,

$$\vec{M}_{mn}^{(3)}(r^j,\theta^j,\phi^j)=\sum_{l=1}^{\infty}\sum_{k=-l}^{l}[A_{kl}^{mn}(r^{ji},\theta^{ji},\phi^{ji})\vec{M}_{kl}^{(1)}(r^i,\theta^i,\phi^i)+B_{kl}^{mn}(r^{ji},\theta^{ji},\phi^{ji})\vec{N}_{kl}^{(1)}(r^i,\theta^i,\phi^i)] \tag{7}$$

$$\vec{N}_{mn}^{(3)}(r^j,\theta^j,\phi^j)=\sum_{l=1}^{\infty}\sum_{k=-l}^{l}[A_{kl}^{mn}(r^{ji},\theta^{ji},\phi^{ji})\vec{N}_{kl}^{(1)}(r^i,\theta^i,\phi^i)+B_{kl}^{mn}(r^{ji},\theta^{ji},\phi^{ji})\vec{M}_{kl}^{(1)}(r^i,\theta^i,\phi^i)] \tag{8}$$

$(r^{ji},\theta^{ji},\phi^{ji})$ denotes the center of sphere i with respect to the center of sphere j. The calculations of $A_{kl}^{mn}(r^{ji},\theta^{ji},\phi^{ji})$ and $B_{kl}^{mn}(r^{ji},\theta^{ji},\phi^{ji})$ are given by Ref. [6]. Combining Eqs. (1)–(8) we get the linear equations for all a_{mn}^i and b_{mn}^i as follows:

$$\begin{pmatrix}a_{mn}^i\\b_{mn}^i\end{pmatrix}=\begin{pmatrix}-\alpha_n^ip_{mn}^i\\-\beta_n^iq_{mn}^i\end{pmatrix}+\begin{pmatrix}-\alpha_n^iA_{mn}^{kl}(r^{ji},\theta^{ji},\phi^{ji}) & -\alpha_n^iB_{mn}^{kl}(r^{ji},\theta^{ji},\phi^{ji})\\-\beta_n^iB_{mn}^{kl}(r^{ji},\theta^{ji},\phi^{ji}) & -\beta_n^iA_{mn}^{kl}(r^{ji},\theta^{ji},\phi^{ji})\end{pmatrix}\times\begin{pmatrix}a_{kl}^j\\b_{kl}^j\end{pmatrix} \tag{9}$$

The coefficients α_n^i and β_n^i are given as

$$\alpha_n^i=\frac{m^i\psi_n'(x^i)\psi_n(m^ix^i)-\psi_n(x^i)\psi_n'(m^ix^i)}{m^i\xi_n'(x^i)\psi_n(m^ix^i)-\xi_n(x^i)\psi_n'(m^ix^i)} \tag{10}$$

$$\beta_n^i=\frac{\psi_n'(x^i)\psi_n(m^ix^i)-m^i\psi_n(x^i)\psi_n'(m^ix^i)}{\xi_n'(x^i)\psi_n(m^ix^i)-m^i\xi_n(x^i)\psi_n'(m^ix^i)} \tag{11}$$

where $x^i=ka^i$, $\psi_n(\rho)=\rho j_n(\rho)$, and $\xi_n(\rho)=\rho h_n(\rho)$. The primes in Eqs. (10) and (11) denote the differentiations with respect to arguments.

The expansion coefficients for the internal field of sphere, c_{mn}^i, and d_{mn}^i, are calculated by using boundary conditions (5) and (6). We get

$$c_{mn}^{i} = \frac{\mathrm{i}m^{i}}{\psi_n'(x^i)\psi_n(m^i x^i) - m^i\psi_n(x^i)\psi_n'(m^i x^i)} b_{mn}^{i} \tag{12}$$

$$d_{mn}^{i} = \frac{\mathrm{i}m^{i}}{m^i\psi_n'(x^i)\psi_n(m^i x^i) - \psi_n(x^i)\psi_n'(m^i x^i)} a_{mn}^{i} \tag{13}$$

Important properties of the multiple-sphere system are calculated by using the expansion coefficients. For example, the energy absorption (unit: Watt) by sphere i is

$$W_{\mathrm{abs}}^{i} = \frac{1}{2}\mathrm{Re}\left\{\int_{A(r^i=x^i)} (\vec{E}_1^i \times \vec{H}_1^i)\cdot(-\hat{e}_r)\right\}$$
$$= \frac{2\pi E_0^2}{|m^i|^2\omega}\sum_{n=1}^{\infty}\sum_{m=-n}^{n}\frac{n(n+1)(n+m)!}{(2n+1)(n-m)!}\mathrm{Re}\left\{\frac{\mathrm{i}}{k\mu}\psi_n'(m^i x^i)\psi_n^*(m^i x^i) \times (m^{i*}|d_{mn}|^2 + m^i|c_{mn}|^2)\right\} \tag{14}$$

where * denotes a complex conjugate. Similarly, the energy extinction (the separated energy from the original, incident flow of light) by sphere i is

$$W_{\mathrm{ext}}^{i} = \frac{1}{2}\mathrm{Re}\left\{\oint_{A(r^i=x^i)} (\vec{E}_0^i \times \vec{H}_s^i + \vec{E}_s^i \times \vec{H}_0^i)\cdot(-\hat{e}_r)\right\}$$
$$= \frac{2\pi E_0^2}{\omega}\sum_{n=1}^{\infty}\sum_{m=-n}^{n}\frac{n(n+1)(n+m)!}{(2n+1)(n-m)!}\mathrm{Re}\left\{\frac{\mathrm{i}}{k\mu}(a_{mn}^i p_{mn}^{i*} + b_{mn}^i q_{mn}^{i*}) \times (\psi_n^*(x^i)\xi_n'(x^i) - \psi_n'^*(x^i)\xi_n(x^i))\right\} \tag{15}$$

The energy scattered by sphere i is simply the difference between W_{abs}^i and W_{ext}^i,

$$W_{\mathrm{sca}}^{i} = W_{\mathrm{ext}}^{i} - W_{\mathrm{abs}}^{i} \tag{16}$$

The energy flux I_i (unit: $\mathrm{W/m^2}$) of the incident wave equals $(E_0^2/2\omega)\cdot\mathrm{Re}\{k/\mu\}$. Three constantly used properties [7], the absorption, extinction, and scattering cross sections (unit: $\mathrm{m^2}$), are given by $C_{\mathrm{abs}}^i = W_{\mathrm{abs}}^i/I_i$, $C_{\mathrm{ext}}^i = W_{\mathrm{ext}}^i/I_i$, and $C_{\mathrm{sca}}^i = W_{\mathrm{sca}}^i/I_i$.

The number n for a_{mn}^i and b_{mn}^i expands from 1 to infinity. Technically, the solution for Eqs. (1)–(3) will be sufficiently precise at a certain order N ($n=1,2,\ldots,N$). In general, a larger N is needed to solve a problem of closer spheres [8].

3 Modeling the Interaction Between Two Gold Nanospheres Under Irradiation

We study the multiple-scattering effect between two gold nanospheres by using the modified Mie theory. We used two kinds of medium dielectric constant ε_m to study the enhancement of electromagnetic field outside the spheres. Reference [9] was used for the dielectric constant ε_m of water, and $\varepsilon_m=1$ was used for vacuum. The diameter of each gold sphere is 40 nm. The dielectric constant of the bulk-material of gold, $\varepsilon_{s,\mathrm{bulk}}$, is from Ref. [10]. Because the size of a 40 nm gold sphere is comparable to the mean-free-path of electrons in a gold bulk-material [11], modification terms are needed to cover the damping effect from the confinement of electrons by the particle surface [12],

$$\varepsilon_s = \varepsilon_{s,\mathrm{bulk}} + \frac{\omega_p^2}{\omega^2 + i\gamma_{\mathrm{bulk}}\omega} - \frac{\omega_p^2}{\omega^2 + i\gamma\omega} \tag{19}$$

where $\gamma = \gamma_{\mathrm{bulk}} + Av_f/a$. a is the sphere radius. A is a constant normally assigned 1. For a gold bulk-material, the damping constant γ_{bulk} is 1.1×10^{14} Hz, the plasma frequency ω_p is 1.37×10^{16} Hz [13], and the Fermi velocity v_f equals 1.39×10^{6} m/s [14].

The order N of the linear equation was carefully selected to make sure that the error of the calculated absorption by the spheres is less than 1%.

The spheres are both positioned at the X-axis and are aligned parallel to the incident electric field. Different interparticle spaces were used in our simulation: 10 nm, 5 nm, 1 nm, and 0.1 nm. Figure 2 shows the field enhancement at the X-Y plane of our bispherical system irradiated by 700 nm light in vacuum environment. The energy density I ($\mathrm{W/m^3}$) was calculated according to $I=\frac{1}{4}(\vec{E}\cdot\vec{D}+\vec{B}\cdot\vec{H})$ [7]. The plot illustrates the intensity ratio of the enhanced field to the incident light. The result shows that the field-intensity at the mass-center of the two spheres grows sharply and nonlinearly as the spheres become closer. In the case of 0.1 nm spacing, as shown by Fig. 2(d), the intensity grows more than 10^5-fold compared with the incident plane-wave.

Figure 3 shows the spectrum of absorption cross section of the bispherical system (in vacuum) of different interparticle spaces. For comparison, the same figure also shows the spectrum of an isolated sphere. When the interparticle space is large (10 nm and beyond), the spectrum is very close to double that of the isolated-particle spectrum, because there is no significant coupling between the scatterings of the two spheres. As the spheres become closer to each other, the multiple-scattering effect raises the total absorption. Note that the absorption-peak of the bispherical system undergoes a major redshift as the spheres approach each other. This redshifting shows the interaction between the two spheres through their scattering field. A simple yet effective model that explains the forming of this spectrum-shifting by a nanoparticle pair is given in Ref. [15]. In brief, when two particles are aligned parallel to the incident electric field, the electric dipoles formed at each sphere interact and delay the response to the incident field. The delay causes the redshifting at the system's resonance frequency.

Figure 4 shows the simulation result about the bispherical system in a water medium. The results show a strong enhancement of absorption by water in the gap between the two spheres. Figures 4(a) and 4(b) show the absorption spectrum of water ($\mathrm{W/m^3}$) at the center of the gap. Figure 4(b) is the logarithmic plot of Fig. 4(a). The water-absorption is increased over 1000-fold when the interparticle spacing changes from 10 nm to 0.1 nm. The enhancement of the finger-print absorption-peak for water at 970 nm is clearly seen in the simulation result. The trapping of high-density photo-energy in the space between close spheres, as shown in Fig. 2(d), explains the enhanced water-absorption. This simulation was later compared with the result of the experiment using our nanoparticle-coated, photodeformable microshells. The effect of quantum confinement may become important when the interparticle spacing is very small. For simplicity, we only focus on using the modified Mie's theory and show the trend of surface plasmon enhancement in a classical approach. In a real case, however, the interparticle spacing may become no smaller than 1 nm due to the space taken by surface ligands (citric acid) on the Au nanoparticles.

4 Experiment

To experimentally demonstrate the near-field enhancement among nanospheres, in a previous study [17], we fabricated microshells using a photosensitive polymer. These microshells shrink upon the irradiation by ultraviolet (UV) light. We coated the surface of the microshells with 40 nm gold nanospheres. Upon UV irradiation, the microshell shrank and the shrinkage reduces the interparticle spaces of the nanospheres on the surface. The spectrum of the microshells was taken to study the change in absorption during different stages of shrinking. The microshell contains a chemical called azobenzene (AZO). Azobenzene undergoes a *trans*-to-*cis* isomerization [16] (at which the molecule atoms realign without changing the original connections) by absorbing UV light. An isomerized azobenzene molecule reduces its

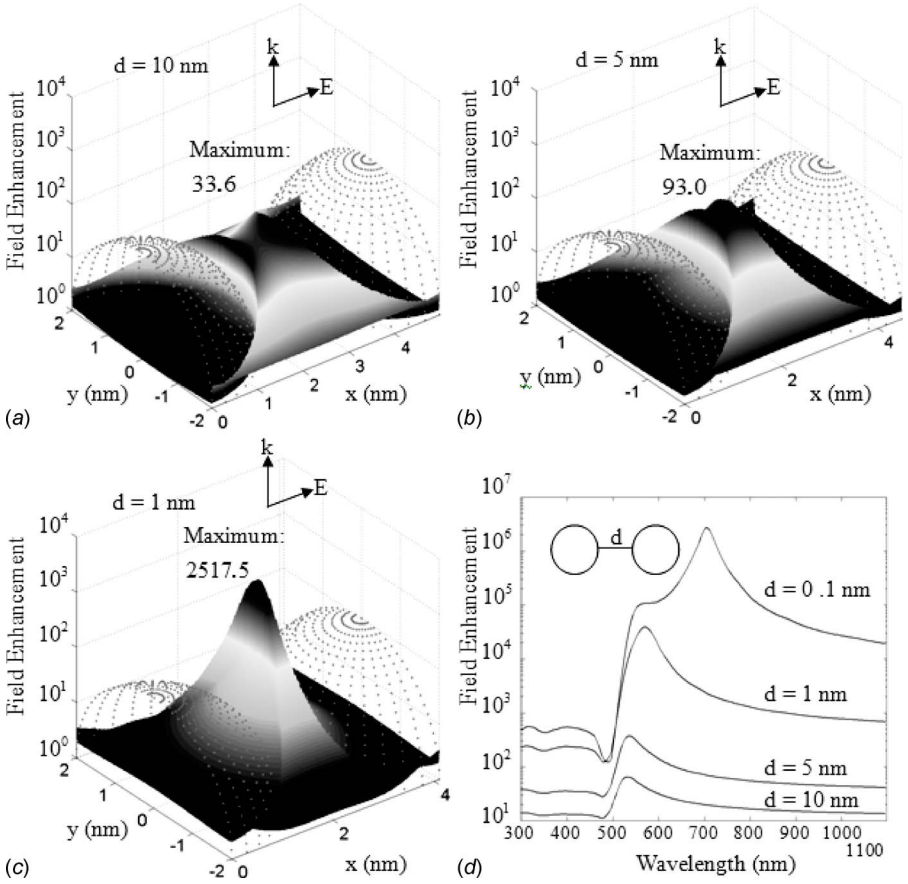

Fig. 2 The simulated enhancement of energy density between two close spheres in vacuum. (*a*)–(*c*) illustrate the intensity ratio of the enhanced field to the incident light; the wavelength is 700 nm in these plots and the interparticle spaces in the plots are (*a*) 10 nm, (*b*) 5 nm, and (*c*) 1 nm. (*d*) shows the spectra of field-enhancement at the center of different gaps, from 10 nm to 0.1 nm.

length from approximately 0.9 nm to 0.55 nm and converts light directly to mechanical deformation. Details about the fabrication of the microshells are given in Ref. [17]. In brief, the AZO-contained polymer was coated onto the surface of a 6 μm silica microsphere through electrostatic adhesion in water environment. After electrostatically coating the 40 nm Au nanospheres onto the polymer layer, the silica core was etched away by buffered hydrofluoric (BHF) acid. The structure of the nanosphere-coated shell remains intact during the etching.

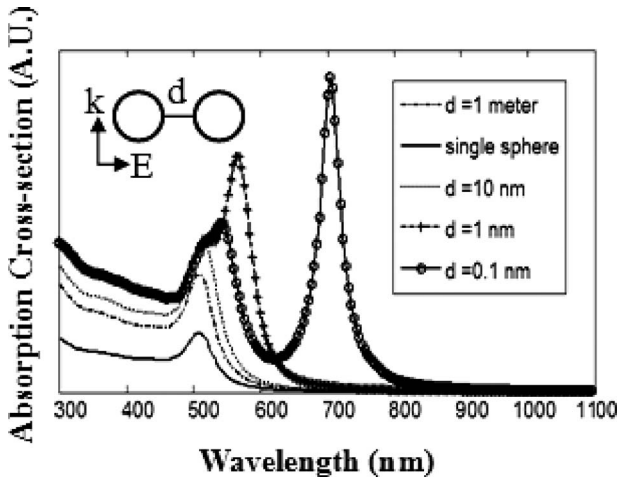

Fig. 3 The simulated absorption-spectra of the bispherical system of different gaps. The medium is vacuum. The absorption spectrum of a single particle is included for comparison.

A scanning electron microscopy (SEM) picture (Fig. 5(*a*)) of the microshell before the removal of the silica core shows the initial interparticle spaces among nanospheres (inset of Fig. 5(*a*)). Most of the gaps were comparable to the sphere diameter (40 nm), while a few nanospheres were originally in contact. The microshells, which collapse when dried (Fig. 5(*b*)), were turgid and slightly swelled in water (Fig. 5(*c*)). The shell diameter was approximately 6.2 μm. Upon UV irradiation, the microshells gradually shrank to a final size of 4.0 μm (Fig. 5(*d*)). The number of contacting nanospheres grew after the shrinkage.

Figure 6(*a*) shows the change in absorption spectrum of the microshells. Our experiment shows a dramatic rise in the near-infrared (NIR) region and a drop in the peak around 560 nm, which is close to the absorption-peak (~530 nm) of the gold nanosphere (Fig. 6(*b*)). This change indicates a redshift of absorption by the nanospheres. Because the distribution of Au nanospheres was random, the peak-shifting from our simulation is unobservable in the experimental result. Instead, we observed a broadening from the original 560 nm peak toward the NIR region. In our previous study [17], we compared this effect with a controlled experiment using the photoshrinkable microshells of no Au nanoparticles. Upon UV irradiation, the blank microshells show a slight spectrum change, which came from the photo-isomerization of the AZO-group and also by the change in molecule concentration during shrinking. The change in control spectrum, however, was negligible compared with the change in Fig. 6(*a*).

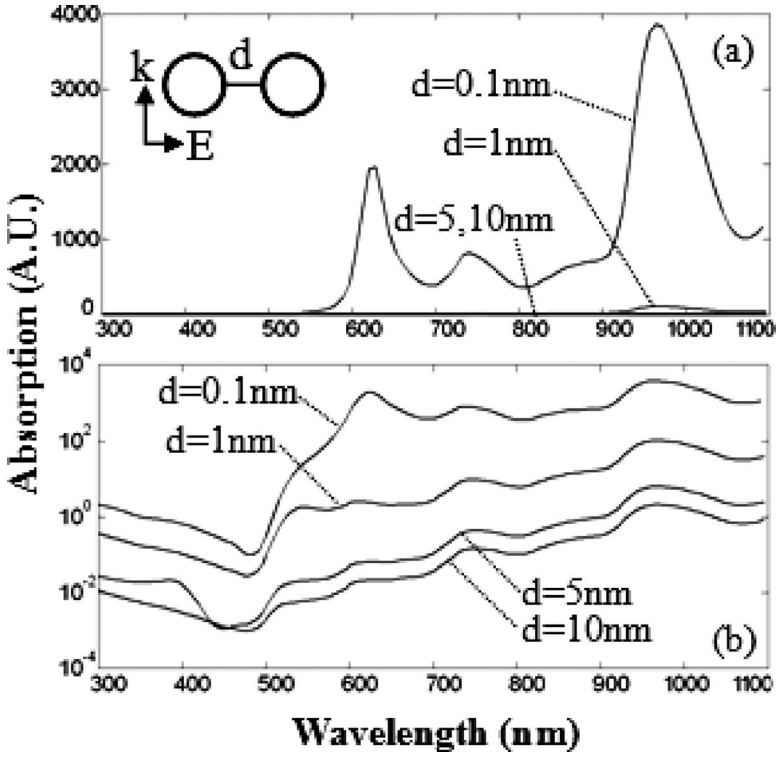

Fig. 4 (*a*) **The spectra of water at the center of different particle gaps. Note the rising peak at 970 nm, which indicates the enhancement of water-absorption. This change was observed in our experiment.** (*b*) **A logarithmic plot of** (*a*)**.**

Importantly, these experimental results confirmed the effect of field-enhancement, which stems from the interaction among neighboring nanospheres. The spectra show that the enhanced NIR absorption has another source, in addition to the nanosphere interactions. The increasing peak at 970 nm, which is from the second overtune frequency of water molecule [18], indicates a significantly increased absorption of water. Compared with the original 970 nm peak of the spectrum of nonirradiated microshells, the absorption of water in the NIR region was increased more than 100-fold. The enhanced water-absorption confirmed that a strong field-enhancement had taken place due to the shrinkage of microshells, as shown by our simulation shown in Fig. 4.

5 Conclusion

We used a modified Mie scattering theory to calculate the exact solutions for a bispherical system of a changing interparticle

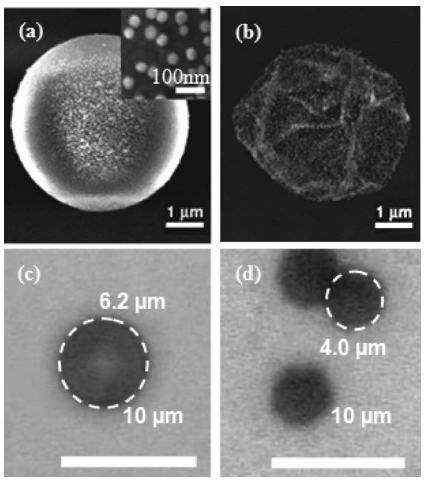

Fig. 5 The photodeformable microshell(s). (*a*) **The SEM picture of one microshell before the removal of its silica core. The inset shows a close look at the surface nanospheres.** (*b*) **The SEM picture of a dried, collapsed microshell.** (*c*) **A nonirradiated microshell in water, under an optical microscope.** (*d*) **Microshells after the irradiation by UV light. The shell-diameters reduced about 35%.**

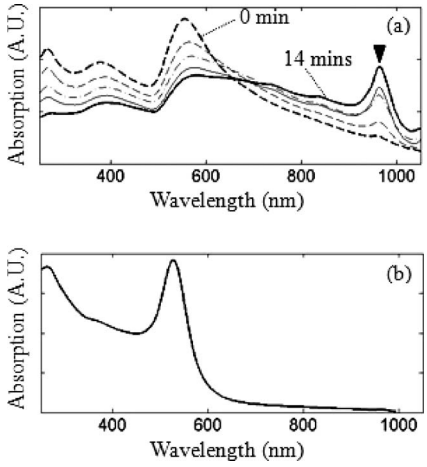

Fig. 6 (*a*) **The experimental spectra of the microshells under different stages of irradiation, from 0 min to 14 min. The triangle indicates the raising peak of water-absorption at 970 nm. The broadening of absorption-peak at 560 nm indicates the change in particle-interaction during the shell-shrinking, as shown by the simulation.** (*b*) **The spectrum of diluted 40 nm gold nanospheres in water. This figure is used to compare with the spectra of** (*a*)**.**

space. Based on the simulation results, we showed that a redshift in gold-sphere absorption and a significant field-enhancement in the sphere-gap would take place when the interparticle space approaches zero. The theoretical result was confirmed by a previous experiment using our nanosphere-coated, photodeformable microshells. We show that the modified Mie model is an effective tool for solving the multiple-scattering problem. This article also sheds light on the application of electromagnetic-interaction between small particles to different research fields, such as photonics, photochemistry, and probably photovoltaic materials.

Acknowledgment

This work was partially supported by grants from the U.S. National Science Foundation, Office of Naval Research, and the Air Force Office of Scientific Research. We thank Professor Stephen E. Webber in the Department of Chemistry and Biochemistry at UT-Austin for equipment support.

References

[1] Mie, G., 1908, "Beiträge zur Optik trüber Medien speziell kolloidaler Metallösungen," Ann. Phys., **25**, pp. 376–445.
[2] Craig, F. B., and Donld, R. H., 1983, *Absorption and Scattering of Light by Small Particles*, Wiley, Canada, pp. 83–129.
[3] Shvalagin, V. V., Stroyuk, A. L., and Kuchmii, S. Y., 2007, "Photochemical Synthesis of ZnO/Ag Nanocomposites," J. Nanopart. Res., **9**(3), pp. 427–440.
[4] Vandenbem, C., and Vigneron, J. P., 2005, "Mie Resonances of Dielectric Spheres in Face-Centered Cubic Photonic Crystals," J. Opt. Soc. Am. A, **22**(6), pp. 1042–1047.
[5] Banerjee, M., Datta, S. K., and Saha, H., 2005, "Enhanced Optical Absorption in a Thin Silicon Layer With Nanovoids," Nanotechnology, **16**(9), pp. 1542–1548.
[6] Mackowski, D. W., 1991, "Analysis of Radiative Scattering for Multiple Sphere Configurations," Proc. R. Soc. London, Ser. A, **433**, pp. 599–614.
[7] Jackson, J. D., 1999, *Classical Electrodynamics*, 3rd ed., Wiley, New York, pp. 352–356.
[8] Chern, R., Liu, X., and Chang, C., 2007, "Particle Plasmons of Metal Nanospheres: Application of Multiple Scattering Approach," Phys. Rev. E, **76**, p. 016609.
[9] Segelstein, D., 1981, "The Complex Refractive Index of Water," MS thesis, University of Missouri, Kansas City, MO.
[10] Weaver, J. H., and Frederikse, H. P. R., 2001, *Optical Properties of Selected Elements*, 82nd ed., CRC, Boca Raton, FL.
[11] Kreibig, U., and Vollmer, M., 1995, *Optical Properties of Metal Clusters*, Springer, New York.
[12] Kawata, S., 2001, *Near-Field Optics and Surface Plasmon Polaritons*, Springer, New York.
[13] Johnson, P. B., and Christy, R. W., 1972, "Optical Constants of the Noble Metals," Phys. Rev. B, **6**, pp. 4370–4379.
[14] Kittel, C., 1971, *Introduction to Solid State Physics*, 4th ed., Wiley, Canada, p. 248.
[15] Rechberger, W., Hohenau, A., Leitner, A., Krenn, J. R., Lamprecht, B., and Aussenegg, F. R., 2003, "Optical Properties of Two Interacting Gold Nanoparticles," Opt. Commun., **220**, pp. 137–141.
[16] Feringa, B. L., 2001, *Molecular Switches*, Wiley-VCH, Weinheim, p. 399.
[17] Han, L., Tang, T., and Chen, S., 2006, "Tuning the Absorptions of Au Nanospheres on a Microshell by Photo-Deformation," Nanotechnology, **17**, pp. 4600–4605.
[18] Palmer, K. F., and Williams, D., 1974, "Optical Properties of Water in the Near Infrared," J. Opt. Soc. Am., **64**(8), pp. 1107–1110.

Microscale Transport Phenomena in Materials Processing

Yogesh Jaluria
Board of Governors Professor
Mechanical and Aerospace Engineering Department,
Rutgers University,
Piscataway, NJ 08854
e-mail: jaluria@jove.rutgers.edu

Microscale transport mechanisms play a critical role in the thermal processing of materials because changes in the structure and characteristics of the material largely occur at these or smaller length scales. The heat transfer and fluid flow considerations determine the properties of the final product, such as in a crystal drawn from silicon melt or a gel from the chemical conversion of a biopolymer. Also, a wide variety of material fabrication processes, such as the manufacture of optical glass fiber for telecommunications, fabrication of thin films by chemical vapor deposition, and surface coating, involve microscale length scales due to the requirements on the devices and applications for which they are intended. For example, hollow fibers, which are used for sensors and power delivery, typically need fairly precise microscale wall thicknesses and hole diameters for satisfactory operation. The basic transport mechanisms underlying these processes are discussed in this review paper. The importance of material characterization in accurate modeling and experimentation is brought out, along with the coupling between the process and the resulting properties such as uniformity, concentricity, and diameter. Of particular interest are thermally induced defects and other imperfections that may arise due to the transport phenomena involved at these microscale levels. Additional aspects such as surface tension, stability, and free surface characteristics that affect the material processing at microscale dimensions are also discussed. Some of the important methods to treat these problems and challenges are presented. Characteristic numerical and experimental results are discussed for a few important areas. The implications of such results in improving practical systems and processes, including enhanced process feasibility and product quality, are also discussed. [DOI: 10.1115/1.3056576]

1 Introduction

Microscale thermal transport processes are particularly important in materials processing, which is presently one of the most active areas of research in heat transfer. We have seen substantial growth and development of new advanced materials and processing methods to meet the critical demand for special material properties in a variety of new and emerging applications that arise in energy, bioengineering, transportation, communications, computers, and other fields. Many of the relevant devices and systems are in the microscale range due to the dimensions involved. Also, the quality and characteristics of the final product resulting from materials processing are strongly dependent on the transport processes that arise at microscale, or nanoscale, levels. Due to growing international competition and stringent demands placed on devices, sensors, and equipment, it is has become critical to improve the quality and characteristics of the product, while optimizing the processing techniques and the manufacturing systems involved.

Fluid flow and the associated heat and mass transfer are extremely important in the thermal processing of materials, which refers to manufacturing and material fabrication techniques that are strongly dependent on the thermal transport mechanisms. With the growing interest in new and advanced materials such as composites, ceramics, polymers, glass, coatings, specialized alloys, and semiconductor materials, thermal processing has become particularly important since the properties and characteristics of the product can be largely controlled by thermal transport mechanisms, as discussed by Jaluria [1,2]. Besides the traditional processes, such as welding, metal forming, polymer extrusion, casting, heat treatment, and drying, thermal processing includes new and emerging methods, such as crystal growing, chemical vapor deposition, thermal sprays, fabrication of composite materials, processing of nanopowders to fabricate system components, optical fiber drawing and coating, microgravity materials processing, laser machining, and reactive extrusion.

A few of these processes, in which microscale transport phenomena are of particular importance in determining the quality and characteristics of the device or item being fabricated, are shown in Fig. 1. These include thin film fabrication by chemical vapor deposition (CVD), the optical glass fiber drawing process in which a specially fabricated glass preform is heated, drawn, cooled, and coated into a fiber, and Czochralski crystal growing in which molten material such as silicon is allowed to solidify across an interface as a seed of pure crystal is withdrawn. In all these processes, the quality and characteristics of the final product and the rate of fabrication are strong functions of the underlying microscale thermal transport processes; see, for instance, Refs. [3–6]. For example, the flows that arise in the molten material in crystal growing due to temperature and concentration differences affect the quality of the crystal and, thus, of the semiconductors fabricated from the crystal. Also, the microstructure of the crystal is determined by the micro- and nanoscale processes occurring at the solid-liquid interface. It is important to understand these flows and develop methods to minimize or control their effects. Similarly, the profile of the neck-down region in an optical fiber drawing process is governed by the viscous flow of molten glass, which is in turn determined by the thermal field in the glass. Thermally induced defects arise due to the breaking of the Si–O bonds, microcracks result from the tension, and other defects are caused by local instabilities. Microscale transport of dopants added to the material in order to enhance or modify the optical behavior of the fiber is also important in the determination of the characteristics of the fiber obtained. The buoyancy-driven flows generated in the liquid melt in casting processes strongly influence the microstructure of the casting and the shape, movement, and other characteristics of the solid-liquid interface. In chemical vapor deposition, the heat and mass transfer processes occurring at

Contributed by the Heat Transfer Division of ASME for publication in the JOURNAL OF HEAT TRANSFER. Manuscript received August 3, 2008; final manuscript received September 27, 2008; published online January 26, 2009. Review conducted by Robert D. Tzou.

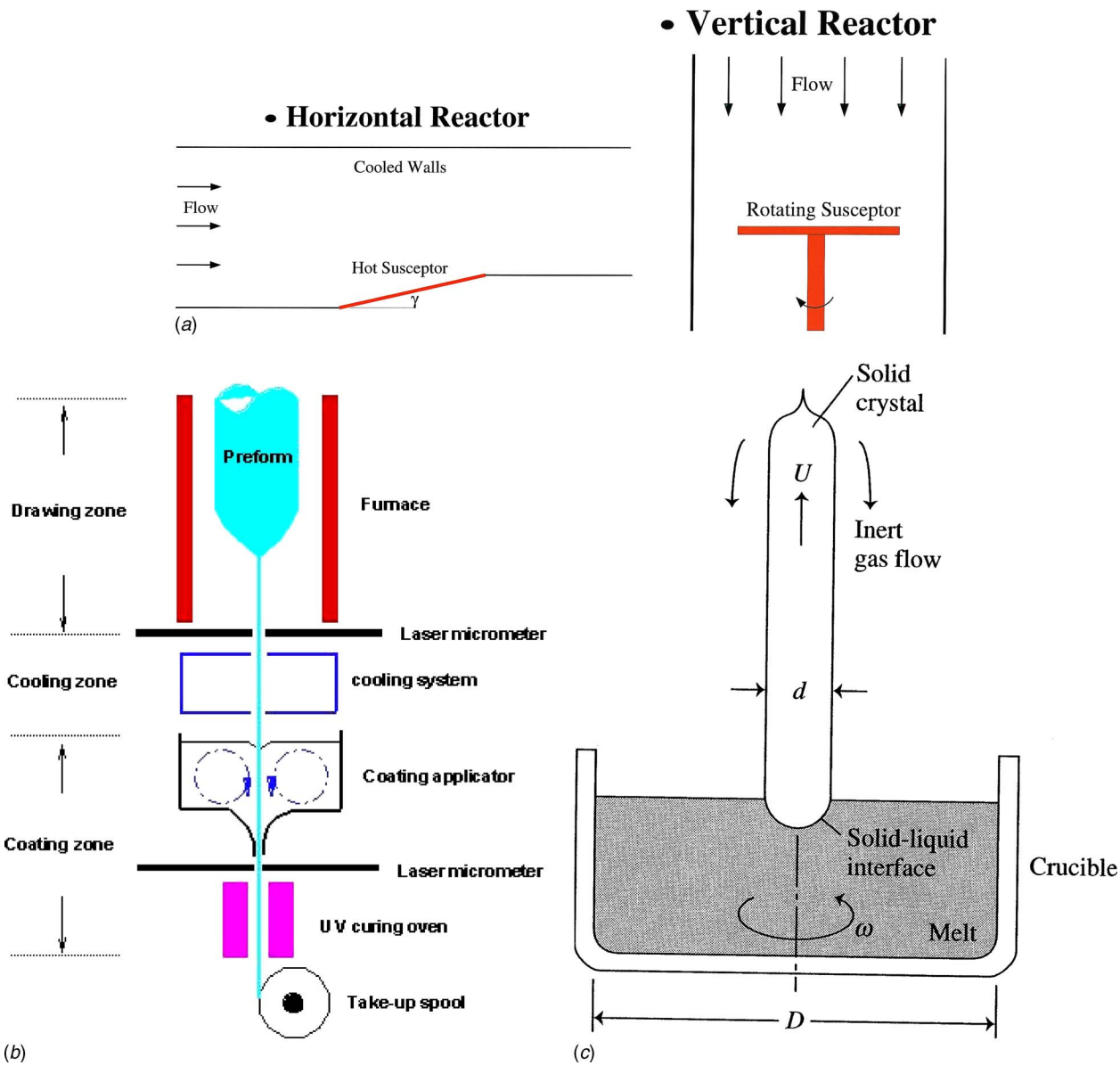

Fig. 1 Sketches of a few thermal materials processing applications that involve microscale transport phenomena. (*a*) Chemical vapor deposition. (*b*) Optical fiber drawing. (*c*) Czochralski crystal growing.

micro- and nanometer dimensions determine the deposition rate, uniformity, and the overall quality of the thin film produced.

Another important aspect is the link between the microscale transport and the materials processing systems, which involve macroscale or commercial scale considerations. An understanding of the microscale mechanisms that determine material characteristics is important, but these must be linked with the boundary conditions that are usually imposed at the macroscale level in the thermal materials processing system, as is evident from the systems shown in Fig. 1.

This review paper is directed at these important issues, focusing on microscale transport in thermal processing of materials and linking these with the characteristics of the product and with the system. A range of processes is considered in order to discuss the important basic considerations that arise in microscale devices, experimental and analytical/numerical approaches to deal with the microscale transport mechanisms, and their effect on the processed material. As mentioned above, the two main aspects that are considered in this paper are as follows:

1. applications and devices at microscale dimensions
2. microscale mechanisms that determine material characteristics during processing

Thus, the paper first focuses on microscale devices and discusses the major basic concerns and challenges that arise at these dimensions, which typically range from a few microns to around 200 μm. These include, for instance, numerical modeling with very fine grids, strong viscous dissipation effects, high pressures needed for the flow, experimentation over micrometer scales, applicability of traditional analyses, and mechanisms, such as surface tension, that could increase in significance as the dimensions are reduced. The paper next discusses the considerations related to underlying microscale mechanisms in materials processing and their effects on the quality of the device or product being fabricated. Examples include thermally induced defects, material conversion due to shear and temperature, chemical reactions leading to deposition, and microstructure changes as the material undergoes processing. The link between these aspects and the quality

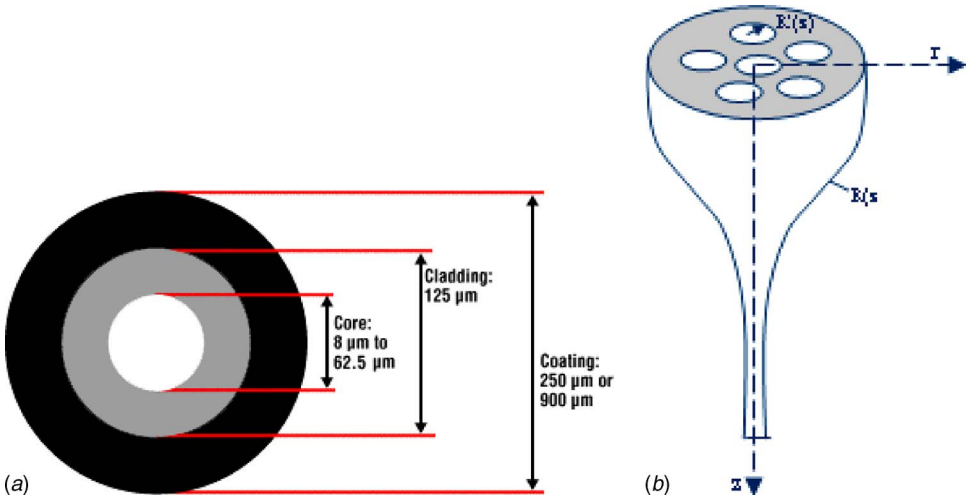

Fig. 2 (*a*) **Structure of a typical optical fiber;** (*b*) **sketch of a microstructured optical fiber**

and characteristics of the product, rate of production, cost, process feasibility, and process optimization are also discussed.

2 Applications and Devices at Microscale Dimensions

As mentioned earlier, the flow and heat transfer at micrometer dimensions are of interest in many thermal materials processing applications. Because of the small dimensions, the major concerns that arise are high-pressure differences, significant viscous dissipation, difficulty in measurements, particularly near the surfaces, and analytical/numerical modeling. However, if the problem involves dimensions that are much larger than the mean free path of the molecules, no-slip conditions at the walls and continuity can be assumed, resulting in modeling, which is similar to modeling at the macroscale.

For telecommunication purposes, the optical fiber usually consists of three components, core, cladding, and coating, as shown in Fig. 2(*a*) for the so-called "weakly guiding fiber." In this multilayered structure, the light-guiding central portion, or core, is covered by a dielectric layer, or cladding, which generally has a refractive index lower than that of the core to obtain total internal reflection in the core. In practice, core sizes vary from 8.3 μm to 62.5 μm. Radiation heat transfer is the dominant mode of transport in the heating process and the viscosity of the glass, which is a subcooled liquid, affects the flow and the draw tension, which in turn affects the transmission properties and also results in strength degradation [7]. Coating of the fiber with a jacketing material is carried out for protection against abrasion and for increased strength. Again, the coating thickness is in microns and defects in the coating are important for the quality of the final optical properties of the fiber. Interest in hollow or microstructure fibers, which form an important class of optical fibers, has grown recently since these fibers have many advantages over the conventional solid-core optical fibers. These include high laser power thresholds, low insertion loss, no end reflection, ruggedness, and small beam divergence. Due to the presence of the air core, microstructure fibers can achieve a low attenuation through structural design rather than high-transparency material selection and can be used to provide infrared laser beam and the high-power delivery [8]. Microstructure optical fibers are widely used for medical applications, sensor technology, diagnostics, and CO_2 and laser delivery, besides traditional telecommunications [9]. Figure 2(*b*) shows a sketch of a microstructured fiber, with several microchannels that contain air or inert gases and that are typically 10–20 μm in diameter. The typical dimensions that are of interest in these and other such applications are given in Table 1.

2.1 Furnace Drawing of Optical Fibers. The manufacture of an optical fiber typically begins with a silica preform, which generally consists of two concentric cylinders called the core and the cladding and which may be doped with various elements or chemicals to achieve desired optical properties. In a draw tower, the preform is traversed vertically through a high-temperature cylindrical furnace. The glass is heated beyond its softening point T_{melt} of about 1900 K for silica and is drawn into a fiber of diameter around 125 μm by applying axial tension. Studies on pure, single-layer, solid, silica optical fiber drawing have been carried out by a number of researchers. Paek and Runk [10] studied the neck-down profile and temperature distribution within the neck-down region using a one-dimensional analysis. Myers [11] developed a one-dimensional model for unsteady glass flow. More comprehensive models have been developed by Jaluria and coworkers [12–15]. They investigated the flow and the thermal transport in detail, including the convective and radiative heat transfer in the axisymmetric configuration of the glass preform and the inert gas flow. An analytical/numerical method was developed to generate the neck-down profile. The effects of fiber draw speed, inert gas velocity, furnace dimensions and furnace temperature distribution on the flow, temperature distribution, tension, and neck-down shape were obtained and discussed. Initially, the preform was assumed to be optically thick, which is not valid in the

Table 1 Typical dimensions of some microscale devices and applications

Solid optical fibers
Single mode: 5–10 μm
Multimode: 10–50 μm
Coatings
Primary coating: 30–50 μm
Secondary coating: 50–100 μm
Hollow fibers
Hole diameter: 10–50 μm
Multistructured: Hole diameter 5–10 μm
Chemical vapor deposition
Coatings: 1–10 μm
Films: 10–50 μm
Chemical conversion, defect generation
Submicron scale (micro- and nanoscale)

lower neck-down region and which was later modeled with the zonal method. High-speed optical fiber drawing, up to 20 m/s, with preform diameters of 5–10 cm was investigated. More recently, Wei et al. [16] used the discrete ordinate method to solve the radiative transfer equation and numerical results for higher-speed (25 m/s) drawing were obtained. However, the major constraint has been the availability of accurate radiative property data.

The flow of the glass and of the aiding purge gas in a cylindrical furnace is assumed to be axisymmentric. The governing equations for the glass and the gas are given as

$$\frac{\partial v}{\partial z} + \frac{1}{r}\frac{\partial (ru)}{\partial r} = 0 \tag{1}$$

$$\frac{\partial v}{\partial t} + u\frac{\partial v}{\partial r} + v\frac{\partial v}{\partial z} = -\frac{1}{\rho}\frac{\partial p}{\partial z} + \frac{1}{r}\frac{\partial}{\partial r}\left[r\nu\left(\frac{\partial v}{\partial r} + \frac{\partial u}{\partial z}\right)\right] + 2\frac{\partial}{\partial z}\left(\nu\frac{\partial v}{\partial z}\right) \tag{2}$$

$$\frac{\partial u}{\partial t} + u\frac{\partial u}{\partial r} + v\frac{\partial u}{\partial z} = -\frac{1}{\rho}\frac{\partial p}{\partial r} + \frac{2}{r}\frac{\partial}{\partial r}\left(r\nu\frac{\partial u}{\partial r}\right) + \frac{\partial}{\partial z}\left[\nu\left(\frac{\partial v}{\partial r} + \frac{\partial u}{\partial z}\right)\right] - \frac{2\nu u}{r^2} \tag{3}$$

$$\rho C_p\left(\frac{\partial T}{\partial t} + u\frac{\partial T}{\partial r} + v\frac{\partial T}{\partial z}\right) = \frac{1}{r}\frac{\partial}{\partial r}\left(rK\frac{\partial T}{\partial r}\right) + \frac{\partial}{\partial z}\left(K\frac{\partial T}{\partial z}\right) + \Phi + S_r \tag{4}$$

where Φ is the viscous dissipation term and S_r is the radiation source term. The other variables are defined in the Nomenclature.

For glass, the material properties are strong functions of the temperature T. They also vary with composition and changes in the microstructure, the main effect being on the radiation properties and on the refractive index. The variation in the viscosity is the most critical one for the flow, since it varies quite dramatically with temperature. An equation based on the curve fit of available data for kinematic viscosity ν is written for silica, in SI units, as

$$\nu = 4545.45 \exp\left[32\left(\frac{T_{\text{melt}}}{T} - 1\right)\right] \tag{5}$$

indicating the strong exponential variation of ν with temperature. Variations in all the other relevant properties of glass need to be considered as well, even though the variation with T is not as strong as that of viscosity. The properties of the purge gas in the furnace may be considered to be constant since their variations are small over the temperature ranges encountered. The radiative source term S_r in Eq. (4) is nonzero for the glass preform/fiber because glass emits and absorbs energy. The variation of the absorption coefficient with wavelength λ can often be approximated in terms of bands with constant absorption over each band. A two- or three-band absorption coefficient distribution has been effectively used. One of the methods that have been used successfully to model the radiative transport is the zonal model. Figure 3 shows the typical finite volume zones used for radiative transfer. Because of the small fiber diameter, being around 125 μm, there is a temptation to assume uniform temperature across the fiber. However, because of the high-temperature dependence of the viscosity, this assumption does not yield accurate results and a large number of grid points, typically around 50, are needed across the fiber radius of around 62.5 μm to capture changes in temperature and the consequent effects on properties, viscous dissipation, thermally induced defects, and dopant movement.

Figures 4 and 5 show some typical results obtained from the numerical simulation. The fiber drawing process involves modeling the free surface flow of glass. A solution of the transport equations, along with a surface force balance, is needed for the determination of the neck-down profile. The normal force balance and the vertical momentum equations are used to obtain a correction scheme for the neck-down profile and the iterative process is continued until the neck-down shape does not change from one iteration to the next. It was found that viscous and gravitational forces are dominant in the determination of the profile. Surface tension effects are small, despite the small dimensions involved. For convergent cases, perturbations to the initial profile and different starting shapes lead to the converged neck-down profile, indicating the robustness of the scheme and the stability of the drawing process, as seen in Fig. 4(*a*).The force balance conditions are also closely satisfied if the iterations converge [14]. However, as expected, it is not possible to draw the fiber under all imposed conditions. If the furnace temperature is not high enough, it is found that the fiber breaks due to lack of material flow, a phenomenon that is known as viscous rupture. This is first indicated by the divergence of the numerical correction scheme for the profile and is then confirmed by excessive tension in the fiber. Similarly, it is determined that, for a given furnace temperature, there is a limit on the draw speed beyond which drawing is not possible, as this leads to rupture. A region in which drawing is feasible can be identified, as shown in Fig. 4(*b*). Beyond the boundaries of this region, drawing is not possible. Similarly, different combinations of other physical and process variables, such as the inert gas flow velocity, flow configuration, furnace wall temperature distribution, furnace length and diameter, and preform and fiber diameters, may be considered to determine the feasibility of the process [17].

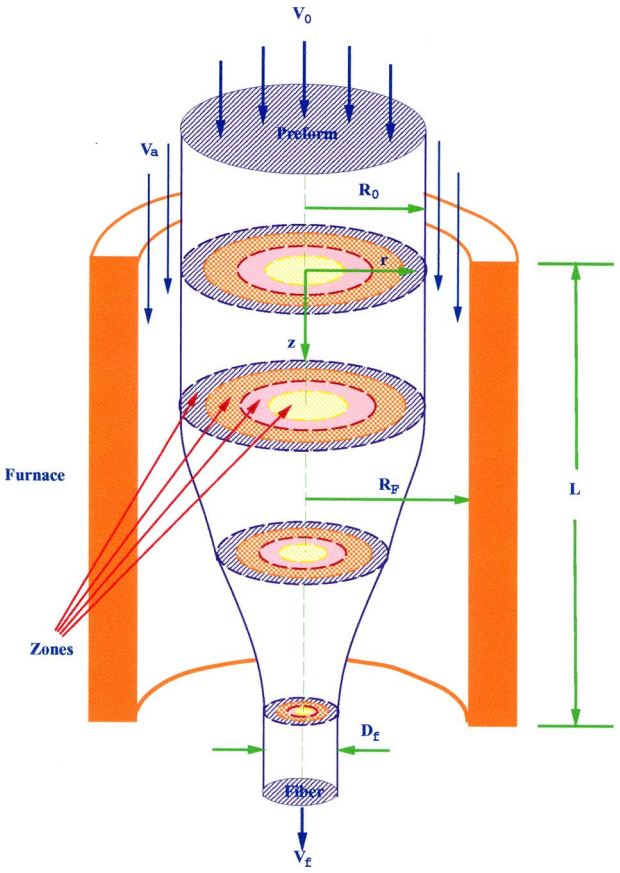

Fig. 3 Axisymmetric finite volume zones for the calculation of radiation in the glass preform and fiber

Typical computed results in the neck-down region are shown in Fig. 5 in terms of the temperature distribution and the viscous dissipation. The flow was found to be smooth and well layered because of the high viscosity. Typical temperature differences of 50–100°C arise across the fiber. Viscous dissipation, though relatively small compared with the total energy transport, is mainly concentrated near the end of the neck-down, in the microscale

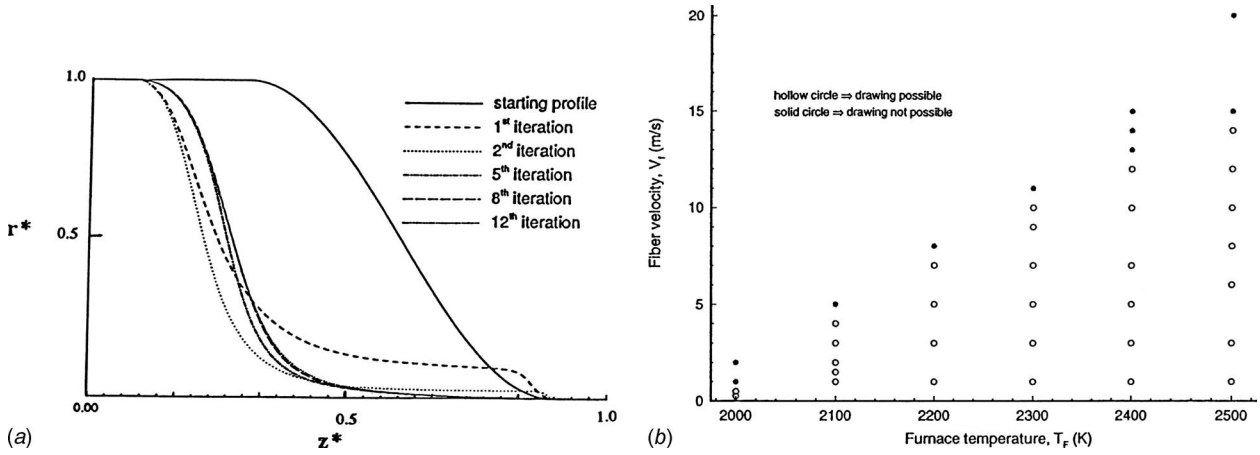

Fig. 4 (*a*) **Iterative convergence of the neck-down profile in optical fiber drawing. Here,** $r^* = r/R$ **and** $z^* = z/L$**, where** *R* **is the preform radius and** *L* **is the furnace length;** (*b*) **feasibility of the optical fiber drawing process, as indicated by regions where drawing is not possible due to viscous rupture resulting from excessive draw tension.**

region, and plays an important role in maintaining the temperatures above the softening point. Figure 6 shows a comparison with experimental results on the neck-down profile and thus lends support to the modeling of the process. However, experiments are considerably complicated due to the small dimensions of the fiber, high temperatures in the draw furnace, and large draw speeds. Such experimental results are fairly difficult and are obtained on the draw tower by stopping the draw process and studying the drawdown shape of the preform [18].

2.2 Multilayer and Hollow Fibers. As mentioned earlier, for telecommunication purposes, the optical fiber usually consists of the core and the cladding, with standard core sizes in use today being 8.3 μm, 50 μm, and 62.5 μm, and the diameter of the cladding surrounding each of these cores being around 125 μm [10,18]. The core-cladding structure may be treated as different fluids with different properties. Separate body-fitted grids are applied to the different layers and to the inert gas. Each separate layer in the glass is assumed to have a uniform refractive index, bounded by diffuse surfaces. The zonal method is applied to calculate the radiation transfer inside the three enclosures, as developed by Chen and Jaluria [19]. The two-band model presented by Myers [11] for the absorption coefficient a of pure silica was used. This is given by the equations

$$a = 0 \quad \text{for} \quad \lambda < 3.0 \ \mu\text{m} \tag{6}$$

$$a = 400.0 \ \text{m}^{-1} \quad \text{for} \quad 3.0 \ \mu\text{m} \leq \lambda < 4.8 \ \mu\text{m} \tag{7}$$

$$a = 15{,}000 \ \text{m}^{-1} \quad \text{for} \quad 4.8 \ \mu\text{m} \leq \lambda < 8.0 \ \mu\text{m} \tag{8}$$

Figure 7(*a*) shows a typical mesh for the two-layer optical fiber drawing process. The preform typically goes from a diameter of around 10 cm to the fiber diameter of 125 μm in a distance of around 0.3 m. Thus, extra care has to be exercised near the bottom of the region to avoid highly distorted grids due to the small diameter of the fiber. The optimal grid can be obtained by numerical experimentation. The core is shown as half in diameter as the cladding. However, it can be much smaller in diameter for single-mode telecommunication applications, being as small as around 8 μm. Again, it is not accurate to assume uniform temperature and velocity in the core, despite the small dimension, because of the large changes in viscosity due to temperature differences. The boundary conditions of shear, pressure, velocity, and temperature continuity have to be satisfied at the interface between the two layers. A typical example of the numerically calculated neck-down profile for a two-layer optical fiber is shown in Fig. 7(*b*). The force balance conditions are checked at all the interfaces and the radiation calculations are much more involved than for a single-layer fiber discussed earlier.

When the core and the cladding are doped with various dopants, the refractive index and absorption coefficients are affected [20]. Since radiation heat transfer is the dominant mode of transport in the heating process, a nonuniform distribution of radiation properties in the preform due to this microscale doping will cause significant local effects and will thus affect the draw process. Assumed magnitudes of change in the refractive index and absorption coefficients were used by Chen [21] to capture the generic effects of variation in these two properties. The core is taken as pure fused silica and the cladding is doped.

GeO_2 is mainly used as a dopant for the core to increase the refractive index, which will also increase the ultraviolet radiation absorption and lower the viscosity. In this study, the core is doped with 5.5 mol %, 11.1 mol %, and 16.6 mol % GeO_2, respectively, to obtain relative refractive index differences of 0.5%, 1.0%, and 1.5% in the fiber. In Fig. 8(*a*), the isotherms for various GeO_2 concentrations are shown with a reference profile to demonstrate the variations in temperature levels in the axial direction. It is seen that, when the core is doped with GeO_2, the core is heated up to the same temperature level in a shorter distance than the cladding. The distance to reach a certain temperature level for the whole preform decreases with increasing GeO_2 concentration. The reason is that, since GeO_2-doped silica core has a larger radiation coefficient in the ultraviolet region and the transmissivity of pure silica cladding is very high in this region, the GeO_2-doped silica core absorbs more energy by radiation than pure silica core. Figure 8(*b*) shows the temperature of the preform along the centerline for pure silica and GeO_2-doped silica core with a pure silica cladding, for various GeO_2 concentrations. As expected, a significant increase in the centerline temperature is observed in the upper neck-down region with greater GeO_2 doping. Beyond that, the fiber with a higher GeO_2 concentration maintains a slightly higher temperature along the centerline. Several other results are given by Chen [21].

Similar considerations arise for the drawing of a hollow fiber, where the hollow core is a microchannel of diameter 40–80 μm. Some characteristic results are given here. The furnace diameter is taken as 7 cm and its length is 30 cm. The inner and outer diameters of the preform are 2.5 cm and 5 cm, respectively. The furnace temperature is assumed to be a parabolic profile with a maximum of 2500 K in the middle and a minimum of 2000 K at the two ends. The fiber drawing speed is 10 m/s. The velocity of the

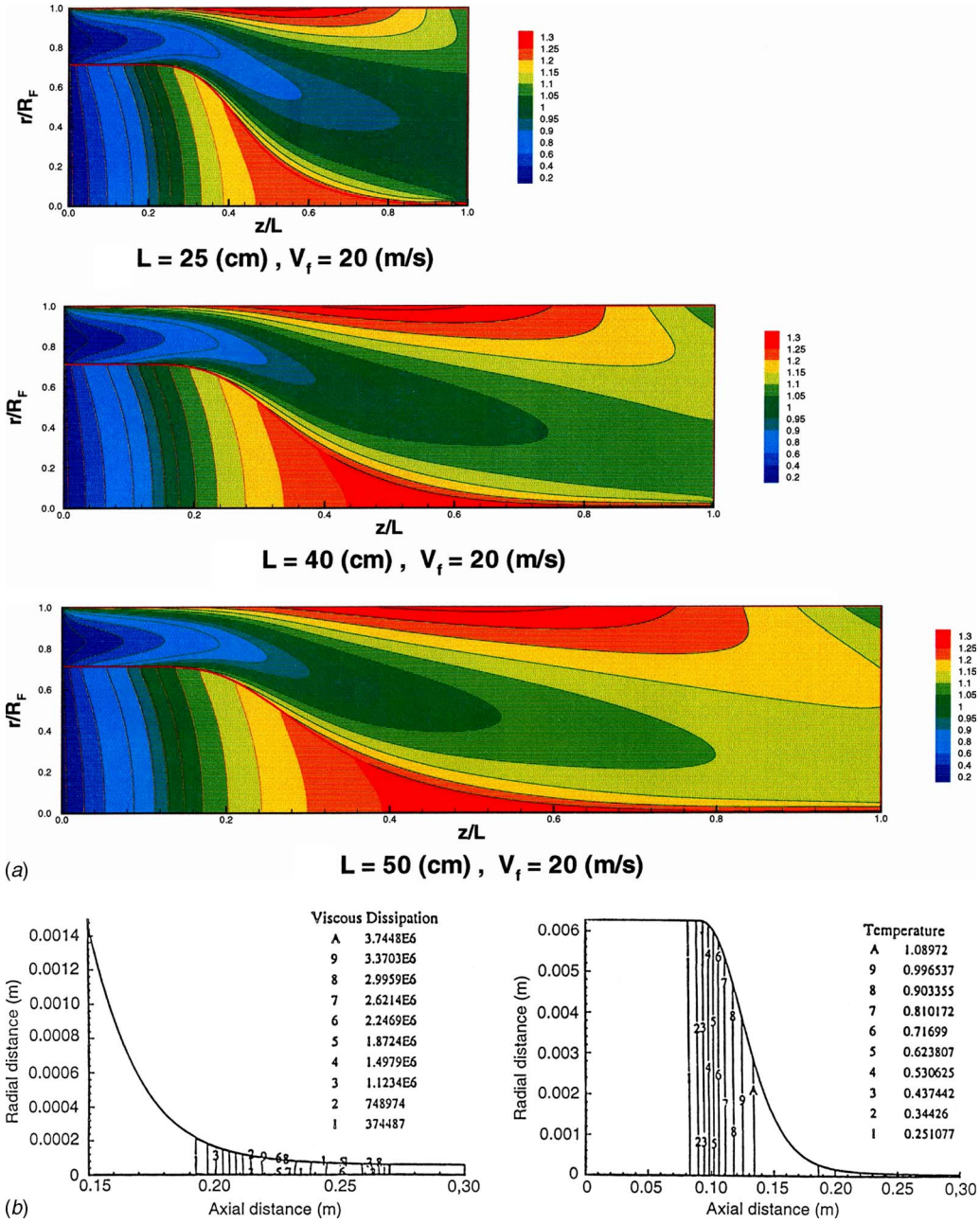

Fig. 5 (*a*) **Calculated temperature field in the glass during drawing of a single-layer optical fiber for three furnace lengths;** (*b*) **calculated viscous dissipation and temperature contours in the optical fiber drawing process for typical drawing conditions**

purge gas at the inlet is 0.1 m/s. Pressurization of the gas in the core is neglected. The results in terms of streamlines and isotherms are shown in Fig. 9. The thicker black lines indicate the two neck-down profiles. The isotherms are in terms of the nondimensional temperature, with the softening temperature as the characteristic temperature. It is clear that the flow and temperature distributions in the fiber and in the external gas in hollow fiber drawing are similar to those in the solid-core fiber drawing. Because of the thinness of the central core, the air in the core is dragged by the moving fiber. A slug flow approximation is made for the airflow to simplify the analysis. The magnitude of the velocity of the natural convection flow is so small that thermal diffusion dominates in the central cavity.

A collapse ratio C is defined to describe the collapse process of the central microchannel as

$$C(z) = 1 - (R_1(z)/R_2(z))/(R_{10}/R_{20}) \tag{9}$$

Thus, $C=0$ when the radius ratio of the final fiber equals the initial radius ratio, and $C=1$ when the central cavity is closed. The effects of the perform feeding and fiber drawing speeds and the furnace temperature on collapse ratio are studied. The variation of the collapse ratio with the axial distance for different feeding and drawing speeds and for different furnace temperatures is shown in Fig. 10(*a*). It is seen that the collapse ratio increases along the axis and increases with a decrease in drawing speed or a decrease in feeding speed. The effect of preform feed rate on the collapse ratio is much larger than that of the fiber drawing speed. The collapse ratio increases at larger furnace temperature. All these trends are similar to the results from Chakravarthy and Chiu [22]. These phenomena can be explained by using the "collapse time" of

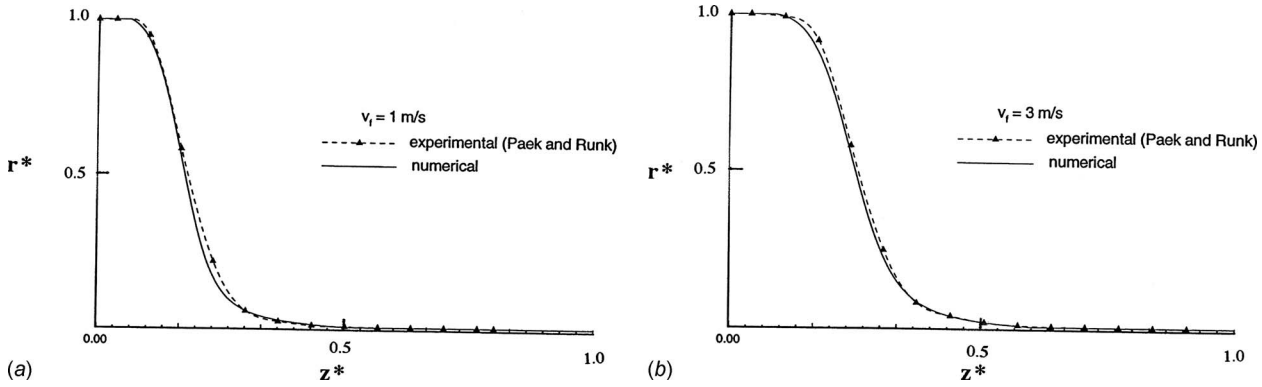

Fig. 6 Comparison of the numerical predictions of the neck-down profile with experimental results

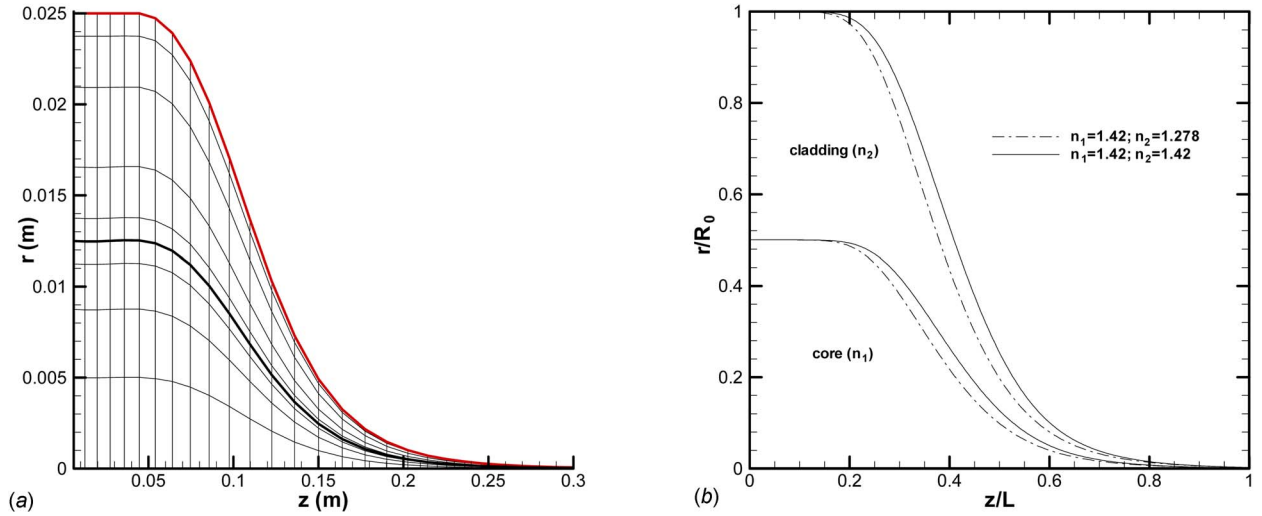

Fig. 7 Numerical grid and calculated neck-down profiles for a preform with a core-cladding structure at two values of the refractive index of the outer layer

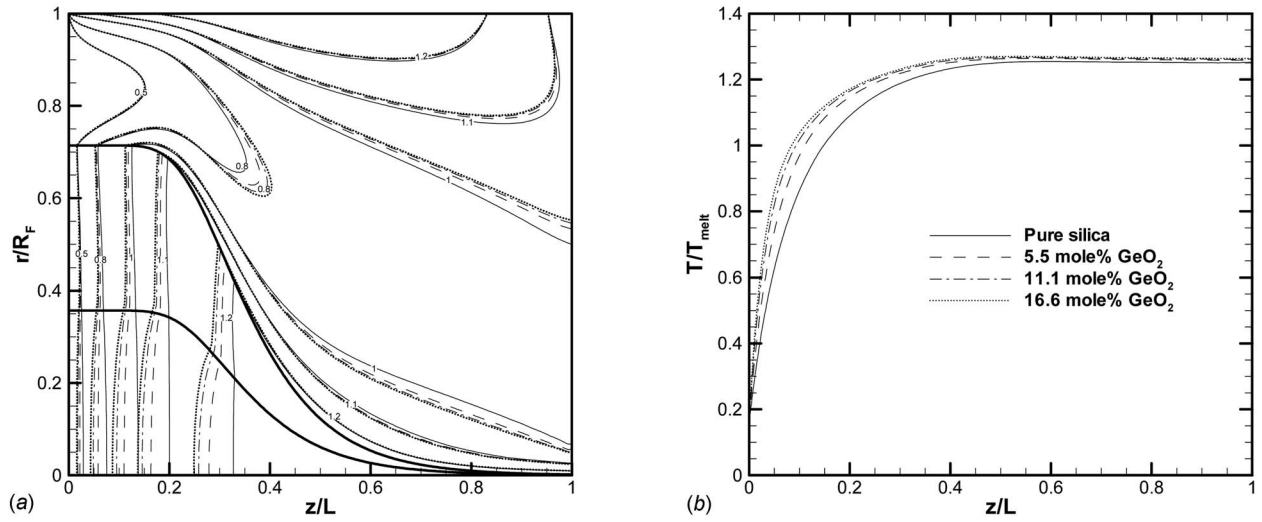

Fig. 8 (*a*) Isotherms for various GeO_2 concentrations (solid line: pure silica; dashed line: 5.5 mol % GeO_2; dashed dotted line: 11.1 mol % GeO_2; dotted line: 16.6 mol % GeO_2); (*b*) temperature variation along the centerline for various GeO_2 concentrations

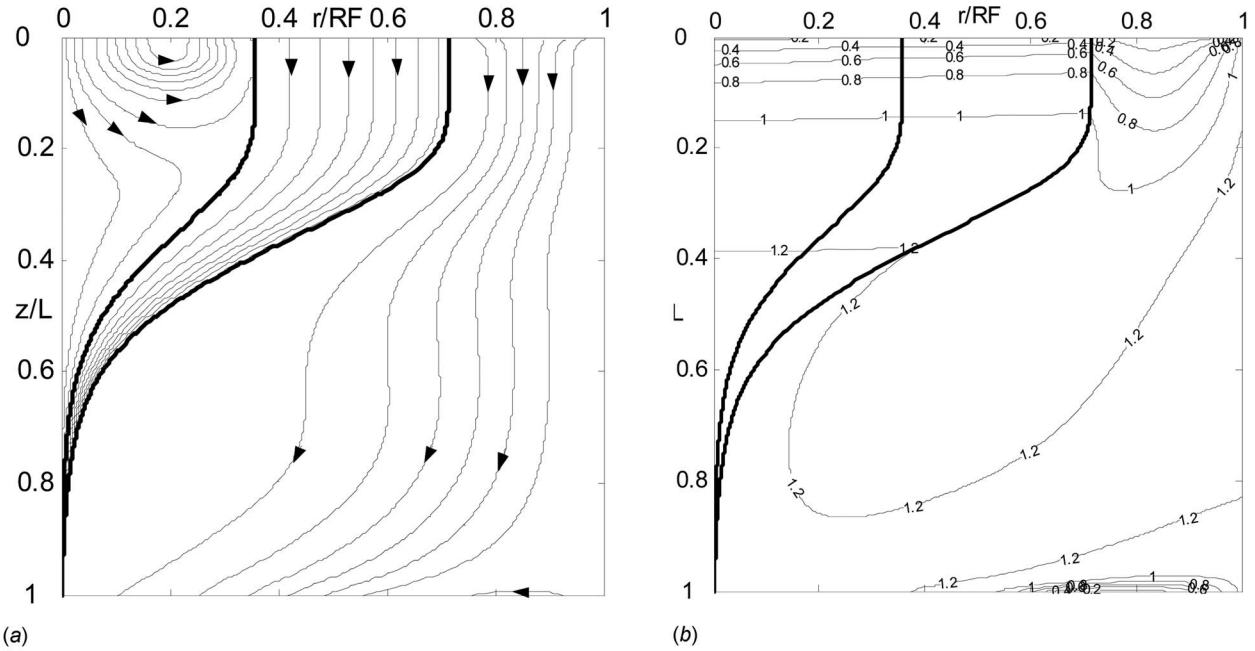

Fig. 9 Streamlines and isotherms in the furnace for a typical case of hollow fiber drawing with a parabolic furnace temperature distribution at a drawing speed of 10 m/s

preform/fiber in the drawing furnace. When the drawing or feeding speed decreases, the total time of preform/fiber in the furnace increases. The total time of preform/fiber in the furnace is comprised of the time to heat the preform up to the softening temperature and the time for the preform/fiber to collapse. The collapse time increases since the time to heat the preform is nearly the same for different drawing or feeding speeds. Therefore, the collapse ratio increases due to an increase in the collapse time when the drawing or feeding speed decreases. Since the drawing speed is much higher than the feeding speed, the collapse time is more sensitive to the feeding speed than the drawing speed. Also the time to heat the preform is shorter at higher furnace temperature, which implies the collapse time increases at given feeding and drawing speeds. Hence, the collapse ratio increases at higher furnace temperature, as seen in Fig. 10(*b*). In order to avoid the collapse of the central cavity, we can increase the drawing and feeding speeds, decrease the furnace temperature, or increase the preform radius ratio. The collapse ratio is also influenced by the pressure difference between the purge gas and the central cavity. It was shown that the collapse ratio decreases with a decrease in the pressure difference. This is because higher pressure in the central cavity tends to prevent collapse of the central cavity [23]. It was also seen that high negative pressure difference may cause the central cavity to enlarge during the drawing process. This is called "explosion" in the drawing process. Because of the size of the core, surface tension is an important parameter and plays a very significant role in the collapse.

The hollow fiber cannot be drawn at any arbitrary combination of critical drawing parameters, as seen earlier for solid-core fibers. Figure 11(*a*) shows an infeasible case, which arises due to the lack of material flow. It is seen that the neck-down profiles become quite flat after 12 iterations. This phenomenon is similar to that seen in the solid-core fiber drawing process [14]. Figure 11(*b*) illustrates the feasible domain in terms of drawing temperature and drawing speed. Drawing speed is in the range 1–20 m/s. It shows that drawing process is possible only in the region between

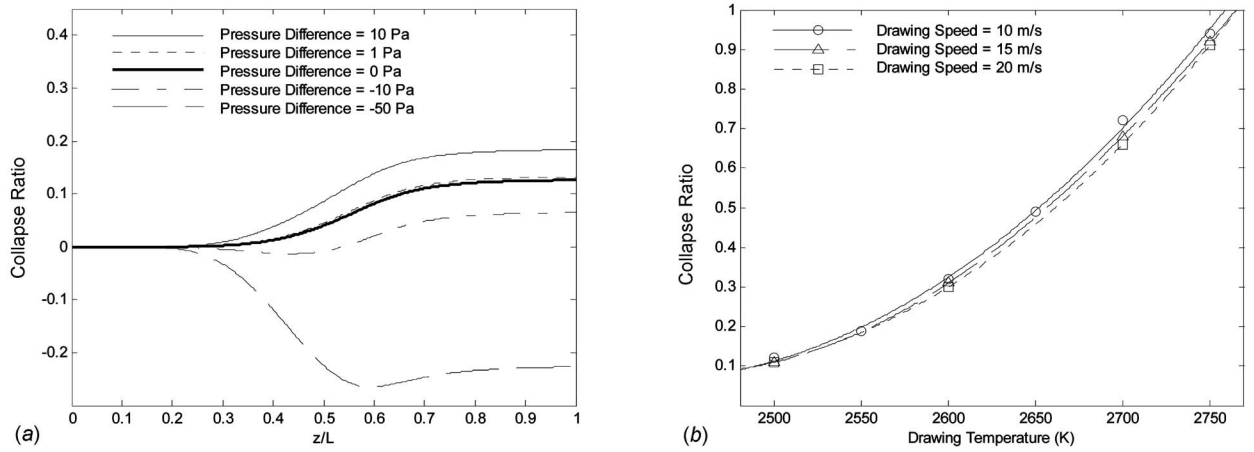

Fig. 10 (*a*) Variation of collapse ratio along the axis with different pressurizations in the core and (*b*) with the drawing temperature for different drawing speeds

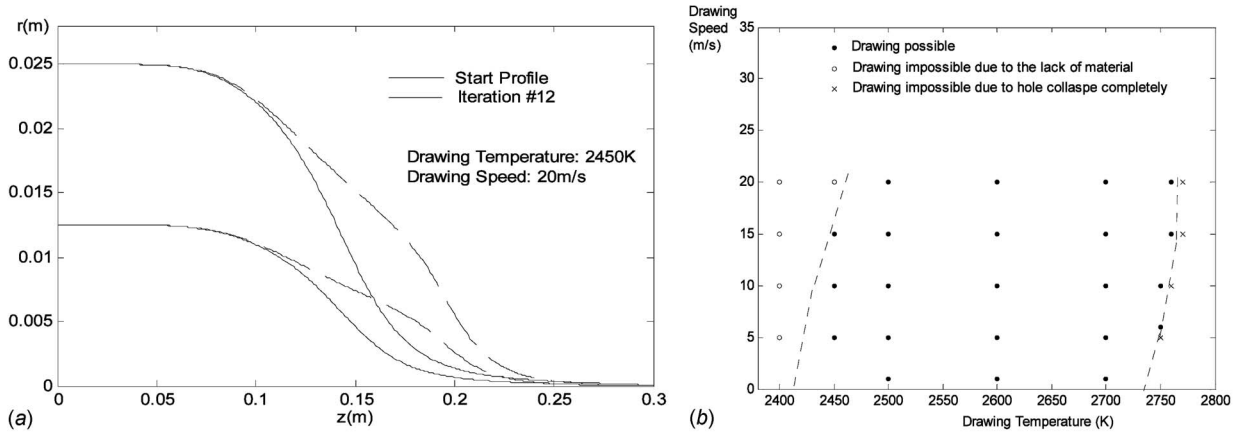

Fig. 11 (*a*) **Neck-down profile corrections for an infeasible drawing case;** (*b*) **feasible domain for hollow fiber drawing in terms of the drawing speed and the drawing temperature**

two dashed lines. The left boundary exists because the continuous drawing process may fail due to the lack of material flow at low furnace temperature or high drawing speeds, which is initially indicated by the divergence of the numerical correction scheme for the profiles. The right boundary exists only for hollow optical fiber because high furnace temperature or low drawing speeds may cause the central air core to collapse completely. At the right side of this boundary line, the central air core is closed during the drawing process. Therefore, there are two thresholds for the drawing temperature at the same drawing speed. These two boundary lines are nearly vertical since the effect of the drawing speed is relatively weak, which has been indicated by the earlier parameter study [23].

2.3 Fiber Coating. Optical fibers are coated with a jacketing material for protection against abrasion, to increase strength, and to reduce stress-induced microbending losses. Typical coating thicknesses are of the order of 40–50 μm and are applied to the uncoated fiber or as secondary coating to a coated fiber. The basic coating process involves drawing the fiber of diameter around 125 μm through a reservoir of coating fluid, with inlet and outlet dies. This is immediately followed by a curing process of the polymer coating material around the fiber. Figure 12(*a*) shows a schematic of a typical coating applicator and die system. Though the chamber is 1–2 cm in diameter, the entrance and exit dies are channels with diameters to yield gap thickness between the moving fiber and the die wall of 50–100 μm. Viscous shear due to the moving fiber results in a circulatory fluid motion within the fluid. A balance between surface tension, viscous, gravitational, and pressure forces results in an upstream meniscus at the cup entrance, as shown in Fig. 12(*b*). A downstream meniscus at the die exit results again from a balance of viscous, gravitational, and inertia forces, along with the surface tension forces. Centering forces within the tapered die contribute to the positioning of the fiber at the die exit center. Successful coatings are concentric, of uniform thickness, and free of particle inclusions or bubbles [24].

Under ideal operating conditions, at the entrance die, the coating liquid in the vicinity of a dynamic contact surface, which forms an upstream meniscus between the air, the liquid, and the moving fiber, replaces the air entrained with the moving fiber. However, at high speeds, the meniscus breaks down, with "sawtooth" instability, as shown in Fig. 12(*b*), and air entrained into the coating. The use of high draw rates requires consideration of alternate pressurized applicator designs, where pressure induced motion of the coating material is used to reduce the shear at the fiber surface and helps in the establishment of a stable free surface flow. An additional benefit resulting with such pressurized dies has been the incorporation of gas bubble reducing, or bubble stripping, designs, which have resulted in minimizing gas bubbles entrained at the coating cup entrance and then trapped within the coating layer.

At the die exit, the coating material is drawn out with the fiber, forming a downstream meniscus, whose shape is primarily deter-

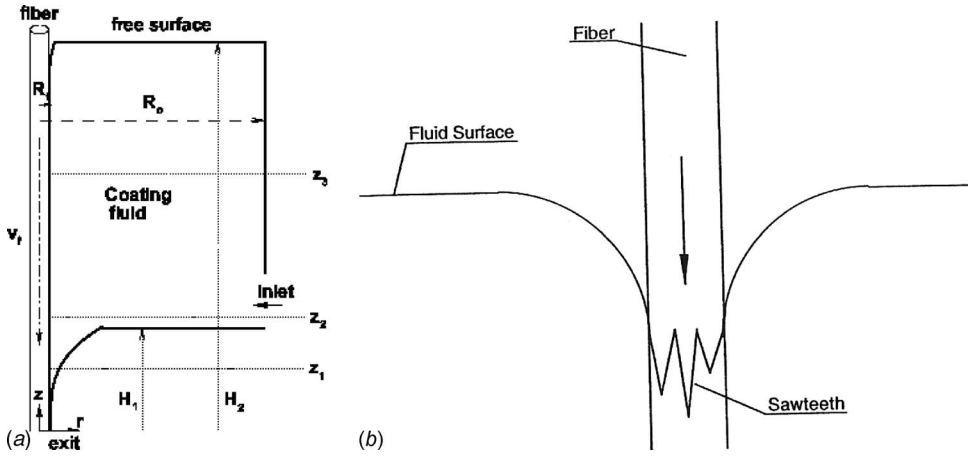

Fig. 12 (*a*) **A typical optical fiber coating applicator;** (*b*) **instability and breakdown of the entrance meniscus in the microchannel inlet at high speeds**

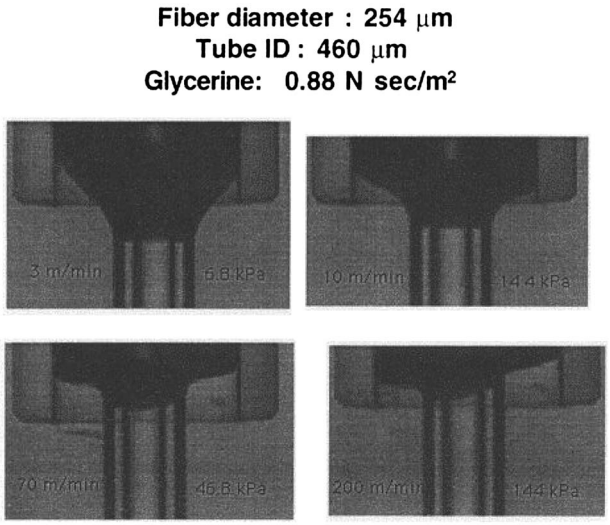

Fig. 13 Entrance flow in the microchannel inlet of annular gap thickness 103 μm at different pressures and draw speeds

mined by a balance between viscous, gravitational, and inertia forces. The control of the coating characteristics is of major concern in the industry. These considerations have become particularly important as the coating speeds have been increased to values beyond 20 m/s to enhance productivity and as the interest in specialty fibers and fibers of different materials, including polymer fibers, has grown. The physical properties of the polymer coating materials, particularly the viscosity, and their dependence on temperature are of primary importance in the coating process. Surface tension has a significant effect on the flow near the free surface, which represents the interface between liquid and gas in many cases, and on the shape, stability, and other characteristics of the interface. Surface tension affects the force balance on a free surface and affects the equilibrium shape of the interface. For typical optical fiber dimensions, the diameter being of order 125 μm, surface tension effects are often very large and gravitational effects are often small. However, for larger dimensions, particularly for plates and cylinders of diameter in centimeters, gravity could dominate over surface tension and over several other forces.

A few typical results from these studies are discussed here. The experimental work has been carried out on a fiber coating facility to study the upstream and downstream menisci, with glycerin/water solutions as test fluids. Glycerin is convenient for such studies because its viscosity at 20°C is in the range 1 N s/m^2, which is similar to that used in coating applications. The microchannels that form the inlet and exit dies can be changed so that different geometries and diameters can be investigated [25].

Figures 13 and 14 show images of the meniscus formed with the fiber moving through the micropipette inlet tube into the applicator. The fiber speed ranges from 3 m/min to 200 m/min. Different diameters and imposed pressures are employed. Figure 14(*c*) clearly shows the breakdown of the meniscus into sawtooth patterns and tip streaming as previously mentioned. On the other hand, at higher imposed pressures, the meniscus image appears to be smooth, suggesting suppression of large-scale breakdown at the same fiber speed. The unpressurized meniscus generates a large number of relatively large air bubbles compared with the pressurized meniscus. A comparison of the shape of the menisci in the figures shows that the effect of the imposed pressure is to flatten the meniscus and to increase the slope of the liquid-air interface near the fiber compared with that for an unpressurized meniscus. This results in a smaller air volume available for entrainment, accounting for the difference between the figures. The effect of the imposed pressure on the meniscus shape for a fiber moving in a tube is also seen, indicating the flattening of the profile as well as an upward movement of the meniscus as the pressure increases. These results are summarized in Fig. 15. The first part gives the fiber speed for breakdown as a function of the applicator pressure, indicating higher speeds before breakdown occurs at larger pressure. Figure 15(*b*) shows the dependence of the location of the meniscus in the microchannel, which forms the inlet die, on the imposed pressure for a given fiber speed. Clearly, the pressure flattens and moves the meniscus upward, imparting greater stability to it and reducing the chances of a breakdown [25].

The flow and heat transfer in the coating applicator and die have also been investigated numerically. The shape of the meniscus was prescribed on the basis of experimental data and axisymmetric transport was assumed. The typical height of the meniscus was found to vary from around 10 μm to 100 μm. Typical

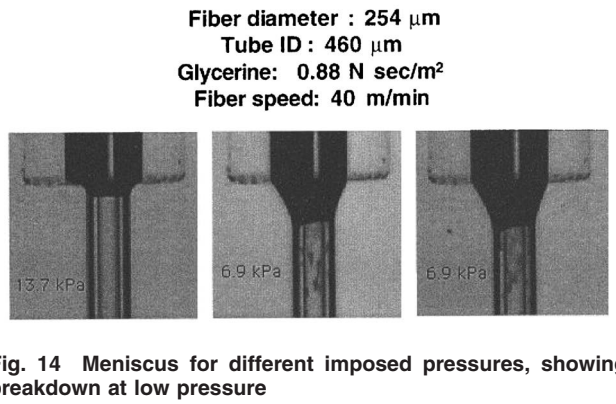

Fig. 14 Meniscus for different imposed pressures, showing breakdown at low pressure

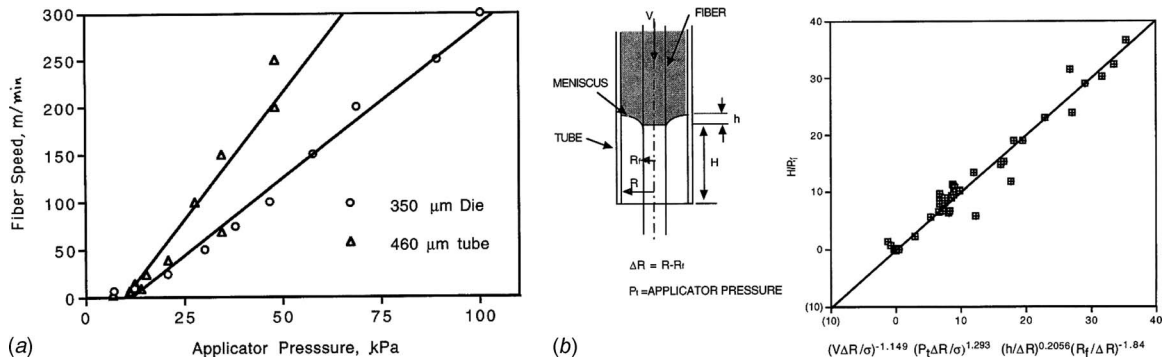

Fig. 15 (*a*) Dependence of fiber speed, for breakdown for a fiber entering a microchannel inlet, on the imposed pressure; (*b*) location of the meniscus in the microchannel as function of the pressure

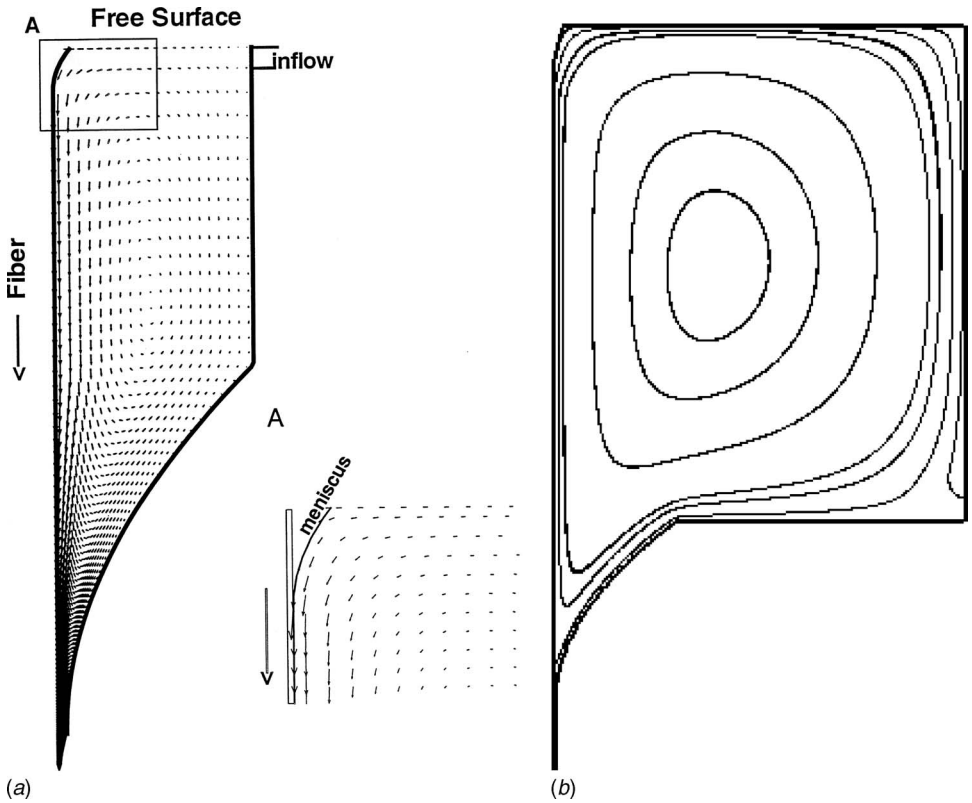

Fig. 16 Calculated flow field in the applicator and exit microchannel, with a prescribed meniscus of height around 100 μm obtained experimentally

numerical results are shown here from Yoo and Jaluria [26] and Ravinutala et al. [27]. Figure 16 shows the computed velocity field in the applicator, with a prescribed upper meniscus. Thus, experimental inputs on the microscale phenomena underlying the meniscus are used to allow simulation of the macroscale flows. Even though the flow near the meniscus changed substantially with a change in the meniscus, the flow far away remained largely unaffected. A nanosecond double pulse laser source was used to map and probe the flow field in the applicator, particularly in the vicinity of the moving 125 μm fiber, using particle image velocimetry. Figure 17 shows a typical comparison between the two in terms of the velocity profiles. Several other such measurements and computations were carried out. The agreement between the two provided strong support to the modeling effort.

As mentioned earlier, the exit die consists of a microchannel of varying cross section. In most cases, it is a converging channel to the desired final diameter of the coating, though different geometries are used for stability and better control over coating characteristics. Figure 18 shows typical results obtained in terms of the pressure distribution in the applicator and the exit die for isothermal conditions. It is seen that a maximum arises somewhere near the midsection of the die. This pressure was found to be quite large due to the small diameter of the microchannel and to be much larger than the typical pressure imposed at the fluid inlet to the applicator. Thus, the exit conditions are largely dominated by the die shape and fiber speed, rather than the pressure in the applicator chamber. A properly designed die can help in controlling the thickness and quality of the coating. Thermal effects can also have a strong effect on the flow due to the dependence of fluid properties on temperature. The corresponding pressure distribution when thermal effects due to heat transfer from the fiber, viscous dissipation, and heat loss to the surroundings are included is shown in Fig. 18(*b*). The pressures were found to decrease as the temperatures increase due to the reduction in fluid viscosity. The flow was also found to be more stable, leading to greater uniformity of the coating, as the temperatures were increased. Thus, the thermal conditions at the boundaries can be used to affect the coating characteristics.

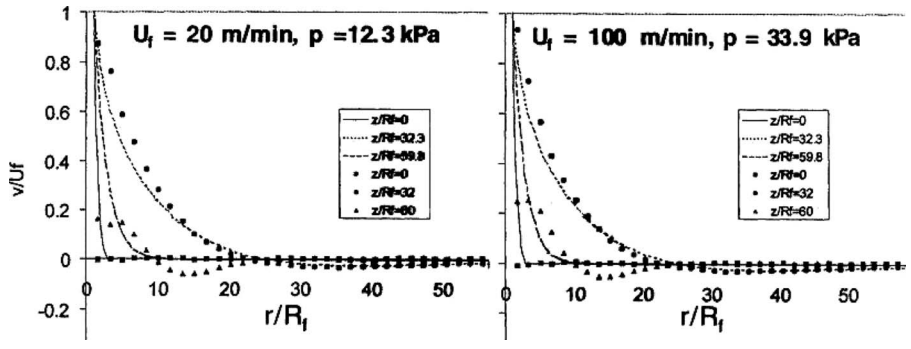

Fig. 17 Calculated and measured velocity distributions near the moving optical fiber

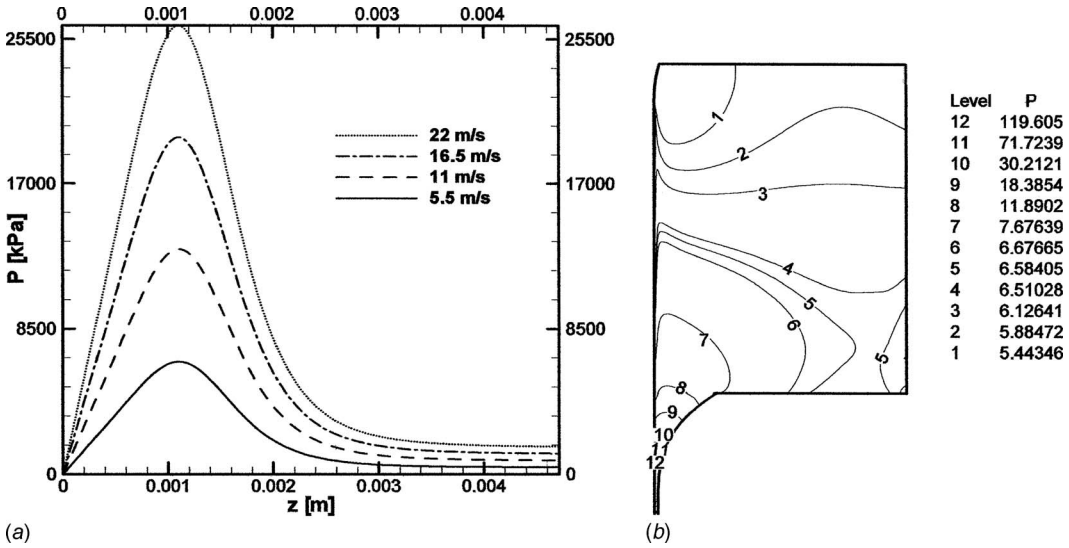

Fig. 18 Pressure distribution in the chamber and the exit die, which consists of a converging microchannel, for polymer coating of a moving fiber (*a*) under isothermal conditions and (*b*) when thermal effects are included for a fiber speed of 11 m/s

2.4 Chemical Vapor Deposition. Chemical vapor deposition involves the deposition of thin films from a gas phase on to a solid substrate by means of a chemical reaction that takes place during the deposition process. The activation energy needed for the chemical reactions is provided by an external heat source; see Fig. 19(*a*). The products of the reactions form a solid crystalline or an amorphous layer on the substrate. After material deposition on the surface, the byproducts of the reactions are removed by carrier gases, as reviewed by Mahajan [28]. Film thicknesses range from a few nanometers to tens of microns. The quality of the film deposited is characterized in terms of its purity, composition, thickness, adhesion, surface morphology, and crystalline structure. The level of quality needed depends on the intended application, with electronic and optical materials imposing the most stringent demands. This technique has become quite important in materials processing and is used in a wide range of applications, such as those in the fabrication of microelectronic circuits, optical and magnetic devices, high performance cutting and grinding tools, and solar cells. Much of the initial effort on this problem was directed at silicon deposition because of its importance in the semiconductor industry. However, recent efforts have been directed at the deposition of materials such as titanium nitride, silicon carbide, diamond, and metals such as titanium, tungsten, aluminum, and copper.

Many different types of CVD reactors have been developed and applied for different applications. The quality, uniformity, and rate of deposition are dependent on the heat and mass transfer, and on the chemical reactions that are themselves strongly influenced by temperature and concentration levels. The flow, heat transfer, and chemical reactions in CVD reactors have been investigated by several researchers [29–31]. Some typical results obtained for silicon deposition are shown in Fig. 19(*b*), indicating a comparison between numerical and experimental results from Ref. [29]. A fairly good agreement is observed, given the uncertainty with material property data and with the chemical kinetics. The two results from Ref. [32] are labeled as present and refer to two different values of the diffusion coefficient; the one labeled as the reference case employs the same values as those in Ref. [30].

2.5 Summary. Several important and interesting aspects, as well as challenges, have been brought out in the preceding discussion. Because of the need to determine temperature and flow dif-

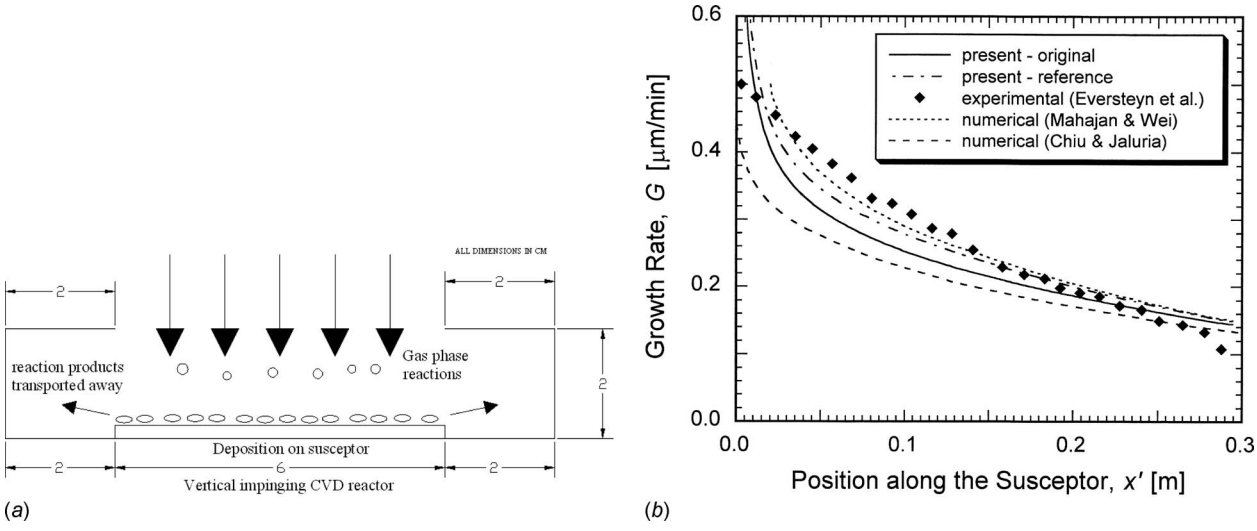

Fig. 19 (*a*) A sketch of an impingement type CVD reactor; (*b*) comparison between numerical predictions and experiments for chemical vapor deposition of silicon in a horizontal reactor

ferentials over very short distances, it is often not possible to treat the microscale region as uniform or lumped, making it necessary to place a substantial number of grid points over microscale dimension for an accurate and realistic numerical simulation. Viscous dissipation effects are large locally due to the small length scales. Similarly, large pressure differences arise in flows through microchannels. Large changes in length scale are often encountered in materials processing, going from several centimeters to micrometers in a short physical distance, as seen in optical fiber drawing. The traditional analysis, with no-slip conditions, is valid in many cases, particularly with liquids over lengths scales ranging down to a few microns. The experiments are usually much more involved than in commercial scales due to the device size and positioning of the probe. Validation of the models similarly becomes complicated because of the complexity of the experiments and because many experimental data are available at the macroscale or system level. A coupling between the different scales, therefore, becomes critical.

3 Underlying Processes That Occur at Micro/Nanoscale

3.1 Nano-, Micro-, and Macroscale Coupling. The characteristics and quality of the material being processed are generally determined by the transport processes that occur at the micro- or nanometer scale in the material, for instance, at the solid-liquid interface in casting or crystal growing, over molecules involved in a chemical reaction in chemical vapor deposition and reactive extrusion, or at sites where defects are formed in an optical fiber. However, engineering aspects are generally concerned with the commercial or macroscale, involving practical dimensions, systems, and appropriate boundaries. Therefore, it is crucial to link the two approaches so that the appropriate boundary conditions for a desired micro- or nanostructure can be imposed in a physically realistic system. A considerable interest exists today in this aspect of materials processing. For instance, interest lies in understanding microscopic phenomena associated with solidification, and intense research work has been directed at this problem. The solidification front can be divided into various morphological forms such as planar, cellular, and dendritic. Various models have been proposed and experiments carried out to characterize such structures and growth [33]. This includes, for instance, equiaxed and columnar dendritic crystals. Averaging volumes and dendrite envelopes that may be used for modeling of the microscopic phenomena are developed.

The properties of the material undergoing thermal processing must be known and appropriately modeled to accurately predict the resulting flow and transport, as well as the characteristics of the final product. However, there is an acute lack of data and the accuracy of the numerical simulation is often constrained due to the unavailability of material properties. Numerical modeling yields the prediction of the thermal history of the material as it undergoes a given thermal process. Similarly, the pressure, stress, mass transfer, and chemical reactions can be determined. The next step is to determine the changes in the structure or composition of the material as it goes through the system. But this requires detailed information on material behavior and how structural or chemical changes occur in the material as a consequence of the temperature, pressure, and other conditions to which it is subjected. A few examples that involve these considerations are outlined here.

3.2 Chemical Conversion in Biopolymers. In reactive thermal processing, such as food and reactive polymer extrusion, the microscopic changes in the material are linked with the operating conditions that are imposed on the system. A simple approach to model the chemical conversion process in reactive materials, such as food, is based on the governing equation for chemical conversion, given as [34]

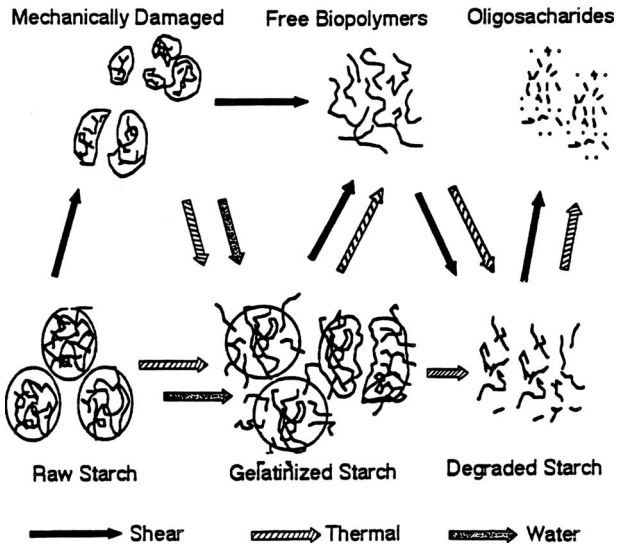

Fig. 20 A schematic indicating the mechanisms underlying starch conversion

$$\frac{d}{dt}[(1-X)] = -K(1-X)^m \tag{10}$$

where X is the degree of conversion, defined as

$$X = \frac{M_i - M_t}{M_i - M_f} \tag{11}$$

Here M_i is the initial amount of unconverted material, taken as starch here, M_f is the final amount of unconverted starch, and M_t is the amount of unconverted starch at time t. The order of the reaction is m and K is the reaction rate, these generally being determined experimentally using a digital scanning calorimeter. The order of the reaction m in Eq. (10) has been shown to be zero for starches and the rate of the reaction K given as a combination of thermal (T) and shear (S) driven conversion as

$$K = K_T + K_S \tag{12}$$

$$\text{where} \quad K_T = K_{To}\exp(-E_T/RT), \quad K_S = K_{So}\exp(-E_S/\tau\eta) \tag{13}$$

Here, τ is the shear stress, and η is a constant, which is obtained experimentally for the material, along with other constants in the equation. Figure 20 shows these mechanisms qualitatively in the form of a schematic. A simple approximation may be applied to model the degree of conversion defined in Eq. (11), as given by [35]

$$w\frac{dX}{dz} = K \tag{14}$$

Here, w is the velocity in the down-channel direction z in an extruder. Thus, numerical results on conversion in the channel are obtained by integrating this equation.

Using the microscale conversion mechanisms given above, the flow, heat transfer, and conversion in a screw extruder can be obtained. The viscosity is a function of the conversion and this complicates the physical process, as well as the simulation. Figure 21 shows some typical results obtained from such a simulation [36]. Figure 21(a) shows the temperature field and the conversion in a tapered single-screw extruder. As expected, conversion increases as the flow goes from the inlet to the outlet at the die. Figure 21(b) shows the feasible domain for a twin-screw extruder with Amioca, or pure starch, as the extruded material. The feasibility of the process is determined largely by the flow and the pressure and temperature rise in the extruder. An upper limit is

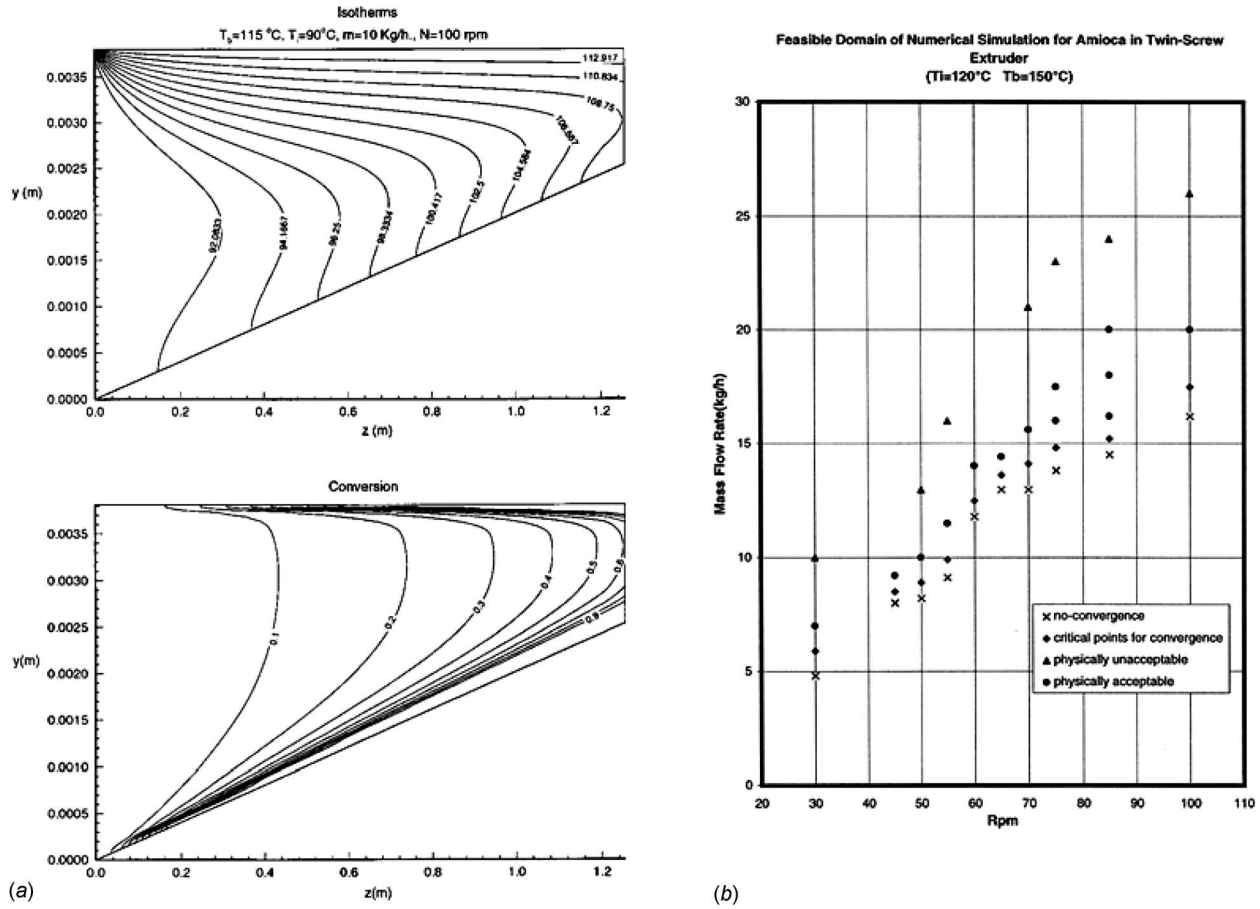

Fig. 21 (*a*) Conversion of starch in a tapered screw extruder channel; (*b*) feasible domain for twin-screw extrusion of starch

obtained for the mass flow rate, beyond which it is necessary to impose a favorable pressure gradient to push the material down the channel. Therefore, a negative pressure gradient along the axial direction will occur in the channel and that is not physically acceptable for an extruder. A lower limit on mass flow rate is also obtained because of recirculation of the flow, which makes the process unstable and leads to high pressures and material degradation. Thus, a fairly narrow range of mass flow rates yields a feasible extrusion process.

3.3 Thermally Induced Defects. Another area in which the changes at the molecular level are considered is that of generation of thermally induced defects in optical fiber drawing. The differential equation for the time dependence of the E' defect concentration was formulated by Hanafusa et al. [37] based on the theory of the thermodynamics of lattice vacancies in crystals. The E' defect is a point defect, which is generated at high temperature during the drawing process and which causes transmission loss and mechanical strength degradation in the fiber. It was assumed that the E' defects are generated through breaking of the Si–O band, and, at the same time, part of the defects recombine to form Si–O again. The net concentration of the E' defects is the difference between the generation and the recombination. The equation for E' defect concentration is given as [37]

$$v\frac{dn_d}{dz} = n_p(0)v\,\exp\left(-\frac{E_p}{KT}\right) - n_d v\left[\exp\left(-\frac{E_p}{KT}\right) + \exp\left(-\frac{E_d}{KT}\right)\right] \tag{15}$$

where n_d and E_d represent the concentration and activation energy of the E' defect, and n_p and E_p represent those of the precursors. The initial values and constants are defined as [37] $n_d(0)=0$, $n_p(0)=7\times10^{22}$ g^{-1}, $E_p=6.4087\times10^{-19}$ J, $E_d=0.3204\times10^{-19}$ J, $v=8\times10^{-3}$ s^{-1}, and $K=1.380658\times10^{-23}$ J/K.

Figure 22(*a*) shows the dependence of the average concentration of E' defects on the drawing temperature, indicating an increase with temperature as expected from the higher breakage of the Si–O bond. Figure 22(*b*) shows the final concentration of the defects as obtained from the luminescence of the fibers. If the fiber is rapidly cooled slowly after the draw furnace, the defects are reduced due to the annealing of the fiber resulting in recombination of the broken bonds. If they are cooled very fast by forced convection, the defects are frozen and yield a higher concentration. Again, these effects arise due to the microscopic mechanisms operating at the level of the defects. Figure 23 shows the neck-down profile and the defects for a doped fiber. As expected, the concentration of E' defects is found to be larger in the double-layer preform due to higher temperatures, as seen earlier. It is indicated that the fiber quality is degraded with an increase in refractive index difference between the core and the cladding in terms of E' defects.

3.4 CVD Thin Film Deposition. Similarly, chemical kinetics plays a critical role in the deposition of material from the gas phase in chemical vapor deposition systems [28]. The concentrations of the chemical species in the reactor affect the chemical kinetics, which in turn affect the deposition. In many cases, the process is chemical kinetics limited, implying that the transport processes are quite vigorous and the deposition is restricted largely by the kinetics. The chemical kinetics for several materials is available in literature. For instance, the chemical kinetics for the

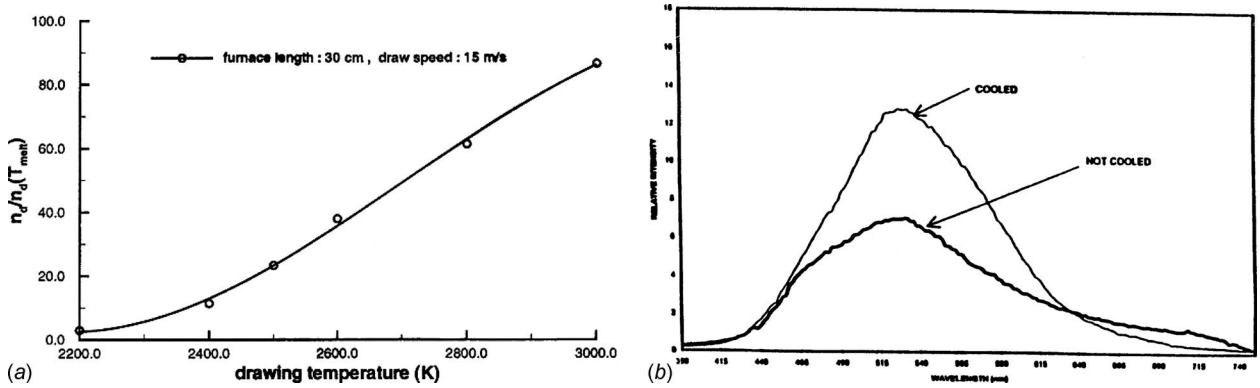

Fig. 22 (*a*) Dependence of average concentration of E' defects on furnace wall temperature; (*b*) luminescence versus wavelength of fibers drawn at 2050°C and 80 m/min, indicating concentration of E' defects

deposition of silicon from silane (SiH_4) with hydrogen as the carrier gas in a CVD reactor is given by the expression [29]

$$K = \frac{K_0 p_{SiH_4}}{1 + K_1 p_{H_2} + K_2 p_{SiH_4}} \tag{16}$$

where the surface reaction rate K is in mole of $Si/m^2\,s$, $K_0 = A\exp(-E/RT)$, E being the activation energy, and A, K_1, and K_2 are constants that are obtained experimentally. The ps are the partial pressures of the two species in the reactor.

Figure 24 shows the deposition characteristics for silicon at various susceptor temperatures and inlet velocities. At high temperatures, the surface reactions are fast and all the reactants reaching the surface get consumed by the surface reactions. The diffusion or transport of the reactant species to the substrate then becomes the limiting step. At low flow velocities, the gas stream has sufficient residence time to equilibrate with the substrate surface. The deposition rate then increases with flow rate. At high flow velocities, the surface concentrations cannot quickly adapt to the flow of products in the deposition zone and diffusion becomes the controlling factor. At sufficiently high flow velocities, the decomposition becomes kinetically controlled and is independent of the total flow rate. The variation of deposition uniformity with the susceptor temperature for various inlet velocities is also shown. The lower the value of the logarithm of the uniformity parameter U_p, the better the uniformity of the film thickness. Thus, the process can be optimized to obtain high uniformity and high deposition rates.

3.5 Summary. It is seen that transport processes occurring at micro- or nanometer scale determine the resulting characteristics of the material undergoing thermal processing. However, the operating conditions are generally imposed at macroscale, or at the system level. Therefore, it is important to study the processes at the microscale level and link these with the conditions at the macroscale. From the few examples discussed, it is seen that experimental results at microscale, or smaller dimensions, can often be employed, along with numerical modeling at larger scales. Analysis can also be used at the molecular level, as done for thermally induced defects, to obtain the inputs for the overall model.

4 Conclusions and Future Research Needs

This paper presents a review on microscale transport involved with thermal processing of materials. It focuses on two major aspects. The first concerns devices and applications that occur in the microscale range. The second deals with underlying microscale mechanisms that affect the characteristics of the material undergoing processing. Important challenges that arise when dealing with microscale devices are discussed. These include modeling and numerical simulation, which are similar to those at macroscale if the dimensions are typically much larger than the mean free path of the energy carriers in the fluid, the extensive care needed to obtain accurate experimental results at these small scales, the special instrumentation frequently needed to study basic processes, and validation of the models since imposed boundary conditions are largely at macroscale. Important considerations

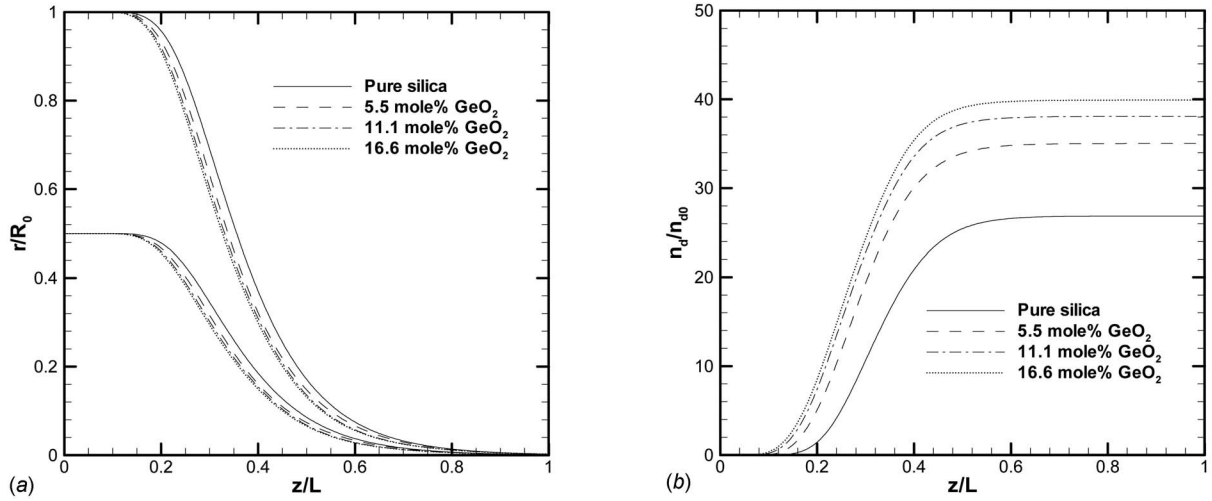

Fig. 23 (*a*) Neck-down profiles for various GeO_2 concentrations; (*b*) concentration of E' defects along the centerline for various GeO_2 concentrations

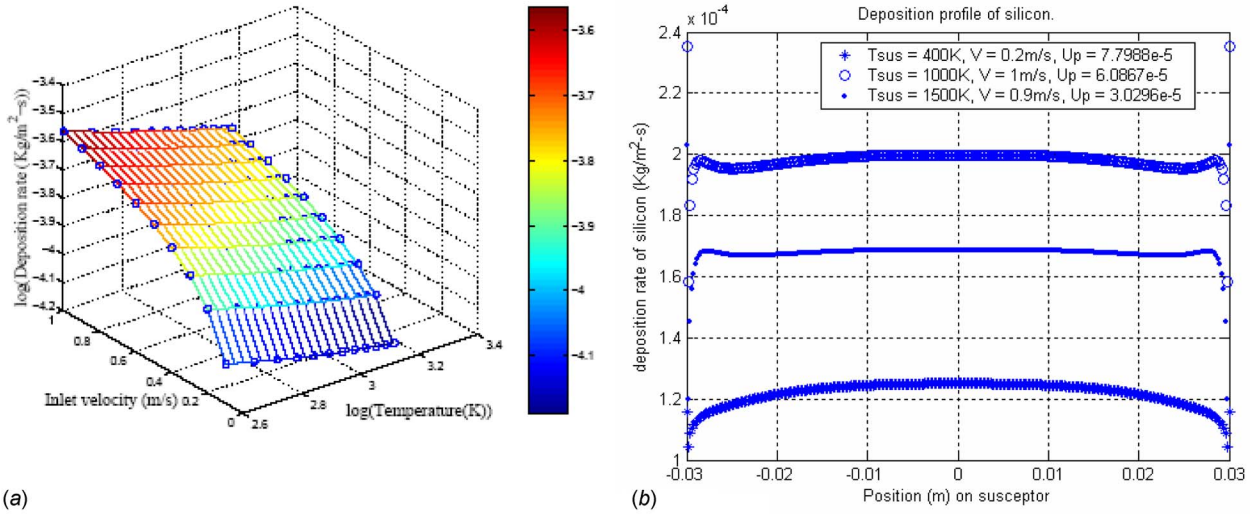

(*a*) (*b*)

Fig. 24 (*a*) Response surface on deposition rate for an impingement CVD reactor for depositing silicon; (*b*) variation of deposition rate with location for different inlet velocities and susceptor temperatures

that are of particular significance at these dimensions, such as surface tension effects, high viscous dissipation, and high pressures needed for flow in microchannels, are discussed, in terms of several examples of thermal materials processing. Since processes at micro- and nanoscale strongly affect product quality, the review next discusses experiments often needed to characterize material changes, thermally induced defects generated, local stresses, and other imperfections. The effects on material and product characteristics are outlined, along with the link between micro- or nanoscale processes and operating conditions imposed at macroscale. Again, several examples from processes such as optical fiber drawing, thin film deposition, and reactive extrusion are taken to present the basic approach and typical results. The further work needed on process simulation, feasibility, control, design and optimization, material characterization, and experimentation for validation and insight at microscale is briefly discussed in terms of the thermal processing of advanced materials and devices.

Acknowledgment

The author acknowledges the support of the National Science Foundation, through several grants, of the Fiber Optic Materials Research Program at Rutgers University, and of Corning, Inc., for donated equipment. The author also acknowledges the interactions with Professor C. Polymeropoulos, Professor George Sigel, Professor M.V. Karwe, and Professor H.C. Gea, and the work done by several students, as referenced here, that made it possible to carry out this work and thus present this review.

Nomenclature

a = absorption coefficient
C = collapse ratio in hollow fiber drawing
c_p = specific heat at constant pressure
H = height
J = radiosity
K = thermal conductivity
L = preform length
n = refractive index, power-law index
p = pressure
q = heat flux
r = radial coordinate distance
R = radius
S_r = radiation source term
t = time
T = temperature
u = radial velocity
v = axial velocity
z = axial coordinate distance

Greek Symbols

ε = emissivity
λ = wavelength
μ = dynamic viscosity
υ = kinematic viscosity
Φ = viscous dissipation term
ρ = density, reflectivity
τ = shear stress, transmissivity
$\dot{\gamma}$ = shear rate
σ = Stefan–Boltzmann constant
ζ = surface tension

Subscripts

f = fiber
F = furnace
0 = preform inlet
C = centerline

Superscripts

(1) = core, inner surface
(2) = cladding, outer surface
(3) = gas

References

[1] Jaluria, Y., 2003, "Thermal Processing of Materials: From Basic Research to Engineering," ASME J. Heat Transfer, **125**, pp. 957–979.
[2] Jaluria, Y., 2006, "Numerical Modeling of Manufacturing Processes," *Handbook of Numerical Heat Transfer*, W. J. Minkowycz, E. M. Sparrow, and J. Murthy, eds., Wiley, New York, pp. 729–784.
[3] Szekely, J., 1979, *Fluid Flow Phenomena in Metals Processing*, Academic, New York.
[4] Viskanta, R., 1988, "Heat Transfer During Melting and Solidification of Metals," ASME J. Heat Transfer, **110**, pp. 1205–1219.
[5] Li, T., ed., 1985, *Optical Fiber Communications*, Vol. 1, Academic, New York.
[6] Poulikakos, D., ed., 1996, "Transport Phenomena in Materials Processing," Adv. Heat Transfer, **28**, pp. 1–425.
[7] Paek, U. C., 1999, "Free Drawing and Polymer Coating of Silica Glass Optical Fibers," ASME J. Heat Transfer, **121**, pp. 774–788.
[8] Fitt, A. D., Furusawa, K., Monro, T. M., and Please, C. P., 2001, "Modeling the Fabrication of Hollow Fibers: Capillary Drawing," J. Lightwave Technol., **19**, pp. 1924–1931.
[9] van Eijkelenborg, M. A., Argyros, A., Barton, G., Bassett, I. M., Fellew, M., Henry, G., Issa, N. A., Large, M. C. J., Manos, S., Padden, W., Poladian, L., and Zagari, J., 2003, "Recent Progress in Microstructured Polymer Optical Fibre Fabrication and Characterisation," Opt. Fiber Technol., **9**, pp. 199–209.

[10] Paek, U. C., and Runk, R. B., 1978, "Physical Behavior of the Neck-Down Region During Furnace Drawing of Silica Fibers," J. Appl. Phys., **49**, pp. 4417–4422.
[11] Myers, M. R., 1989, "A Model for Unsteady Analysis of Preform Drawing," AIChE J., **35**, pp. 592–602.
[12] Lee, S. H.-K., and Jaluria, Y., 1997, "Simulation of the Transport Process in the Neck-Down Region of a Furnace Drawn Optical Fiber," Int. J. Heat Mass Transfer, **40**(4), pp. 843–856.
[13] Choudhury, R. S., and Jaluria, Y., 1998, "Thermal Transport Due to Material and Gas Flow in a Furnace for Drawing an Optical Fiber," J. Mater. Res., **13**(2), pp. 494–503.
[14] Choudhury, R. S., Jaluria, Y., and Lee, S. H.-K., 1999, ""A Computational Method for Generating the Free-Surface Neck-Down Profile for Glass Flow in Optical Fiber Drawing," Numer. Heat Transfer, Part A, **35**, pp. 1–24.
[15] Yin, Z., and Jaluria, Y., 1998, "Thermal Transport and Flow in High-Speed Optical Fiber Drawing," ASME J. Heat Transfer, **120**, pp. 916–930.
[16] Wei, Z., Lee, K., Tchikanda, S. W., Zhou, Z., and Hong, S., 2004, "Free Surface Flow in High Speed Fiber Drawing With Large-Diameter Glass Preforms," ASME J. Heat Transfer, **126**, pp. 713–722.
[17] Cheng, X., and Jaluria, Y., 2004, "Feasibility of High Speed Furnace Drawing of Optical Fibers," ASME J. Heat Transfer, **126**, pp. 852–857.
[18] Paek, U. C., 1986, "High-Speed High-Strength Fiber Drawing," J. Lightwave Technol., **4**(8), pp. 1048–1060.
[19] Chen, C., and Jaluria, Y., 2007, "Numerical Simulation of Transport in Optical Fiber Drawing With Core-Cladding Structure," ASME J. Heat Transfer, **129**, pp. 559–567.
[20] Izawa, T., and Sudo, S., 1987, *Optical Fibers: Materials and Fabrication*, KTK Scientific, Tokyo.
[21] Chen, C., 2007, "Transport Processes in Drawing of Optical Fibers With Core-Cladding Structure," Ph.D. thesis, Rutgers University, New Brunswick, NJ.
[22] Chakravarthy, S. S., and Chiu, W. K. S., 2005, "Collapse Prediction During Hollow Optical Fiber Fabrication," 2005 ASME Summer Heat Transfer Conference, San Francisco, CA.
[23] Yang, Y., and Jaluria, Y., 2008, "Transport Processes Governing the Drawing of a Hollow Optical Fiber," ASME Summer Heat Transfer Conference, Jacksonville, FL.
[24] Quere, D., 1999, "Fluid Coating on a Fiber," Annu. Rev. Fluid Mech., **31**, pp. 347–384.
[25] Ravinulata, S., and Polymeropoulos, C. E., 2002, "Entrance Meniscus in a Pressurized Optical Fiber Coating Applicator," Exp. Therm. Fluid Sci., **26**, pp. 573–580.
[26] Yoo, S. Y., and Jaluria, Y., 2007, "Fluid Flow and Heat Transfer in an Optical Fiber Coating Process," Int. J. Heat Mass Transfer, **50**, pp. 1176–1185.
[27] Ravinutala, S., Polymeropoulos, C. E., Jaluria, Y., Elliott, G., and Finberg, G., 2001, "Experimental and Calculated Velocity Distributions Within a Pressurized Optical Fiber Coating Applicator," *Proceedings of the 50th International Wire Cable Symposium*, Orlando, FL.
[28] Mahajan, R. L., 1996, "Transport Phenomena in Chemical Vapor-Deposition Systems," Adv. Heat Transfer, **28**, pp. 339–425.
[29] Eversteyn, F. C., Severin, P. J. W., Brekel, C. H. J., and Peek, H. L., 1970, "A Stagnant Layer Model for the Epitaxial Growth of Silicon From Silane in a Horizontal Reactor," J. Electrochem. Soc., **117**, pp. 925–931.
[30] Mahajan, R. L., and Wei, C., 1991, "Buoyancy, Soret, Dufour and Variable Property Effects in Silicon Epitaxy," ASME J. Heat Transfer, **113**, pp. 688–695.
[31] Chiu, W. K. S., and Jaluria, Y., 2000, "Continuous Chemical Vapor Deposition Processing With a Moving Finite Thickness Susceptor," J. Mater. Res., **15**, pp. 317–328.
[32] Yoo, H., and Jaluria, Y., 2002, "Thermal Aspects in the Continuous Chemical Vapor Deposition of Silicon," ASME J. Heat Transfer, **124**, pp. 938–946.
[33] Beckermann, C., and Wang, C. Y., 1995, "Multiphase/-Scale Modeling of Alloy Solidification," Annu. Rev. Heat Transfer, **6**, pp. 115–198.
[34] Wang, S. S., Chiang, C. C., Yeh, A. I., Zhao, B., and Kim, I. H., 1989, "Kinetics of Phase Transition of Waxy Corn Starch at Extrusion Temperatures and Moisture Contents," J. Food. Sci., **54**, pp. 1298–1301.
[35] Chiruvella, R. V., Jaluria, Y., and Karwe, M. V., 1996, "Numerical Simulation of Extrusion Cooking of Starchy Materials," J. Food. Eng., **30**, pp. 449–467.
[36] Zhu, W., and Jaluria, Y., 2001, "Residence Time and Conversion in the Extrusion of Chemically Reactive Materials," Polym. Eng. Sci., **41**, pp. 1280–1291.
[37] Hanafusa, H., Hibino, Y., and Yamamoto, F., 1985, "Formation Mechanism of Drawing-Induced E' Centers in Silica Optical Fibers," J. Appl. Phys., **58**(3), pp. 1356–1361.

Relativistic Molecular Dynamics Simulations of Laser Ablation Process on the Xenon Solid

Yun-Che Wang

Jing-Wen Chen

Department of Civil Engineering,
Materials Program,
National Cheng Kung University,
1 University Road,
Tainan, Taiwan, R.O.C.

Lun-De Liao

Hong-Chang Lin

Chi-Chuan Hwang[1]
e-mail: chchwang@mail.ncku.edu.tw

Department of Engineering Science,
National Cheng Kung University,
1 University Road,
Tainan, Taiwan, R.O.C.

The phenomena of Coulomb explosion require the consideration of special relativity due to the involvement of high energy electrons or ions. It is known that laser ablation processes at high laser intensities may lead to the Coulomb explosion, and their released energy is in the regime of kEV to MeV. In contrast to conventional molecular dynamics (MD) simulations, we adopt the three-dimensional relativistic molecular dynamics (RMD) method to consider the effects of special relativity in the conventional MD simulation for charged particles in strong electromagnetic fields. Furthermore, we develop a Coulomb force scheme, combined with the Lennard-Jones potential, to calculate interactions between charged particles, and adopt a Verlet list scheme to compute the interactions between each particle. The energy transfer from the laser pulses to the solid surface is not directly simulated. Instead, we directly assign ion charges to the surface atoms that are illuminated by the laser. By introducing the Coulomb potential into the Lennard-Jones potential, we are able to mimic the laser energy being dumped into the xenon (Xe) solid, and track the motion of each Xe atom. In other words, the laser intensity is simulated by using the repulsive forces from the Coulomb potential. Both nonrelativistic and relativistic simulations are performed, and the RMD method provides more realistic results, in particular, when high-intensity laser is used. In addition, it is found that the damage depth does not increase with repeated laser ablation when the pulse frequency is comparable to the duration of the pulse. Furthermore, we report the time evolution of energy propagation in space in the laser ablation process. The temporal-spatial distribution of energy indirectly indicates the temperature evolution on the surface of the Xe solid under intense laser illumination. [DOI: 10.1115/1.3056607]

Keywords: relativistic molecular dynamics, Coulomb explosion, laser ablation, xenon solid

1 Introduction

Laser ablation with the use of ultrashort pulsed laser has been widely used in material processing in recent years. It involves the removal of material from a solid (or occasionally liquid) surface by irradiating it with a laser beam. At low laser flux, the material is heated by the absorbed laser energy and evaporates or sublimates. At high laser flux, the material is typically converted to plasma. Usually, laser ablation refers to removing material with a pulsed laser, but it is possible to ablate a material with a continuous wave laser beam if the laser intensity is high enough. The depth over which the laser energy is absorbed, and thus the amount of material removed by a single laser pulse, depends on the material's optical properties and the laser wavelength. Laser pulses can vary over a very wide range of duration (milliseconds to femtoseconds) and fluxes and can be precisely controlled. This makes laser ablation very valuable for both research and industrial applications. The computations showed that the ion energy spectrum is composed of an isotropic low energy component and an anisotropic high energy component much like the experimental observations [1]. The experimentally measured electron energy spectrum has also been reasonably well predicted for the case of Xe solid [2].

The most important phenomenon during the laser ablation is the Coulomb explosion. When a solid is under the bombardment of fast ions, tracks of excitations are formed [3]; the tracks are known as thermal spikes. The incident ions promote atoms to be in excited states and create electron hole pairs. They gradually thermalize, screen the holes, and finally recombine with the holes in a time scale depending on the material. If hole mobility is low and recombination is slow, the holes can repel each other leading to a "Coulomb explosion" (CE). In this case, charges acquire large velocities and transfer energy to their neighbors. CE has been suggested to produce track amorphization, material damage [4,5], surface modification [6], and particle ejection (sputtering) [7–9]. Laser ablation is a means of creating the Coulomb explosions. The computation techniques used in the present study have earlier been used to predict the experimentally measured ion and energy spectra [10].

Laser ablation involves two phenomena. One is the photoelectric effect and the other is heating of the material leading to thermionic emission [11]. It is known that femtosecond laser heating takes place in times comparable to the mean-free-time (MFT) of energy carriers; 10 fs for electrons to electrons, 1 ps for electrons to phonons, and 10 ps for phonons to phonons. On the contrary, for long-pulse lasers, vaporization of local material induced strong recoil pressure governs the ablation processes, and hence its mechanisms are thermal stresses due to volumetric expansions, solid-to-liquid phase change, and ejection of the molten phase. In the literature, the two-step heat transfer model is well received by the researchers and describes the laser-material interaction due to (1) phonon energy absorption in electrons and (2) lattice heating through interaction with electrons. In modeling, many variant methods are adopted for laser beam absorption, such as exciting the potential energy of atoms [12] and the breathing sphere model for vibrational excitation of molecules, as well as heat conduction

[1]Corresponding author.

Contributed by the Heat Transfer Division of ASME for publication in the JOURNAL OF HEAT TRANSFER. Manuscript received March 11, 2008; final manuscript received October 16, 2008; published online January 27, 2009. Review conducted by Robert D. Tzou. Paper presented at the 2008 International Conference on Micro/Nanoscale Heat Transfer (MNHT 2008), Tainan, Taiwan, January 6–9, 2008.

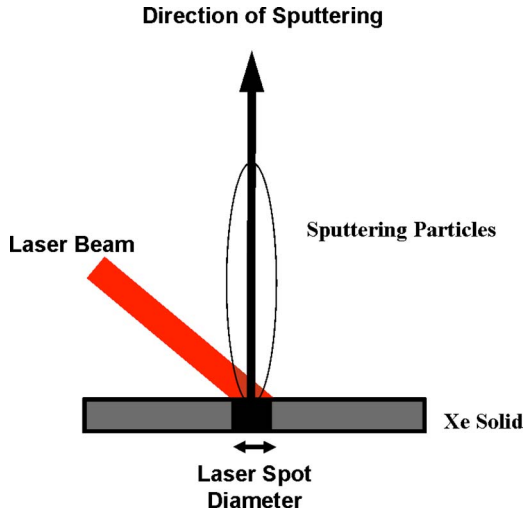

Fig. 1 Schematic of the physical problem of laser ablation. The radius of the laser spot is 8 Å. The atoms that are assumed to be ionized are in the hemispherical region under the laser spot.

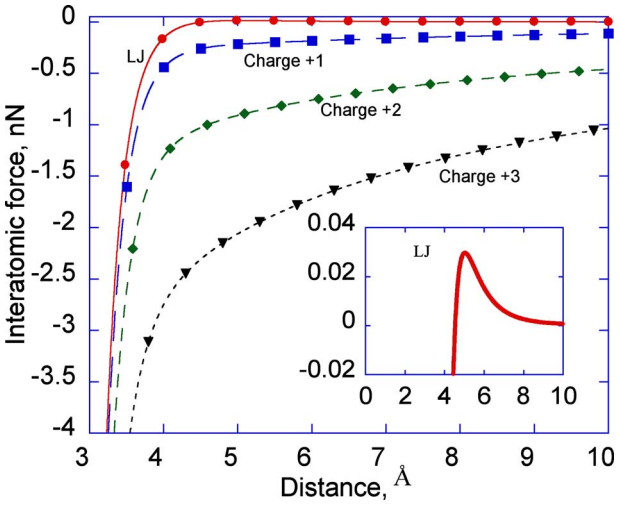

Fig. 2 Relationship between the interatomic force and atom distance for the combination of the Lennard-Jones and Coulomb potentials for the xenon solid. The inset shows the Lennard-Jones potential for neutral xenon atoms with σ =4.3 Å and ε=0.0197 eV.

by electron gas by the finite difference method based on the thermal conductivity of metal [13]. Furthermore, it is known that the atomic absorption of energy increase in its atomic lattice position and vibration and the range increases with increasing temperature, and makes the energy of mutual impact of atomic energy transfer increase [14–17]. Hence, it can be observed that the amplitude of stress wave will increase with the positive charges. In order to identify the Coulomb explosion experimentally, the ions will have to be detected time-resolved in situ, which is difficult. On the other hand, simulations provide a convenient means of probing the phenomenon. In the case of the Coulomb explosion, the smallest distance between 2 atoms is 4.3 Å, and the average distance between atoms at maximum compression is 4.56 Å and reached 250 fs after the onset of the laser. As for cluster problems, simulation results have been shown to be in agreement with the experimental findings obtained from field ionization of the atoms and the solid by the strong electric field of the infrared laser [18,19].

In the present work, we carried out MD simulations, both nonrelativistic and relativistic ones, with the combination of the Lennard-Jones and Coulomb potentials to simulate the laser ablation process. Focus is placed on the effects of relativistic effects. As for the energy transfer from the laser to the material surface, we adopt the method of direct assignment of charges to the atoms in the hemispherical region of the laser spot. The radius of the laser spot is 8 Å. The rationale is that ionization occurs under ultrashort laser illumination, and hence the atoms are assumed to be fully ionized. In this paper, we compare three cases, different in their charge levels. Atoms in the hemispherical region under the surface laser spot are also assumed to be ionized. For the three charge states, the laser fluences are 0.13 J/m^2, 0.2 J/m^2, and 0.4 J/m^2. The ionization for the singly, doubly, and triply charged states are 1170.4 kJ/mol, 2046.4 kJ/mol, and 3099.4 kJ/mol [20].

2 Relativistic Molecular Dynamics Modeling

In the present study, the xenon solid is chosen due to the simplicity of its atomic interactions. The Xe potential used in the MD code is of the Lennard-Jones type [21]. Hence, the total potential was modified by the electrostatic Coulomb potential and the Lennard-Jones potential. Figure 1 shows the schematic of the physical problem of laser ablation. In this paper, the energy transfer process from the laser to the Xe solid is simulated by directly assigning ionization charges to the atoms being irradiated by the laser. Emphasis is placed on the difference between conventional and relativistic MD simulations. The plume of sputtered particles are depicted.

For the charge particle interactions, we describe the repulsion between such ionized atoms using a Coulomb potential in addition to the Lennard-Jones potential. The interactions are modeled using the Coulomb potential smoothly splined to the electrostatic term. Although it can be argued that more highly charged ions would experience even greater core-core repulsion than singly charged Coulomb repulsion, for simplicity, this is not considered here. Our focus is to study relativistic effects in the molecular dynamics simulation. The Coulomb force is specially developed in the present work to simulate the phenomena of the Coulomb explosion. It is noted that the Coulomb force is the most computationally intensive part of the MD model [22–25]. Hence, we adopt a Verlet list scheme to compute the interactions among particles.

The Xe^{+n}–Xe^{+n} interactions were assumed to be purely electrostatic and repulsive. The total potential for the Xe^{+n}–Xe interactions can be calculated with Eqs. (1)–(3) as follows:

$$V_{\mathrm{LJ}}(r_{ij}) = 4\varepsilon\left[\left(\frac{\sigma}{r_{ij}}\right)^{12} - \left(\frac{\sigma}{r_{ij}}\right)^{6}\right] \tag{1}$$

$$V_C(r_{ij}) = \frac{q_i q_j}{4\pi\varepsilon_0 r_{ij}} \tag{2}$$

$$V_{\mathrm{total}}(r) = V_{\mathrm{LJ}}(r_{ij}) + V_C(r_{ij}) = \sum_{i<j}\left\{4\varepsilon\left[\left(\frac{\sigma}{r_{ij}}\right)^{12} - \left(\frac{\sigma}{r_{ij}}\right)^{6}\right] + \left[\frac{q_i q_j}{4\pi\varepsilon_0 r_{ij}}\right]\right\} \tag{3}$$

The constants in the Lennard-Jones potential are given as σ =4.3 Å and ε=0.0197 eV. In Fig. 2, the interatomic force and distance relationships for the combination of the Lennard-Jones and Coulomb potentials are shown. The inset shows the Lennard-Jones potential for neutral xenon atoms. It can be seen that highly charged ions diminish the positive forces between atoms. The label "LJ" indicates the interatomic force with neutral atoms, and labels Charge +1, Charge +2, and Charge +3 denote the interatomic forces combining the LJ force and Coulomb force with the specified charges.

With the force acting on ion i being known, the equations of motion for this particle can be solved according to

$$\boldsymbol{F} = \frac{m\boldsymbol{a}}{\left(1-\frac{v^2}{c^2}\right)^{3/2}}, \quad P = \gamma m V = \frac{mV}{\sqrt{1-\frac{V^2}{C^2}}} \tag{4}$$

where V is the velocity of the particle and t is the duration of a time step in the simulation.

In our simulations, the Xe solid lattice (fcc) is used as target and Xe^{+1}, Xe^{+2}, and Xe^{+3} are considered as being ionized by the femtosecond laser in the laser spot. All the particles in the system were evaluated using both the relativistic and nonrelativistic methods. The y direction is perpendicular to the surface, and fixed boundaries were taken along the x and z directions. The system size is on the order of 140,000 atoms, and from the total energy calculation of the Xe system, the laser fluence transmitted to the solid is about a few tenths of J/m^2. The simulations are run for times not exceeding about 10 ps. The velocity Verlet algorithm was used to integrate the equations of motion with a time step of 10^{-3} fs. Three sets of simulations are carried out: Charge +1, Charge +2, and Charge +3 are assigned to the ionized Xe atoms in the laser spot, assumed to be 8 Å in diameter.

The system size representing all particles (atom, ion) in our RMD code was chosen to be of the order of $120\times60\times60$ $Å^3$. In this limit, the microscopic interactions of all charged particles are taken care of by the relativistic molecular dynamics formalism. The RMD code contains no free parameters and presents a virtual experiment.

We remark that ionization [26–30] in a cluster of bombarded particles is a combined process of optical field and collisional ionization. The newly created electrons from these are generally placed inside the solid, treated as inner electrons. Accordingly, the ion charge of all ions is increased. For solids, electrons can be removed from or recaptured by the solids. Outer ionization is the process in which an inner electron leaves the parent solid and becomes an outer electron. The reverse process of electron recapture is also possible. It can occur when an outer electron is attracted to the positively charged particles through Coulomb forces or due to Coulomb explosion. In the present work, these phenomena are not included in our models.

3 Results and Discussion

Results and discussion are presented in this section. First, damages on the surface of the xenon solid are discussed, and then the propagation of laser energy inside the solid is presented.

3.1 Damages on the Surface of the Xe Solid Due to Laser Ablation. In our simulation from the energy due to Coulomb repulsion, the three cases studied here, Charges +1, +2, and +3, are equivalent to laser fluences 0.13 J/m^2, 0.2 J/m^2, and 0.4 J/m^2, respectively. Considering the time step (10^{-3} fs), these fluences are equivalent to the laser intensities 3×10^{18} W/cm^2, 1.2×10^{19} W/cm^2, and 2.56×10^{19} W/cm^2.

The total energy of the Xe system under laser ablation with Charge +1, Charge +2, and Charge +3 is shown in Fig. 3. The short dashed-line (black) labeled with "no laser" indicates the baseline case that no laser energy is applied to the Xe system. The laser energy is applied by assigning charges to the atoms in the laser spot (8 Å in diameter) at 40 fs, after the system has reached sufficient equilibration. The system energy decays in an exponential manner, indicating the diffusional nature of heat transfer in the classical sense. The results show that the high energy bombardment leaves higher residual energy in the system at long times, possibly due to the creation of defects.

In Fig. 4, the side-view morphology of the Xe solid under the Charge +1 bombardment is shown, and a dimple (50 ± 3) Å in diameter and (50 ± 3) Å in depth can be created. Both nonrelativistic and relativistic MD studies are performed, and their differences are small in this case. Similar results for the case of Charge +2 and Charge +3 are shown in Figs. 5 and 6, respectively. For the Charge +2 case, our simulation predicts a dimple (100 ± 3) Å in diameter and (100 ± 3) Å in depth. In Fig. 6, it is predicted that a dimple (150 ± 3) Å in diameter and (150 ± 3) Å in depth for the Charge +3 case will be formed. In all of the three figures, the insets show the morphology at a later time. Again, the initial regime that is irradiated with the laser is 8 Å in diameter. From the system energy calculated in these three cases, we find the correlation that when the mean charge state increases from 1 to 3, the corresponding laser power density increases from 3×10^{18} W/cm^2 to 2.56×10^{19} W/cm^2. This provides a justification to use charge assignments to simulate laser ablation. Further studies to include the energy transfer calculation from the laser to the solid surface are under way.

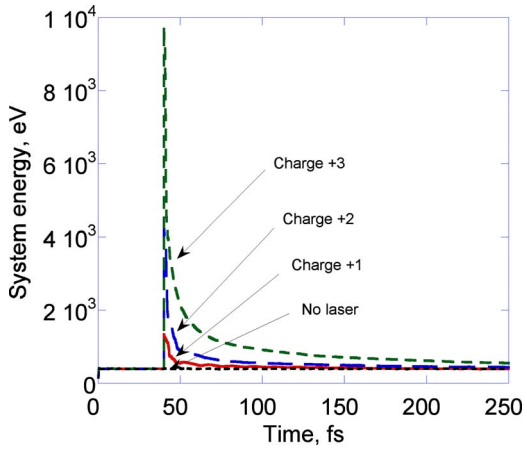

Fig. 3 Total energy versus time for the Xe system under laser ablation with Charge +1, Charge +2, and Charge +3. The short dashed-line (black) labeled with no laser indicates the baseline case that no laser energy is applied into the Xe system.

It should be noted that the ablation rate for the laser pulse case shows that the amount of removed particles per pulse decreases with successive pulses. When a laser pulse is simulated, a very large amount of ions is produced at the center of the target, which leads to Coulomb explosion. As a result of the immense forces related to this approach, fast ions are ejected from the surface within a few hundred femtoseconds. In Figs. 5 and 6, we can see that nonrelativistic models predict too many atoms moving away from the surface. The ions of the lower layers, on the other hand, get accelerated into the bulk and lead to extensive damage and further material removal in the picoseconds time range. Therefore the Coulomb explosion does not necessarily lead to a different ablation result and will be difficult to identify by analysis of the bulk after the ablation process.

In Fig. 7, the relationship between the depth of the dimples and charges is shown. The equilibration takes the first 40 fs, and the system reaches stable depth after 80 fs. The 40 fs transition time to stability shows that the laser ablation process is time dependent. The penetration depths for the cases studied here are 20 Å, 35 Å, and 48 Å for the cases of Charges +1, +2, and +3, respectively.

Effects of repeated bombardments are shown in Fig. 8 by its transmissivity, defined as the ratio of the ablation depths between two consecutive laser illuminations. The transmissivity is different from penetration depth and absorption depth. The former measures how deep light can penetrate into a material, and the latter is related to light being absorbed exponentially with an optical absorption depth. From machining viewpoints, high energy laser can produce large damage (or dimple), but its transmissivity is the smallest due to bombarded atoms reducing the energy transfer from the laser to the xenon solid. Transmissivity is defined as the ratio of two successive penetration depths under repeated laser

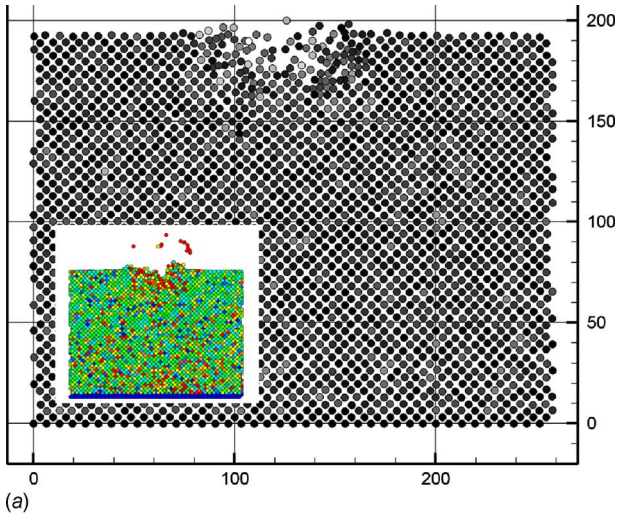

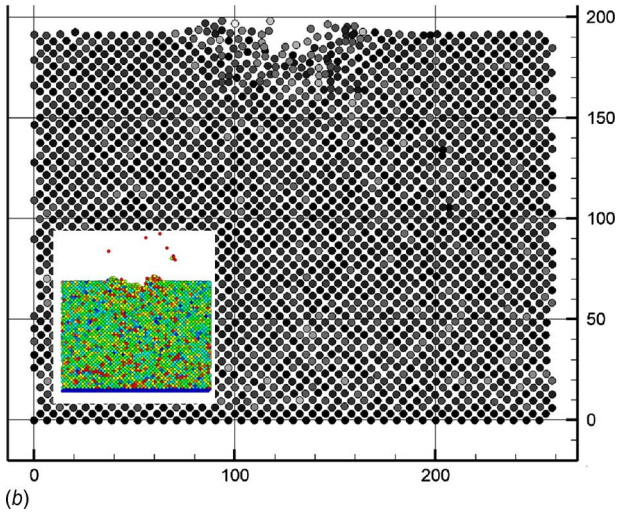

Fig. 4 Side-view morphology under the Charge +1 bombardment, a dimple (50±3) Å in diameter and (50±3) Å in depth is formed. (*a*) Nonrelativistic MD case and (*b*) relativistic MD case. Laser spot size is 8 Å in diameter. Insets show the morphology at a later time.

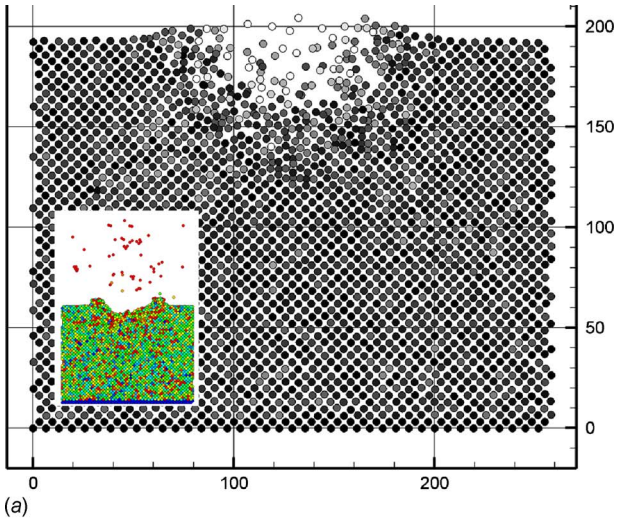

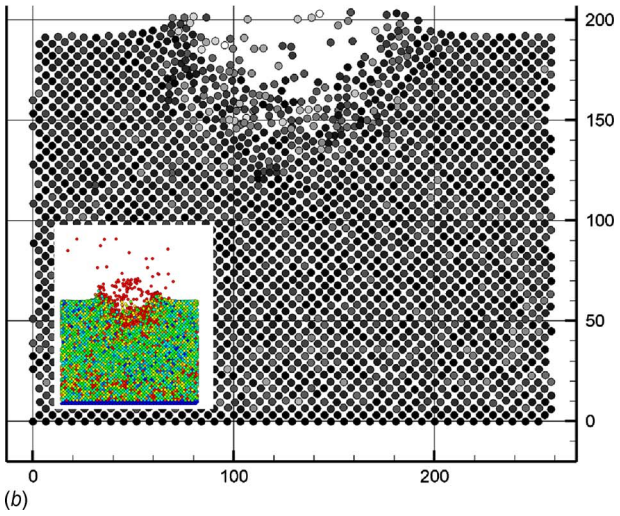

Fig. 5 Side-view morphology under the Charge +2 bombardment, a dimple (100±3) Å in diameter and (100±3) Å in depth is formed. (*a*) Nonrelativistic MD case and (*b*) relativistic MD case. Laser spot size is 8 Å in diameter. Insets show the morphology at a later time.

ablation. For low energy laser, repeated bombardments can lead to similar transmissivity with the high energy one. The plateau region of the Charge 1 case indicates that low energy laser processing can make the dimple deeper by repeating bombardments. However, the Charge 2 and 3 cases show that repeated processing does not increase the aspect ratios of the dimples.

As shown in Fig. 9, mean speeds of the particles in the nonrelativistic and relativistic models are significantly different. The speeds are in units of multiples of light speed, and the particles move away from the top surface. To calculate the mean speed of the atoms moving away from the surface, we fix the observation time equal to 10^{-2} fs, and average the speeds of atoms layer by layer away from the top surface. In the calculation, each layer is assumed to be about 1 Å. The results in Fig. 9 are from the case Charge +3. From the distribution of the mean speed, it can be seen that the particles with the highest speed are located at about 2–3 Å away from the top surface. This finding shows that nonrelativistic models cannot reflect reality.

3.2 Spatiotemporal Energy Propagation of Laser Ablation. The surface morphologies of the laser-processed Xe solid are shown in Figs. 10–12 for the three cases, Charges +1, +2, and +3, respectively. In all of the cases, the initial laser spot size is 8 Å. In Figs. 10(*a*) and 10(*b*), it can be seen that the initial periods of the ablation processes create local melting and transient to equilibrium. The local melting can be identified by observing the atomic arrangements on the figures as they lose their crystallinity. To be able to quantitatively distinguish crystalline and amorphous regions requires further analysis of their structural factors. Figures 10(*c*)–10(*f*) delineate the energy propagation away from the ablation center. When equilibrium is reached, Fig. 10(*f*) shows a triangular finish (40 Å), indicating that low energy ablation cannot form a circular hole even though the laser spot has a circular shape. Again, in this case, the penetration depth is 20 Å. For the Charge +2 case, Fig. 11 shows a similar feature to Fig. 10 in terms of the time evolution of energy distribution in space. When equilibrium is reached, Fig. 11(*f*) shows a most circular finish (90 Å in diameter). It is noted that the penetration depth in this case is 25 Å. We remark that the circularity of the damage depends on the interaction between the material and the laser intensity. When the laser energy increases to Charge +3, Fig. 12 shows large local melting. A high energy wave front is formed around the ablation hole (Fig. 12(*c*)). Figures 12(*c*)–12(*f*) delineate the energy propagation away from the ablation center. When equilibrium is reached, Figure 12(*f*) shows a rough circular finish (110 Å in

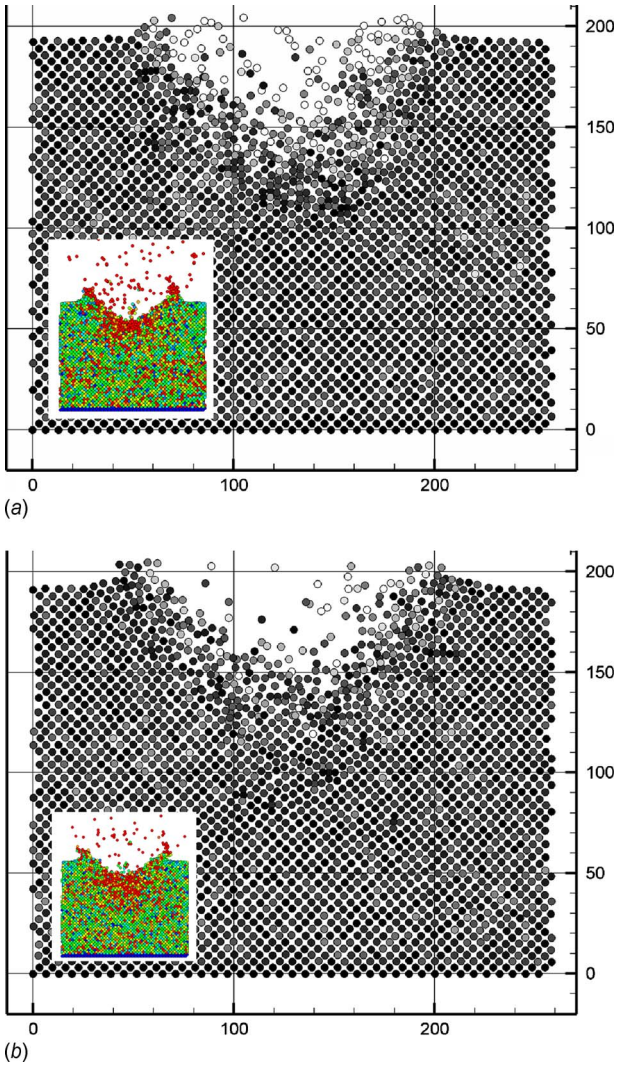

Fig. 6 Side-view morphology under the Charge +3 bombardment, a dimple (150±3) Å in diameter and (150±3) Å in depth is formed. (*a*) Nonrelativistic MD case and (*b*) relativistic MD case. Laser spot size is 8 Å in diameter. Insets show the morphology at a later time.

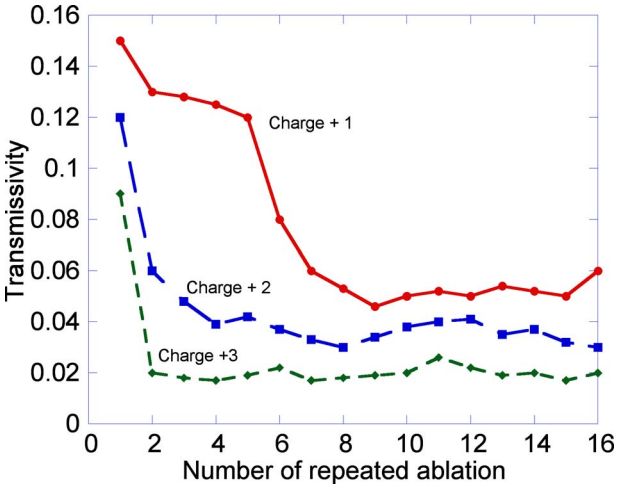

Fig. 8 Effects of repeated bombardments on the ablation depth. The transmissivity is defined as the ratio of the ablation depths between two consecutive laser illuminations.

diameter), indicating that high energy ablation cannot form a circular hole even though the laser spot has a circular shape (8 Å in diameter). The less noncircular shape may be due to the defect formation. The penetration depth is 50 Å. Remark that in Figs. 10–12 the simulation time runs from 1 ps to 25 ps, less than 100 ps (stabilized, as shown in Fig. 7), and hence the surface features continuously change, as well as the depth of the laser ablation.

Snapshots of the spatiotemporal distribution of energy wave are shown in Fig. 13 at time equal to 1 fs, 5 fs, and 10 fs after laser irradiation for the case of Charge +3. The inset shows the schematic of the direction of energy propagation away from the dimple. Remark that the atoms moving away from the surface more than 100 Å are not included in the energy calculation. Energy peaks are at $D=10$ Å, 15 Å, and 25 Å away from the center of ablation for $t=1$ fs, 5 fs, and 10 fs, respectively. It is noted that the energy wave is circularly symmetric when observed on the surface of xenon. The speed of wave is not constant. From 1 fs to 5 fs, the wave speed is about 1 Å/fs (or 100 m/s), and from 5 fs to 10 fs, it reduces to about 0.5 Å/fs (or 50 m/s). The reduction in the wave speed indicates that wave propagation is not reversible. Energy loss occurs in the process of propagation. Furthermore, the

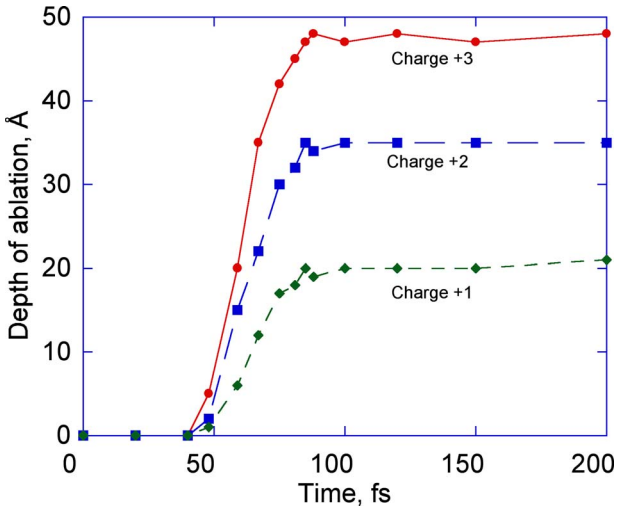

Fig. 7 Relationship with the depth of the dimples and the difference positive charge under the bombardment of a single laser pulse

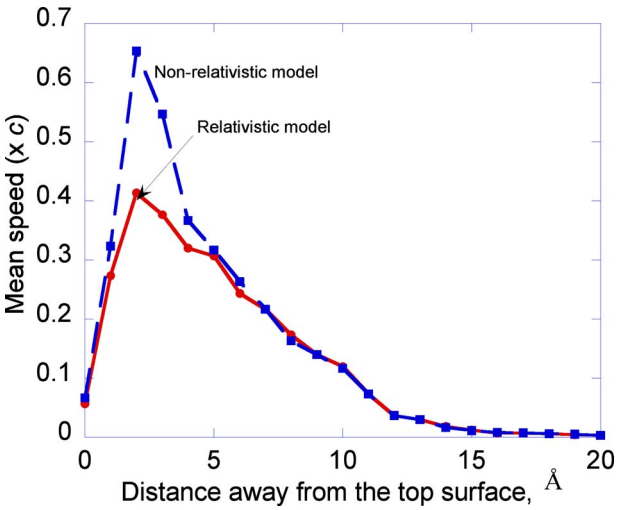

Fig. 9 Mean speed of the particles in the nonrelativistic and relativistic models. The speed is in units of multiples of light speed.

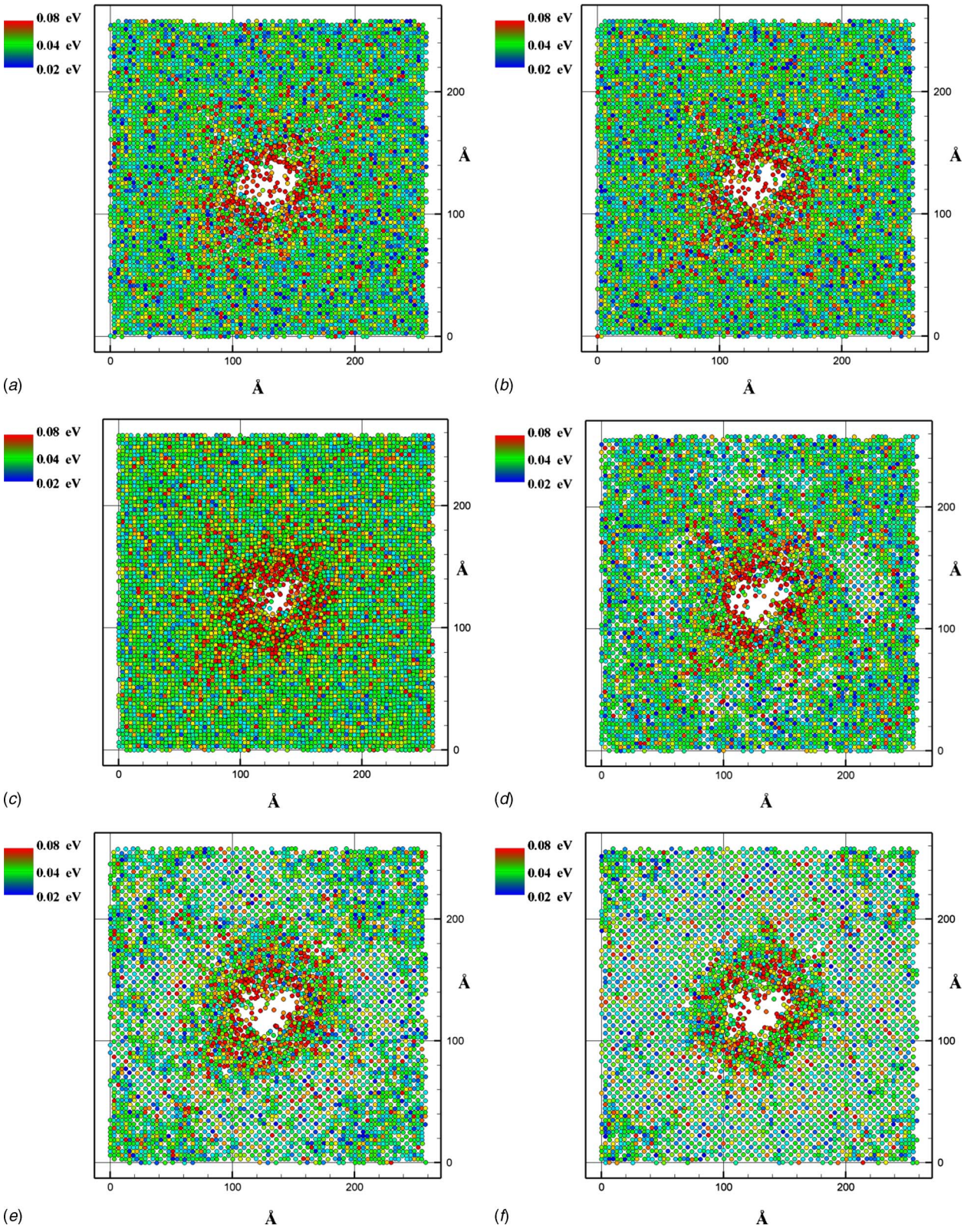

Fig. 10 Time evolution of energy distribution for the Charge 1 case. (*a*) $t=1$ ps, (*b*) $t=5$ ps, (*c*) $t=10$ ps, (*d*) $t=15$ ps, (*e*) $t=20$ ps, and (*f*) $t=25$ ps.

energy peaks 0.055, 0.041, and 0.031 at $D=10$, 15, and 25 Å, respectively, for the three cases show that the energy wave is of the dispersive type. The decay rate of the energy peaks is 0.71. The tail behavior of the energy wave for the case of $t=5$ and 10 fs shows no exponential decay. Remark that periodic boundary conditions are adopted. The mechanisms for the wave propagation are related to diffusional processes and a high thermal gradient due to laser ablation. The connection between classical continuum modeling and RMD simulation in this respect needs to be further explored in a later paper.

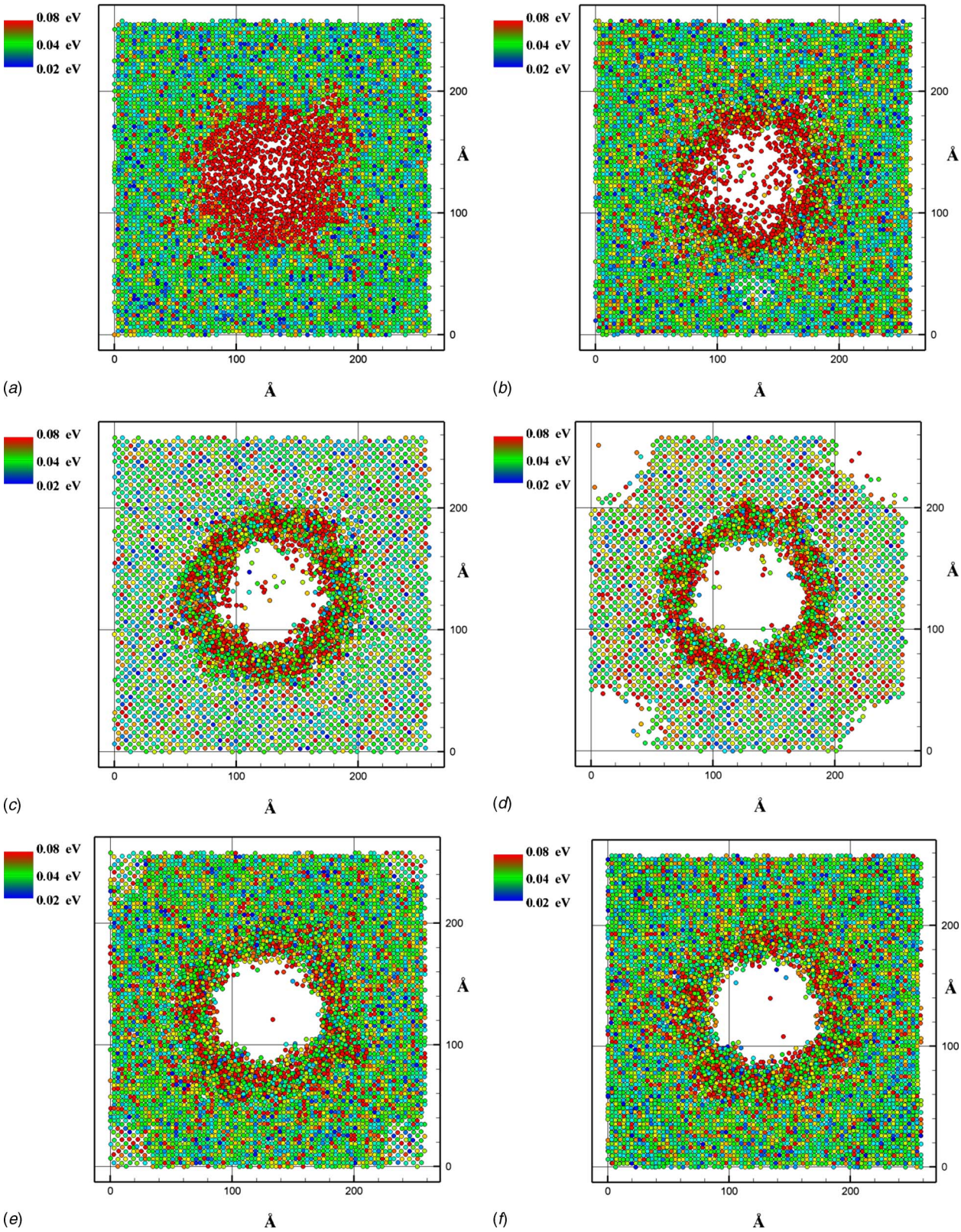

Fig. 11 Time evolution of energy distribution for the Charge 2 case. (*a*) *t*=1 ps, (*b*) *t*=5 ps, (*c*) *t*=10 ps, (*d*) *t*=15 ps, (*e*) *t*=20 ps, and (*f*) *t*=25 ps.

Figure 14 below shows the temperature versus time right of center, 50 Å on the top surface. During laser ablation at the center point at time of 40 fs, the temperature wave propagates to view points first at 59 fs with a temperature of 157 K. As shown in Fig. 15, the initial energy is about 52 MeV during the first 40 fs in the simulation. This energy is the equilibrium energy before the laser is illuminated on the xenon surface. At 40 fs, the system receives energy from assigning charges to the atoms in the laser spot;

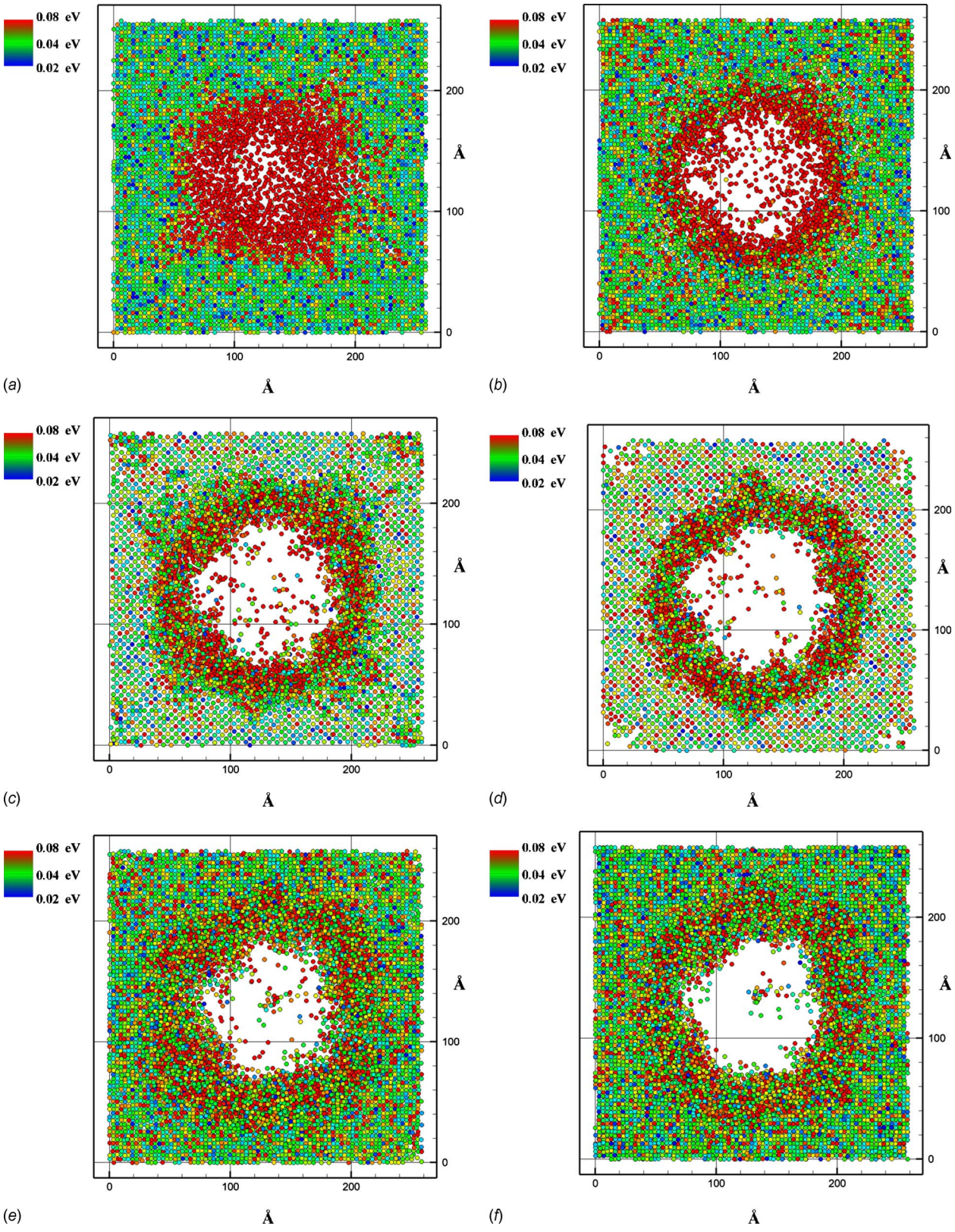

Fig. 12 Time evolution of energy distribution for the Charge 3 case. (*a*) *t*=1 ps, (*b*) *t*=5 ps, (*c*) *t*=10 ps, (*d*) *t*=15 ps, (*e*) *t*=20 ps, and (*f*) *t*=25 ps.

maximum energy is about 83 MeV. From 40 fs to 60 fs, the drop of total energy is associated with (1) the numerical error induced from the prechosen cutoff radius in our molecular dynamics simulation, (2) the existence of temperature control layers above the fixed substrate, and (3) atoms moving away from the top surface by more than 100 Å. The temperature control layers behave as an

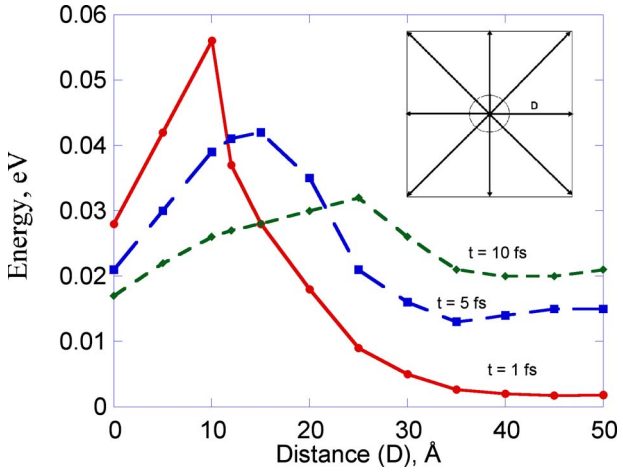

Fig. 13 Spatiotemporal distribution of energy wave at time=1, 5, and 10 fs after laser ablation for the case of Charge +3. The inset shows the schematic of the direction of energy propagation away from the dimple.

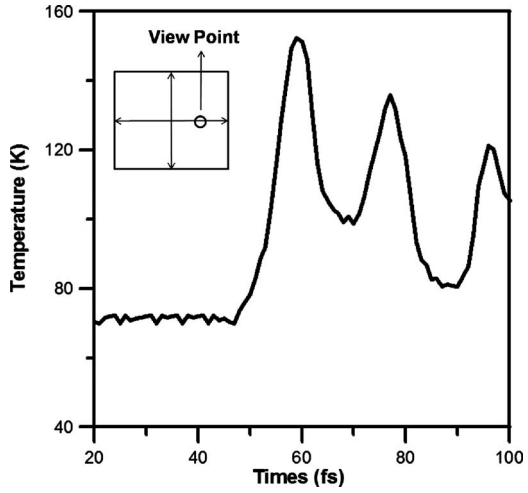

Fig. 14 Temperature variations versus time. The inset indicates the location of the temperature measurement that has been taken on the surface of the model.

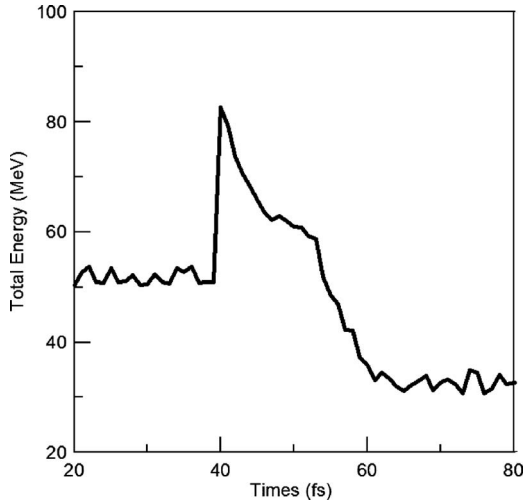

Fig. 15 Total energy of the system from the beginning to the end of the simulation. At time equal to 40 fs, ion Charge +1 is assigned to atoms affected by the laser pulse.

energy source or sink to maintain the temperature of the model. Therefore, our system is not a conserved system. Between 60 fs and 80 fs, the system energy reaches about 30 MeV, different from the initial 52 MeV due to the removal of atoms.

4 Conclusions

With the consideration of relativistic effects, our particle-dynamics simulations of the interaction of intense (being inferred from ionized charges) femtosecond (being considered as the atoms in the laser spot being ionized in the single time step of our molecular dynamics simulation) laser pulses have shown that the damage shape depends on the fluence of the laser and the number of laser pulses being received by the surface atoms. The novel combination of the Coulomb and Lennard-Jones potential, as well as the consideration of special relativity in the conventional molecular dynamics simulation, enables realistic predictions of the ablation process. The results of our simulations show that using the Coulomb potential is suitable to simulate the Coulomb explosion phenomenon of the laser ablation process. Furthermore, we show that to reach the same damage depth, one can use low laser ablation fluence with several repeated laser pulse bombardments, or a high fluence laser. From the present simulations, it is found that low energy laser pulses may induce certain thermal expansion and vibration with no removal of surface atoms. However, for high energy pulses, surface atoms may be removed and the shapes of final finishing can be controlled by the level of energy, as well as the illumination time for moderate laser power. Longer illumination time ensures that several pulses will be received by the surface atoms. When the energy of laser pulses is too high, damage in terms of the activation of slip systems may occur.

Acknowledgment

The authors thank the computer and network center at NCKU for helpful support on high speed computing and gratefully acknowledge the financial support to this research by the National Science Council of Taiwan under Grant No. NSC 95-2221-E-006-385-MY3.

References

[1] Kumarappan, V., Krishnamurthy, M., and Mathur, D., 2001, "Asymmetric High-Energy Ion Emission From Argon Clusters in Intense Laser Fields," Phys. Rev. Lett., **87**, p. 085005.
[2] Kumarappan, V., Krishnamurthy, M., and Mathur, D., 2003, "Explosions of Water Clusters in Intense Laser Fields," Phys. Rev. A, **67**, p. 043204.
[3] Fleischer, R. L., Price, P. B., and Walker, R. M., 1965, "Ion Explosion Spike Mechanism for Formation of Charged-Particle Tracks in Solids," J. Appl. Phys., **36**, pp. 3645–3652.
[4] Trautmann, C., Klaumunzer, S., and Trinkaus, H., 2000, "Effect of Stress on Track Formation in Amorphous Iron Boron Alloy: Ion Tracks as Elastic Inclusions," Phys. Rev. Lett., **85**, pp. 3648–3651.
[5] Lesueur, D., and Dunlop, A., 1993, "Damage Creation Via Electronic Excitations in Metallic Targets Part II: A Theoretical Model," Radiat. Eff. Defects Solids, **126**, pp. 163–172.
[6] Papaleo, R. M., de Oliveira, L. D., Farenzena, L. S., de Araujo, M. A., and Livi, R. P., 2000, "Probing Thermomechanical Behavior of Polymers at the Nanometer Scale With Single-Ion Bombardment and Scanning Force Microscopy," Phys. Rev. B, **62**, pp. 11273–11276.
[7] Johnson, R. E., and Brown, W. L., 1982, "Electronic Mechanisms for Sputtering of Condensed-Gas Solids by Energetic Ions," Nucl. Instrum. Methods Phys. Res., **198**, pp. 103–118.
[8] Pande, C. S., and Suenaga, M., 1976, "A Model of Flux Pinning by Grain Boundaries in Type-II Superconductors," Appl. Phys. Lett., **29**, pp. 443–444.
[9] Schenkel, T., Hamza, A. V., Barnes, A. V., and Schneider, D. H., 1998, "Ablation of GaAs by Intense, Ultrafast Electronic Excitation From Highly Charged Ions," Phys. Rev. Lett., **81**, pp. 2590–2593.
[10] Jungreuthmayer, C., Geissler, M., Zanghellini, J., and Brabec, T., 2004, "Microscopic Analysis of Large-Cluster Explosion in Intense Laser Fields," Phys. Rev. Lett., **92**, p. 133401.
[11] Anisimov, S. I., Kapeliovich, B. L., and Perel'man, T. L., 1974, "Electron Emission From Metal Surfaces Exposed to Ultrashort Laser Pulses," Sov. Phys. JETP, **39**, pp. 375–377.
[12] Kotake, S., and Kuroki, M., 1993, "Molecular Dynamics Study of Solid Melting and Vaporization by Laser Irradiation," Int. J. Heat Mass Transfer, **36**, pp. 2061–2067.
[13] Girifalco, L. A., and Weizer, V. G., 1959, "Application of Morse Potential Function to Cubic Metals," Phys. Rev., **114**, pp. 687–690.

[14] Ohmura, E., Fukumoto, I., and Miyamoto, I., 1996, "Molecular Dynamics Simulation of Ablation Process With Ultrashort-Pulse Laser," RIKEN Rev., **32**, pp. 19–22.
[15] Etcheverry, J. I., and Mesaros, M., 1999, "Molecular Dynamics Simulation of the Production of Acoustic Waves by Pulsed Laser Irradiation," Phys. Rev. B, **60**, pp. 9430–9434.
[16] Wang, X., and Xu, X., 2002, ""Molecular Dynamics Simulation of Heat Transfer and Phase Change During Laser Material Interaction," ASME J. Heat Transfer, **124**, pp. 265–274.
[17] Wang, X., and Xu, X., 2003, "Molecular Dynamics Simulation of Thermal and Thermomechanical Phenomena in Picosecond Laser Material Interaction," Int. J. Heat Mass Transfer, **46**, pp. 45–53.
[18] Ditmire, T., Tisch, J. W. G., Springate, E., Mason, M. B., Hay, N., Smith, R. A., Marangos, J., and Hutchinson, M. H. R., 1997, "High-Energy Ions Produced in Explosions of Superheated Atomic Clusters," Nature (London), **386**, pp. 54–56.
[19] Quaglia, L., and Cornaggia, C., 2000, "Experimental Evidence of Excited Multicharged Atomic Fragments Coming From Laser-Induced Coulomb Explosion of Molecules," Phys. Rev. Lett., **84**, pp. 4565–4568.
[20] Rabinovich, V. A., Vasserman, A. A., Nedostup, V. I., and Veksler, L. S., 1988, *Thermophysical Properties of Neon, Argon, Krypton and Xenon*, Hemisphere, Washington, DC.
[21] Lennard-Jones, J. E., 1931, "Cohesion," Proc. Phys. Soc. London, **43**, pp. 461–482.
[22] Codling, K., and Frasinski, L. J., 1993, "Dissociative Ionization of Small Molecules in Intense Laser Fields," J. Phys. B, **26**, pp. 783–809.
[23] Stapelfeldt, H., Constant, E., and Corkum, P. B., 1995, "Wave Packet Structure and Dynamics Measured by Coulomb Explosion," Phys. Rev. Lett., **74**, pp. 3780–3783.
[24] Stapelfeldt, H., Sakai, H., Constant, E., and Corkum, P. B., 1997, "Formation and Measurement of Molecular Quantum Picostructures," Phys. Rev. A, **55**, pp. R3319–R3322.
[25] Watson, C., and Tombrello, T., 1985, "A Modified Lattice Potential Model of Electronically Mediated Sputtering," Radiat. Eff. Defects Solids, **89**, pp. 263–283.
[26] Last, I., and Jortner, J., 1999, "Quasiresonance Ionization of Large Multicharged Clusters in a Strong Laser Field," Phys. Rev. A, **60**, pp. 2215–2221.
[27] Last, I., and Jortner, J., 2000, "Dynamics of the Coulomb Explosion of Large Clusters in a Strong Laser Field," Phys. Rev. A, **62**, p. 013201.
[28] Brewczyk, M., Clark, C. W., Lewenstein, M., and Rzazewski, K., 1998, "Stepwise Explosion of Atomic Clusters Induced by a Strong Laser Field," Phys. Rev. Lett., **80**, pp. 1857–1860.
[29] Krainov, V. P., and Roshchupin, A. S., 2001, "Dynamics of Coulomb Explosion of Large Xe Clusters Irradiated by a Super-Intense Ultra-Short Laser Pulse," J. Phys. B, **34**, pp. L297–L303.
[30] Okino, T., Yamanouchi, K., Shimizu, T., Furusawa, K., Hasegawa, H., Nabekawa, Y. and Midorikawa, K., 2006, "Attosecond Molecular Coulomb Explosion," Chem. Phys. Lett., **432**(1–3), pp. 68–73.